UNIVERSITY OF IOANNINA
SCHOOL OF HEALTH SCIENCES
DEPARTMENT OF MEDICINE

MORPHOLOGICAL AND CLINICAL-LABORATORY SCIENCES SECTOR
LABORATORY OF MEDICAL PHYSICS

BONE QUALITY ASSESSMENT IN NORMAL AND DISEASED TISSUES USING VIBRATIONAL SPECTROSCOPY, NEUTRON DIFFRACTION AND MULTIVARIATE ANALYSIS

ELEFTHERIOS PAVLOU

Ph.D. THESIS

IOANNINA 2025

UNIVERSITY OF IOANNINA
SCHOOL OF HEALTH SCIENCES
DEPARTMENT OF MEDICINE

MORPHOLOGICAL AND CLINICAL-LABORATORY SCIENCES SECTOR
LABORATORY OF MEDICAL PHYSICS

BONE QUALITY ASSESSMENT IN NORMAL AND DISEASED TISSUES USING VIBRATIONAL SPECTROSCOPY, NEUTRON DIFFRACTION AND MULTIVARIATE ANALYSIS

ELEFTHERIOS PAVLOU

Ph.D. THESIS
IOANNINA 2025

This research is co-financed by Greece and the European Union (European Social Fund-ESF) through the Operational Programme «Human Resources Development, Education and Lifelong Learning» in the context of the project "Strengthening Human Resources Research Potential via Doctorate Research – 2nd Cycle" (MIS-5000432), implemented by the State Scholarships Foundation (IKY).

ΠΑΝΕΠΙΣΤΗΜΙΟ ΙΩΑΝΝΙΝΩΝ
ΣΧΟΛΗ ΕΠΙΣΤΗΜΩΝ ΥΓΕΙΑΣ
ΤΜΗΜΑ ΙΑΤΡΙΚΗΣ

ΜΟΡΦΟΛΟΓΙΚΟΣ - ΚΛΙΝΙΚΟΕΡΓΑΣΤΗΡΙΑΚΟΣ ΤΟΜΕΑΣ
ΕΡΓΑΣΤΗΡΙΟ ΙΑΤΡΙΚΗΣ ΦΥΣΙΚΗΣ

ΑΞΙΟΛΟΓΗΣΗ ΟΣΤΙΚΗΣ ΠΟΙΟΤΗΤΑΣ ΥΓΙΩΝ ΚΑΙ ΠΑΘΟΛΟΓΙΚΩΝ ΟΣΤΩΝ ΜΕ ΤΕΧΝΙΚΕΣ ΔΟΝΗΤΙΚΗΣ ΦΑΣΜΑΤΟΣΚΟΠΙΑΣ, ΠΕΡΙΘΛΑΣΗΣ ΝΕΤΡΟΝΙΩΝ ΚΑΙ ΠΟΛΥΠΑΡΑΜΕΤΡΙΚΗΣ ΑΝΑΛΥΣΗΣ

ΕΛΕΥΘΕΡΙΟΣ ΠΑΥΛΟΥ

ΔΙΔΑΚΤΟΡΙΚΗ ΔΙΑΤΡΙΒΗ
ΙΩΑΝΝΙΝΑ 2025

Το έργο συγχρηματοδοτείται από την Ελλάδα και την Ευρωπαϊκή Ένωση (Ευρωπαϊκό Κοινωνικό Ταμείο) μέσω του Επιχειρησιακού Προγράμματος «Ανάπτυξη Ανθρώπινου Δυναμικού, Εκπαίδευση και Διά Βίου Μάθηση», στο πλαίσιο της Πράξης «Ενίσχυση του ανθρώπινου ερευνητικού δυναμικού μέσω της υλοποίησης διδακτορικής έρευνας – 2ος Κύκλος» (MIS-5000432), που υλοποιεί το Ίδρυμα Κρατικών Υποτροφιών (ΙΚΥ).

Ευρωπαϊκή Ένωση
Ευρωπαϊκό Κοινωνικό Ταμείο

Επιχειρησιακό Πρόγραμμα
Ανάπτυξη Ανθρώπινου Δυναμικού,
Εκπαίδευση και Διά Βίου Μάθηση
Με τη συγχρηματοδότηση της Ελλάδας και της Ευρωπαϊκής Ένωσης

ΕΣΠΑ 2014-2020
ανάπτυξη - εργασία - αλληλεγγύη

Η έγκριση της διδακτορικής διατριβής από το Τμήμα Ιατρικής του Πανεπιστημίου Ιωαννίνων δεν υποδηλώνει αποδοχή των γνωμών του συγγραφέα Ν. 5343/32, άρθρο 202, παράγραφος 2 (νομική κατοχύρωση του Ιατρικού Τμήματος).

Ημερομηνία αίτησης του κ. Παύλου Ελευθέριου: 05-12-2017

Ημερομηνία ορισμού Τριμελούς Συμβουλευτικής Επιτροπής: Γ.Σ. αριθμ. 846α/27-03-2018

Μέλη Τριμελούς Συμβουλευτικής Επιτροπής:

Επιβλέπων:

Κουρκουμέλης Νικόλαος, Επίκουρος Καθηγητής Υγιεινής Ιατρικής Φυσικής του Τμήματος Ιατρικής του Πανεπιστημίου Ιωαννίνων

Μέλη:

Εμφιετζόγλου Δημήτριος, Αναπληρωτής Καθηγητής Ιατρικής Φυσικής-Ακτινοφυσικής του Τμήματος Ιατρικής του Πανεπιστημίου Ιωαννίνων

Jian Wang, Associate Professor Southern Medical University, Nanfang Hospital China

Ημερομηνία ορισμού θέματος: 16-04-2018

«Συγκριτική μελέτη της οστικής ποιότητας υγιών και παθολογικών οστών με τεχνικές δονητικής φασματοσκοπίας, μικροσκοπίας και πολυπαραμετρικής ανάλυσης»

«Bone Quality Assessment in Normal and Diseased Tissues using Vibrational Spectroscopy, Microscopy and Multivariate Analysis»

Τροποποίηση τίτλου θέματος διδακτορικής διατριβής: Γ.Σ. αριθμ. 960α/21-04-2021

«Αξιολόγηση οστικής ποιότητας υγιών και παθολογικών οστών με τεχνικές δονητικής φασματοσκοπίας, περίθλασης νετρονίων και πολυπαραμετικής ανάλυσης»

«Bone Quality Assessment in Normal and Diseased Tissues using Vibrational Spectroscopy, Neutron Diffraction and Multivariate Analysis»

ΟΡΙΣΜΟΣ ΕΠΤΑΜΕΛΟΥΣ ΕΞΕΤΑΣΤΙΚΗΣ ΕΠΙΤΡΟΠΗΣ: 1080α/14-12-2023

1. Κουρκουμέλης Νικόλαος, Αναπληρωτής Καθηγητής Ιατρικής Φυσικής-Βιοφυσικής του Τμήματος Ιατρικής του Πανεπιστημίου Ιωαννίνων
2. Εμφιετζόγλου Δημήτριος, Καθηγητής Ιατρικής Φυσικής-Ακτινοφυσικής του Τμήματος Ιατρικής του Πανεπιστημίου Ιωαννίνων
3. Wang Jian, Professor of Orthopedics, Southern Medical University, China
4. Χατζηκακού Σωτήριος, Καθηγητής Χημείας του Τμήματος Χημείας του Πανεπιστημίου Ιωαννίνων
5. Μπούμπα Βασιλική, Καθηγήτρια Ιατροδικαστικής-Τοξικολογίας με έμφαση στη Δικαστική Τοξικολογία του Τμήματος Ιατρικής του Πανεπιστημίου Ιωαννίνων
6. Σπυρίδωνος Παναγιώτα, Επίκουρη Καθηγήτρια Ιατρικής Πληροφορικής του Τμήματος Ιατρικής του Πανεπιστημίου Ιωαννίνων
7. Κυριακού Ιωάννα, Επίκουρη Καθηγήτρια Ιατρικής Φυσικής με έμφαση στη Μικροδοσιμετρία του Τμήματος Ιατρικής του Πανεπιστημίου Ιωαννίνων

Έγκριση Διδακτορικής Διατριβής με βαθμό **«ΑΡΙΣΤΑ»** στις **09-01-2025**

Ιωάννινα 09-05-2025

ΠΡΟΕΔΡΟΣ ΤΟΥ ΤΜΗΜΑΤΟΣ ΙΑΤΡΙΚΗΣ

Σπυρίδων Κονιτσιώτης

Καθηγητής Νευρολογίας

ΙΑΤΡΙΚΗ ΣΧΟΛΗ · ΠΑΝΕΠΙΣΤΗΜΙΟ ΙΩΑΝΝΙΝΩΝ · 1977

Η Γραμματέας του Τμήματος

Αικατερίνη Λαγού

Table of Contents

Table of Figures

The mean preprocessed healthy and osteoporotic spectra collected from the periosteal surfaces of tibias, humeri, femurs, and ribs are shown in Fig. 8.59. All characteristic spectral features of bone are present, with the exception, as in the case of the transverse measurements, of the phenylalanine peak at ~1003 cm^{-1}, which appears as a shoulder on the lower end of the carbonate

Index of Tables

Acknowledgement – Ευχαριστίες

The following acknowledgement is written in Greek to honor and express gratitude to individuals who provided support in my native language.

Η παρούσα διδακτορική διατριβή εκπονήθηκε στο εργαστήριο Ιατρικής Φυσικής του τμήματος Ιατρικής του Πανεπιστημίου Ιωαννίνων υπό την επίβλεψη του καθηγητή Ιατρικής Φυσικής κ. Νικόλαου Κουρκουμέλη. Η ολοκλήρωση της διατριβής δε θα ήταν εφικτή εάν στη μακρά αυτή προσπάθεια δεν είχα τη συνεισφορά ορισμένων ανθρώπων στους οποίους θα ήθελα να εκφράσω τις ειλικρινείς και θερμές ευχαριστίες μου.

Πρωτίστως, θέλω να ευχαριστήσω τον κ. Κουρκουμέλη για την αμέριστη συμπαράσταςή του, τη συνεχή καθοδήγηση και την ουσιαστική υποστήριξη του, τόσο επιστημονική όσο και ψυχολογική. Επίσης τον ευχαριστώ θερμά για την εμπιστοσύνη που μου έδειξε, την ενθάρρυνση που μου παρείχε όλο αυτό το διάστημα, και τον χρόνο που μου αφιέρωσε συζητώντας για θέματα σχετικά με τη διατριβή, αλλά και άσχετα με αυτή. Επιπλέον, τον ευχαριστώ για την αγάπη του για το εργαστήριο Ιατρικής Φυσικής και την προσπάθειά του να υπάρχει κλίμα φιλίας και αλληλοϋποστήριξης μεταξύ των μελών του.

Επίσης, θα ήθελα να ευχαριστήσω τα μέλη της τριμελούς συμβουλευτικής επιτροπής: τον Καθηγητή Ιατρικής Φυσικής-Ακτινοφυσικής κ. Εμφιετζόγλου Δημήτριο και τον Καθηγητή Jian Wang που με τίμησαν με τη συμμετοχή και την υποστήριξη τους. Ακομή ευχαριστώ τα μέλη της επταμελούς εξεταστικής επιτροπής: τον Καθηγητή του τμήματος Χημείας κ. Χατζηκακού Σωτήρη, την Αναπληρώτρια Καθηγήτρια του τμήματος Ιατρικής κα Σπυρίδωνος Παναγιώτα, την Καθηγήτρια του τμήματος Ιατρικής κα Μπούμπα Βασιλική, και την Επίκουρη Καθηγήτρια του τμήματος Ιατρικής κα Κυριακού Ιωάννα.

Ευχαριστώ τον Dr. Robert Papoular, Senior Sientist at Commissariat à l'Énergie Atomique et aux Énergies Alternatives, France, για την πολύτιμη βοήθειά του στην εκτέλεση πειραμάτων περίθλασης νετρονίων και στην ανάλυση των διαγραμμάτων περίθλασης. Η υποστήριξη και η καθοδήγησή του υπήρξαν καθοριστικές για την επιτυχία της παρούσας διατριβής.

Επίσης ευχαριστώ την κα Αθηνά Λάνη, γενική ιατρό, για την εφαρμογή του πρωτοκόλλου επαγόμενης οστεοπόρωσης στα κουνέλια.

Ενα μεγάλο ευχαριστώ οφείλω σε όλους τους προπτυχιακούς και μεταπτυχιακούς φοιτητες, καθώς και στους υποψήφιους διδάκτορες του εργαστηρίου με τους οποίους συνυπήρξαμε στον ίδιο χώρο ή συνεργαστήκαμε. Ιδιαιτέρως θα ήθελα να ευχαριστήσω τη μεταδιδακτορική ερευνήτρια Δρ Μάρθα Βαρδάκη, τον νυν Δρ, Γιώργο Ρώσσο, και τις υποψήφιες διδακτόρισσες Χρύσα Πετροκιλίδου και Χριστίνα Κοτρούμπελου για το συναδελφικό και φιλικό κλίμα που

αναπτύξαμε τις αμέτρητες ώρες που εργαστήκαμε μαζί και για τα λογοπαίγνια που αναγκάστηκαν να υπομείνουν.

Ευχαριστώ το Ιδρυμα Κρατικών Υποτροφιών (ΙΚΥ) για την οικονομική υποστήριξη που μου παρείχε, χωρίς την οποία δε θα ήταν δυνατή η εκπόνηση αυτής της εργασίας.

Τέλος, θα ήθελα να ευχαριστήσω την οικογένειά μου για την ηθική υποστήριξη που μου παρείχε σε όλες τις δυσκολίες που αντιμετώπισα, καθώς και τη σύντροφό μου, Μαριάννα, που είναι δίπλα μου όλα αυτά τα χρόνια.

Ελευθέριος Παύλου

“Κι ας μη νικήσουμε ποτέ, θα πολεμάμε πάντα…”

Β. Μάγγος

1. Bone

1.1. Introduction

Bone is one of the hardest substances of the body of vertebrate animals, with human bones rated at 5 according to the Mohs hardness scale, with 1 being the softest material (talc) and 10 the hardest (diamond), and the organ that constitutes the main rigid part of their skeletal system [1,2]. Other parts of the skeletal system of vertebrates include joints, cartilages, and ligaments. Bones are charged with the crucial role of providing structural stability and support to the body, as well as protecting vital internal organs, such as the brain, spinal cord, heart, lungs, etc. from external forces by enclosing them within a sturdy framework. Additionally, bones play a pivotal role in the mobility of organisms: skeletal muscles are attached to bones by tendons and effectively use them as levers, allowing the body as a whole and the different body parts to move.

Apart from the mechanical roles in support, protection, and movement, bones also have important functional roles that contribute to the homeostasis of the body. Bones serve as storage for various minerals, with calcium (Ca), more than 99% of which is stored in bones, and phosphorus (P) (both combined mainly in the form of hydroxyapatite) being the most important [3]. Furthermore, the internal (marrow) structure of bone contains numerous interconnecting cavities which are filled with adipose tissue (fat cells), often referred to as yellow or white marrow, whose function is not yet completely clear, but recent evidence shows that it plays a role in maintaining bone marrow homeostasis and affects the metabolism of the whole body [4]. Along with yellow marrow, red marrow also occupies the internal cavities of bones, primarily of flat bones in adult organisms, which is composed of mesenchymal stem cells, hematopoietic stem cells (hematopoiesis meaning “blood formation”), and progenitor cells that mature into myeloid, and lymphoid cells. Red bone

marrow is the basic hematopoietic center of the body, where red blood cells, white blood cells, and platelets are produced [5].

1.2. Bone structure

Bones are composed of osseous tissue, a specialized, hard, and dense form of connective tissue that constitutes most of the skeletal framework. Bone tissue is essential for supporting the body's structure, protecting vital organs, storing minerals, and facilitating blood cell production in the bone marrow. It consists of a mineralized matrix and three major types of mature cells: osteoblasts, which synthesize the organic components of the matrix; osteocytes, which are differentiated osteoblasts enclosed in the material they secrete (lacunae); and osteoclasts, large multinucleated cells essential for bone growth and remodeling. The matrix comprises an organic component, primarily made of collagen fibers that provide elasticity, and an inorganic component, primarily composed of hydroxyapatite crystals, which impart strength and rigidity to bones [6].

The skeletal system of vertebrates varies across classes (e.g., mammals, fish, birds) and species (e.g., humans, mice, rabbits); however, they all share a similar set of bone types, which, depending on their shape, can be classified into the following categories: long bones, short bones, flat bones, sesamoid bones, and irregular bones [7,8].

- Long bones (e.g., tibia, femur, humerus) are usually located in the limbs and have a tubular shape with a shaft (diaphysis) between two wider ends (epiphyses). They are generally elongated in shape and function as levers that enable movement through muscle contraction.
- Short bones (e.g., carpals, tarsals) are roughly cube-shaped, with approximately equal length, width, and thickness. They provide stability and support to the skeletal system and allow for limited movement.
- Flat bones (e.g., bones of the cranium, pelvis, and ribs) are thin and broad, often resembling flat plates (which may also be curved). Their role is to provide anchoring surfaces for muscles and protect vital internal organs.
- Sesamoid bones (e.g., the patella in humans) are small bones embedded within tendons, helping them withstand excessive forces. Their smooth surfaces allow tendons to slide over them, acting as pulleys that improve stress distribution and muscle efficiency.
- Irregular bones (e.g., vertebrae, facial bones) have complex, non-uniform shapes that do not fit into any other category. They are uniquely adapted for specific functions, such as support, protection, and muscle attachment, due to their varied structures and complex forms.

In addition to the classification by shape, bones can also be macroscopically categorized based on their internal structure into cortical or trabecular types, depending on the structure of the osseous tissue.

- Cortical bone, also known as compact bone, is the dense and hard outer layer of bones, providing strength to withstand external forces. It appears smooth and white and accounts for approximately 80% of the total mass of an adult human skeleton [9].
- Trabecular bone, also known as cancellous or spongy bone, is found internally and consists of a lattice of numerous interconnecting cavities that create a honeycomb-like structure. This configuration reduces the bone's weight and provides space that is filled by bone marrow.

1.2.1. Bone cells

Bone is a dynamic tissue that undergoes continuous remodeling throughout an organism's life as a result of both physiological and pathological responses. The activities of bone-forming cells, such as osteoblasts, and bone-resorbing cells, such as osteoclasts, are in constant interplay to maintain a delicate balance. When this balance is disrupted, it can lead to diseases such as osteoporosis. It is, therefore, essential to understand how the various bone cell types contribute to bone formation, maintenance, and resorption, ultimately influencing overall skeletal health.

Osteoblasts

Osteoblasts are the cells responsible for the formation and storage of new bone tissue. They have a single nucleus and do not undergo mitosis, meaning they do not multiply. Osteoblasts arise from osteoprogenitor cells (which in turn originate from mesenchymal stem cells), which are undifferentiated precursors that can differentiate into osteoblasts in response to specific signaling factors [9]. Found exclusively at the surface of the bone matrix, osteoblasts produce the organic components of the bone matrix (such as type I collagen, proteoglycans, and glycoproteins) in the form of a secreted protein called osteoid. The osteoid subsequently undergoes mineralization to form mature bone tissue [6]. During this process, some osteoblasts become encased in the newly-formed matrix and they differentiate into osteocytes, the most abundant cell type in mature bone. Depending on the bone tissue needs and microenvironment, osteoblasts can also become bone-lining cells that create a thin layer covering the internal and external surfaces of bones, known as the periosteum and endosteum, respectively (Fig. 1.1). The life cycle of osteoblasts ends with apoptosis (programmed cell death).

Osteocytes

Osteocytes are single-nucleus cells and are the most common cells in bone tissue (90-95% of total cellular component) [7]. They originate from differentiated osteoblasts, which become encased in cavities surrounded by the matrix they secrete. Each of these cavities, known as lacunae, contains a single osteocyte. Morphologically, osteocytes differ from osteoblasts; they have extended dendritic processes that connect to other bone cells—such as osteoblasts, bone-lining cells, and other osteocytes—as well as to blood vessels. Through these processes and an extensive network of small channels approximately 300 nm in diameter (canaliculi), osteocytes communicate with neighboring cells via gap junctions and function as a network of mechanical sensors, detecting stress and damage and triggering bone remodeling. Like osteoblasts, they cannot undergo mitosis and, in humans, can live for several decades [9]. Following apoptosis, signaling molecules attract osteoclasts to resorb the bone around the dead cells, initiating a remodeling cycle in which osteoblasts lay down new bone and replace the lost osteocytes, preserving bone structure and quality [10]. Diseases like osteoporosis can shorten the lifespan of osteocytes, leading to decreased bone quality.

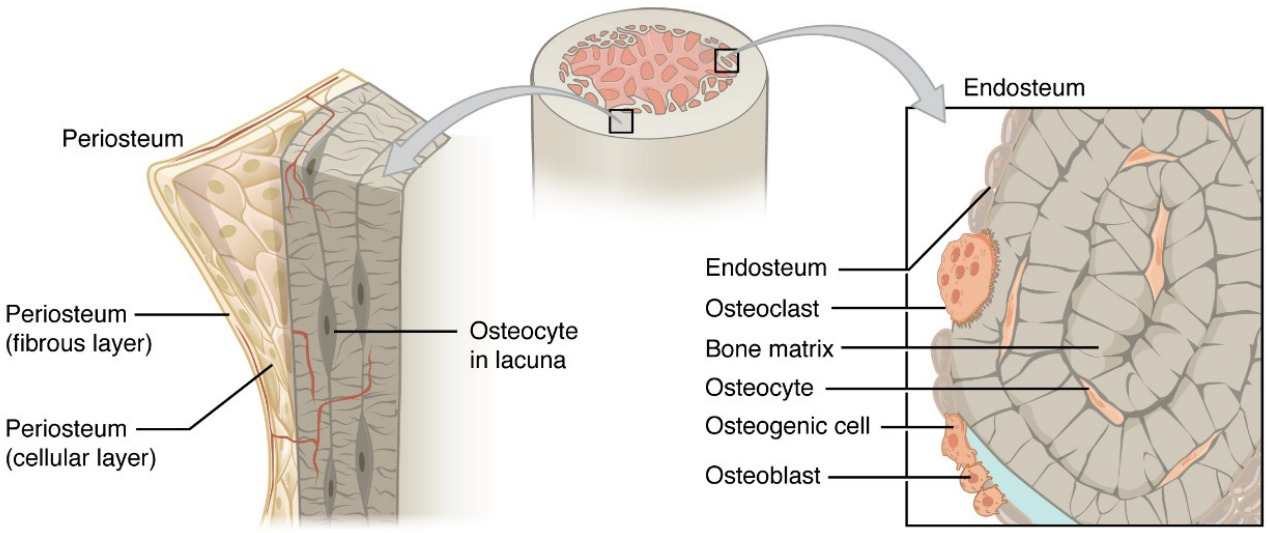

Figure 1.1: Bone structure at the cellular level. Zoomed-in insets near the periosteum and endosteum highlight the tissue's cellular structure at these regions. Figure from [7], licensed under CC BY 4.0.

Osteoclasts

Osteoclasts are large, multinucleated cells that can contain anywhere from 5 to more than 50 nuclei, and they are the only known cells capable of resorbing bone [9]. Unlike osteoblasts, which arise from the mesenchymal stem cell lineage involved in the differentiation of connective tissues, osteoclasts originate from the fusion of mononuclear precursor cells within the monocyte-

macrophage lineage, which is associated with hematopoiesis [11]. This difference in origin underscores the distinct functions and developmental pathways of bone-forming and bone-resorbing cells. During bone resorption, osteoclasts adhere to the bone surface using a specialized structure known as the ruffled border, which increases their surface area and enhances their resorptive capabilities. They create a sealed microenvironment called the resorption lacuna, or Howship's lacuna. Within this environment, osteoclasts secrete protons, which acidify the area, facilitating the dissolution of hydroxyapatite crystals in the bone matrix. They also release lytic enzymes, such as collagenase and cathepsin K, which degrade the organic components of the bone matrix [9]. This coordinated activity not only allows for the resorption of old or damaged bone but also plays a critical role in maintaining calcium and phosphate homeostasis in the body.

1.2.2. Cortical bone

Cortical bone, also known as compact bone, is the dense, hard layer of bone tissue that forms the external surface of bones. It represents approximately 80% of the total bone mass of an adult human, with the remaining 20% being trabecular bone [9]. The primary role of cortical bone is to provide rigidity and mechanical strength, enabling bones to withstand external loads, support weight-bearing functions, and protect internal structures, including the marrow cavity (Fig. 1.3). It is the main type of bone found in the diaphyses of long bones and the surrounding surfaces of flat bones. Macroscopically, cortical bone appears white, smooth, and solid; however, a more complex structure is revealed under a microscope.

At the microscopic level, cortical bone presents a highly organized arrangement of coaxial cylinders, forming the compact, fundamental units known as osteons or Haversian systems. Osteons have a diameter of 200-250 µm and are oriented parallel to the bone's long axis [12]. The osteon is composed of multiple coaxial layers (lamellae) of mineralized matrix around a central canal (Haversian canal), which contains blood vessels, nerves, and lymphatic channels that provide nutrients and support the cellular activity [6,13]. Adjacent Haversian canals are interconnected by transverse canals, called Volkmann's canals, and link the internal (endosteum) and external (periosteum) surfaces of the bone. The presence of Haversian canals within the cortical bone make it porous, with an average porosity of about 5-15%, depending on the age and other factors [9,14,15].

The spaces between osteons are filled with irregularly shaped arrangements of parallel lamellae, called interstitial lamellae, which are remnants of osteons partially resorbed by osteoclasts during bone growth and remodeling. Directly beneath the periosteum and above the endosteum are layers of parallel lamellae, known as the external circumferential lamellae and internal circumferential lamellae, respectively. These lamellae encircle the entire bone shaft, providing additional support and reinforcing the overall cortical structure. Between the layers of lamellae there are osteocytes residing inside their lacunae, with their processes interconnecting through the canaliculi [6,7,9].

Each concentric lamella of an osteon has a thickness of 3-7 µm and is composed of collagen fibers and a calcified matrix [16]. According to the most widely accepted “twisted plywood” model by Giraud-Guille et al. [17], the collagen fibers within a lamella are generally oriented in the same direction, often following a helical pattern around the lamella. This intricate arrangement is believed to significantly enhance the bone’s ability to resist tensile and shear forces, allowing it to withstand impact and bending stresses from multiple directions. However, it must be noted that other studies challenge this model and suggest that the orientation of collagen fibers can exhibit more complex arrangements; while adjacent lamellae may display some degree of alternating orientation, they may also show smooth, continuous transitions, oscillations, twists, or differences in lamellae density [13,18,19].

At the nanoscale, collagen fibers are composed of fibrils primarily made of Type I collagen molecules, interspersed with thin, flat hydroxyapatite crystals, approximately 2-3 nm in thickness, oriented roughly parallel to the fibril’s long axis. These fibrils display a periodic banding pattern with 67 nm spacing and 40 nm gaps occupied by the crystals [13,20,21].

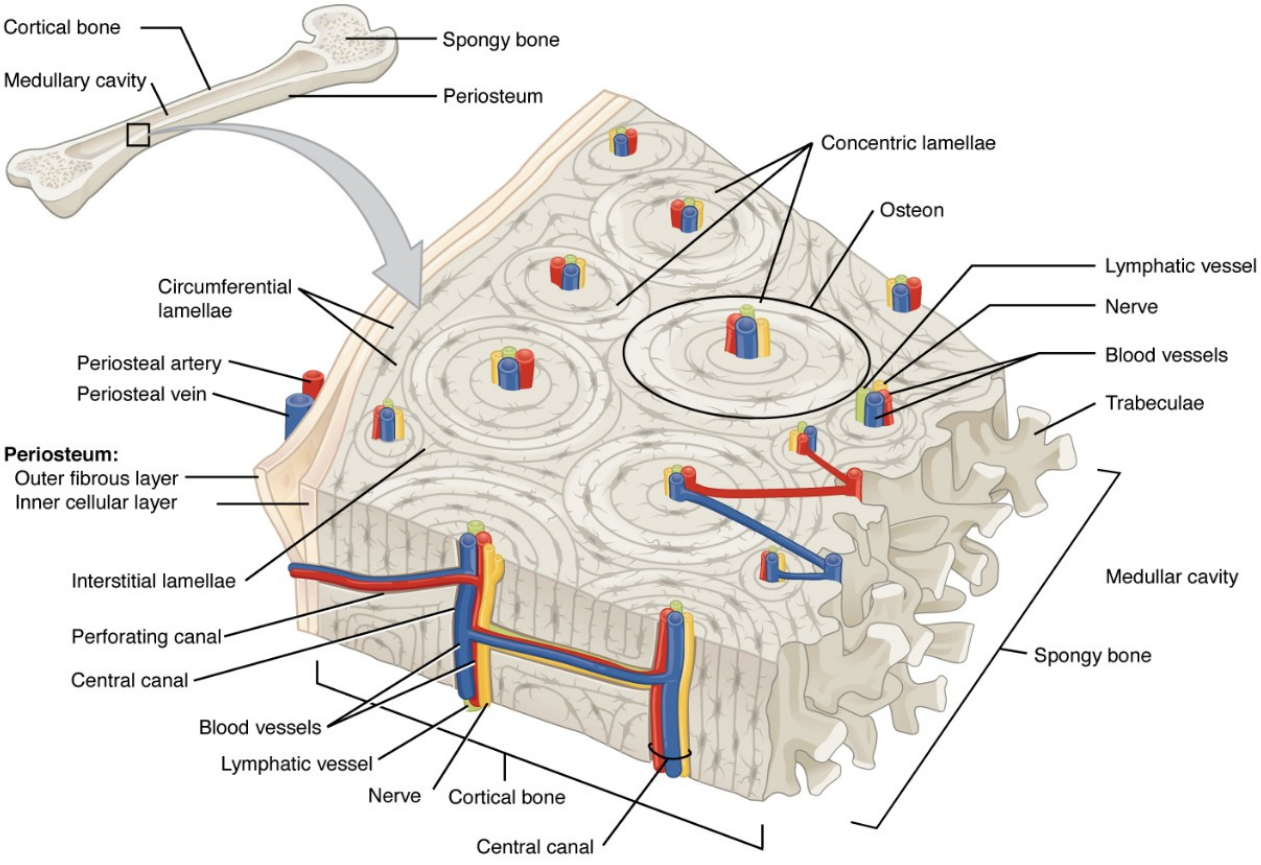

Figure 1.2: Cross-sectional diagram of cortical bone showing the arrangement of osteons, the basic structural units of cortical bone. Figure from [7], licensed under CC BY 4.0.

1.2.3. Trabecular bone

Trabecular bone, also known as cancellous or spongy bone, constitutes approximately 20% of the total bone mass of an adult human [9]. Unlike the dense and smooth macroscopic appearance of cortical bone, which has a low porosity (typically around 5-15%), trabecular bone is heterogeneous, anisotropic, and highly porous, with a porosity ranging between 50-90%, depending on its location and function [14,15]. Trabecular bone is primarily located in regions that endure compressive forces, such as the vertebrae, pelvis, and epiphyses of long bones, where its porous nature allows it to absorb and distribute forces efficiently. Additionally, this structure reduces the overall bone's weight and increases its flexibility.

The significant porosity of trabecular bone comes as a result of its characteristic honeycomb structure (Fig. 1.3(b)), consisting of an intricate network of thin, rod- or plate-like projections called trabeculae, that range from 50 to 400 nm in thickness [9]. Despite its porosity, the arrangement of trabeculae along lines of stress enables trabecular bone to transfer mechanical loads efficiently to the cortical bone, reducing stress concentrations [22]. This alignment also allows trabecular bone to adapt its microarchitecture to changing mechanical demands, a phenomenon described by Wolff's Law [22,23].

Trabecular bone differs from cortical bone in terms of vascularization and nutrient supply mechanisms. Unlike cortical bone, which has a dense network of blood vessels within its Haversian canals, trabecular bone lacks blood vessels within the trabeculae themselves. Instead, the thin structure of trabeculae allows them to remain close to the highly vascularized bone marrow that fills the spaces between trabeculae. This proximity enables efficient nutrients and gaseous exchange via diffusion from the surrounding marrow. The bone envelope system, along with the interconnected network of osteocytes within trabecular bone, supports sufficient nutrient and oxygen delivery to sustain cellular viability, even in the absence of an internal vascular network within the trabeculae [22,24–28].

Structurally, trabecular bones are highly dynamic and undergo rapid remodeling at a rate higher than that of cortical bone. This increased remodeling is due to trabecular bone's high porosity and greater surface area relative to its volume, which provides more surfaces for remodeling activity, but that also depends on age and site [29–31]. The high remodeling rate allows trabecular bone to quickly adapt to mechanical stresses and contributes to calcium homeostasis within the body.

At the nanoscale, trabecular bone shares compositional similarities with cortical bone, with both featuring a matrix composed of Type I collagen fibers interspersed with hydroxyapatite crystals [28]. However, the hydroxyapatite crystals in trabecular bone tend to be smaller than those in cortical bone, a difference attributed to the higher remodeling rate of trabecular bone, which affects the maturity of its mineral crystals [32]. This collagen-hydroxyapatite matrix provides both flexibility and rigidity, allowing trabecular bone to withstand compressive forces while retaining some elasticity. The mineralized collagen fibrils are organized in a periodic pattern with 67 nm

spacing, a feature that enhances the bone's mechanical properties and enables it to absorb impact forces effectively despite its porous structure [13,20,21].

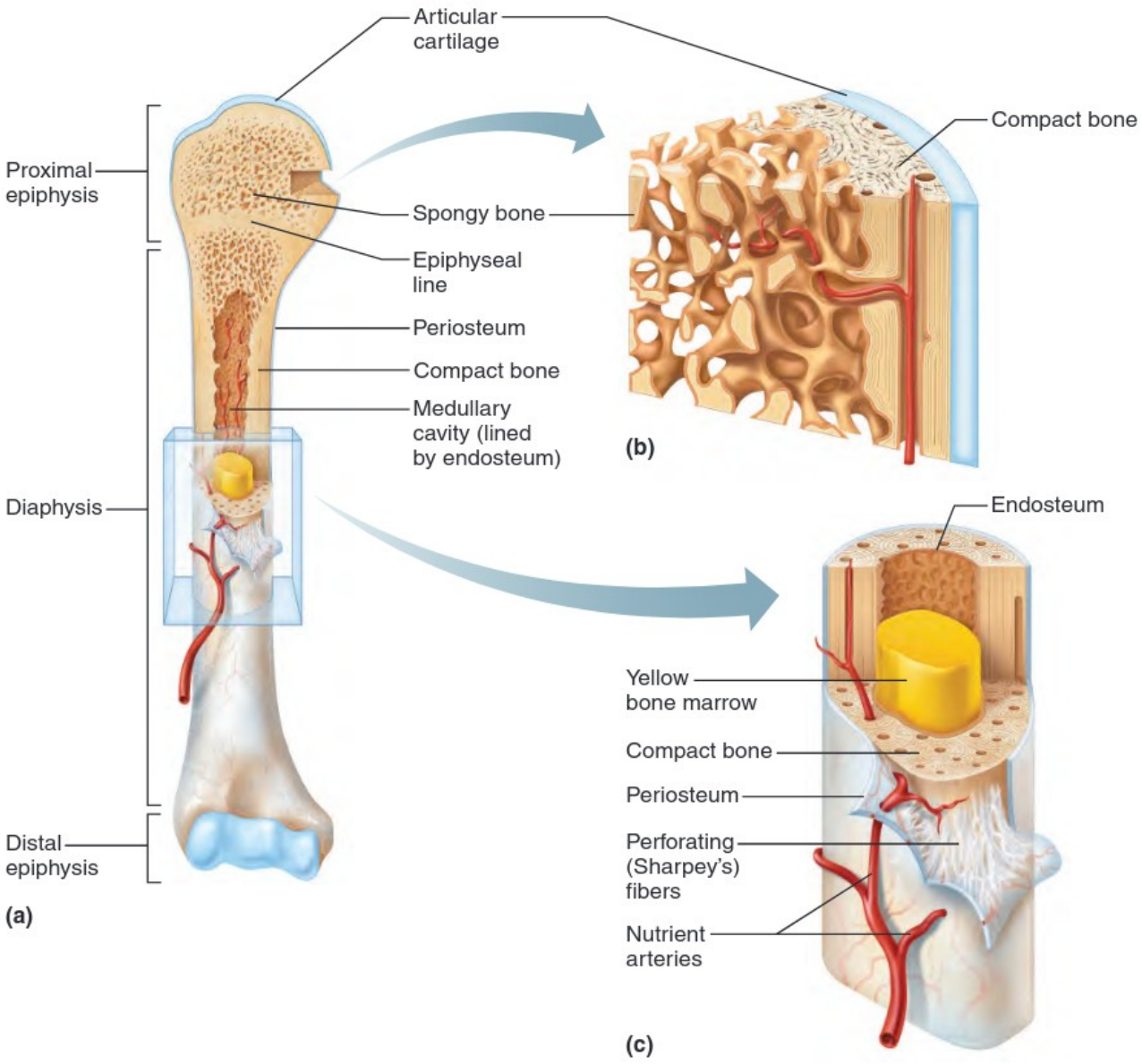

Figure 1.3: Structure of a long bone. (a) Anterior view with longitudinal cross-sectional cut where the internal structure is shown. The diaphysis primarily consists of cortical (compact) bone while the epiphyses consist of trabecular (spongy) bone. (b) Part of the bone showing the cortical and trabecular regions. (c) Part of the diaphysis. Figure from [8].

1.3. Bone composition

Bone is a specialized, supportive tissue, composed of a complex matrix with organic and inorganic components and water [8,9,28]. Roughly 25% of bone weight consists of organic components, primarily Type I collagen fibers, with smaller contributions from non-collagenous proteins. This

collagenous framework grants bones flexibility, tensile strength, and shock-absorbing capabilities, helping them resist fractures under stress. The remaining 60-70% of bone consists of inorganic elements, mainly hydroxyapatite crystals—calcium phosphate structures that create a stiff, dense network within the collagen matrix. These mineral crystals provide the compressive strength needed for load-bearing functions and protect internal structures. Water, which accounts for around 10-15% of bone's weight, exists within the collagen matrix and around the mineral crystals, playing a crucial role in nutrient transport and cushioning against mechanical forces. It also supports the viscoelastic properties of bone, allowing it to adapt to various physiological demands and mechanical loads. Together, the bone's components provide it with the necessary durability and resilience, enabling it to adapt to physiological demands and mechanical loads while supporting the body and protecting the internal organs.

1.3.1. Organic

The organic matrix of bone constitutes approximately 30-35% of bone's dry weight, with around 90% of it composed of Type I collagen fibers [33,34], which establish the primary structural framework, providing bone the necessary tensile strength and flexibility to perform its function. The remaining 10% consists of non-collagenous proteins, including osteocalcin, osteopontin, bone sialoprotein, and others, which play essential roles in regulating mineralization, cellular signaling, and matrix organization [28,35]. These organic components enhance bone's resilience to mechanical stress and support dynamic processes crucial for remodeling and repair.

Collagen

Collagen is the principal structural protein in the extracellular matrix of connective tissues, playing an essential role in providing strength, stability, and elasticity to various body structures. As the most abundant protein in mammals, collagen forms the framework of bones, tendons, ligaments, skin, and cartilage [36]. In the human body, collagen constitutes about 30% of its protein mass [33]. Its structure consists of three polypeptide chains coiled into a triple helix, which assemble into fibrils and further aggregate into organized fiber networks. These fibers create a resilient matrix that adapts to the specific demands of each tissue. In bones, for instance, collagen fibrils align and mineralize to enhance rigidity and facilitate load-bearing [37].

Collagen types can be broadly categorized into fibrillar and non-fibrillar collagens, each serving distinct structural functions. Over 29 different types of collagen have been identified [38,39]. Fibrillar collagens (containing Types I, II, III, V, and XI) are the most common in vertebrates and assemble into thick, rope-like fibrils that confer tensile strength and are essential in load-bearing tissues like bone, tendons, and cartilage [33]. These fibrillar structures are highly organized and support tissue integrity under mechanical stress. In contrast, non-fibrillar collagens (such as Type IV) do not form fibrils; instead, they create network-like or sheet structures. These collagens are

prominent in basement membranes, where they provide support for cell layers, contribute to filtration functions, and act as barriers in tissues like the skin and kidneys [40]. The difference in structure between fibrillar and non-fibrillar collagens enables them to fulfill distinct functional roles, tailored to the mechanical and physiological needs of different tissues.

Molecular structure of collagen

Despite their structural variations, all collagen molecules share a common fundamental architecture characterized by the presence of three polypeptide chains, known as α-chains. Each α-chain is coiled into a left-handed helix, and the three chains then intertwine around a common axis, resulting in the formation of a right-handed, rope-like triple helix [33]. The synthesis of collagen begins in the cell with procollagen, a precursor form that contains additional peptide extensions at both ends of each α-chain. After secretion into the extracellular matrix, these extensions are removed by an enzyme, procollagen peptidase, resulting in the formation of mature collagen molecules, referred to as tropocollagen, which has a length of approximately 300 nm and thickness of about 1.4 nm [41]. This distinctive triple helical structure is essential for the mechanical properties and stability of collagen.

The primary structure of collagen is notable for its high glycine, proline, and hydroxyproline content, with glycine making up approximately one-third of all amino acid residues. Each α-chain coil contains the characteristic repeating amino acid sequence, X-Y-Gly. In this sequence, glycine (Gly, $C_2H_5NO_2$) consistently occupies the first position, while the second (X) and third (Y) positions are often filled by proline (Pro, $C_5H_9NO_2$) and hydroxyproline (Hyp, $C_5H_9NO_3$) (Fig. 1.4). This X-Y-Gly sequence is highly conserved among collagen types, with glycine present in almost every third position across each α-chain [42].

Glycine's essential role in collagen arises from its small size and single hydrogen side chain, which allow the three α-chains to pack tightly together to form the triple helix, as illustrated on Fig. 1.4 [33]. The stability of this triple helix is further reinforced by hydrogen bonds that form between the carbonyl oxygen of one amino acid and the amide hydrogen of another in adjacent chains, which significantly contributes to the structural integrity of collagen [43]. Notably, only the telopeptides found at the ends of the α-chains, which account for about 2% of the molecule, deviate from the X-Y-Gly sequence and the triple-helical conformation [42]. Proline and hydroxyproline collectively account for roughly 20% of the residues in the α-chains, contributing additional rigidity and stabilization due to their cyclic structures. It should be noted that the Pro-Hyp-Gly sequence is more common in fibrillar collagen [36].

Different types of collagen are composed of different combinations of α-chains, which can vary in amino acid composition and length. Each α-chain typically contains about 1,000 residues, contributing to the overall structure and function of collagen [39]. For instance, type I collagen is primarily formed from two α1 chains and one α2 chain, where the α1 chain is longer and more prevalent, providing the tensile strength necessary for load-bearing tissues. In contrast, type II

collagen consists entirely of α1 chains, typically found in cartilage, which helps form a mesh-like structure to resist compressive forces. Type III collagen, also containing three α1 chains, differs from type I in its amino acid profile, contributing to its role in flexible tissues such as skin and blood vessels. Type IV collagen, found in basement membranes, possesses α-chains that create a network structure instead of forming fibrils, allowing for filtration and support [39,42]. This diversity in α-chain composition and structure is essential for collagen's mechanical strength and biochemical properties.

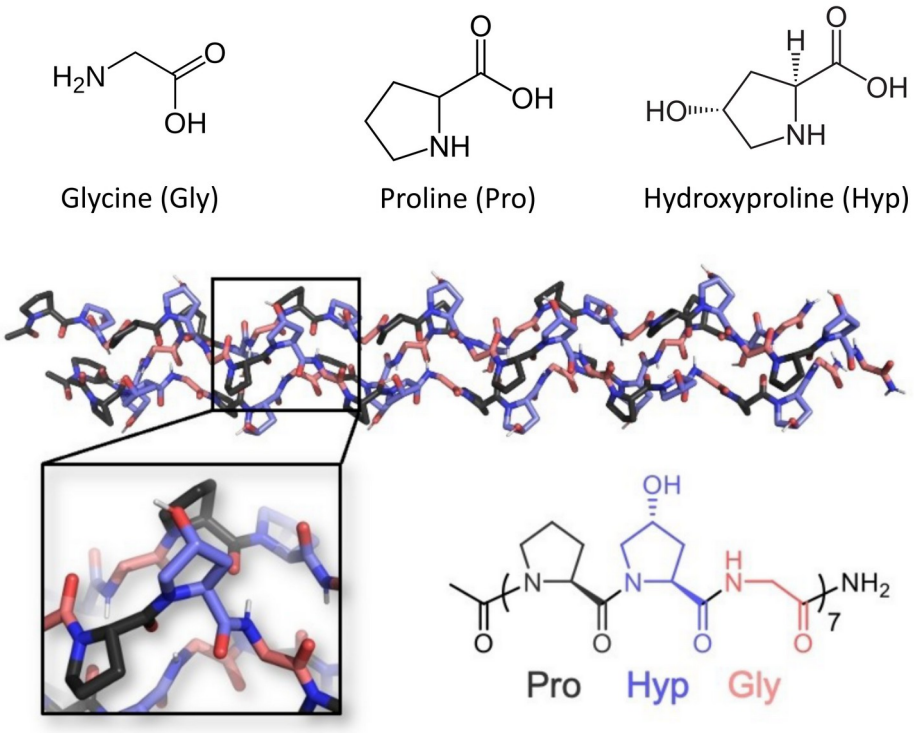

Figure 1.4: Top: Skeletal formulas of glycine, proline, and hydroxyproline, the most common amino acid residues in collagen. Bottom: 3D representation of the triple helix of collagen with repetition of Pro-Hyp-Gly sequences and structural formula of Pro-Hyp-Gly sequence. Figures from [99–102].

Of particular importance in the effective packing of the α-chains of collagen into a stable triple helix is its interaction with surrounding water molecules. These water molecules form hydrogen bonds with various functional groups on the polypeptide chains, particularly with the carbonyl and amide groups within the backbone of the α-chains. A critical aspect of these interactions involves Hyp residues, especially when positioned in the Y position of the repeating X-Y-Gly sequence. This specific positioning enables the hydroxyl group of Hyp to form additional water-mediated hydrogen bonds with nearby chains, which greatly enhances the stability of the triple helix [44]. Hyp-dependent, water-mediated hydrogen bonds effectively align and link neighboring chains in the helix, counteracting disruptive forces. Additionally, water molecules around collagen form a

dynamic hydration layer that promotes slight conformational flexibility, which is essential for tissues subjected to repetitive stress, such as tendons and cartilage. This interaction not only maintains the structural integrity of collagen but also contributes to the mechanical resilience required for collagen-rich tissues to withstand and adapt to physiological loads. However, although Pro-Hyp-Gly is a common sequence in Type I collagen, the frequency of Hyp is generally limited; thus, water-bridging occurs at specific sites rather than forming an extensive network [36].

The rope-like triple helix of the collagen molecule provides flexibility and sturdiness, as well as high tensile strength, making it well-suited to diverse functions across various body tissues [45]. Additionally, the helical structure exposes molecules which can be used as binding sites that other molecules can attach to. This way collagen can work as a scaffold around which tissue can be developed. The same sites can also be used as binding sites for enzymes, other proteins, and integrins (cell surface receptors) [46–49]. These interactions are critical for various biological processes, including cell signaling, tissue remodeling, and immune responses.

Organization in collagen fibers

Collagen molecules self-assemble to form fibrils and fibers as shown in Fig. 1.5. The initial step involves the lateral aggregation of individual collagen molecules, which align in a staggered arrangement, driven by molecular interactions between the triple-helical collagen molecules [36]. The collagen fibrils exhibit a characteristic banding pattern, known as D-banding, which can be observed under electron microscopy. This pattern arises from the periodic overlap of collagen molecules, with each molecule shifted slightly (roughly 67 nm for Type I collagen) relative to its neighbor [41].

Molecular interactions at the collagen fibril level are further enhanced by covalent cross-linking, which begins with the oxidation of lysine and hydroxylysine residues in the telopeptides of adjacent collagen molecules by the enzyme lysyl oxidase. This enzymatic process generates aldehyde groups, which then react with amino groups or other aldehyde groups to form stable covalent cross-links. Initial reducible (chemically labile), divalent cross-links, such as dehydro-dihydroxylysinonorleucine (deH-DHLNL) and dehydro-hydroxylysinonorleucine (deH-HLNL), are considered immature forms. These cross-links can further mature into more stable, non-reducible, trivalent structures, such as pyridinoline (PYD) and deoxypyridinoline (DPD), which significantly enhance the mechanical stability of collagen fibrils [36,41,50–52]. The ratio of PYD/deH-DHLNL can be used as an index of collagen maturity [53].

As collagen fibrils mature, they aggregate into fibers, ranging in thickness from 0.3 µm to 1 µm in Type I collagen. Additional enzymes, such as transglutaminase, play a role in further modifying and stabilizing the fibers in certain tissues. Non-enzymatic processes, including glycation, also contribute to cross-linking. Advanced glycation end-products (AGEs), formed by reactions between reducing sugars and lysine or arginine residues, accumulate over time and can stiffen collagen

fibers. However, excessive AGE accumulation, particularly in aging or diabetic conditions, can reduce fiber elasticity, leading to brittleness and increased fracture risk [51,54,55].

The balance between enzymatic cross-linking, which enhances fibril stability and flexibility, and non-enzymatic cross-linking, which can impair these properties, is critical for maintaining the structural and mechanical integrity of collagen fibers. Alterations in this balance are implicated in aging, osteoporosis, and other conditions that compromise bone quality.

Collagen in bone

The extracellular matrix of bone is largely composed of three primary types of collagen: Type I, Type V, and, to a lesser extent, Type III. Each type plays a role in defining the matrix's structural integrity and biomechanical properties of bones, particularly providing it flexibility and resistance to fractures. Type I collagen is the most abundant, accounting for around 90% of the organic matrix [35,54]. Type I collagen molecules are composed of two α1(I) and one α2(I) polypeptide chains, as described in the previous section. Type I collagen fibrils serve as a scaffold for mineral deposition, with hydroxyapatite crystals anchoring between collagen fibers, thus providing the rigidity and resilience necessary for bone's structural integrity [36,42]. Type V collagen is typically composed of two α1(V) and one α2(V) chains, forming a smaller triple-helix that associates closely with Type I fibrils. Its positioning within fibrils supports matrix stability and bone strength and plays a role in defining the characteristics of Type I collagen fibrils, such as diameter and spacing [56]. Type III collagen is composed of three identical α1(III) chains and plays a role in bone development and remodeling [57,58].

Collagen in bone mainly serves a structural role, providing the matrix in which the bone mineral in the form of hydroxyapatite is stored and is essential for maintaining the mechanical properties of bone. However, research has shown that it also plays a secondary role by influencing cellular activities involved in bone remodeling. During bone resorption, collagen breakdown products, such as specific peptide fragments, are released and can signal to bone cells, thus regulating osteoclast and osteoblast activity, which are important for bone's health and regeneration [59,60].

Bone diseases often target collagen, as defects in collagen production, structure, or function directly compromise bone's integrity. Genetic mutations, such as those in Type I collagen genes, can lead to diseases like osteogenesis imperfecta, characterized by fragile bones due to defective collagen fibrils that fail to provide the necessary structural support [61]. Similarly, metabolic bone diseases, such as osteoporosis, involve accelerated collagen breakdown, which reduces bone density and increases fracture risk. Inflammatory diseases can further degrade collagen in bone, as enzymes released during inflammation, such as matrix metalloproteinases, break down collagen, weakening the bone matrix [60]. Thus, maintaining collagen integrity is essential not only for bone strength but also for its metabolic and regenerative functions.

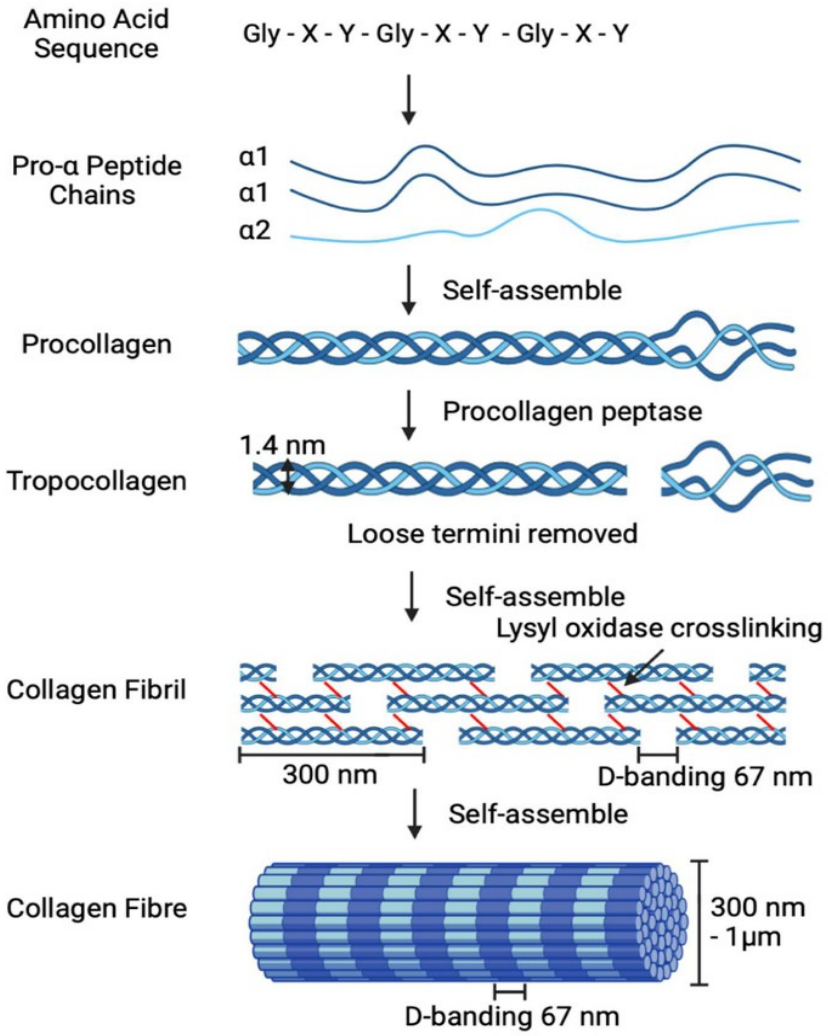

Figure 1.5: Hierharchical structure of Type I collagen, the most abundant type of colalgen in bone. The amino acid residues form α-chains which self-assemble to form procollagen molecules. The loose procollagen ends are trimmed by the enzym procollagen peptase to form tropocollagen. Finally, tropocollagen molecules are cross-linked to form collagen fibrils, which in turn are assembled into collagen fibers. Figure from [41].

Non-collagenous proteins

Non-collagenous proteins (NCPs) make up only a minor fraction of the bone matrix (about 5%), they are, however, of significant importance in regulating bone mineralization, matrix organization, and cellular activities. These proteins, including glycoproteins, proteoglycans, and various signaling molecules, contribute to bone's structural and functional integrity by mediating interactions between collagen fibers and mineral components [35,62]. While each NCP has a distinct role, some contribute more broadly to bone's stability and adaptability.

One of the most abundant NCPs in bone tissue is osteocalcin, which comprises about 1-20% of NCPs, with the percentage depending on species, age, and specific bone site [63]. It is a small (49

amino acids long), vitamin K-dependent protein (i.e. its activity depends on the levels of vitamin K) that is secreted by osteoblasts and presents high affinity for Ca^{2+} [64]. This makes osteocalcin bind strongly to hydroxyapatite, contributing to the regulation of bone mineralization [65]. Beyond its structural role, osteocalcin acts as a hormone, impacting energy metabolism and influencing other body systems [66,67]. It is also considered as a potential biomarker for osteoporosis [65].

Another key protein, osteopontin, plays an essential role in remodeling and repairing processes. Along with bone sialoprotein (BSP), it is a member of the SIBLING (Small Integrin-Binding LIgand, N-linked Glycoprotein) family of glycoproteins, which are particularly important in the mineralization of bone and dentin [68]. As a glycoprotein that binds both minerals and cell surfaces, osteopontin bridges cells and the matrix, facilitating osteoclast attachment to bone surfaces. This promotes bone resorption and crystal growth regulation, making osteopontin essential for the ongoing maintenance and renewal of bone tissue [69]. BSP is also important, particularly in early bone formation. Highly expressed in mineralized tissues, BSP promotes nucleation sites for hydroxyapatite deposition, crucial for the initial stages of mineralization [65,70]. Additionally, BSP enhances cell adhesion by binding to integrins on osteoblast and osteoclast surfaces, supporting stable cell-matrix interactions during bone formation [71].

Several other NCPs contribute to specific but complementary aspects of bone structure and function. Osteonectin, also known as SPARC (Secreted Protein Acidic and Rich in Cysteine), is critical for connecting the organic and mineral phases of bone. Produced primarily by osteoblasts, osteonectin binds both collagen and hydroxyapatite, promoting mineral deposition and organizing the matrix. This interaction is essential for the formation and growth of hydroxyapatite crystals within the collagen matrix, reinforcing bone's structural integrity [65,72]. Proteoglycans, such as decorin and biglycan, play a structural role by organizing collagen fibrils, directly affecting the mechanical properties of bone by enhancing its durability and flexibility [73,74]. Additionally, these proteoglycans influence cell signaling pathways involved in osteoblast and osteoclast activity during remodeling [75].

Finally, various growth factors and cytokines stored within the bone matrix—such as transforming growth factor-beta (TGF-β) and bone morphogenetic proteins (BMPs)—are released during bone remodeling. These molecules activate signaling pathways that regulate bone formation, differentiation, and repair, ensuring bone maintains its strength and functionality over time [65,76,77]. Although not unique to bone, these factors play a supportive role in bone health by orchestrating the cellular activities needed for bone regeneration.

1.3.2. Inorganic

The inorganic component of bone primarily consists of hydroxyapatite, a calcium phosphate mineral that gives bone its rigidity and strength. Unlike the organic matrix, which is mainly composed of collagen and its mechanical role is to provide flexibility and tensile strength to the

bone, the inorganic component is responsible for the bone's ability to resist compressive forces. Apart from hydroxyapatite, the inorganic phase of bone also contains trace elements like magnesium, sodium, and carbonate, which influence bone's mechanical properties and its dynamic response to environmental changes [35].

Hydroxyapatite

Hydroxyapatite (HA) is a member of the apatite group of phosphate minerals, which share a similar crystal structure. The general formula for apatites is $M_{10}(PO_4)_6X_2$, where M is typically calcium (Ca), and X represents various anions such as hydroxide (OH^-) and carbonate (CO_3^-) [78]. Hydroxyapatite, with the formula $Ca_{10}(PO_4)_6(OH)_2$, is the most common and biologically significant apatite found in bones and teeth. It is the principal mineral component that provides bone with its rigidity and structural integrity. The mineralization of bone, which involves the deposition of hydroxyapatite within the collagen matrix, is essential for bone to withstand mechanical stresses and maintain its strength over time [35].

Molecular structure of stoichiometric hydroxyapatite

Hydroxyapatite, the principal mineral component of bone, is a calcium phosphate crystalline structure with the chemical formula $Ca_{10}(PO_4)_6(OH)_2$. HA crystallizes in the hexagonal $P6_3/m$ space group, characterized by a six-fold c-axis oriented perpendicularly to three equivalent a-axes, each angled at 120° relative to the others, all lying on the same plane. The lattice parameters for HA's hexagonal structure are a = 9.42 Å and c = 6.88 Å [78–80]. The growth of HA crystals takes place along the crystallographic c-axis, perpendicularly to the hexagonal planes, enabling strong structural integrity along this axis [36].

The crystalline structure of stoichiometric HA (Fig. 1.6) consists of two non-equivalent types of calcium sites, denoted Ca1 and Ca2. In the unit cell, Ca1 ions of HA form four 9-fold coordinated polyhedra (calcium ions surrounded by nine oxygen atoms), positioned in columns aligned along the crystallographic c-axis, while the Ca2 ions form six 7-fold coordinated polyhedra (calcium ions surrounded by seven oxygen atoms) and surround the phosphate groups (PO_4^{3-}), providing stability to the network of interconnected PO_4^{3-} tetrahedra. Six phosphate groups are contained in the unit cell, which are arranged in a way that balances their negative charge with the surrounding calcium ions, contributing to the structural integrity of the crystal lattice. The hydroxyl ions (OH^-) are located at the corners of the unit cell [78–80]. This orderly arrangement forms layers and dictates the direction of the crystal's growth and elongation to be along the crystallographic c-axis.

Within the crystal lattice of HA, partial or full ionic substitutions can occur, where the primary ions of HA (Ca^{2+}, PO_4^{3-}, OH^-) are replaced by other ions, which can alter the mechanical properties of HA and influence its stability, solubility, and bioactivity [81]. Common substitutions include Na^+, Mg^{2+}, Sr^{2+}, Pb^{2+}, and Ba^{2+} for Ca^{2+}; CO_3^{2-} and HPO_4^{2-} for PO_4^{3-}; F^- and Cl^- for OH^- [80]. To maintain

charge neutrality, any difference in charge from substitutions must be balanced. This can occur through a compensatory substitution of an ion with the appropriate charge or by introducing vacancies within the HA structure. For example, when PO_4^{3-} is substituted by CO_3^{2-}, the resulting negative charge deficit can be compensated by the removal of Ca^{2-} or OH^- ions [82]. Substitutions in HA's structure induce changes in lattice parameters and bond characteristics, which can be detected using analytical techniques such as X-ray and Neutron Diffraction or vibrational spectroscopy methods, including Fourier-transform Infrared (FTIR) and Raman spectroscopy [21,78,80–83].

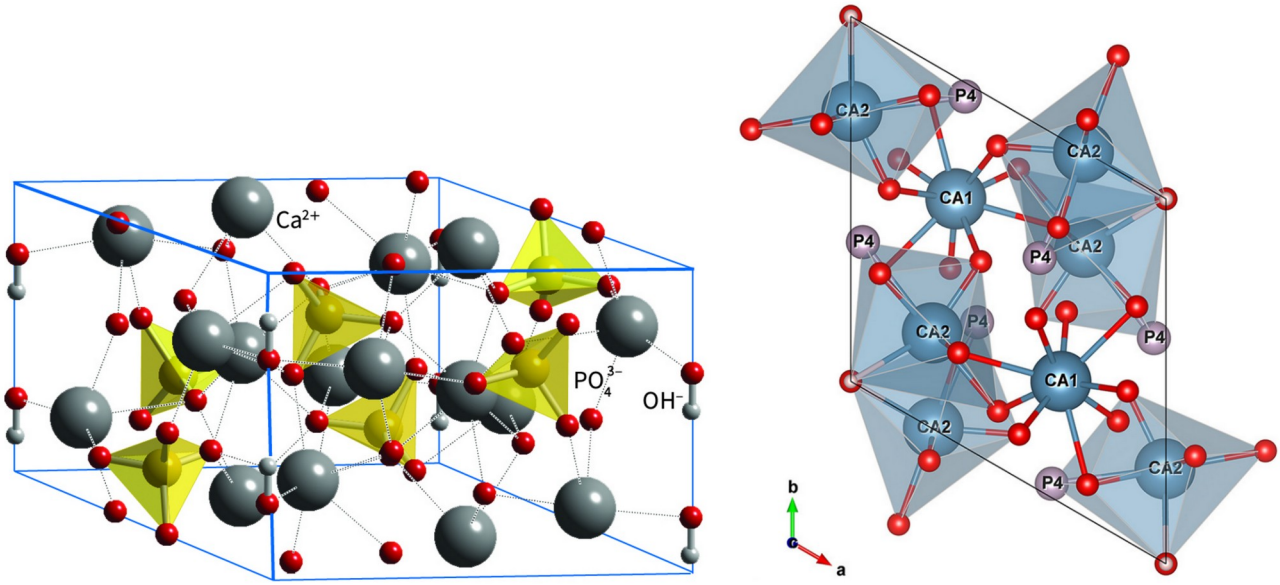

Figure 1.6: Left: Crystal structure of stoichiometric hydroxyapatite ($Ca_{10}(PO_4)_6(OH)_2$) with the tetrahedric structure of PO_4^{3-} highlighted. Figure from [103]. Right: Unit cell of stoichiometric hydroxyapatite with a focus on the Ca1 and Ca2 atoms. The connections of the Ca1 and Ca2 ions with their surrounding ions are shown as bars and the 7-fold Ca2 polyhedra are highlighted. Figure from [79].

Hydroxyapatite in bone

In bone tissue, hydroxyapatite plays an essential role by providing structural stability, hardness, and resistance to compressive forces. The HA found in bone, often referred to as biological apatite or bioapatite, differs significantly from stoichiometric hydroxyapatite due to its composition, crystal size, and structural adaptations. Bioapatite contains various ionic substitutions within its crystal lattice, including carbonate (CO_3^{2-}), sodium (Na^+), magnesium (Mg^{2+}), fluoride (F^-), and monohydrate phosphate (HPO_4^{2-}), which are responsible for the mechanical and chemical properties of biological HA [35].

The ionic substitutions in bioapatite lead to differences in crystal size and shape when compared to pure HA. While synthetic or stoichiometric HA typically forms larger, hexagonal, prism- or needle-

like crystals that can reach several micrometers in length, bioapatite crystals in bone are nanoscale, generally measuring between 20–100 nm in length, 10–40 nm in width, and only 1–5 nm in thickness [82,84,85]. Bioapatite crystals have a smaller, plate-like, and irregular shape, which results from lattice distortions and vacancies created by ionic substitutions. These disruptions limit crystal growth, increase solubility, and enhance reactivity.

One of the primary ionic substitutions that take place in bone HA is carbonate, which can replace either OH^- or PO_4^{3-} ions within the HA lattice. These substitutions are categorized as Type A and Type B substitutions. Type A substitution occurs when carbonate ions replace hydroxyl groups, whereas Type B substitution involves the replacement of phosphate by carbonate ions. Type B substitution is more prevalent than Type A in bone and typically constitutes about 5–9% of the total mineral content by weight [84]. This substitution has a significant impact on the solubility and reactivity of bioapatite, with carbonate content increasing the solubility of HA crystals. This higher solubility facilitates bone remodeling by enabling HA to be resorbed and redeposited in response to metabolic and mechanical demands, allowing for a balance of bone formation and resorption under normal physiological conditions [80,82].

Another important difference between stoichiometric HA and bioapatite is the calcium-to-phosphorus (Ca/P) ratio [86,87]. Stoichiometric HA has a Ca/P ratio of 1.67, representing an idealized structure with exact proportions of calcium and phosphate ions. In contrast, the Ca/P ratio of bioapatite in bone is typically lower, often ranging from 1.5 to 1.67, due to the presence of substitutions and vacancies within the lattice. CO_3^{2-} substitutions, as well as the presence of HPO_4^{2-} in place of PO_4^{3-}, contribute to this variability [88]. Age-related factors further influence the Ca/P ratio in bioapatite. As bone ages, it undergoes gradual changes in mineral composition, with older bone often showing a slight increase in the Ca/P ratio, leading to a ratio closer to that of stoichiometric HA. This is attributed to an accumulation of mineral content and a reduction in ionic substitutions over time, which leads to a more stable, less soluble mineral phase. Additionally, younger bone generally exhibits a higher degree of carbonate and HPO_4^{2-} substitutions, contributing to a lower Ca/P ratio and greater reactivity, facilitating bone remodeling. With age, the gradual reduction in these substitutions contributes to a slower turnover rate and decreased adaptability of the bone matrix, affecting its mechanical properties and overall resilience [89,90].

Bioapatite in bone is organized within a collagen matrix, forming a composite structure that combines the strength of mineralized HA with the flexibility of collagen. Bioapatite crystals align along the collagen fibrils in an organized, hierarchical arrangement, which is essential for effective load transfer between the mineral and organic phases of bone. Within this composite structure, collagen fibrils provide tensile strength, while the bioapatite crystals confer compressive strength, allowing bone to resist various mechanical forces. The crystallographic c-axis of the bioapatite crystals is oriented along the longitudinal axis of the collagen fibrils, an arrangement that enhances bone's ability to bear loads and absorb impact. The staggered arrangement of bioapatite along collagen fibrils also allows for controlled deformation, where collagen and mineral components can work together to distribute stress, reducing the risk of fractures under mechanical load [13,34].

In addition to its role as a structural unit, bioapatite serves as a reservoir for essential ions, playing a critical role in calcium and phosphate metabolism. Bioapatite in bone acts as a readily accessible mineral source, releasing calcium and phosphate ions into the bloodstream when needed for physiological functions such as nerve conduction, muscle contraction, and cellular signaling. Trabecular bone, with its higher turnover rate and greater metabolic activity, is particularly responsive to changes in mineral demands, making it an active participant in mineral homeostasis [91]. This metabolic function of bioapatite is crucial in maintaining serum calcium levels, which are tightly regulated by hormonal mechanisms involving parathyroid hormone (PTH) and calcitonin. When calcium levels are low, PTH stimulates osteoclast activity, leading to bioapatite resorption and release of calcium ions into the bloodstream. Conversely, when calcium levels are high, calcitonin reduces osteoclast activity, slowing bioapatite resorption and promoting mineral deposition. This dynamic balance allows bone to act as both a structural and metabolic organ, adapting its mineral content to meet systemic demands [90,92].

1.4. Bone quality

“Bone quality” refers to the combination of structural and compositional attributes that determine a bone's material and mechanical properties [93]. Bone mineral density (BMD) is a widely used metric for assessing bone health that primarily quantifies the mineralized tissue in a given area or volume, providing an estimate of bone mass. However, BMD alone does not account for critical qualitative factors that influence bone strength and fracture resistance. These factors include the heterogeneity of bone at both microscopic and molecular levels, such as variations in trabecular connectivity and mineral crystallinity; the organization of collagen fibers, which affects tensile strength; microarchitecture, such as cortical porosity and trabecular alignment; and the accumulation of microdamage, which can weaken bone over time [53,94]. Together, these elements determine the overall strength, toughness, and resilience of bone.

Advances in imaging and spectroscopic techniques can improve our understanding of bone quality [53,95–97]. Vibrational spectroscopy techniques like Fourier-transform infrared spectroscopy (FTIR) and Raman spectroscopy, can provide molecular-level insights into bone composition [53,98]. Raman spectroscopy can evaluate mineral-to-matrix ratios, carbonate substitutions in hydroxyapatite, mineral crystallinity, and changes in collagen cross-linking, which are critical for understanding how bone’s molecular composition and organization contribute to its mechanical performance and susceptibility to diseases like osteoporosis [98].

1.5. References

[1] Rothschild BM, Bryant B, Hubbard C, Tuxhorn K, Kilgore GP, Martin L, et al. The Power of the Claw. PLoS ONE 2013;8:e73811. https://doi.org/10.1371/journal.pone.0073811.
[2] Marshak S. Essentials of Geology. W.W. Norton; 2019.

[3] Yu E, Sharma S. Physiology, Calcium. StatPearls, Treasure Island (FL): StatPearls Publishing; 2023.
[4] Piotrowska K, Tarnowski M. Bone Marrow Adipocytes-Role in Physiology and Various Nutritional Conditions in Human and Animal Models. Nutrients 2021;13:1412. https://doi.org/10.3390/nu13051412.
[5] Nguyen LH, Duenas V, Chen MY, Jandial R. Progenitor Cells: Role and Usage in Bone Tissue Engineering Approaches for Spinal Fusion. In: Jandial R, Chen MY, editors. Regen. Biol. Spine Spinal Cord, New York, NY: Springer; 2012, p. 188–210. https://doi.org/10.1007/978-1-4614-4090-1_12.
[6] Mescher AL. Junqueira's basic histology: text and atlas. 16th ed. New York: McGraw-Hill; 2021.
[7] Biga LM, Bronson S, Dawson S, Harwell A, Hopkins R, Kaufmann J, et al. Anatomy & Physiology. OpenStax/Oregon State University; 2019.
[8] Marieb EN, Keller SM. Essentials of Human Anatomy & Physiology. Pearson; 2022.
[9] Clarke B. Normal Bone Anatomy and Physiology. Clin J Am Soc Nephrol CJASN 2008;3:S131. https://doi.org/10.2215/CJN.04151206.
[10] Bonewald L. The Amazing Osteocyte. J Bone Min Res 2011;26:229–38. https://doi.org/10.1002/jbmr.320.
[11] Boyle WJ, Simonet WS, Lacey DL. Osteoclast differentiation and activation. Nature 2003;423:337–42. https://doi.org/10.1038/nature01658.
[12] Bullough PG. Atlas of orthopedic pathology: with clinical and radiologic correlations. 2nd ed. New York: Gower Medical Publ; 1992.
[13] Rho J-Y, Kuhn-Spearing L, Zioupos P. Mechanical properties and the hierarchical structure of bone. Med Eng Phys 1998;20:92–102. https://doi.org/10.1016/S1350-4533(98)00007-1.
[14] Augat P, Schorlemmer S. The role of cortical bone and its microstructure in bone strength. Age Ageing 2006;35:ii27–31. https://doi.org/10.1093/ageing/afl081.
[15] Morgan EF, Unnikrisnan GU, Hussein AI. Bone Mechanical Properties in Healthy and Diseased States. Annu Rev Biomed Eng 2018;20:119. https://doi.org/10.1146/annurev-bioeng-062117-121139.
[16] Marotti G. A new theory of bone lamellation. Calcif Tissue Int 1993;53 Suppl 1:S47-55; discussion S56. https://doi.org/10.1007/BF01673402.
[17] Giraud-Guille MM. Twisted plywood architecture of collagen fibrils in human compact bone osteons. Calcif Tissue Int 1988;42:167–80. https://doi.org/10.1007/BF02556330.
[18] Mitchell J, Van Heteren AH. A literature review of the spatial organization of lamellar bone. Comptes Rendus Palevol 2016;15:23–31. https://doi.org/10.1016/j.crpv.2015.04.007.
[19] Varga P, Pacureanu A, Langer M, Suhonen H, Hesse B, Grimal Q, et al. Investigation of the three-dimensional orientation of mineralized collagen fibrils in human lamellar bone using synchrotron X-ray phase nano-tomography. Acta Biomater 2013;9:8118–27. https://doi.org/10.1016/j.actbio.2013.05.015.
[20] Martínez-Reina J, Domínguez J, García-Aznar JM. Effect of porosity and mineral content on the elastic constants of cortical bone: a multiscale approach. Biomech Model Mechanobiol 2011;10:309–22. https://doi.org/10.1007/s10237-010-0236-4.
[21] Ziv V, Weiner S. Bone Crystal Sizes: A Comparison of Transmission Electron Microscopic and X-Ray Diffraction Line Width Broadening Techniques. Connect Tissue Res 1994;30:165–75. https://doi.org/10.3109/03008209409061969.

[22] Zhang J, Li H, Zhou Y, Chen S, Rong Q. An Analysis of Trabecular Bone Structure Based on Principal Stress Trajectory. Bioengineering 2023;10:1224. https://doi.org/10.3390/bioengineering10101224.
[23] Ruff C, Holt B, Trinkaus E. Who's afraid of the big bad Wolff?: "Wolff's law" and bone functional adaptation. Am J Phys Anthropol 2006;129:484–98. https://doi.org/10.1002/ajpa.20371.
[24] Taichman RS. Blood and bone: two tissues whose fates are intertwined to create the hematopoietic stem-cell niche. Blood 2005;105:2631–9. https://doi.org/10.1182/blood-2004-06-2480.
[25] Smit TH, Burger EH. Is BMU-Coupling a Strain-Regulated Phenomenon? A Finite Element Analysis. J Bone Miner Res 2000;15:301–7. https://doi.org/10.1359/jbmr.2000.15.2.301.
[26] Grüneboom A, Hawwari I, Weidner D, Culemann S, Müller S, Henneberg S, et al. A network of trans-cortical capillaries as mainstay for blood circulation in long bones. Nat Metab 2019;1:236. https://doi.org/10.1038/s42255-018-0016-5.
[27] Littrell TA. Normal Anatomy. Clin. Imaging, Elsevier; 2014, p. 266–330. https://doi.org/10.1016/B978-0-323-08495-6.00006-3.
[28] Burr DB. Basic and Applied Bone Biology. 2nd ed. San Diego: Elsevier Science & Technology; 2019.
[29] Moreira CA, Dempster DW, Baron R. Anatomy and Ultrastructure of Bone – Histogenesis, Growth and Remodeling. In: Feingold KR, Anawalt B, Blackman MR, Boyce A, Chrousos G, Corpas E, et al., editors. Endotext, South Dartmouth (MA): MDText.com, Inc.; 2000.
[30] Parfitt AM. Misconceptions (2): turnover is always higher in cancellous than in cortical bone. Bone 2002;30:807–9. https://doi.org/10.1016/S8756-3282(02)00735-4.
[31] Ott SM. Cortical or Trabecular Bone: What's the Difference? Am J Nephrol 2018;47:373–5. https://doi.org/10.1159/000489672.
[32] Boivin G, Bala Y, Doublier A, Farlay D, Ste-Marie LG, Meunier PJ, et al. The role of mineralization and organic matrix in the microhardness of bone tissue from controls and osteoporotic patients. Bone 2008;43:532–8. https://doi.org/10.1016/j.bone.2008.05.024.
[33] Myllyharju J, Kivirikko KI. Collagens, modifying enzymes and their mutations in humans, flies and worms. Trends Genet 2004;20:33–43. https://doi.org/10.1016/j.tig.2003.11.004.
[34] Weiner S, Wagner HD. THE MATERIAL BONE: Structure-Mechanical Function Relations. Annu Rev Mater Res 1998;28:271–98. https://doi.org/10.1146/annurev.matsci.28.1.271.
[35] Boskey AL, Robey PG. The Composition of Bone. In: Bilezikian JP, Bouillon R, Clemens T, Compston J, Bauer DC, Ebeling PR, et al., editors. Primer Metab. Bone Dis. Disord. Miner. Metab. 1st ed., Wiley; 2018, p. 84–92. https://doi.org/10.1002/9781119266594.ch11.
[36] Shoulders MD, Raines RT. Collagen Structure and Stability. Annu Rev Biochem 2009;78:929–58. https://doi.org/10.1146/annurev.biochem.77.032207.120833.
[37] Fratzl P. Collagen: Structure and Mechanics, an Introduction. In: Fratzl P, editor. Collagen Struct. Mech., Boston, MA: Springer US; 2008, p. 1–13. https://doi.org/10.1007/978-0-387-73906-9_1.
[38] Ricard-Blum S. The Collagen Family. Cold Spring Harb Perspect Biol 2011;3:a004978. https://doi.org/10.1101/cshperspect.a004978.
[39] Ahmed M, Verma AK, Patel R. Collagen extraction and recent biological activities of collagen peptides derived from sea-food waste: A review. Sustain Chem Pharm 2020;18:100315. https://doi.org/10.1016/j.scp.2020.100315.

[40] Yurchenco PD. Basement Membranes: Cell Scaffoldings and Signaling Platforms. Cold Spring Harb Perspect Biol 2011;3:a004911. https://doi.org/10.1101/cshperspect.a004911.
[41] Carr B, Chen Z, Chung J, Wallace G. Collagen Alignment via Electro-Compaction for Biofabrication Applications: A Review. Polymers 2022;14:4270. https://doi.org/10.3390/polym14204270.
[42] Kadler KE, Holmes DF, Trotter JA, Chapman JA. Collagen fibril formation. Biochem J 1996;316:1. https://doi.org/10.1042/bj3160001.
[43] Charvolin J, Sadoc J-F. About collagen, a tribute to Yves Bouligand. Interface Focus 2012;2:567–74. https://doi.org/10.1098/rsfs.2012.0014.
[44] Suzuki E, Fraser RDB, MacRae TP. Role of hydroxyproline in the stabilization of the collagen molecule via water molecules. Int J Biol Macromol 1980;2:54–6. https://doi.org/10.1016/0141-8130(80)90013-6.
[45] Gautieri A, Vesentini S, Redaelli A, Buehler MJ. Hierarchical Structure and Nanomechanics of Collagen Microfibrils from the Atomistic Scale Up. Nano Lett 2011;11:757–66. https://doi.org/10.1021/nl103943u.
[46] Elango J, Hou C, Bao B, Wang S, Val JEMS de, Wenhui W. The Molecular Interaction of Collagen with Cell Receptors for Biological Function. Polymers 2022;14:876. https://doi.org/10.3390/polym14050876.
[47] Leitinger B. Transmembrane Collagen Receptors. Annu Rev Cell Dev Biol 2011;27:265–90. https://doi.org/10.1146/annurev-cellbio-092910-154013.
[48] Farndale RW. Collagen-binding proteins: insights from the Collagen Toolkits. Essays Biochem 2019;63:337–48. https://doi.org/10.1042/EBC20180070.
[49] Collagen interactions: Drug design and delivery - ScienceDirect n.d. https://www.sciencedirect.com/science/article/pii/S0169409X1500277X?via%3Dihub (accessed November 6, 2024).
[50] Yamauchi M, Sricholpech M. Lysine post-translational modifications of collagen. Essays Biochem 2012;52:113–33. https://doi.org/10.1042/bse0520113.
[51] Saito M, Marumo K. Collagen cross-links as a determinant of bone quality: a possible explanation for bone fragility in aging, osteoporosis, and diabetes mellitus. Osteoporos Int 2010;21:195–214. https://doi.org/10.1007/s00198-009-1066-z.
[52] Viguet-Carrin S, Garnero P, Delmas PD. The role of collagen in bone strength. Osteoporos Int 2006;17:319–36. https://doi.org/10.1007/s00198-005-2035-9.
[53] Kourkoumelis N, Zhang X, Lin Z, Wang J. Fourier Transform Infrared Spectroscopy of Bone Tissue: Bone Quality Assessment in Preclinical and Clinical Applications of Osteoporosis and Fragility Fracture. Clin Rev Bone Miner Metab 2019;17:24–39. https://doi.org/10.1007/s12018-018-9255-y.
[54] Amirrah IN, Lokanathan Y, Zulkiflee I, Wee MFMR, Motta A, Fauzi MB. A Comprehensive Review on Collagen Type I Development of Biomaterials for Tissue Engineering: From Biosynthesis to Bioscaffold. Biomedicines 2022;10:2307. https://doi.org/10.3390/biomedicines10092307.
[55] Paul RG, Bailey AJ. Glycation of collagen: the basis of its central role in the late complications of ageing and diabetes. Int J Biochem Cell Biol 1996;28:1297–310. https://doi.org/10.1016/S1357-2725(96)00079-9.
[56] Mak KM, Png CYM, Lee DJ. Type V Collagen in Health, Disease, and Fibrosis. Anat Rec 2016;299:613–29. https://doi.org/10.1002/ar.23330.

[57] Volk SW, Shah SR, Cohen AJ, Wang Y, Brisson BK, Vogel LK, et al. Type III collagen regulates osteoblastogenesis and the quantity of trabecular bone. Calcif Tissue Int 2014;94:621. https://doi.org/10.1007/s00223-014-9843-x.
[58] Kuivaniemi H, Tromp G. Type III collagen (COL3A1): Gene and protein structure, tissue distribution, and associated diseases. Gene 2019;707:151. https://doi.org/10.1016/j.gene.2019.05.003.
[59] Seibel MJ. Biochemical Markers of Bone Turnover Part I: Biochemistry and Variability. Clin Biochem Rev Aust Assoc Clin Biochem 2005;26:97.
[60] Henriksen K, Neutzsky-Wulff AV, Bonewald LF, Karsdal MA. Local communication on and within bone controls bone remodeling. Bone 2009;44:1026–33. https://doi.org/10.1016/j.bone.2009.03.671.
[61] Rauch F, Glorieux FH. Osteogenesis imperfecta. The Lancet 2004;363:1377–85. https://doi.org/10.1016/S0140-6736(04)16051-0.
[62] Boskey AL. Bone composition: relationship to bone fragility and antiosteoporotic drug effects. BoneKEy Rep 2013;2:447. https://doi.org/10.1038/bonekey.2013.181.
[63] Hauschka PV, Lian JB, Cole DE, Gundberg CM. Osteocalcin and matrix Gla protein: vitamin K-dependent proteins in bone. Physiol Rev 1989;69:990–1047. https://doi.org/10.1152/physrev.1989.69.3.990.
[64] Boskey AL. Noncollagenous matrix proteins and their role in mineralization. Bone Miner 1989;6:111–23. https://doi.org/10.1016/0169-6009(89)90044-5.
[65] Licini C, Vitale-Brovarone C, Mattioli-Belmonte M. Collagen and non-collagenous proteins molecular crosstalk in the pathophysiology of osteoporosis. Cytokine Growth Factor Rev 2019;49:59–69. https://doi.org/10.1016/j.cytogfr.2019.09.001.
[66] Lee NK, Sowa H, Hinoi E, Ferron M, Ahn JD, Confavreux C, et al. Endocrine Regulation of Energy Metabolism by the Skeleton. Cell 2007;130:456–69. https://doi.org/10.1016/j.cell.2007.05.047.
[67] Ferron M, Wei J, Yoshizawa T, Fattore AD, DePinho RA, Teti A, et al. Insulin signaling in osteoblasts integrates bone remodeling and energy metabolism. Cell 2010;142:296. https://doi.org/10.1016/j.cell.2010.06.003.
[68] Qin C, Baba O, Butler WT. Post-translational Modifications of SIBLING Proteins and Their Roles in Osteogenesis and Dentinogenesis. Crit Rev Oral Biol Med 2004;15:126–36. https://doi.org/10.1177/154411130401500302.
[69] Fisher LW, Torchia DA, Fohr B, Young MF, Fedarko NS. Flexible Structures of SIBLING Proteins, Bone Sialoprotein, and Osteopontin. Biochem Biophys Res Commun 2001;280:460–5. https://doi.org/10.1006/bbrc.2000.4146.
[70] Hunter GK, Goldberg HA. Nucleation of hydroxyapatite by bone sialoprotein. Proc Natl Acad Sci U S A 1993;90:8562. https://doi.org/10.1073/pnas.90.18.8562.
[71] Baht GS, Hunter GK, Goldberg HA. Bone sialoprotein–collagen interaction promotes hydroxyapatite nucleation. Matrix Biol 2008;27:600–8. https://doi.org/10.1016/j.matbio.2008.06.004.
[72] Harris BS, Zhang Y, Card L, Rivera LB, Brekken RA, Bradshaw AD. SPARC regulates collagen interaction with cardiac fibroblast cell surfaces. Am J Physiol-Heart Circ Physiol 2011;301:H841–7. https://doi.org/10.1152/ajpheart.01247.2010.
[73] Mochida Y, Parisuthiman D, Pornprasertsuk-Damrongsri S, Atsawasuwan P, Sricholpech M, Boskey AL, et al. Decorin modulates collagen matrix assembly and mineralization. Matrix Biol 2009;28:44–52. https://doi.org/10.1016/j.matbio.2008.11.003.

[74] Bianco P, Fisher LW, Young MF, Termine JD, Robey PG. Expression and localization of the two small proteoglycans biglycan and decorin in developing human skeletal and non-skeletal tissues. J Histochem Cytochem 1990;38:1549–63. https://doi.org/10.1177/38.11.2212616.
[75] Kram V, Shainer R, Jani P, Meester JA, Loeys B, Young MF. Biglycan in the Skeleton. J Histochem Cytochem 2020;68:747. https://doi.org/10.1369/0022155420937371.
[76] Canalis E, Economides AN, Gazzerro E. Bone Morphogenetic Proteins, Their Antagonists, and the Skeleton. Endocr Rev 2003;24:218–35. https://doi.org/10.1210/er.2002-0023.
[77] Šromová V, Sobola D, Kaspar P. A Brief Review of Bone Cell Function and Importance. Cells 2023;12:2576. https://doi.org/10.3390/cells12212576.
[78] Elliott JC. Structure and chemistry of the apatites and other calcium orthophosphates. Amsterdam [The Netherlands] : New York: Elsevier; 1994.
[79] Kourkoumelis N. Osteoporosis and strontium-substituted hydroxyapatites. Ann Transl Med 2016;4:S10–S10. https://doi.org/10.21037/atm.2016.10.03.
[80] Zapanta LeGeros R. Apatites in biological systems. Prog Cryst Growth Charact 1981;4:1–45. https://doi.org/10.1016/0146-3535(81)90046-0.
[81] Terra J, Dourado ER, Eon J-G, Ellis DE, Gonzalez G, Rossi AM. The structure of strontium-doped hydroxyapatite: an experimental and theoretical study. Phys Chem Chem Phys 2009;11:568–77. https://doi.org/10.1039/B802841A.
[82] Wopenka B, Pasteris JD. A mineralogical perspective on the apatite in bone. Mater Sci Eng C 2005;25:131–43. https://doi.org/10.1016/j.msec.2005.01.008.
[83] Akazawa H. Characterization of crystallographic orientation and lattice disorder in hydroxyapatite thin films by Raman scattering. Ceram Int 2022;48:624–31. https://doi.org/10.1016/j.ceramint.2021.09.141.
[84] Von Euw S, Wang Y, Laurent G, Drouet C, Babonneau F, Nassif N, et al. Bone mineral: new insights into its chemical composition. Sci Rep 2019;9:8456. https://doi.org/10.1038/s41598-019-44620-6.
[85] Fleet M. Carbonated hydroxyapatite: materials, synthesis, and applications. Singapore: Pan Stanford Publishing; 2015.
[86] Balatsoukas I, Kourkoumelis N, Tzaphlidou M. Auger electron spectroscopy for the determination of sex and age related Ca/P ratio at different bone sites. J Appl Phys 2010;108.
[87] Kourkoumelis N, Balatsoukas I, Tzaphlidou M. Ca/P concentration ratio at different sites of normal and osteoporotic rabbit bones evaluated by Auger and energy dispersive X-ray spectroscopy. J Biol Phys 2011;38:279. https://doi.org/10.1007/s10867-011-9247-3.
[88] Wang B, Zhang Z, Pan H. Bone Apatite Nanocrystal: Crystalline Structure, Chemical Composition, and Architecture. Biomimetics 2023;8:90. https://doi.org/10.3390/biomimetics8010090.
[89] Grynpas M. Age and disease-related changes in the mineral of bone. Calcif Tissue Int 1993;53:S57–64. https://doi.org/10.1007/BF01673403.
[90] Driessens FCM, Van Dijk JWE, Verbeeck RMH. The Role of Bone Mineral in Calcium and Phosphate Homeostasis. Bull Sociétés Chim Belg 1986;95:337–42. https://doi.org/10.1002/bscb.19860950508.
[91] Zaidi M, Yuen T, Sun L, Rosen CJ. Regulation of Skeletal Homeostasis. Endocr Rev 2018;39:701–18. https://doi.org/10.1210/er.2018-00050.
[92] Shaker JL, Deftos L. Calcium and Phosphate Homeostasis. In: Feingold KR, Anawalt B, Blackman MR, Boyce A, Chrousos G, Corpas E, et al., editors. Endotext, South Dartmouth (MA): MDText.com, Inc.; 2000.

[93] Bouxsein ML. Bone quality: where do we go from here? Osteoporos Int 2003;14:118–27. https://doi.org/10.1007/s00198-003-1489-x.
[94] Fonseca H, Moreira-Gonçalves D, Coriolano H-JA, Duarte JA. Bone Quality: The Determinants of Bone Strength and Fragility. Sports Med 2014;44:37–53. https://doi.org/10.1007/s40279-013-0100-7.
[95] Paschalis EP, Gamsjaeger S, Klaushofer K. Vibrational spectroscopic techniques to assess bone quality. Osteoporos Int 2017;28:2275–91. https://doi.org/10.1007/s00198-017-4019-y.
[96] Wang F, Zheng L, Theopold J, Schleifenbaum S, Heyde C-E, Osterhoff G. Methods for bone quality assessment in human bone tissue: a systematic review. J Orthop Surg 2022;17:1–24. https://doi.org/10.1186/s13018-022-03041-4.
[97] Mandair GS, Morris MD. Contributions of Raman spectroscopy to the understanding of bone strength. BoneKEy Rep 2015;4:620. https://doi.org/10.1038/bonekey.2014.115.
[98] Morris MD, Mandair GS. Raman Assessment of Bone Quality. Clin Orthop Relat Res 2011;469:2160–9. https://doi.org/10.1007/s11999-010-1692-y.
[99] Glycine. Wikipedia 2024.
[100] Proline. Wikipedia 2024.
[101] Hydroxyproline. Wikipedia 2024.
[102] Nomura K, Fiala T, Wennemers H. Carbohydrate Co-Solutes Stabilize Collagen Triple Helices. ChemBioChem 2024;25:e202300860. https://doi.org/10.1002/cbic.202300860.
[103] Hydroxyapatite Ca5(OH)(PO4)3. ChemTube3D n.d. https://www.chemtube3d.com/sshydroxyapatite/ (accessed November 9, 2024).

2. Osteoporosis

2.1. Introduction

Osteoporosis is a chronic metabolic disorder affecting the skeletal system, characterized by a progressive decline in bone mass and alterations in the microarchitecture of bone tissue. These changes weaken the structural integrity of bones, making them more fragile and significantly increasing the likelihood of fractures, even with minimal trauma. [1]. It is the most common metabolic bone disease, predominantly affecting older adults, with postmenopausal women experiencing higher rates than men due to hormonal changes during this period that accelerate bone resorption [2]. Although older adults are at greater risk, osteoporosis can also develop in younger individuals, particularly in the presence of risk factors such as prolonged glucocorticoid use, endocrine disorders, or chronic illnesses [3].

From an epidemiological perspective, osteoporosis represents a significant global health challenge. Approximately 500 million people worldwide are estimated to suffer from the disease, with its prevalence increasing alongside aging populations [4]. In Europe and North America, approximately 30% of women are affected, with one in three women and one in five men over the age of 50 experiencing osteoporotic fractures [2,4]. These fractures, particularly in the hip, spine, and wrist, result in substantial morbidity and mortality, including a one-year mortality rate of 20–25% following hip fractures in older adults, as well as loss of mobility, independence, and increased long-term care needs [7–9].

In Greece, osteoporosis affects approximately 5.7% of the population, with 99,000 individuals experiencing osteoporosis-related fractures in 2019. This number is expected to increase to 121,000 in 2034 [5]. The prevalence of the disease is even higher in China, estimated at 13% of the population, with a predicted annual cost of cost approximately $19.92 billion by 2035 [6].

Racial and ethnic variations in osteoporosis prevalence and fracture risk are also notable. In the USA, 17% of postmenopausal Caucasian women have hip osteoporosis, compared to 12% of Hispanic-American women and 8% of African-American women. Similar trends are observed among men [10,11].

In addition to its societal impact, osteoporosis imposes a considerable economic burden. In the European Union, the annual cost of osteoporosis-related fractures was estimated at over €56.9 billion in 2019 [12], while in the United States, these costs are expected to exceed $25 billion in 2025 [13]. With aging populations, longer lifespans, and increasing fracture rates, the economic burden of osteoporosis is expected to rise significantly in the coming decades [14].

Osteoporosis arises from an imbalance in the bone remodeling process, where bone resorption by osteoclasts surpasses bone formation by osteoblasts. This imbalance leads to changes not only in bone density but also in its microstructural integrity and composition. Alterations in collagen cross-linking, mineral crystal size, and the proportion of non-collagenous proteins are among the key factors that affect bone fragility [15]. These compositional and structural changes at the molecular level emphasize the importance of understanding osteoporosis beyond the traditional focus on bone mineral density (BMD), as captured by dual-energy X-ray absorptiometry (DXA), to include broader aspects of bone quality. Understanding the multifactorial interplay between the biological, compositional, and mechanical aspects of osteoporotic bone is essential for developing effective diagnostic and therapeutic strategies.

2.2. Pathophysiology

Osteoporosis occurs as a result of imbalanced bone remodeling, where bone resorption by osteoclasts exceeds bone formation by osteoblasts. This imbalance, primarily driven by dysregulated activities of osteoclasts and osteoblasts and influenced by hormonal, genetic, and biochemical factors, leads to decreased bone mass and compromised microarchitecture [15].

Osteoporosis can be classified into primary and secondary forms. Primary osteoporosis is the most common type and mainly arises due to age-related changes or hormonal deficiencies. It includes postmenopausal osteoporosis in women, which is largely driven by estrogen deficiency and primarily affects trabecular bones, and senile osteoporosis, which occurs with aging as bone remodeling becomes increasingly imbalanced [2,10]. In contrast, secondary osteoporosis results from external factors or underlying medical conditions that disrupt bone homeostasis, including endocrine disorders (hyperthyroidism, hyperparathyroidism, etc.), chronic diseases (rheumatoid arthritis, Crohn’s disease, etc.), specific medications (long-term glucocorticoid therapy), and lifestyle factors (vitamin D insufficiency, prolonged immobilization, etc.) [2,10].

Of central importance to the regulation of bone remodeling is the RANKL-RANK-OPG system. Receptor activator of NF-κB ligand (RANKL) is a protein that belongs to the tumour necrosis factor (TNF) family of proteins and is expressed by osteoblasts and osteocytes. RANKL binds to its

receptor, RANK, which is located on the surface of osteoclast precursors and mature osteoclasts. This interaction promotes the differentiation, activation, and survival of osteoclasts, leading to bone resorption. To counterbalance this process, osteoblasts produce osteoprotegerin (OPG), a decoy receptor that binds to RANKL and prevents it from interacting with RANK. By inhibiting osteoclastogenesis, OPG acts as a key regulator of bone remodeling. The balance between RANKL and OPG is essential for maintaining bone homeostasis, and disruptions in this system are implicated in conditions like osteoporosis, where elevated RANKL or reduced OPG levels result to excessive bone resorption [16,17].

Estrogen deficiency, particularly post-menopause, is the main contributor to primary osteoporosis and significantly affects the RANKL-RANK-OPG system, disrupting the balance between bone formation and resorption. Normally, estrogens suppress RANKL expression and enhance OPG production, limiting osteoclast activity. Its deficiency leads to heightened osteoclast activity and accelerated bone turnover [18]. Additionally, estrogens influence osteocyte viability and their absence increases osteocyte apoptosis, further compromising bone quality and structural integrity [19,20].

Chronic inflammation is a critical contributor to secondary osteoporosis, particularly in cases associated with autoimmune diseases or other inflammatory conditions. Pro-inflammatory cytokines, such as tumor necrosis factor-alpha (TNF-α), interleukin-1 (IL-1), and interleukin-6 (IL-6), disrupt bone homeostasis by directly influencing the RANKL-RANK-OPG system [21]. These cytokines enhance RANKL expression and suppress OPG production, favoring bone resorption. Elevated levels of these cytokines are observed in conditions such as rheumatoid arthritis, inflammatory bowel disease, and systemic lupus erythematosus, which are often associated with secondary osteoporosis [22–24]. Additionally, chronic inflammation impairs osteoblast function and decreases their lifespan, reducing bone formation. Oxidative stress, frequently accompanying inflammation, intensifies this process by inducing apoptosis in osteocytes and osteoblasts, further compromising bone quality [25]. The cumulative effect of these mechanisms is a net loss of bone mass and increased fracture risk in patients with chronic inflammatory diseases.

The treatment of inflammatory and autoimmune diseases frequently involves the use of corticosteroids. However, chronic use of corticosteroids disrupts bone remodeling through multiple mechanisms. They reduce osteoblast lifespan, differentiation, and activity, negatively affecting bone formation. Corticosteroids also increase osteocyte apoptosis, weakening the structural integrity and signaling capacity of bone. Furthermore, they increase RANKL expression while suppressing OPG production, promoting bone resorption by osteoclasts [26]. As a result, individuals on long-term corticosteroid therapy are at risk for glucocorticoid-induced osteoporosis (GIOP), characterized by rapid bone loss and increased fracture likelihood.

2.3. Bone composition in osteoporosis

2.3.1. Microscopic changes

Osteoporosis causes changes to the microscopic structure of both cortical and trabecular bone, with distinct patterns of deterioration in each type. In cortical bone, one pronounced change is the increased porosity within its structure. This porosity occurs primarily in the Haversian system, where osteoclastic resorption outpaces osteoblastic formation, leading to the enlargement of existing Haversian canals and the creation of new resorption cavities. Volkmann's canals, which interconnect adjacent Haversian systems, also become enlarged, increasing connectivity and further contributing to overall porosity [15].

With aging and osteoporosis, the geometry of cortical bone also adapts to mechanical changes. Both the outer and inner diameters of cortical bone increase, while the cortical thickness is reduced (Fig. 2.1(A-C)) [27]. This geometric adaptation, combined with increasing porosity, results in dramatic changes to the endocortical surface. In advanced stages, the coalescence of Haversian canals and fragmentation of the endocortical region lead to trabecularization of cortical bone, where cortical remnants take on a trabecular-like structure (Fig. 2.1(D)) [15]. Porosity in cortical bone increases from about 4% in young, healthy bones to nearly 12% by age 60 and up to 50% in very elderly individuals [28]. These changes significantly impair the structural and mechanical integrity of cortical bone, exacerbating fragility and increasing the risk of fractures.

In trabecular bone, the changes are even more pronounced due to its inherently higher metabolic activity and higher surface-to-volume ratio compared to cortical bone. Osteoporotic trabeculae experience a decrease in thickness and connectivity, leading to a less dense and more fragmented trabecular network [29,30]. Moreover, the structural integrity of trabeculae changes from plate-like to more rod-like structures, further compromising the bone’s ability to withstand and distribute mechanical loads effectively [31,32]. These changes increase the risk of fractures, particularly in weight-bearing bones such as the femoral neck and vertebrae [33]. While thinning is the predominant change, some studies suggest that localized thickening of remaining trabeculae may occur as a compensatory response to increased mechanical loads. However, this adaptation is insufficient to restore the mechanical strength of the trabecular network [30,34].

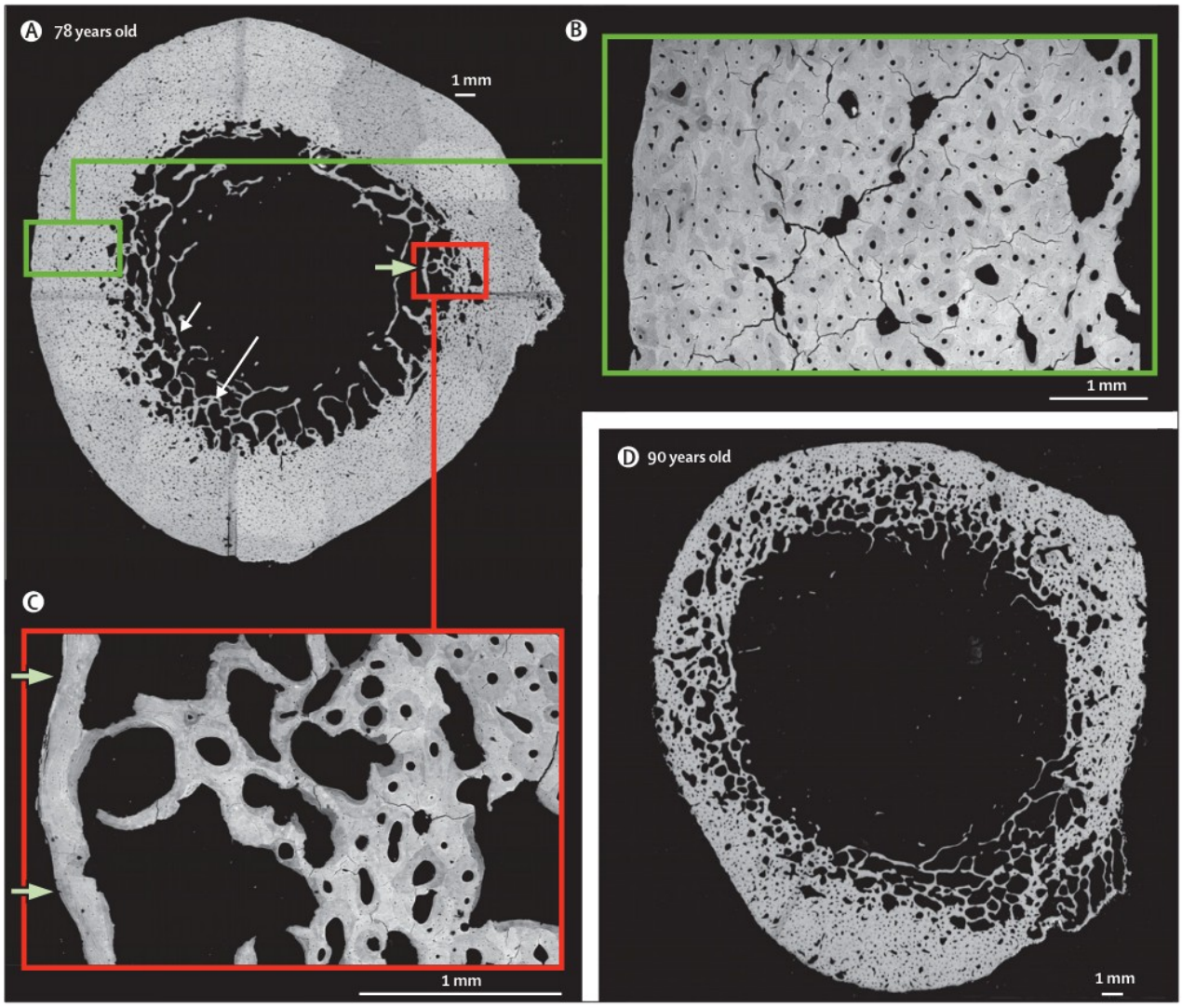

Figure 2.1: (A) Micrograph of cortical bone specimen from a 78 years old woman where increased porosity and cortical thinning can be observed. (B) Zoomed-in region showing increased porosity and crack formation but no trabecularization. (C) Zoomed-in region showing preserved endocortical envelope (arrows) which is indicative of bone thinning occurring from within the bone. (D) Micrograph of cortical bone specimen from a 78 years old woman where extended trabecularization can be observed. Figure from [28].

2.3.2. Molecular changes

On a molecular level, osteoporosis involves alterations in both the organic and mineral components of bone, leading to reduced bone quality. In the organic matrix, changes in collagen cross-linking patterns and disruptions in collagen turnover affect the structural and mechanical integrity of bone. The balance between enzymatic cross-links, which provide stability, and non-enzymatic cross-links, which increase brittleness, is disrupted in osteoporosis [35,36]. In the mineral phase, alterations in hydroxyapatite crystal properties, including changes in size, shape,

and composition, impact the mechanical behavior of bone. These mineral modifications, along with a reduced mineral-to-matrix ratio, contribute to increased bone fragility.

Organic matrix

The primary organic component of bone, Type I collagen, undergoes significant modifications in osteoporosis. Collagen's structural integrity is critical for bone's flexibility and resistance to fractures, and its role is compromised by changes in both enzymatic and non-enzymatic cross-linking. Enzymatic cross-links, both reducible, such as deH-DHLNL, deH-HLNL, and non-reducible, such as PYD and DPD, contribute to the mechanical stability of the collagen network. Studies have shown that while the concentration of non-reducible cross-links remains largely unchanged in osteoporotic bone, the concentration of reducible cross-links has been observed to decrease, weakening the matrix and increasing the risk of microcracks [35–39]. Simultaneously, non-enzymatic cross-linking, mediated by advanced glycation end-products (AGEs), tends to increase with aging and osteoporosis. AGEs alter the flexibility of collagen fibrils, making the bone matrix brittle and less capable of withstanding impact forces [35].

Mineral phase

The structure and elemental composition of hydroxyapatite is also affected in osteoporosis. Studies in human and animal models of osteoporosis have shown that the mineral-to-matrix ratio is decreased in osteoporotic bone, suggesting an overall decrease in the mineral content [40,41]. Additionally, osteoporotic bone often exhibits an increased mineral crystal size and a higher degree of crystallinity, possibly as a compensatory response to structural weakening [42]. While larger and more organized mineral crystals improve stiffness, they reduce the bone's ability to deform under stress, making it more prone to fracture.

Alterations in carbonate and acid phosphate substitutions within the hydroxyapatite lattice are characteristic features of osteoporotic bone. Increased carbonate and/or acid phosphate levels can influence the crystal lattice, potentially leading to decreased Type A carbonate substitutions [39]. Acid phosphate levels are indicative of crystal size and perfection, being particularly elevated in regions of active bone formation where crystals are smaller and less mature [43]. The carbonate-to-phosphate ratio, however, is a more variable parameter in osteoporosis and has been reported to either increase or decrease in FTIR studies depending on local remodeling dynamics and mineralization heterogeneity [39,44]. In Raman studies, carbonate-to-phosphate ratio has been found to increase in general in osteoporosis, however this is also region-dependent, as on studies on iliac crest biopsies of women it has been observed to increase in cortical bone, but not in trabecular bone [45,46].

Alterations in the calcium-to-phosphorus (Ca/P) ratio have been reported in osteoporotic bone [47]. The Ca/P ratio is a key indicator of bone health, playing a critical role in maintaining bone

homeostasis and supporting its metabolic activity. This ratio has been found to decrease between healthy and osteoporotic bones in animal models [47]. Changes in this ratio can reflect disruptions in mineral composition and bone remodeling processes, making it a valuable biomarker for assessing bone quality and metabolic status.

2.4. Diagnosis

The diagnosis of osteoporosis primarily relies on the measurement of bone mineral density (BMD) through dual-energy X-ray absorptiometry (DXA), which is considered the gold standard [1]. BMD is evaluated at key skeletal sites such as the lumbar spine, femoral neck, and total hip, as these are most predictive of fracture risk. According to the World Health Organization (WHO), osteoporosis is diagnosed when the BMD T-score is ≤ -2.5, reflecting a bone density more than 2.5 standard deviations below the mean of a healthy young adult population [10].

Although DXA is widely used, it does not consider the heterogeneity of the bone tissue and provides limited information about bone quality, including microarchitecture, mineralization, and the organic matrix, which are critical determinants of bone strength [48]. Advanced imaging modalities, such as quantitative computed tomography (QCT), high-resolution peripheral quantitative computed tomography (HR-pQCT), and magnetic resonance imaging (MRI), are developed and allow for the assessment of these parameters. However, their use in clinical practice is limited by cost, availability, and exposure to radiation in the case of QCT [49].

Biochemical markers of bone turnover (BTMs), such as procollagen type I N-terminal propeptide (P1NP) for bone formation and C-terminal telopeptide of type I collagen (CTX) for bone resorption, serve as adjuncts to imaging. Elevated levels of these markers can indicate high bone turnover, correlating with increased fracture risk [Eastell et al., 2016].

Spectroscopic techniques, particularly Raman spectroscopy, emerge as promising tools for advancing osteoporosis biochemical and biophysical etiology, as it can provide detailed information about the mineral and organic components of bone. In osteoporosis, compositional changes such as a reduced mineral-to-matrix ratio, altered hydroxyapatite crystallinity, and changes in carbonate substitution levels can be quantified using Raman spectra. These parameters reflect impaired mineralization and structural integrity that contribute to decreased bone quality and bone fragility [46]. Raman spectroscopy also allows for the assessment of the quality of the collagen matrix, a crucial determinant of bone strength. For example, shifts in the ratio of enzymatic to non-enzymatic cross-links, indicative of aging and pathological conditions, can be identified. Such changes directly impact the mechanical properties of bone and are challenging to detect using conventional methods [50]. Other spectroscopic techniques, such as Fourier-transform infrared spectroscopy (FTIR), have been used to study bone quality, but Raman spectroscopy offers advantages in spatial resolution and its capacity to analyze hydrated samples [44]. These features

make it particularly suited for detailed compositional analysis, complementing traditional diagnostic methods like DXA.

Recent advancements in Raman technology, including portable and fiber-optic systems, as well as the development of the spatially-offset Raman spectroscopy (SORS) technique, which allows for the extraction of information from deeper layers of the bone tissue, have facilitated its potential application in clinical settings [51,52]. These developments have the potential of being applied for in vivo measurements of superficial bone layers, offering a non-invasive approach to assess bone quality. However, the most significant facet of spectroscopic analysis is its ability to detect the subtle molecular changes occurring in bone tissue affected by osteoporosis.

2.5. References

[1] Kanis JA, McCloskey EV, Johansson H, Cooper C, Rizzoli R, Reginster J-Y, et al. European guidance for the diagnosis and management of osteoporosis in postmenopausal women. Osteoporos Int 2012;24:23. https://doi.org/10.1007/s00198-012-2074-y.

[2] Sözen T, Özışık L, Başaran NÇ. An overview and management of osteoporosis. Eur J Rheumatol 2016;4:46. https://doi.org/10.5152/eurjrheum.2016.048.

[3] Compston J, Cooper A, Cooper C, Gittoes N, Gregson C, Harvey N, et al. UK clinical guideline for the prevention and treatment of osteoporosis. Arch Osteoporos 2017;12:43. https://doi.org/10.1007/s11657-017-0324-5.

[4] Epidemiology of osteoporosis and fragility fractures | International Osteoporosis Foundation n.d. https://www.osteoporosis.foundation/facts-statistics/epidemiology-of-osteoporosis-and-fragility-fractures (accessed November 16, 2024).

[5] Willers C, Norton N, Harvey NC, Jacobson T, Johansson H, Lorentzon M, et al. Osteoporosis in Europe: a compendium of country-specific reports. Arch Osteoporos 2022;17:23. https://doi.org/10.1007/s11657-021-00969-8.

[6] Zeng Q, Li N, Wang Q, Feng J, Sun D, Zhang Q, et al. The Prevalence of Osteoporosis in China, a Nationwide, Multicenter DXA Survey. J Bone Miner Res 2019;34:1789–97. https://doi.org/10.1002/jbmr.3757.

[7] NIH Consensus Development Panel on Osteoporosis Prevention D and Therapy. Osteoporosis Prevention, Diagnosis, and Therapy. JAMA 2001;285:785–95. https://doi.org/10.1001/jama.285.6.785.

[8] Rachner TD, Khosla S, Hofbauer LC. Osteoporosis: now and the future. The Lancet 2011;377:1276–87. https://doi.org/10.1016/S0140-6736(10)62349-5.

[9] Johnell O, Kanis JA. An estimate of the worldwide prevalence and disability associated with osteoporotic fractures. Osteoporos Int 2006;17:1726–33. https://doi.org/10.1007/s00198-006-0172-4.

[10] World Health Organization. Prevention and Management of Osteoporosis: Report of a WHO Scientific Group. Geneva: World Health Organization; 2003.

[11] Kanis JA, McCloskey EV, Johansson H, Oden A, Melton LJ, Khaltaev N. A reference standard for the description of osteoporosis. Bone 2008;42:467–75. https://doi.org/10.1016/j.bone.2007.11.001.

[12] Kanis JA, Norton N, Harvey NC, Jacobson T, Johansson H, Lorentzon M, et al. SCOPE 2021: a new scorecard for osteoporosis in Europe. Arch Osteoporos 2021;16:82. https://doi.org/10.1007/s11657-020-00871-9.
[13] Singer A, McClung MR, Tran O, Morrow CD, Goldstein S, Kagan R, et al. Treatment rates and healthcare costs of patients with fragility fracture by site of care: a real-world data analysis. Arch Osteoporos 2023;18:42. https://doi.org/10.1007/s11657-023-01229-7.
[14] Hernlund E, Svedbom A, Ivergård M, Compston J, Cooper C, Stenmark J, et al. Osteoporosis in the European Union: medical management, epidemiology and economic burden: A report prepared in collaboration with the International Osteoporosis Foundation (IOF) and the European Federation of Pharmaceutical Industry Associations (EFPIA). Arch Osteoporos 2013;8:136. https://doi.org/10.1007/s11657-013-0136-1.
[15] Osterhoff G, Morgan EF, Shefelbine SJ, Karim L, McNamara LM, Augat P. Bone mechanical properties and changes with osteoporosis. Injury 2016;47:S11. https://doi.org/10.1016/S0020-1383(16)47003-8.
[16] Burr DB. Basic and Applied Bone Biology. 2nd ed. San Diego: Elsevier Science & Technology; 2019.
[17] Rachner TD, Khosla S, Hofbauer LC. Osteoporosis: now and the future. Lancet Lond Engl 2011;377:1276–87. https://doi.org/10.1016/S0140-6736(10)62349-5.
[18] Streicher C, Heyny A, Andrukhova O, Haigl B, Slavic S, Schüler C, et al. Estrogen Regulates Bone Turnover by Targeting RANKL Expression in Bone Lining Cells. Sci Rep 2017;7:6460. https://doi.org/10.1038/s41598-017-06614-0.
[19] Hughes DE, Dai A, Tiffee JC, Li HH, Mundy GR, Boyce BF. Estrogen promotes apoptosis of murine osteoclasts mediated by TGF-beta. Nat Med 1996;2:1132–6. https://doi.org/10.1038/nm1096-1132.
[20] Krum SA, Miranda-Carboni GA, Hauschka PV, Carroll JS, Lane TF, Freedman LP, et al. Estrogen protects bone by inducing Fas ligand in osteoblasts to regulate osteoclast survival. EMBO J 2008;27:535–45. https://doi.org/10.1038/sj.emboj.7601984.
[21] Lacativa PGS, Farias MLF de. Osteoporosis and inflammation. Arq Bras Endocrinol Metabol 2010;54:123–32. https://doi.org/10.1590/s0004-27302010000200007.
[22] Tanaka Y, Nakayamada S, Okada Y. Osteoblasts and osteoclasts in bone remodeling and inflammation. Curr Drug Targets Inflamm Allergy 2005;4:325–8. https://doi.org/10.2174/1568010054022015.
[23] Ali T, Lam D, Bronze MS, Humphrey MB. Osteoporosis in Inflammatory Bowel Disease. Am J Med 2009;122:599–604. https://doi.org/10.1016/j.amjmed.2009.01.022.
[24] Lane NE. Therapy Insight: osteoporosis and osteonecrosis in systemic lupus erythematosus. Nat Clin Pract Rheumatol 2006;2:562–9. https://doi.org/10.1038/ncprheum0298.
[25] Zhang C, Li H, Li J, Hu J, Yang K, Tao L. Oxidative stress: A common pathological state in a high-risk population for osteoporosis. Biomed Pharmacother 2023;163:114834. https://doi.org/10.1016/j.biopha.2023.114834.
[26] Briot K, Roux C. Glucocorticoid-induced osteoporosis. RMD Open 2015;1:e000014. https://doi.org/10.1136/rmdopen-2014-000014.
[27] Tong X, Burton IS, Isaksson H, Jurvelin JS, Kröger H. Cortical Bone Histomorphometry in Male Femoral Neck: The Investigation of Age-Association and Regional Differences. Calcif Tissue Int 2015;96:295–306. https://doi.org/10.1007/s00223-015-9957-9.
[28] Zebaze RM, Ghasem-Zadeh A, Bohte A, Iuliano-Burns S, Mirams M, Price RI, et al. Intracortical remodelling and porosity in the distal radius and post-mortem femurs of women: a cross-

sectional study. The Lancet 2010;375:1729–36. https://doi.org/10.1016/S0140-6736(10)60320-0.
[29] Legrand E, Chappard D, Pascaretti C, Duquenne M, Krebs S, Rohmer V, et al. Trabecular Bone Microarchitecture, Bone Mineral Density, and Vertebral Fractures in Male Osteoporosis. J Bone Miner Res 2000;15:13–9. https://doi.org/10.1359/jbmr.2000.15.1.13.
[30] Parfitt AM. Trabecular bone architecture in the pathogenesis and prevention of fracture. Am J Med 1987;82:68–72. https://doi.org/10.1016/0002-9343(87)90274-9.
[31] Seeman E, Delmas PD. Bone Quality — The Material and Structural Basis of Bone Strength and Fragility. N Engl J Med 2006. https://doi.org/10.1056/NEJMra053077.
[32] Van Der Linden JC, Homminga J, Verhaar JAN, Weinans H. Mechanical Consequences of Bone Loss in Cancellous Bone. J Bone Miner Res 2001;16:457–65. https://doi.org/10.1359/jbmr.2001.16.3.457.
[33] Wehrli FW. Structural and functional assessment of trabecular and cortical bone by micro magnetic resonance imaging. J Magn Reson Imaging 2007;25:390–409. https://doi.org/10.1002/jmri.20807.
[34] Chen H, Zhou X, Fujita H, Onozuka M, Kubo K-Y. Age-Related Changes in Trabecular and Cortical Bone Microstructure. Int J Endocrinol 2013;2013:213234. https://doi.org/10.1155/2013/213234.
[35] Saito M, Marumo K. Collagen cross-links as a determinant of bone quality: a possible explanation for bone fragility in aging, osteoporosis, and diabetes mellitus. Osteoporos Int 2010;21:195–214. https://doi.org/10.1007/s00198-009-1066-z.
[36] Viguet-Carrin S, Garnero P, Delmas PD. The role of collagen in bone strength. Osteoporos Int 2006;17:319–36. https://doi.org/10.1007/s00198-005-2035-9.
[37] Oxlund H, Sekilde Li, Ørtoft G. Reduced concentration of collagen reducible cross links in human trabecular bone with respect to age and osteoporosis. Bone 1996;19:479–84. https://doi.org/10.1016/S8756-3282(96)00283-9.
[38] Bailey A, Wotton S, Sims T, Thompson P. Post-translational modifications in the collagen of human osteoporotic femoral head. Biochem Biophys Res Commun 1992;185:801–5. https://doi.org/10.1016/0006-291X(92)91697-O.
[39] Kourkoumelis N, Zhang X, Lin Z, Wang J. Fourier Transform Infrared Spectroscopy of Bone Tissue: Bone Quality Assessment in Preclinical and Clinical Applications of Osteoporosis and Fragility Fracture. Clin Rev Bone Miner Metab 2019;17:24–39. https://doi.org/10.1007/s12018-018-9255-y.
[40] Paschalis EP, DiCarlo E, Betts F, Sherman P, Mendelsohn R, Boskey AL. FTIR microspectroscopic analysis of human osteonal bone. Calcif Tissue Int 1996;59:480–7. https://doi.org/10.1007/BF00369214.
[41] Gadeleta SJ, Boskey AL, Paschalis E, Carlson C, Menschik F, Baldini T, et al. A physical, chemical, and mechanical study of lumbar vertebrae from normal, ovariectomized, and nandrolone decanoate-treated cynomolgus monkeys (*macaca fascicularis*). Bone 2000;27:541–50. https://doi.org/10.1016/S8756-3282(00)00362-8.
[42] Boivin G, Bala Y, Doublier A, Farlay D, Ste-Marie LG, Meunier PJ, et al. The role of mineralization and organic matrix in the microhardness of bone tissue from controls and osteoporotic patients. Bone 2008;43:532–8. https://doi.org/10.1016/j.bone.2008.05.024.
[43] Spevak L, Flach CR, Hunter T, Mendelsohn R, Boskey A. FTIRI Parameters describing Acid Phosphate Substitution in Biologic Hydroxyapatite. Calcif Tissue Int 2013;92:418–28. https://doi.org/10.1007/s00223-013-9695-9.

[44] Kourkoumelis N, Lani A, Tzaphlidou M. Infrared spectroscopic assessment of the inflammation-mediated osteoporosis (IMO) model applied to rabbit bone. J Biol Phys 2012;38:623–35. https://doi.org/10.1007/s10867-012-9276-6.
[45] McCreadie BR, Morris MD, Chen T-C, Sudhaker Rao D, Finney WF, Widjaja E, et al. Bone tissue compositional differences in women with and without osteoporotic fracture. Bone 2006;39:1190–5. https://doi.org/10.1016/j.bone.2006.06.008.
[46] Morris MD, Mandair GS. Raman Assessment of Bone Quality. Clin Orthop Relat Res 2011;469:2160–9. https://doi.org/10.1007/s11999-010-1692-y.
[47] Kourkoumelis N, Balatsoukas I, Tzaphlidou M. Ca/P concentration ratio at different sites of normal and osteoporotic rabbit bones evaluated by Auger and energy dispersive X-ray spectroscopy. J Biol Phys 2012;38:279–91. https://doi.org/10.1007/s10867-011-9247-3.
[48] Fonseca H, Moreira-Gonçalves D, Coriolano H-JA, Duarte JA. Bone Quality: The Determinants of Bone Strength and Fragility. Sports Med 2014;44:37–53. https://doi.org/10.1007/s40279-013-0100-7.
[49] Link TM. Osteoporosis Imaging: State of the Art and Advanced Imaging. Radiology 2012;263:3–17. https://doi.org/10.1148/radiol.12110462.
[50] Unal M, Ahmed R, Mahadevan-Jansen A, Nyman JS. Compositional assessment of bone by Raman spectroscopy. The Analyst 2021;146:7464. https://doi.org/10.1039/d1an01560e.
[51] Matousek P, Stone N. Development of deep subsurface Raman spectroscopy for medical diagnosis and disease monitoring. Chem Soc Rev 2015;45. https://doi.org/10.1039/c5cs00466g.
[52] Vardaki MZ, Pavlou E, Simantiris N, Lampri E, Seretis K, Kourkoumelis N. Towards non-invasive monitoring of non-melanoma skin cancer using spatially offset Raman spectroscopy. The Analyst 2023;148:4386–95. https://doi.org/10.1039/D3AN00684K.

3. Raman spectroscopy

3.1. Introduction

Raman spectroscopy is a form of vibrational spectroscopy that is widely used to study the chemical composition of a material through the interaction of light with the vibrational and rotational modes of the material's molecules. The technique is based on the Raman effect or Raman scattering, which was theoretically predicted by A. Smekal in 1923 and named after the Indian physicist C. V. Raman who, along with K. S. Krishnan, first observed it experimentally in 1928 [1,2]. For this discovery, Raman received the 1930 Nobel prize in Physics, making him the first Asian to ever accomplish that.

Raman scattering is the inelastic scattering of electromagnetic radiation by matter, producing photons with different energy and direction to the initial radiation. Raman experiments usually utilize monochromatic laser radiation in the ultraviolet (UV), visible, near-infrared (NIR) range and in the X-ray region [3,4].

Various Raman spectroscopy techniques have been developed over the years, such as resonance Raman spectroscopy (RSR) [5], confocal Raman microscopy [6], surface-enhanced Raman spectroscopy (SERS) [7], spatially-offset Raman spectroscopy (SORS) [8,9] and more. Raman spectroscopy allows for the non-destructive study and molecular characterization of both organic and inorganic materials, in either solid or liquid state or in solutions, with minimal preparation prior to measurement. By containing characteristic vibrational information specific to the chemical bonds of a molecule, Raman spectra can provide a molecular fingerprint of a substance. Due to its versatility, rapid use, and ability to provide both qualitative and quantitative results, Raman spectroscopy has evolved into a valuable analytical tool with applications in many scientific fields,

including, but not limited to, life sciences [10], pharmacology [11], geology [12], and semiconductors physics [13].

3.2. Theory of Raman scattering

3.2.1. Elastic and inelastic scattering

When electromagnetic radiation hits a material, the photons making up the radiation can interact with the material's molecules by being absorbed or scattered, or may not interact at all, passing straight through the material. During absorption, when the photon's energy matches the energy gap between two molecular states, the photon is absorbed and the molecule transitions from its lower-energy state to a higher-energy state. Scattering, on the other hand, refers to the deviation of electromagnetic radiation from a straight path due to its interaction with the material, specifically by localized non-uniformities of various sizes (also known as scattering centers or scatterers). It can be split into two major categories: elastic and inelastic scattering.

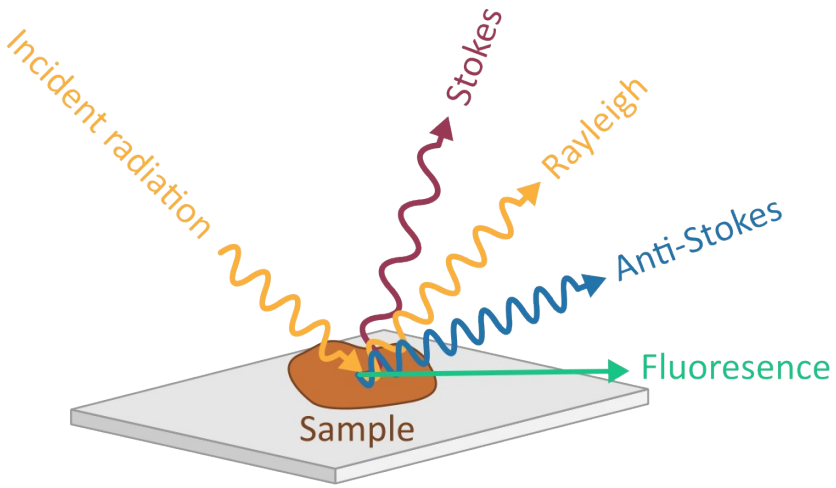

Figure 3.1: Rayleigh scattering, Raman scattering (Stokes and anti-Stokes), and fluorescence occurring upon irradiation of a sample with monochromatic radiation.

In elastic scattering the energy of the scattered radiation is equal to the energy of the incident radiation. When the scatterers are smaller than the wavelength of the incident light, the process is known as Rayleigh scattering. If their size is comparable to the wavelength, it is called Mie scattering. Finally, when the scatterers are larger than the wavelength, it is referred to as geometric

scattering and the behavior of light can be described using geometric optics [14,15]. In most Raman experiments, the scattering centers are much smaller (i.e., molecular level) than the excitation wavelength and Rayleigh scattering is the dominant type of elastic scattering. However, the Raman signal, which arises from inelastic scattering, is only a small fraction of the incident radiation intensity (typically 0.1–0.01%), while most of the scattered light is the result of Rayleigh scattering [16].

In inelastic scattering, a form of which is Raman scattering, a scattered photon can have either more or less energy than the incident photon. In the case of Raman scattering, this change in energy occurs due to the interaction and exchange of energy between the incident photon and the vibrational energy states of the target material's molecules. This inelastic scattering process is very weak, with the probability of a Raman scattering event being approximately 10^{-8}–10^{-6} times lower than that of Rayleigh scattering [17]. To observe such a low-probability process, a high photon flux is required, which can be achieved by using lasers to generate sufficient signal for detection, while microscopes can additionally focus the light into small volumes or areas.

3.2.2. Stokes and anti-Stokes scattering

The basic elastic and inelastic processes that take place in Raman scattering are illustrated in Fig. 3.2.

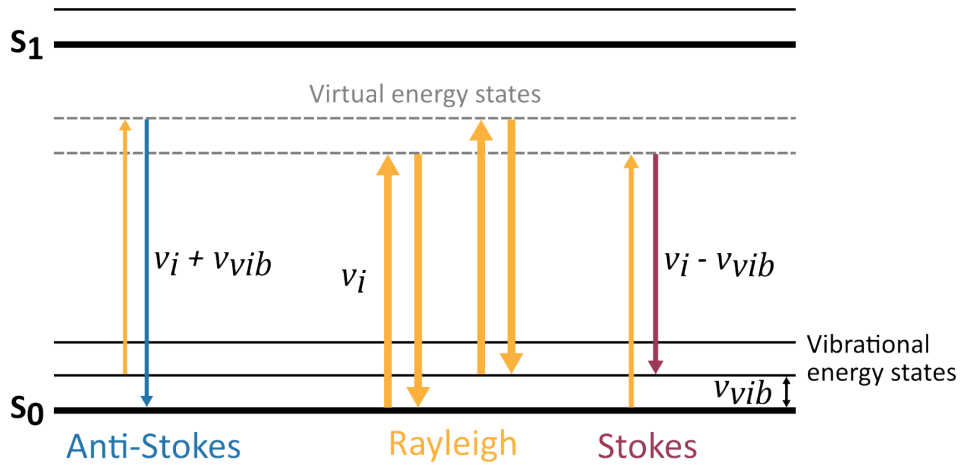

Figure 3.2: Jablonski diagram of Rayleigh and Raman scattering processes for transitions between two vibrational states of a molecule. S_0 and S_1 denote the ground and first excited electronic states of the molecule, respectively.

When a material is at room temperature, most of its molecules occupy the lowest electronic state (ground state) S_0 (depicted with bold, continuous horizontal line) and a small fraction can be at higher vibrational states (depicted with thin, continuous horizontal lines), with the first excited

vibrational state having a frequency difference v_{vib} from S_0. If a photon of energy $h\,v_i$ hits a molecule of the material but that energy is not close to the energy gap between the initial state and a higher energy electronic or vibrational state, it cannot be absorbed. However, it can be considered as getting excited to a virtual energy state (gray dashed horizontal lines). Virtual states are not real (stationary) states of the molecule and arise as a result of induced polarization due to the interaction of the electric field of the incident photon with the electronic cloud of the molecule. They have extremely short lifetime τ (typically of attosecond (10^{-18} s) duration), approximated as:

$$\tau = \frac{h}{4\pi\,\Delta E} \tag{3.1}$$

where $h = 6.626068 \times 10^{-34}\,\mathrm{m^2\,kg\,s^{-1}}$ is Planck's constant, and ΔE is the energy difference between the virtual state and the closest real state [18]. Almost immediately after the excitation to the virtual state, the molecule transitions to a lower energy state, emitting a photon of energy equal to the energy gap between the excited virtual state and the final state in the process.

There are three ways that the transition from the excited virtual state to a lower energy vibrational state may happen. If the molecule returns to its initial energy state, this is the case of Rayleigh scattering and the molecule emits a photon of energy equal to the energy of the photon it initially absorbed ($h\,v_i$). If the molecule returns to a vibrational state of higher energy than the initial, then the emitted photon has lower energy than the initial photon, so this scattering process is inelastic. The energy of the scattered photon is in this case $h(v_i - v_{vib})$, and the process is called Stokes scattering, in memory of G.G. Stokes who described the conversion of absorbed UV radiation by a material to emitted radiation of longer, visible wavelengths (smaller frequencies) [19]. If, on the other hand, the molecule returns to a vibrational state of lower energy than the initial, then the scattered photon has higher energy than the initial photon (again a case of inelastic scattering) with the scattered photon's energy being $h(v_i + v_{vib})$, and the process called anti-Stokes scattering.

The populations of the various energy states of a material's molecules influence the relative intensities of the Stokes and anti-Stokes processes. The number of molecules occupying the ground and higher energy vibrational states is calculated by the Boltzmann equation:

$$\frac{N_f}{N_i} = \frac{g_f}{g_i} e^{-\frac{E_f - E_i}{k_B T}} \tag{3.2}$$

with N_f being the number of molecules in an excited state f, N_i the number of molecules in the ground state i, g_f and g_i the degeneracy of the energy states (number of different energy states with the same energy) i and f respectively, $E_i - E_f$ the energy difference between states *n* and *m*, $k_B = 1.3807 \times 10^{-23}\,\mathrm{J/K}$ is Boltzmann's constant, and T the temperature of the material. Most

molecules of a material at room temperature and before irradiation are most likely to occupy the ground electronic state. This makes the Stokes process stronger overall than the anti-Stokes process at room temperature. Furthermore, while the Stokes and anti-Stokes lines in a Raman spectrum (corresponding to the vibrational levels of the molecules of the material) appear at the same relative frequencies (relative to the frequency of the Rayleigh line, i.e. the excitation frequency of the laser), their intensities are not analogous: in the anti-Stokes spectrum the lines get weaker as the frequency difference increases. This is because the population of molecules decreases exponentially with increasing vibrational energy levels, as described by the Boltzmann distribution. While the temperature of the material increases, the anti-Stokes process also increases in intensity and can be used to measure the material's temperature by evaluating the Stokes-to-antiStokes intensity ratio [20]. Due to its increased intensity, the Stokes part of the Raman spectrum is typically used in experiments. It should also be noted that the intensity of Raman scattering is analogous to the fourth power of the frequency of the excitation source:

$$I_R \propto v^4 I_0 N \left(\frac{\partial a}{\partial Q} \right)^2 \tag{3.3}$$

with v being the excitation frequency, I_0 the intensity of the source radiation, N the number of molecules that take place in the scattering, a the polarizability of the molecules, and Q the vibrational amplitude [21].

3.2.3. Raman shift

The intensity behavior of the Stokes and anti-Stokes scattering processes can be observed in the typical Raman spectrum of Fig. 3.3, where the Stokes and anti-Stokes spectra of CCl_4 are shown as an example [22].

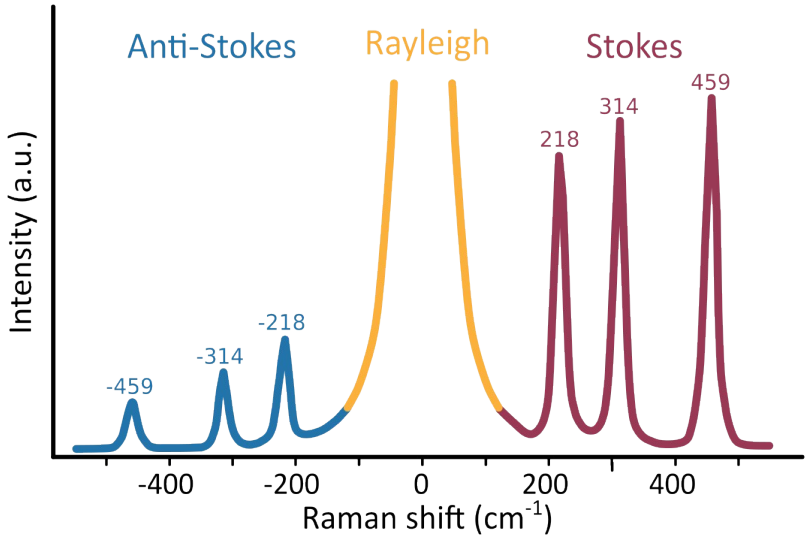

Figure 3.3: Raman spectrum of CCl4, excited with a 532 nm laser. The Rayleigh, Stokes and anti-Stokes scattering regions are highlighted with different colors. Image adapted from [22].

The horizontal axis is labeled as "Raman shift" and represents the shift in energy between the energy of the excitation radiation and the energy of the Raman scattered light. The Raman shift is given by:

$$\Delta\tilde{\nu} = \frac{1}{\lambda_0} - \frac{1}{\lambda} \tag{3.4}$$

where λ_0 is the wavelength of the excitation source and λ is the Raman spectrum wavelength. If the wavelengths are expressed in nanometers (nm), the Raman shift is expressed in units of inverse centimeters (cm^{-1}). In spectroscopy the quantity $\tilde{\nu} = \frac{1}{\lambda}$ is called a "wavenumber".

3.2.4. Fluorescence

In Raman scattering, the incident radiation excites a molecule to a virtual state and shortly after the molecule transitions to a lower energy vibrational state, emitting a photon of higher or lower energy than the incident photon. If, however, the incident photon's energy is enough to get a molecule excited to a higher electronic and vibrational energy state, the photon gets absorbed. The molecule then transitions to a lower energy state non-radiatively through vibrational relaxation (in which the energy dissipates as heat) without the emission of light, and then fluoresces, emitting a photon of lower energy than the initial. The process is depicted in Fig. 3.4. Fluorescence typically takes place in a time-scale of nanoseconds (10^{-9} s). It should be noted that if the frequency of the incident radiation is close to the absorption frequency of a molecular excitation, a case which is usually referred to as a resonance, the occurring Raman scattering is

called Resonance Raman Scattering and has the benefit of greatly increased intensity compared to the non-resonant case [23].

Fluorescence can have multiple effects in Raman spectra, acting as a competing phenomenon. The leading indication of fluorescence is the background signal. Since fluorescence emission is much stronger than Raman scattering, it can lower the signal-to-noise ratio (SNR) and obscure the Raman signal, complicating the acquisition and analysis of Raman spectra. Furthermore, fluorescence can alter the appearance of spectral features in a Raman spectrum by overlapping with Raman bands and distorting their shape, making the determination of peak positions, intensities, and widths challenging [17,24].

Biological samples often exhibit high fluorescence background due to the presence of intrinsic fluorophores, i.e. molecules with conjugated systems, such as aromatic amino acids, porphyrins, and other molecules, allowing for delocalized π-electrons [25,26]. The delocalization lowers the energy gap between the ground and excited states, facilitating the absorption of light in the visible or near-visible spectrum. After excitation, the molecules relax non-radiatively to lower energy states, from which they return to the ground state by emitting broad-spectrum fluorescence that can overwhelm the weaker Stokes Raman signal. The heterogeneity of biological samples, including the presence of pigments, lipids, and other fluorescent components, further contributes to this background.

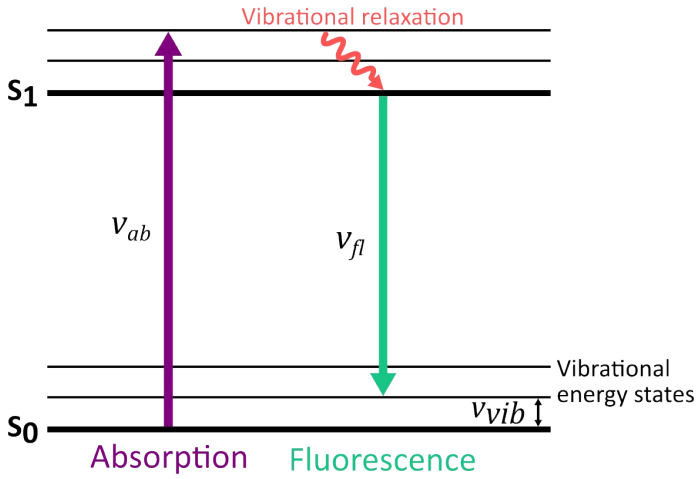

Figure 3.4: Jablonski diagram presenting the processes of absorption to an excited electronic and vibrational state, deexcitation through vibrational relaxation, and fluorescence.

To mitigate the effects of fluorescent emission experimentally, an excitation source of longer wavelength can be preferred (near-infrared (NIR) instead of visible or ultraviolet (UV) source), since NIR excitation wavelengths exhibit significantly less fluorescence than UV wavelengths, due to the

fact that NIR radiation does not have enough energy to excite molecules to electronic states [27]. Furthermore, since fluorescent radiation has less energy than the excitation radiation, anti-Stokes Raman scattering may also be employed as a means of efficient fluorescence reduction, given that anti-Stokes scattering produces photons with higher energy than the excitation radiation [28]. However, this comes at the cost of greatly decreased intensity. Other experimental techniques include, but are not limited to, the use of ultrashort laser pulses [29–35], frequency domain demodulation [36] and frequency-domain phase nulling [37], application of shifted excitation Raman difference spectroscopy (SERDS) [38,39] and subtracted shifted Raman spectroscopy (SSRS) [40], spatially engineered excitation beams [41], photobleching [42], etc [43].

Despite all experimental advancements in suppressing fluorescence, signal background is almost always present in Raman spectra, that can still affect spectral features and analysis. To circumvent this, computational background removal techniques are also used in combination with the above experimental techniques. The most popular computational methods include polynomial fitting [44–47], wavelet transform [48–50], and derivatives [51–53].

3.3. Classical description of Raman scattering

The basic aspects of Raman scattering can be described by using classical electrodynamics [28,54]. While this classical approach does not explain all observed phenomena that take place during Raman scattering, it is simple enough and can provide valuable insights for the frequency dependence of the effect, as well as specific elements of the selection rules. In this approach the molecules are considered as collections of charged particles (nuclei covered by electron clouds) with specific polarizabilities. Upon interaction of a molecule with the oscillating electric field of an incident photon, an oscillating electric dipole moment is induced to the molecule, which forces the molecule to oscillate and emit electromagnetic radiation at specific frequencies. It is this procedure that causes the Rayleigh and Raman scattering.

In more detail, let's consider the oscillating electric field $\vec{E}$ of an incident photon of angular frequency $\omega_i = 2\pi\nu_i$, with ν_i the frequency of the oscillation. The electric field can be considered as a plane wave and is given by:

$$\vec{E} = \vec{E}_0 \cos(\vec{k}_i \cdot \vec{r} - \omega_i t + \varphi) \tag{3.5}$$

with $\vec{E}_0$ the amplitude of the electric field, $\vec{k}_i = \frac{2\pi}{\lambda}\hat{k}$ the wave vector, $\vec{r}$ the position vector, t the time, and φ the phase offset. Without loss of generality, we use $\varphi = 0$ and set the frame of reference at the point where the field interacts with the molecule so that $\vec{r} = 0$ too. The electric field is then simplified to:

$$\vec{E} = \vec{E}_0 \cos(\omega_i t) \tag{3.6}$$

The presence of the electric field induces a dipole moment $\vec{\mu}$ that is given by:

$$\vec{\mu} = \boldsymbol{a}\vec{E} \tag{3.7}$$

with $\boldsymbol{a}$ the polarizability of the molecule. Polarizability is a measure of the ability of an atom or molecule to become polarized when it is influenced by an external electric field. In essence it shows how easily the electron cloud of an atom or molecule can be distorted by an external electric field. As a tensor it is a 3 × 3 matrix of the form:

$$\boldsymbol{a} = \begin{bmatrix} a_{xx} & a_{xy} & a_{xz} \\ a_{yx} & a_{yy} & a_{yz} \\ a_{zx} & a_{zy} & a_{zz} \end{bmatrix} \tag{3.8}$$

The diagonal elements of the matrix represent the response of a material to an electric field applied along the same axis as the dipole moment, while the off-diagonal elements represent the response of the material to electric fields applied in perpendicular directions. For an isotropic material, the off-diagonal elements are zero and the diagonal elements have the same scalar value a, reflecting the homogeneity of the material's response to the electric field in all directions.

For a single molecule that can vibrate without rotating, the polarizability tensor can be expressed as a Taylor expansion of each element $a_{\rho\sigma}$ (with $\rho, \sigma = x, y, z$) around the equilibrium position with respect to the normal coordinates as [54,55]:

$$a_{\rho\sigma} = (a_{\rho\sigma})_0 + \sum_k \left(\frac{\partial a_{\rho\sigma}}{\partial Q_k} \right)_0 Q_k + \frac{1}{2} \sum_{k,l} \left(\frac{\partial^2 a_{\rho\sigma}}{\partial Q_k \partial Q_l} \right)_0 Q_k Q_l + \ldots \tag{3.9}$$

with the subscript "0" denoting elements at the equilibrium position, Q_k, Q_l, … being the normal coordinates of vibration that correspond to the vibrational frequencies ω_k, ω_l, … of the molecule, and the summations taken over all normal coordinates. Using the electrical harmonic approximation, i.e. simplifying the differential equation by considering only terms up to the first derivative and neglecting higher-order derivatives, and also focusing only on one normal mode of vibration Q_k, we can write the following expression:

$$\boldsymbol{a}_k = \boldsymbol{a}_0 + \sum_k \{\boldsymbol{a}_k' Q_k\} \tag{3.10}$$

where $\boldsymbol{a}_k$ represents a tensor with components $(a_{\rho\sigma})_k$, $\boldsymbol{a}_0$ is a tensor with components $(a_{\rho\sigma})_0$, and:

$$\boldsymbol{a}_k^{'}=\left(\frac{\partial a_{\rho\sigma}}{\partial Q_k}\right)_0 \tag{3.11}$$

also called the derived polarizability tensor. For simple harmonic vibrations of the molecule, Q_k is given by:

$$Q_k=Q_{k0}\cos(\omega_k t+\delta_k) \tag{3.12}$$

with Q_{k0} being the normal coordinate's amplitude and δ_k a phase factor. By using Eq. 3.10 and 3.12, we obtain:

$$\boldsymbol{a}_k=\boldsymbol{a}_0+\sum_k \boldsymbol{a}_k^{'}Q_{k0}\cos(\omega_k t+\delta_k) \tag{3.13}$$

By combining this expression with Eq. 3.6 and 3.7, we get:

$$\vec{\mu}=\boldsymbol{a}_0\vec{E}_0\cos(\omega_i t)+\sum_k \boldsymbol{a}_k^{'}\vec{E}_0Q_{k0}\cos(\omega_k t+\delta_k)\cos(\omega_i t) \tag{3.14}$$

Finally, by using the trigonometric identity:

$$\cos(A)\cos(B)=\frac{1}{2}[\cos(A-B)+\cos(A+B)] \tag{3.15}$$

we arrive at:

$$\vec{\mu}=\boldsymbol{a}_0\vec{E}_0\cos(\omega_i t)+\frac{1}{2}\sum_k \boldsymbol{a}_k^{'}\vec{E}_0Q_{k0}\left\{\cos\left[(\omega_i-\omega_k)t-\delta_k\right]+\cos\left[(\omega_i+\omega_k)t+\delta_k\right]\right\} \tag{3.16}$$

The above expression of the induced electric dipole moment has three frequency components: the first component has angular dependence on ω_i and is the one producing radiation of frequency v_i, that is Rayleigh scattering, the second component has angular dependence on $\omega_i-\omega_k$ and is the one producing radiation of frequency v_i-v_k, that is Stokes scattering, and the third component has angular dependence on $\omega_i+\omega_k$ and is the one producing radiation of frequency v_i+v_k, that is anti-Stokes scattering.

The dependence of the two last terms of the electric dipole moment $\vec{\mu}$ as stated in Eq. 3.16 from $\boldsymbol{a}_k'$ also implies that in order for Raman scattering to take place, $\boldsymbol{a}_k'$ has to be non-zero, which in turn means that the first derivative of $a_{\rho\sigma}$ with respect to Q_k (Eq. 3.11), i.e. the slope of the polarizability at equilibrium position, has to be non-zero:

$$\left(\frac{\partial a_{\rho\sigma}}{\partial Q_k}\right)_0 \neq 0 \tag{3.17}$$

Eq. 3.17 sets the fundamental condition for Raman activity, stating that Raman scattering occurs if it induces a change in the polarizability of the molecule

The classical approach is simple but, not unexpectedly, has several limitations, thus is unable to describe all features observed in a Raman spectrum. The most important limitation is that it does not take into account the quantum nature of molecular systems, more specifically that molecular systems have discrete energy levels, and their interaction with light. Additionally, it cannot correctly determine the relative intensity of anti-Stokes to Stokes bands and does not describe resonance phenomena. All these limitations are overcome by using quantum mechanics to describe the Raman effect.

3.4. Quantum description of Raman scattering

In quantum mechanics, electromagnetic radiation is absorbed or emitted when a quantum system (e.g. atom or molecule) makes a transition from a lower energy state to a higher one and vice versa, respectively. This transition takes place if the transition dipole moment between the two states is non-zero. When an electromagnetic wave of frequency v_i interacts with a molecule, its electric field (given by Eq. 3.6) causes a perturbation to the molecule's wave-function. This perturbation gives rise to an induced transition moment $\mu_{f\,i}$ between an initial state i and a final state f that is given by:

$$\mu_{fi} = \int \psi_f^* \, \hat{\mu} \, \psi_i \, d\tau \tag{3.18}$$

where ψ_i and ψ_f are the wave functions of the initial and final state, respectively, $\hat{\mu}$ is the induced dipole moment operator, $d\tau$ is a volume element in configuration space, and the integral is extended to all this space. The star symbol designates the complex conjugate of the wave function, since wave functions are generally complex-valued. The wave functions ψ can be separated into three wave functions: an electronic wave function φ_e, a vibrational wave function φ_v, and a rotational wave function Y_j [56]. Assuming that only the vibrational wave function changes during a vibrational transition, Eq. 3.18 is modified as:

$$\mu_{fi} = \int \varphi_{\upsilon_f}^{*} \hat{\mu} \varphi_{\upsilon_i} d\tau \tag{3.19}$$

The induced dipole moment operator, as the induced dipole vector in the classical case, is given by:

$$\hat{\mu} = \boldsymbol{a} \vec{E} \tag{3.20}$$

with $\boldsymbol{a}$ being the polarizability tensor of the system. By combining this equation with Eq. 3.18, we have:

$$\mu_{fi} = \vec{E} \int \varphi_{\upsilon_f}^{*} \boldsymbol{a} \varphi_{\upsilon_i} d\tau \tag{3.21}$$

For a harmonic oscillation around equilibrium, the polarizability tensor can be expanded to a Taylor series:

$$a_{\rho\sigma} = (a_{\rho\sigma})_0 + \sum_k \left(\frac{\partial a_{\rho\sigma}}{\partial Q_k} \right)_0 Q_k + \frac{1}{2} \sum_{k,l} \left(\frac{\partial^2 a_{\rho\sigma}}{\partial Q_k \partial Q_l} \right)_0 Q_k Q_l + \ldots \tag{3.22}$$

The above equation is essentially the same as the classical one (Eq. 3.9). By keeping only the terms up to first order and focusing only on one normal mode of vibration Q_k, we can write Eq. 3.22 as we did in the classical approach (Eq. 3.10):

$$\boldsymbol{a}_k = \boldsymbol{a}_0 + \sum_k \{ \boldsymbol{a}_k' Q_k \} \tag{3.23}$$

By substituting Eq. 3.23 into Eq. 3.21 we obtain the following relation:

$$\mu_{fi} = \boldsymbol{a_0} \vec{E} \int \varphi_{\upsilon_f}^{*} \varphi_{\upsilon_i} d\tau + \vec{E} \sum_k \left\{ \boldsymbol{a_k'} \int \varphi_{\upsilon_f}^{*} Q_k \varphi_{\upsilon_i} d\tau \right\} \tag{3.24}$$

The vibrational wave functions φ_{υ_f} and φ_{υ_i} are orthogonal, thus the first term of the right-hand side of the equation is non-zero only if the initial and final states are the same. This condition can be mathematically expressed as:

$$\int \varphi_{\upsilon_f}^{*} \varphi_{\upsilon_i} d\tau = 0 \text{ if } \varphi_{\upsilon_f} \neq \varphi_{\upsilon_i} \tag{3.25}$$

and:

$$\int \varphi_{\upsilon_f}^{*} \varphi_{\upsilon_i} d\tau = 1 \text{ if } \varphi_{\upsilon_f} = \varphi_{\upsilon_i} \tag{3.26}$$

This condition suggests that this term corresponds to Rayleigh scattering, for which the initial and final vibrational states are the same. The components of the $\boldsymbol{a_0}$ factor are always non-zero for all atoms and molecules, hence Rayleigh scattering is always allowed.

The second term of Eq. 3.24 can be further analyzed. This term corresponds to the case of Raman scattering and must be non-zero for Raman scattering to occur. Since Raman scattering is inelastic, the initial and final states must be different, which imposes the first term of the equation to be zero. The Raman scattering term shows that the phenomenon takes place if the slope of the polarizability, $\boldsymbol{a_k'}$, at equilibrium is non-zero, or in other words:

$$\left(\frac{\partial a_{\rho\sigma}}{\partial Q_k} \right)_0 \neq 0 \tag{3.27}$$

which is the same selection rule as the one derived in the classical approach (Eq. 3.17).

Additionally, for a harmonic oscillation, the wave functions of the vibrational states are given by [57]:

$$\varphi_\upsilon = N_\upsilon H_\upsilon \left(\sqrt{b} Q \right) e^{-\frac{bQ^2}{2}} \tag{3.28}$$

with $\upsilon = 0, 1, 2, \ldots$ being the vibrational quantum number, and constant b given by:

$$b = \sqrt{\frac{k\, m_{eff}}{\hbar^2}} \tag{3.29}$$

with k the force constant of the system, m_{eff} the effective mass of the oscillator, and $\hbar$ the reduced Planck constant. N_υ is a normalization constant given by:

$$N_\upsilon = \frac{1}{\sqrt{2^\upsilon \upsilon!}} \left(\frac{b}{\pi} \right)^{1/4} \tag{3.30}$$

H_υ is a Hermite polynomial for the vibrational level υ and is expressed as:

$$H_\upsilon (Q) = (-1)^\upsilon e^{Q^2} \frac{d^\upsilon}{dQ^\upsilon} e^{-Q^2} \tag{3.31}$$

The Hermite polynomials are orthogonal and the first 6 are shown in Fig. 3.5.

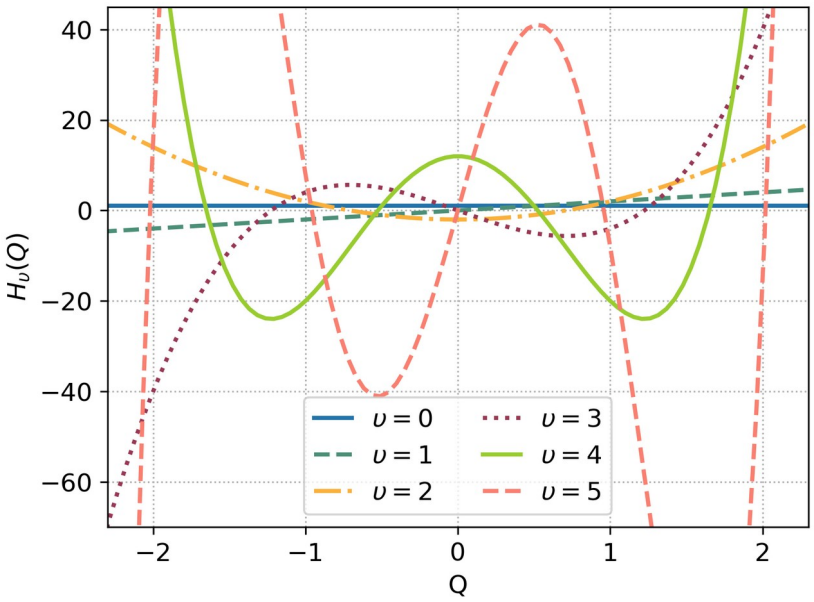

Figure 3.5: First 6 Hermite polynomials.

By substituting Eq. 3.28 into the second term of Eq. 3.24 and using the recurrence relation $xH_n(x)=nH_{n-1}(x)+\frac{1}{2}H_{n+1}(x)$ on the initial state, we reach:

$$\vec{E}\sum_k\left\{\boldsymbol{a}_{\boldsymbol{k}}^{'}\int\varphi_{\upsilon_f}^{*}Q_k\varphi_{\upsilon_i}d\tau\right\}=\vec{E}\sum_k\left\{\boldsymbol{a}_{\boldsymbol{k}}^{'}N_{\upsilon_f}N_{\upsilon_i}v_l\left[\int H_{\upsilon_f}H_{\upsilon_{i-1}}e^{-\frac{Q_k^2}{2}}d\tau+\frac{1}{2}\int H_{\upsilon_f}H_{\upsilon_{i+1}}e^{-\frac{bQ_k^2}{2}}d\tau\right]\right\} \tag{3.32}$$

The first integral on the right-hand side of this equation corresponds to anti-Stokes scattering and, since Hermite polynomials are orthogonal, is non-zero only if $\upsilon_f=\upsilon_{i-1}$, while the second integral, corresponding to Stokes Raman scattering, is non-zero only if $\upsilon_f=\upsilon_{i+1}$. These restrictions can be expressed as the selection rule:

$$\Delta\upsilon=\pm1 \tag{3.33}$$

This means that Raman scattered photons can have either increased or reduced energy, compared to the energy of the incident photon, by a single quantum of energy, which for the harmonic oscillator model is constant and given by:

$$\Delta E = h\nu_{vib} \tag{3.34}$$

since the energy levels of the harmonic oscillator are given by:

$$E_\upsilon = \left(\upsilon + \frac{1}{2}\right) h\nu_{vib} \tag{3.35}$$

with ν_{vib} the frequency difference between two successive vibrational energy levels.

It should be reminded at this point that we have limited our analysis of the quantum approach of the Raman effect to the harmonic case, both by considering the perturbation caused by the electric field to the polarizability of the molecular system as first order only (Eq. 3.23), and by using the wave functions of the quantum harmonic oscillator (Eq. 3.28). Real molecular systems, however, may differ from the harmonic oscillator due to the number of atoms involved (the harmonic oscillator includes only two atoms while most molecules have more than two atoms) and due to the shape of the molecular potential, which is anharmonic (non-symmetric). Due to these reasons and to the existence of higher order terms in the Taylor expansion of polarizability (our approach was limited only to first order polarizability), the selection rule of Eq. 3.33 can be "violated" and $\Delta\upsilon \neq \pm 1$ transitions (overtones), as well as transitions involving combination of vibrational frequencies (combination tones/bands), can be observed. Additionally, the anharmonicity of the molecular potential causes the energy difference of successive vibrational levels to decrease as υ increases. These effects however are fairly weak compared to the ones imposed by the selection rules of Eq. 3.27 and 3.33, thus the harmonic approximation, while simplistic, provides good insight and sufficiently describes the basic principles of the Raman effect [54].

The quantum approach also correctly predicts the experimentally observed ratio of the anti-Stokes to Stokes intensity, which for a non-degenerate vibration is given by:

$$\frac{I_{anti\text{-}Stokes}}{I_{Stokes}} = \left(\frac{\nu_i + \Delta\nu}{\nu_i - \Delta\nu}\right)^4 e^{-\frac{h\Delta\nu}{kT}} \tag{3.36}$$

where ν_i is the frequency of the incident light and $\Delta\nu$ is the magnitude of the Raman shift. The intensity ratio also depends on the temperature T and depends on the populations of molecules occupying primarily the ground and first excited vibrational states (Eq. 3.2).

Finally, the quantum approach predicts resonance effects, i.e. a significant increase in Raman scattering intensity (up to 10^6 times compared to the non-resonant case) when the energy of the incident radiation matches an electronic molecular transition, which are observed in experiments of resonance Raman spectroscopy [58].

3.5. Raman-active molecular vibrations

The movement of molecules through space can be characterized either as external, where a molecule moves as a whole, similarly to a rigid body, or as internal, where the relative motion of atoms within the molecule is considered. A molecule can perform three different types of motions: translations, rotations, and vibrations. Translations describe the motion of an entire molecule moving from one position to another and they are considered as external motion. Rotations refer to the rotational motion of a molecule around an axis or point and can be either external or internal, if only parts of a molecule rotate. Vibrations refer to the oscillation of molecules and is an internal motion.

To describe the motion of molecules, the concept of degrees of freedom (DoF) is used. In this concept, DoF is the number of variables that are required for a molecule to fully describe its motion. All molecules have 3 DoF that describe the translational motion of their center of mass (along the x, y, z axes). A diatomic molecule has 2 additional rotational DoF, since it can rotate along the two axes perpendicular to the molecule's axis, and 1 vibrational degree of freedom. Linear molecules with N atoms have 2 rotational DoF in addition to the translational ones, while non-linear molecules with N atoms have 3 rotational DoF. The vibrational DoF are $3N-5$ for linear molecules, while non-linear molecules have $3N-6$ (3 DoF account for the displacement of each atom along the x, y, z axes minus the sum of translational and rotational DoF of the molecule). The vibrational DoF correspond to the number of normal modes a molecule has, i.e. the number broadly considered as part of independent vibrational motions a molecule can have.

As described in the previous sections, the main rule that must be satisfied for Raman scattering to occur is that there must be a non-zero rate of polarizability change in the equilibrium position of a molecular vibration (Eq. 3.27). Vibrations that satisfy this rule are said to be "Raman-active". A useful construct that helps determine if a vibration is Raman-active is the polarizability ellipsoid. This is a 3-dimensional representation of the polarizability tensor $\boldsymbol{\alpha}$ of a vibrational mode (Eq. 3.8). If the magnitude, shape, or orientation of the ellipsoid is different for a vibration's extremes, then the vibration is Raman-active.

In Fig. 3.6 the normal modes of a linear triatomic molecule (e.g. CO_2) are shown. Such a molecule has 4 normal modes: a symmetric stretching mode (Fig. 3.6 (a)), an asymmetric stretching mode (Fig. 3.6 (b)), and a degenerate bending mode (Fig. 3.6 (c)). Out of these modes, only the symmetric stretch presents a change in polarizability, thus is Raman active, in accordance with the selection rule of Eq. 3.27 [59].

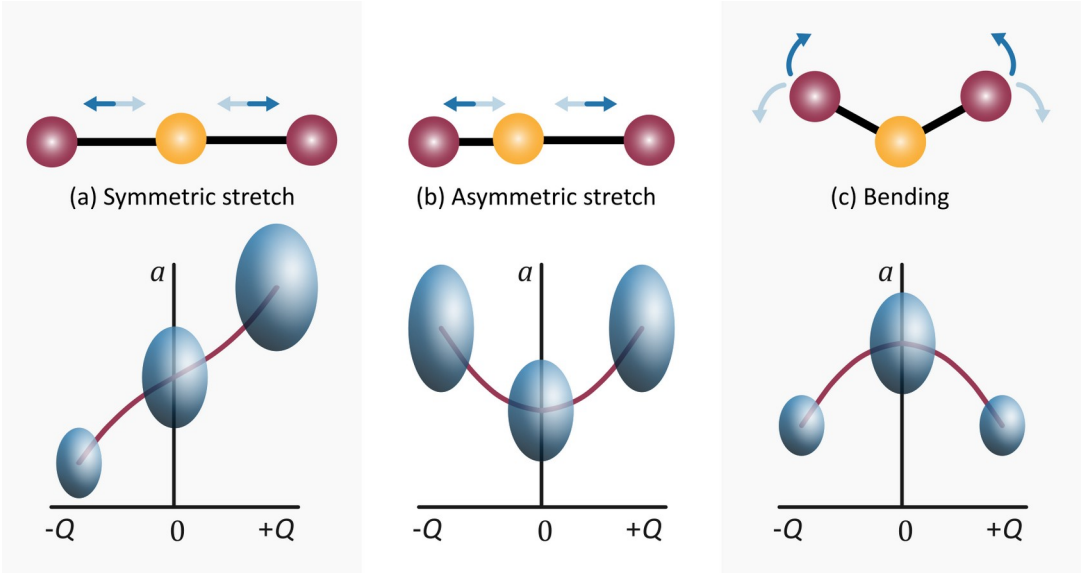

Figure 3.6: Normal modes of a linear triatomic molecule (e.g. CO_2) (top) with their respective one-dimensional polarizabilities graphs (bottom). The polarizability ellipsoids are also drawn over the graphs for the oscillations' extremes and equilibrium positions. Only the symmetric stretch mode has non-zero polarizability in the equilibrium position, thus is Raman-active. Figure adapted from [22,86].

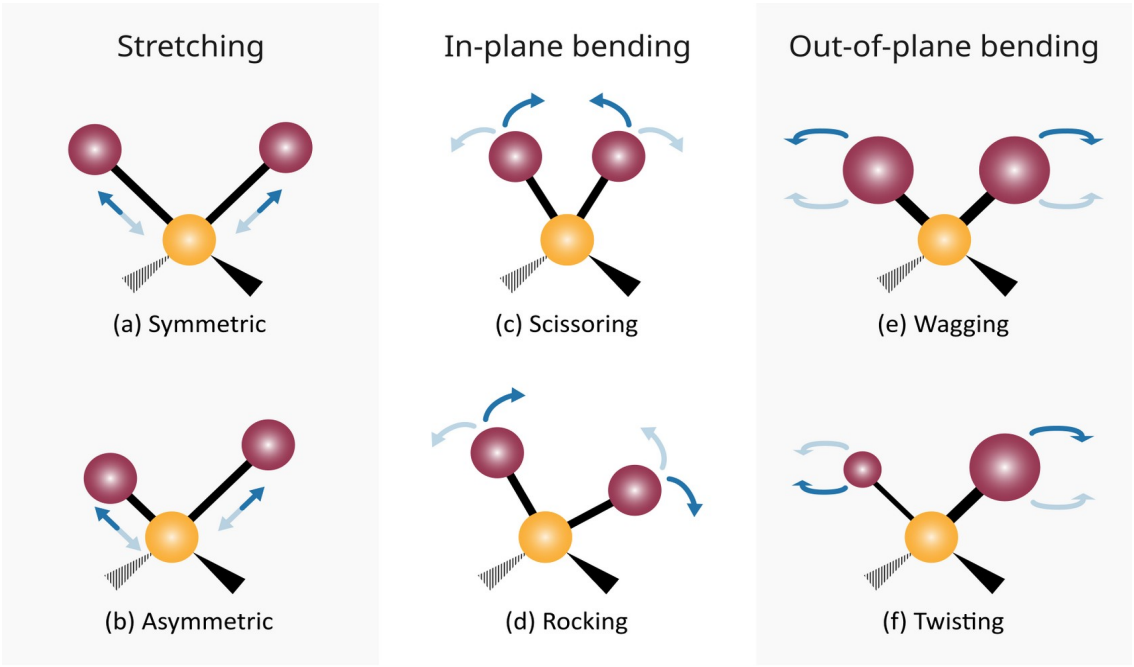

Figure 3.7: Basic types of normal modes of polyatomic molecules. The oscillations of the molecules of the stretching and in-pane bending modes take place on a single plane (i.e. on this page), while the molecules of the out-of-plane bending modes oscillate in 3D space (i.e. out of this page).

Molecules with many atoms have more normal modes, the basic types of which are depicted in Fig. 3.7. These modes include oscillations in which molecules move on a two-dimensional plane (in-plane vibrations), or oscillations where the molecules move in three-dimensional space (out-of-plane vibrations). The former include the symmetric and asymmetric stretching vibrations, and the scissoring and rocking bending vibrations, while the latter include the wagging and twisting bending vibrations.

As the number of atoms in a molecule increases, predicting which vibrations are Raman-active becomes an increasingly difficult task. For this reason, group theory is widely used to assist both in prediction of Raman-active modes of a molecule and in analysis and interpretation of Raman spectra [59]. While group theory is an invaluable tool, the procedure required for determining the Raman-active modes of a molecule is tedious, lengthy, and beyond the scope of this thesis.

3.6. Experimental configuration

A typical Raman setup consists of a laser, a probe, and a spectrometer. A simple experimental configuration that is commonly used in Raman spectroscopy experiments is presented in Fig. 3.8. The laser provides the required energy to drive the sample's molecules to an excited (virtual) state from which they then de-excite, producing Rayleigh- and Raman-scattered (Stokes and anti-Stokes) photons. Due to the inherently low intensity of Raman scattering, relatively high-powered laboratory lasers are required to generate a detectable signal. Various types of lasers are employed in Raman spectroscopy, such as solid-state lasers (e.g. Nd:YAG laser), gas lasers (e.g. He-Ne laser), diode lasers, or Excimer lasers, with wavelengths ranging from near-UV to near-IR (325-1064 nm) and output power of several hundred mW. The selection of laser wavelength and power depends on the particular application. For biomedical applications, diode lasers of 785 nm wavelength are commonly used, since they provide a good compromise between signal intensity, fluorescence interference, cost, and compactness [60].

Experimental Raman configurations may have excitation and signal collection optics coupled in a single probe, or they may use separate optics for the excitation light beam and the collection signal probe. The former case is depicted in Fig. 3.8. Here the laser light is guided by an optical fiber to the coupled probe and gets reflected by a dichroic mirror towards the sample. The dichroic mirror is appropriately constructed to reflect the laser light and let scattered light pass through it and is effectively used as a beam splitter. The laser light then passes through focusing optics (depicted as a single optical lens) and gets focused onto the sample. The scattered light travels through the same focusing optics and gets separated by the excitation light by the dichroic mirror. The scattered light also passes through a longpass filter, which removes most of the Rayleigh-scattered light, and then travels through an optical fiber to the spectrometer [61–63].

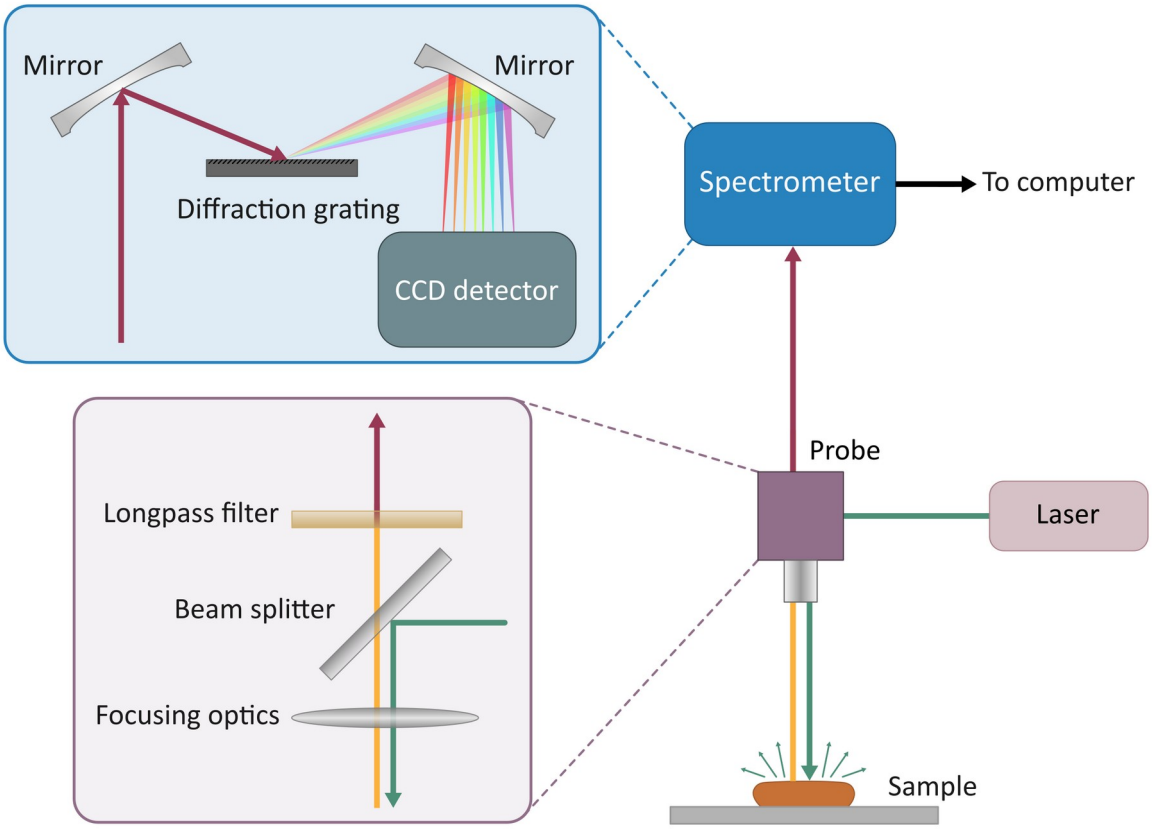

Figure 3.8: Schematic diagram of a typical Raman spectroscopy configuration. A coupled probe is used to excite the molecules of the sample and collect the Raman-scattered light. The spectrometer uses a Czerny-Turner monochromator to resolve the Raman-scattered light and focus it on a CCD detector, which converts the intensity of each frequency of the light to a digitalbut as I see in tutorials how they have no swap space as I do signal. The signal from the CCD detector is then sent to a computer to be stored as a spectrum and further processed.

Inside the Raman spectrometer, single or multiple stages of monochromators can be used to resolve the collected light of the scattered Raman photons to discrete frequencies. Using multiple stages has the benefit of increased spectral resolution of light, however this increased resolving power comes at the cost of lower intensity [61]. In Fig. 3.8 a single-stage Czerny-Turner monochromator is shown [64]. The light that enters the spectrometer gets reflected by a concave mirror onto a reflective grating with, typically, 150-4000 grooves (or lines, for transmission gratings) per mm [61]. The grating disperses the light, causing light of different frequencies to diffract at different angles. A second concave mirror collects the dispersed light and focuses it on a Charged-Coupled Device (CCD) detector [65]. Using this configuration, the whole spectrum of the light that enters the spectrometer is obtained at once. Finally, the intensity of light on each pixel of the CCD detector gets converted to a digital signal and this signal is then sent to a computer to be stored as a spectrum and further processed. To improve the quality of the acquired spectrum, multiple spectra are often recorded and averaged to enhance the signal-to-noise ratio.

The basic configuration described above can be appropriately adjusted and extended to be used in various applications. For example, by coupling the Raman probe to a (confocal) microscope, a technique known as (confocal) Raman microspectroscopy, microscopic structures can be measured (also with depth resolution for confocal instruments) [6,61,66], by positioning the collection probe at an offset compared to the excitation probe, a technique known as Spatially-Offset Raman Spectroscopy (SORS), information from up to several millimeters inside the sample can be obtained [9,67], by using colloidal solutions or substrates of noble metals (usually silver or gold), a technique known as Surface Enhanced Raman Spectroscopy (SERS), the Raman signal can be enhanced up to 10^{11} times [68], etc.

3.7. Advantages and limitations

Raman spectroscopy has a number of advantages that make it a preferred analytical technique over other methods:

- It can be used to study materials in solid, liquid, or gaseous state.
- It is a high specificity technique, allowing for the identification of multiple molecular species within a sample.
- Water (exhibiting low polarizability) only affects Raman spectra to a minimal degree, making Raman spectroscopy an excellent technique for studying wet tissues and aqueous solutions.
- Variants like confocal Raman microscopy can provide sub-micrometer lateral spatial resolution, allowing for the measurement of microscopic regions within a sample.
- Variants like confocal Raman microscopy or SORS can provide depth information for a sample (in the case of SORS, samples inside containers can also be measured).
- It requires minimal to no sample preparation prior to measurement.
- It is non-destructive, allowing for the same samples to be measured repeatedly under varying conditions or by other analytical techniques.
- Spectra are usually obtained in a short time scale (typically a few seconds).

Despite the important advantages, Raman spectroscopy has specific limitations that must be taken into consideration before selecting it as an analytical method:

- Raman scattering has a very small cross-section, making it an overall weak process, thus obtaining a signal with adequate intensity can be challenging.
- Depending on the nature of the sample and the excitation wavelengths used, there may be significant fluorescent background interfering with the signal.

- Cannot be used for obtaining spectra of pure metals or alloys.
- Although Raman spectroscopy is in principle a non-destructive technique, the high intensity of excitation light or prolonged irradiation that may be required for some samples to obtain meaningful spectra may destroy the samples.

3.8. Raman spectra of bone

Raman spectroscopy offers two-fold insights into both the organic and inorganic components of bone, making it a powerful tool for studying changes associated with diseases such as osteoporosis. The majority of diagnostically relevant information in a Raman spectrum is found within the “fingerprint” region, spanning 400–1800 cm^{-1}. This region is so named because the spectral bands within it serve as unique identifiers for the molecular composition of a material, akin to a fingerprint's distinct patterns. Additionally, the high wavenumber region (2800–3800 cm^{-1}) provides complementary information, primarily capturing vibrational modes associated with hydroxyl groups and the CH-stretching vibrations in collagen and lipids [69].

Raman spectra of bone feature multiple bands primarily associated with phosphate, carbonate, and collagen, which are considered as markers of bone quality. Quantitative analysis of biological samples typically involves measuring the intensities or integrated areas of these bands or their subbands. Ratios, whether of intensities or integrated areas, are more commonly used than absolute values to reduce the impact of variations in Raman scattering efficiency and other optical factors, enabling more reliable and consistent comparisons across samples [70,71].

A typical fingerprint region of a preprocessed Raman spectrum of bone is presented in Fig. 3.9 [72].

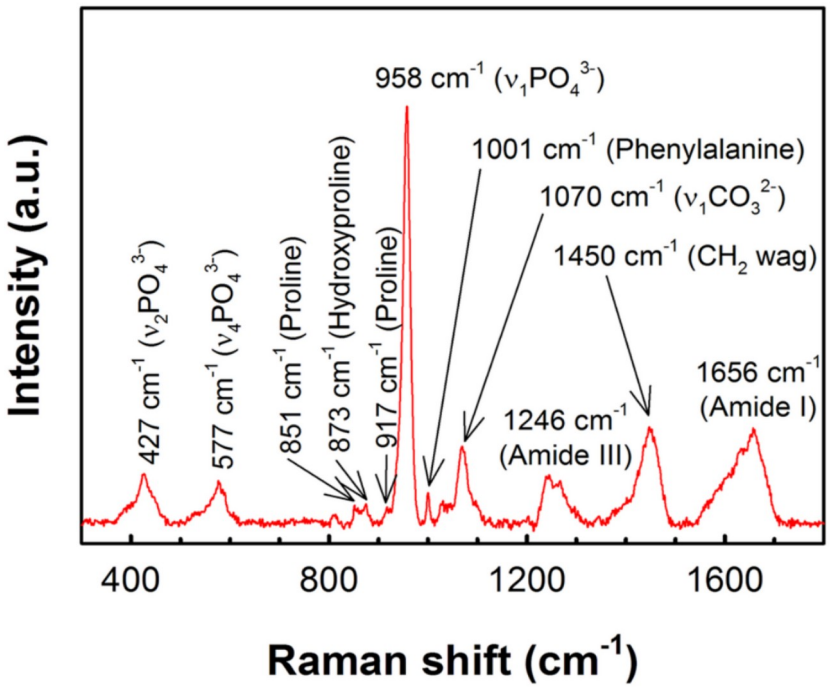

Figure 3.9: Typical fingerprint region (300 – 1800 cm^{-1}) of Raman spectrum of healthy human bone obtained with a 532 nm excitation with the main bands annotated. Figure from [72].

3.8.1. Raman Spectral Regions

The Raman spectrum of bone contains the molecular vibrations of its major components: hydroxyapatite, collagen, and minor constituents like lipids. Each spectral region is composed of multiple sub-bands corresponding to specific molecular vibrations that can provide detailed insights about bone's structural and compositional properties. Below are the main Raman bands of bone found in the fingerprint region, organized by wavenumber ranges to highlight the unique contributions of each region. The main Raman bands of bone along with their assignment are also presented in Table 1.

Low-wavenumber phosphate region (400 – 600 cm^{-1})

This region contains Raman bands related to the mineral phase of bone, primarily hydroxyapatite. The two prominent bands, located at ~430 cm^{-1} and ~580 cm^{-1}, correspond to the v_2 (bending) and v_4 (bending) vibrations of the phosphate ion (PO_4^{3-}), respectively. While these bands are characteristic of the phosphate groups in the mineral lattice, their specific relationship to mineral properties, such as lattice structure and crystallinity, remains less explored in the current literature [69,70].

Proline-Hydroxyproline region (830 – 900 cm^{-1})

This spectral region contains vibrations primarily associated with the amino acids proline at ~856 cm^{-1} and hydroxyproline at ~875 cm^{-1}, which are integral to the structure of Type I collagen, the primary organic component of bone. The peaks within this range primarily arise from *v*(C–C) stretching vibrations in the pyrrolidine rings of proline and hydroxyproline [73]. The intensities and positions of these peaks are sensitive to changes in collagen's secondary structure and stability, reflecting the role of proline and hydroxyproline in maintaining the integrity of the collagen triple helix.

High-wavenumber phosphate region (900 – 980 cm^{-1})

The 900 – 980 cm^{-1} region contains the most prominent Raman band of bone, located at ~960 cm^{-1}. This band is primarily attributed to the v_1 (symmetric stretching) vibration of phosphate. However, it is not a single peak but a composite feature reflecting heterogeneity in the mineral phase, with additional sub-bands observed at ~920 cm^{-1}, ~937 cm^{-1}, and ~947 cm^{-1} [69,74–77]. The sub-bands at 920 cm^{-1} and 937 cm^{-1}, are attributed to *v*(C–C) vibrations of proline in collagen's backbone and the sub-band at 947 cm^{-1} is associated with Type B carbonate substitutions in hydroxyapatite [77–79].

Carbonate region (1000 – 1150 cm^{-1})

The 1000 – 1150 cm^{-1} region contains vibrations associated with the carbonate content of bone, reflecting the incorporation of carbonate ions into the hydroxyapatite lattice through substitution. The most intense and spectroscopically important band in this region is the band located at ~1070 cm^{-1}, which is attributed to the symmetric stretching vibration (v_1) between the carbon and the oxygens atoms of carbonate ions (CO_3^{2-}), primarily linked to Type B carbonate substitution of hydroxyapatite [69]. At the lower end of this region, a small band corresponding to the *v*(C-C) vibration of phenylalanine, an amino acid found in collagen, can be observed at ~1003 cm^{-1} [77]. Additional bands in this region include features at ~1035 cm^{-1}, ~1048 cm^{-1}, and ~1076 cm^{-1}, corresponding to the v_3 asymmetric stretching modes of phosphate, as well as a band at ~1060 cm^{-1} associated with proteoglycans [77]. These bands exhibit significant overlap with other minor contributions, highlighting the complexity of spectral interpretation in this region.

Amide III region (1200 – 1350 cm^{-1})

The amide III region in the Raman spectrum of bone lies between 1200 and 1350 cm^{-1} and is associated with vibrations from the protein backbone, primarily collagen. Amides are functional groups characterized by a carbonyl group (C=O) bonded to a nitrogen atom (N). In proteins, amides form the peptide bonds that link amino acids together, creating the protein's backbone. The amide

III region originates from a combination of N–H bending and C–N stretching vibrations in these peptide bonds, making it a marker for collagen's secondary structure (Fig. 3.10) [80].

The bands within this region provide insights into the organization of collagen. The peak near 1242 cm^{-1} is typically linked to β-sheet structures or disordered regions (random coils), while the peak around 1272 cm^{-1} as well as the peak at 1340 cm^{-1} are attributed to α-helical structures. These features make the amide III region sensitive to changes in collagen organization and integrity. The amide III region in fresh, untreated bone may overlap with CH_2 and CH_3 bending vibrations from lipids and proteins that are found in the 1293–1305 cm^{-1} region [77].

In bone, the amide III region is significant for studying collagen crosslinking and maturity. Variations in peak positions or intensities can indicate differences in enzymatic and non-enzymatic crosslinking patterns, which are critical for bone's mechanical properties. Additionally, shifts in this region may reflect collagen denaturation due to thermal, chemical, or pathological processes, revealing disruptions in its triple-helical structure [70].

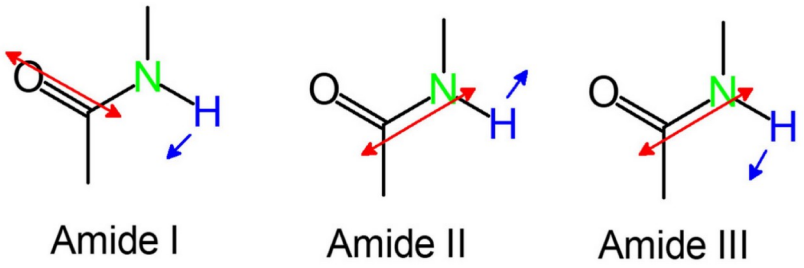

Figure 3.10: Amide vibrations. Red arrows indicate stretching modes, while blue arrows indicate bending modes. In Raman spectra of bone only the amide I and III vibrations are observed in the regions 1590—1750 cm^{-1} and 1200—1350 cm^{-1}, respectively [88]. Figure from [87].

CH_2 region (1400—1500 cm^{-1})

The 1400—1500 cm^{-1} region is primarily attributed to the deformation (wagging) mode of methylene ($\delta(CH_2)$) in the amino acid residues of collagen, typically observed at ∼1450 cm^{-1} [77].

Amide I region (1590—1750 cm^{-1})

The amide I region in the Raman spectrum of bone lies between 1590 and 1750 cm^{-1} and is primarily associated with the C=O stretching vibrations of the peptide bonds in collagen (Fig. 3.10). This region is highly sensitive to the secondary structure of proteins, making it a key feature for analyzing collagen's organization and structural integrity [77]. The band is complex and is composed of several subbands, which correspond to different secondary structures of collagen. The identified subbands include a band at ∼1609 cm^{-1}, which corresponds to the stretching vibrations of the carbon rings in phenylalanine and tyrosine. Another notable band related to the

α-helix structure of collagen is observed at ∼1640 cm^{-1}, manifesting as a shoulder in the amide I envelope. The band at ∼1660 cm^{-1} arises from the stretching vibration of C=O and is the most intense band in this region, representing the primary amide I contribution, and is found to be related to the amount of non-reducible enzymatic cross-linking (mature cross-linking) [69]. Lastly, the band at ∼1690 cm^{-1} is considered as indicative of the disordered secondary structutre of collagen and is related to reducible cross-linking (immature cross-linking) [69,77].

In bone, the amide I region is essential for studying quality and maturity of collagen. Shifts or changes in the intensity of the amide I band can indicate modifications in collagen crosslinking, degradation, or organization. These alterations are particularly relevant in pathological conditions such as osteoporosis, where collagen's structural and functional properties may be compromised [70]. Additionally, this region reflects hydrogen bonding patterns, which are important in maintaining collagen’s stability and triple-helical conformation [69].

Table 1: Tentative assignments of main Raman bands observed in bone spectra [77–79]. *Mineral-related bands are highlighted with light gray background.*

Raman shift (cm^{-1})	Assignment
430	$v_2PO_4^{3-}$
580	$v_4PO_4^{3-}$
856	*v*(C-C) proline
875	*v*(C-C) hydorxyproline
920	*v*(C-C) proline
937	*v*(C-C) proline from collagen backbone
947	$v_1PO_4^{3-}$ with Type B substitutions of CO_3^{2-}
960	$v_1PO_4^{3-}$
1003	*v*(C-C) phenylalanine
1035	$v_3PO_4^{3-}$
1048	$v_3PO_4^{3-}$
1060	Proteoglycans
1070	$v_1CO_3^{2-}$
1076	$v_3PO_4^{3-}$
1242	Amide III β-sheet and random coil
1272	Amide III α-helix
1293–1305	*δ*(=CH) lipids and proteins in fresh bone
1340	Amide III α-helix (CH_2CH_2 wag)
1446	*δ*(CH_2) collagen side chains
1609	*δ*(C=C) phenylalanine, tyrosine
1640	*v*(C-C) α-helix
1660	*v*(C=O) Amide I
1676	Amide I β-sheet
1690	Amide I β-sheet and random coil

3.9. Bone quality parameters in Raman spectroscopy

Raman spectroscopy is an invaluable tool for assessing bone quality by providing molecular-level insights into its composition and structure. It enables the quantification of key parameters that influence bone's mechanical and biological properties, offering a deeper understanding of bone

health and disease. The following parameters are particularly significant in characterizing bone quality through Raman spectroscopy.

Mineral-to-matrix ratio

The mineral-to-matrix ratio (MMR) is a widely used parameter for assessing bone quality, providing information about the relative contributions of the inorganic and organic components of bone. This ratio is typically calculated using the peak intensities or integrated areas of the main phosphate band at 960 cm^{-1} and the amide I band located at 1660 cm^{-1} [70]. In addition to the amide I band, the peak intensities or integrated areas of other collagen-related bands, such as the combined proline (856 + 920 cm^{-1}) or combined proline and hydroxyproline (856 + 875 cm^{-1} or 856 + 920 + 875 cm^{-1}) bands, the CH_2 band at 1450 cm^{-1}, phenylalanine at 1003 cm^{-1}, and the amide III band at 1242 cm^{-1}, have also been employed as measures of the mineral-to-organic content of bone [69,70,77,81]. While the amide I band is widely used due to its high intensity and relevance to collagen, it can be affected by overlapping signals from other proteins or environmental factors, potentially complicating its interpretation [77]. In contrast, proline and hydroxyproline peaks offer higher specificity to collagen, minimizing interference and allowing for more direct assessment of the organic matrix [77].

Carbonate substitution

Carbonate substitution in hydroxyapatite is a key factor that affects bone's biological and mechanical properties. The extent of carbonate substitutions in the apatite lattice of bone can be quantified by calculating the carbonate-to-phosphate ratio (CPR) using the main carbonate band at 1070 cm^{-1} and the main phosphate band at 960 cm^{-1} [70]. However, the proximity of the phosphate band at 1076 cm^{-1}, which partially overlaps with the carbonate band, can reduce the accuracy of CPR measurements, particularly when the carbonate content in hydroxyapatite is low. Additionally, the carbonate-to-amide I ratio, which utilizes the 1660 cm^{-1} band, is another useful metric that may be indicative of bone remodeling [70,82].

Crystallinity

Crystallinity, often referred to as mineral maturity, is a measure of the degree of structural order in a solid and, in the context of bone, reflects the size and perfection of hydroxyapatite crystals [83]. Variations in mineral crystallinity can indicate changes in bone remodeling processes, with higher crystallinity often associated with aging or pathological conditions such as osteoporosis. Higher crystallinity is often linked to stiffer but more brittle bone, while lower crystallinity may indicate increased bone turnover [83]. In Raman spectroscopy, crystallinity is determined by analyzing the full width at half maximum (FWHM) of the main phosphate band at 960 cm^{-1}. This involves fitting

the band with a single Gaussian curve and calculating crystallinity as the inverse of the FWHM of the fitted curve [70].

Collagen quality

Collagen's quality in Raman spectra of bone can be determined by utilizing the amide I region at 1590–1750 cm^{-1}. More specifically, a shift of the amide I band from 1665 to 1678 cm^{-1} may indicate ruptured collagen cross-links, which destabilize the fibrillar structure and reduce the mechanical resilience of the organic matrix. Such shifts are often associated with mechanical or enzymatic damage, oxidative stress, or aging-related changes in bone tissue [69,70]. The intensity or integrated area ratios between the subbands at ∼1690 cm^{-1} and ∼1660 cm^{-1} can show changes in collagen secondary structure, particularly the relative proportions of reducible to non-reducible collagen cross-links [70,84]. This ratio is sensitive to collagen denaturation, with an increased 1660/1690 cm^{-1} ratio often reflecting a transition from an organized triple-helix structure to less ordered or denatured forms, often seen in pathological conditions like osteoporosis or in thermally or chemically degraded bone [69,85].

3.10. References

[1] Smekal A. Zur Quantentheorie der Dispersion. Naturwissenschaften 1923;11:873–5. https://doi.org/10.1007/BF01576902.

[2] Raman CV, Krishnan KS. A New Type of Secondary Radiation. Nature 1928;121:501–2. https://doi.org/10.1038/121501c0.

[3] Hanlon EB, Manoharan R, Koo T-W, Shafer KE, Motz JT, Fitzmaurice M, et al. Prospects for in vivo Raman spectroscopy. Phys Med Biol 2000;45:R1. https://doi.org/10.1088/0031-9155/45/2/201.

[4] Rohringer N. X-ray Raman scattering: a building block for nonlinear spectroscopy. Philos Trans R Soc Math Phys Eng Sci 2019;377:20170471. https://doi.org/10.1098/rsta.2017.0471.

[5] Robert B. Resonance Raman spectroscopy. Photosynth Res 2009;101:147–55. https://doi.org/10.1007/s11120-009-9440-4.

[6] Dieing T, Hollricher O, Toporski J, editors. Confocal Raman Microscopy. vol. 158. Berlin, Heidelberg: Springer Berlin Heidelberg; 2011. https://doi.org/10.1007/978-3-642-12522-5.

[7] Stiles PL, Dieringer JA, Shah NC, Duyne RPV. Surface-Enhanced Raman Spectroscopy. Annu Rev Anal Chem 2008;1:601–26. https://doi.org/10.1146/annurev.anchem.1.031207.112814.

[8] Mosca S, Conti C, Stone N, Matousek P. Spatially offset Raman spectroscopy. Nat Rev Methods Primer 2021;1:1–16. https://doi.org/10.1038/s43586-021-00019-0.

[9] Vardaki MZ, Pavlou E, Simantiris N, Lampri E, Seretis K, Kourkoumelis N. Towards non-invasive monitoring of non-melanoma skin cancer using spatially offset Raman spectroscopy. The Analyst 2023;148:4386–95. https://doi.org/10.1039/D3AN00684K.

[10] Shipp DW, Sinjab F, Notingher I. Raman spectroscopy: techniques and applications in the life sciences. Adv Opt Photonics 2017;9:315–428. https://doi.org/10.1364/AOP.9.000315.

[11] Strachan CJ, Rades T, Gordon KC, Rantanen J. Raman spectroscopy for quantitative analysis of pharmaceutical solids. J Pharm Pharmacol 2007;59:179–92. https://doi.org/10.1211/jpp.59.2.0005.
[12] Jehlička J, Edwards HGM. Raman spectroscopy as a tool for the non-destructive identification of organic minerals in the geological record. Org Geochem 2008;39:371–86. https://doi.org/10.1016/j.orggeochem.2008.01.005.
[13] Milekhin AG, Sveshnikova LL, Duda TA, Yeryukov NA, Rodyakina EE, Gutakovskii AK, et al. Surface-enhanced Raman spectroscopy of semiconductor nanostructures. Phys E Low-Dimens Syst Nanostructures 2016;75:210–22. https://doi.org/10.1016/j.physe.2015.09.013.
[14] Shamey R, editor. Encyclopedia of Color Science and Technology. Cham: Springer International Publishing; 2023. https://doi.org/10.1007/978-3-030-89862-5.
[15] Bohren CF, Huffman DR. Absorption and Scattering of Light by Small Particles. 1st ed. Wiley; 1998. https://doi.org/10.1002/9783527618156.
[16] Keresztury G. Raman Spectroscopy: Theory. In: Chalmers JM, Griffiths PR, editors. Handb. Vib. Spectrosc. 1st ed., Wiley; 2001. https://doi.org/10.1002/0470027320.s0109.
[17] Smith E, Dent G. Modern Raman Spectroscopy: A Practical Approach. 1st ed. Wiley; 2019. https://doi.org/10.1002/9781119440598.
[18] Belfield KD, Liu Y, Negres RA, Fan M, Pan G, Hagan DJ, et al. Two-Photon Photochromism of an Organic Material for Holographic Recording. Chem Mater 2002;14:3663–7. https://doi.org/10.1021/cm0107981.
[19] Stokes GG. On the Change of Refrangibility of Light. Philos Trans R Soc Lond 1852;142:463–562.
[20] Cantu LML, Grohmann J, Meier W, Aigner M. Temperature measurements in confined swirling spray flames by vibrational coherent anti-stokes Raman spectroscopy. Exp Therm Fluid Sci 2018;95:52–9. https://doi.org/10.1016/j.expthermflusci.2018.01.029.
[21] Larkin P. Infrared and raman spectroscopy: principles and spectral interpretation. Amsterdam ; Boston: Elsevier; 2011.
[22] Campanella B, Palleschi V, Legnaioli S. Introduction to vibrational spectroscopies. ChemTexts 2021;7:5. https://doi.org/10.1007/s40828-020-00129-4.
[23] Strommen DP, Nakamoto K. Resonance raman spectroscopy. J Chem Educ 1977;54:474. https://doi.org/10.1021/ed054p474.
[24] Kostamovaara J, Tenhunen J, Kögler M, Nissinen I, Nissinen J, Keränen P. Fluorescence suppression in Raman spectroscopy using a time-gated CMOS SPAD. Opt Express 2013;21:31632. https://doi.org/10.1364/OE.21.031632.
[25] Stockert JC. Fluorescence Microscopy In Life Sciences. Sharjah: Bentham Science Publishers; 2017.
[26] Szabo AG. The Fluorescence Properties of Aromatic Amino Acids: Their Role in the Understanding of Enzyme Structure and Dynamics. In: Cooper A, Houben JL, Chien LC, editors. Enzyme Catal. Process Energ. Mech. Dyn., Boston, MA: Springer US; 1989, p. 123–39. https://doi.org/10.1007/978-1-4757-1607-8_10.
[27] McCreery RL. Raman Spectroscopy for Chemical Analysis. 1st ed. Wiley; 2000. https://doi.org/10.1002/0471721646.
[28] Long DA. The Raman effect: a unified treatment of the theory of Raman scattering by molecules. Chichester ; New York: Wiley; 2002.

[29] Efremov EV, Buijs JB, Gooijer C, Ariese F. Fluorescence rejection in resonance Raman spectroscopy using a picosecond-gated intensified charge-coupled device camera. Appl Spectrosc 2007;61:571–8. https://doi.org/10.1366/000370207781269873.
[30] Matousek P, Towrie M, Stanley A, Parker AW. Efficient Rejection of Fluorescence from Raman Spectra Using Picosecond Kerr Gating. Appl Spectrosc 1999;53:1485–9. https://doi.org/10.1366/0003702991945993.
[31] Watanabe J, Kinoshita S, Kushida T. Fluorescence rejection in Raman spectroscopy by a gated single-photon counting method. Rev Sci Instrum 1985;56:1195–8. https://doi.org/10.1063/1.1138028.
[32] Tahara T, Hamaguchi H-O. Picosecond Raman Spectroscopy Using a Streak Camera. Appl Spectrosc 1993;47:391–8. https://doi.org/10.1366/0003702934335001.
[33] Martyshkin DV, Ahuja RC, Kudriavtsev A, Mirov SB. Effective suppression of fluorescence light in Raman measurements using ultrafast time gated charge coupled device camera. Rev Sci Instrum 2004;75:630–5. https://doi.org/10.1063/1.1646743.
[34] Sahoo SK, Umapathy S, Parker AW. Time-Resolved Resonance Raman Spectroscopy: Exploring Reactive Intermediates. Appl Spectrosc 2011;65:1087–115. https://doi.org/10.1366/11-06406.
[35] Becker W. Fluorescence lifetime imaging--techniques and applications. J Microsc 2012;247:119–36. https://doi.org/10.1111/j.1365-2818.2012.03618.x.
[36] Bright FV, Hieftje GM. A new technique for the elimination of fluorescence interference in Raman spectroscopy. Appl Spectrosc 1986;40:583–7. https://doi.org/10.1366/0003702864508511.
[37] Wirth MJ, Chou SHwa. Comparison of time and frequency domain methods for rejecting fluorescence from Raman spectra. Anal Chem 1988;60:1882–6. https://doi.org/10.1021/ac00169a009.
[38] da Silva Martins MA, Ribeiro DG, Pereira dos Santos EA, Martin AA, Fontes A, da Silva Martinho H. Shifted-excitation Raman difference spectroscopy for in vitro and in vivo biological samples analysis. Biomed Opt Express 2010;1:617–26. https://doi.org/10.1364/BOE.1.000617.
[39] Shreve AP, Cherepy NJ, Mathies RA. Effective Rejection of Fluorescence Interference in Raman Spectroscopy Using a Shifted Excitation Difference Technique. Appl Spectrosc 1992;46:707–11. https://doi.org/10.1366/0003702924125122.
[40] Bell SEJ, Bourguignon ESO, Dennis A. Analysis of luminescent samples using subtracted shifted Raman spectroscopy. Analyst 1998;123:1729–34. https://doi.org/10.1039/A802802H.
[41] Cormack IG, Mazilu M, Dholakia K, Herrington CS. Fluorescence suppression within Raman spectroscopy using annular beam excitation. Appl Phys Lett 2007;91. https://doi.org/10.1063/1.2756311.
[42] Demchenko AP. Photobleaching of organic fluorophores: quantitative characterization, mechanisms, protection*. Methods Appl Fluoresc 2020;8:022001. https://doi.org/10.1088/2050-6120/ab7365.
[43] Wei D, Chen S, Liu Q. Review of Fluorescence Suppression Techniques in Raman Spectroscopy. Appl Spectrosc Rev 2015;50:387–406. https://doi.org/10.1080/05704928.2014.999936.
[44] Zhao J, Lui H, McLean DI, Zeng H. Automated autofluorescence background subtraction algorithm for biomedical Raman spectroscopy. Appl Spectrosc 2007;61:1225–32. https://doi.org/10.1366/000370207782597003.

[45] Lieber CA, Mahadevan-Jansen A. Automated Method for Subtraction of Fluorescence from Biological Raman Spectra. Appl Spectrosc 2003;57:1363–7.
[46] Mazet V, Carteret C, Brie D, Idier J, Humbert B. Background removal from spectra by designing and minimising a non-quadratic cost function. Chemom Intell Lab Syst 2005;76:121–33. https://doi.org/10.1016/j.chemolab.2004.10.003.
[47] Cadusch PJ, Hlaing MM, Wade SA, McArthur SL, Stoddart PR. Improved methods for fluorescence background subtraction from Raman spectra. J Raman Spectrosc 2013;44:1587–95. https://doi.org/10.1002/jrs.4371.
[48] Galloway CM, Le Ru EC, Etchegoin PG. An iterative algorithm for background removal in spectroscopy by wavelet transforms. Appl Spectrosc 2009;63:1370–6. https://doi.org/10.1366/000370209790108905.
[49] Hu Y, Jiang T, Shen A, Li W, Wang X, Hu J. A background elimination method based on wavelet transform for Raman spectra. Chemom Intell Lab Syst 2007;85:94–101. https://doi.org/10.1016/j.chemolab.2006.05.004.
[50] Ramos PM, Ruisánchez I. Noise and background removal in Raman spectra of ancient pigments using wavelet transform. J Raman Spectrosc 2005;36:848–56. https://doi.org/10.1002/jrs.1370.
[51] Cai TT, Zhang D, Ben–Amotz D. Enhanced Chemical Classification of Raman Images Using Multiresolution Wavelet Transformation. Appl Spectrosc 2001;55:1124–30. https://doi.org/10.1366/0003702011953289.
[52] O'Grady A, Dennis AC, Denvir D, McGarvey JJ, Bell SE. Quantitative Raman spectroscopy of highly fluorescent samples using pseudosecond derivatives and multivariate analysis. Anal Chem 2001;73:2058–65. https://doi.org/10.1021/ac0010072.
[53] Leger MN, Ryder AG. Comparison of derivative preprocessing and automated polynomial baseline correction method for classification and quantification of narcotics in solid mixtures. Appl Spectrosc 2006;60:182–93. https://doi.org/10.1366/000370206776023304.
[54] Woodward LA. Introduction to the theory of molecular vibrations and vibrational spectroscopy. Oxford: Clarendon Press; 1972.
[55] Wilson EB, Decius JC, Cross PC. Molecular vibrations: the theory of infrared and Raman vibrational spectra. New York: Dover Publications; 1980.
[56] Browne WR. Resonance Raman spectroscopy and its application in bioinorganic chemistry. Pract. Approaches Biol. Inorg. Chem., Elsevier; 2020, p. 275–324. https://doi.org/10.1016/B978-0-444-64225-7.00008-0.
[57] Physical Chemistry (LibreTexts). Chem Libr 2023. https://chem.libretexts.org/Bookshelves/Physical_and_Theoretical_Chemistry_Textbook_Maps/Physical_Chemistry_(LibreTexts) (accessed October 4, 2023).
[58] Tuschel D. Exploring Resonance Raman Spectroscopy. Spectroscopy 2018;33:12–9.
[59] Tuschel D. Practical Group Theory and Raman Spectroscopy, Part I: Normal Vibrational Modes. Spectroscopy 2014;29:14.
[60] Jones RR, Hooper DC, Zhang L, Wolverson D, Valev VK. Raman Techniques: Fundamentals and Frontiers. Nanoscale Res Lett 2019;14:231. https://doi.org/10.1186/s11671-019-3039-2.
[61] Butler HJ, Ashton L, Bird B, Cinque G, Curtis K, Dorney J, et al. Using Raman spectroscopy to characterize biological materials. Nat Protoc 2016;11:664–87. https://doi.org/10.1038/nprot.2016.036.

[62] Carriere JT, Havermeyer F. Ultra-low frequency Stokes and anti-Stokes Raman spectroscopy at 785nm with volume holographic grating filters. In: Mahadevan-Jansen A, Petrich W, editors., San Francisco, California, USA: 2012, p. 821905. https://doi.org/10.1117/12.909463.
[63] Pitt GD, Batchelder DN, Bennett R, Bormett RW, Hayward IP, Smith BJE, et al. Engineering aspects and applications of the new Raman instrumentation. IEE Proc - Sci Meas Technol 2005;152:241–318. https://doi.org/10.1049/ip-smt:20050015.
[64] Czerny M, Turner AF. Über den Astigmatismus bei Spiegelspektrometern. Z Für Phys 1930;61:792–7. https://doi.org/10.1007/BF01340206.
[65] Boyle WS, Smith GE. Charge coupled semiconductor devices. Bell Syst Tech J 1970;49:587–93. https://doi.org/10.1002/j.1538-7305.1970.tb01790.x.
[66] Confocal Raman Microscopy: Performance, Pitfalls, and Best Practice n.d. https://doi.org/10.1366/000370209789379196.
[67] Matousek P, Clark IP, Draper ERC, Morris MD, Goodship AE, Everall N, et al. Subsurface Probing in Diffusely Scattering Media Using Spatially Offset Raman Spectroscopy. Appl Spectrosc 2005;59:393–400. https://doi.org/10.1366/0003702053641450.
[68] Han XX, Rodriguez RS, Haynes CL, Ozaki Y, Zhao B. Surface-enhanced Raman spectroscopy. Nat Rev Methods Primer 2022;1:1–17. https://doi.org/10.1038/s43586-021-00083-6.
[69] Unal M, Ahmed R, Mahadevan-Jansen A, Nyman JS. Compositional assessment of bone by Raman spectroscopy. The Analyst 2021;146:7464. https://doi.org/10.1039/d1an01560e.
[70] Morris MD, Mandair GS. Raman Assessment of Bone Quality. Clin Orthop Relat Res 2011;469:2160–9. https://doi.org/10.1007/s11999-010-1692-y.
[71] WOPENKA B, KENT A, PASTERIS JD, YOON Y, THOMOPOULOS S. The Tendon-to-Bone Transition of the Rotator Cuff: A Preliminary Raman Spectroscopic Study Documenting the Gradual Mineralization Across the Insertion in Rat Tissue Samples. Appl Spectrosc 2008;62:1285–94. https://doi.org/10.1366/000370208786822179.
[72] Khalid M, Bora T, Al Ghaithi A, Thukral S, Dutta J. Raman Spectroscopy detects changes in Bone Mineral Quality and Collagen Cross-linkage in Staphylococcus Infected Human Bone. Sci Rep 2018;8. https://doi.org/10.1038/s41598-018-27752-z.
[73] Nguyen TT, Gobinet C, Feru J, -Pasco SB, Manfait M, Piot O. Characterization of Type I and IV Collagens by Raman Microspectroscopy: Identification of Spectral Markers of the Dermo-Epidermal Junction. J Spectrosc 2012;27:686183. https://doi.org/10.1155/2012/686183.
[74] Orkoula MG, Vardaki MZ, Kontoyannis CG. Study of bone matrix changes induced by osteoporosis in rat tibia using Raman spectroscopy. Vib Spectrosc 2012;63:404–8. https://doi.org/10.1016/j.vibspec.2012.09.016.
[75] McElderry J-DP, Kole MR, Morris MD. Repeated freeze-thawing of bone tissue affects Raman bone quality measurements. J Biomed Opt 2011;16:071407. https://doi.org/10.1117/1.3574525.
[76] Nieuwoudt MK, Shahlori R, Naot D, Patel R, Holtkamp H, Aguergaray C, et al. Raman spectroscopy reveals age- and sex-related differences in cortical bone from people with osteoarthritis. Sci Rep 2020;10:19443. https://doi.org/10.1038/s41598-020-76337-2.
[77] Mandair GS, Morris MD. Contributions of Raman spectroscopy to the understanding of bone strength. BoneKEy Rep 2015;4:620. https://doi.org/10.1038/bonekey.2014.115.
[78] Movasaghi Z, Rehman S, Rehman IU. Raman Spectroscopy of Biological Tissues. Appl Spectrosc Rev 2007;42:493–541. https://doi.org/10.1080/05704920701551530.

[79] Penel G, Leroy G, Rey C, Bres E. MicroRaman Spectral Study of the PO4 and CO3 Vibrational Modes in Synthetic and Biological Apatites. Calcif Tissue Int 1998;63:475–81. https://doi.org/10.1007/s002239900561.
[80] Frushour BG, Koenig JL. Raman scattering of collagen, gelatin, and elastin. Biopolymers 1975;14:379–91. https://doi.org/10.1002/bip.1975.360140211.
[81] Ishimaru Y, Oshima Y, Imai Y, Iimura T, Takanezawa S, Hino K, et al. Raman Spectroscopic Analysis to Detect Reduced Bone Quality after Sciatic Neurectomy in Mice. Molecules 2018;23:3081. https://doi.org/10.3390/molecules23123081.
[82] McCreadie BR, Morris MD, Chen T-C, Sudhaker Rao D, Finney WF, Widjaja E, et al. Bone tissue compositional differences in women with and without osteoporotic fracture. Bone 2006;39:1190–5. https://doi.org/10.1016/j.bone.2006.06.008.
[83] Kourkoumelis N, Zhang X, Lin Z, Wang J. Fourier Transform Infrared Spectroscopy of Bone Tissue: Bone Quality Assessment in Preclinical and Clinical Applications of Osteoporosis and Fragility Fracture. Clin Rev Bone Miner Metab 2019;17:24–39. https://doi.org/10.1007/s12018-018-9255-y.
[84] Carden A, Rajachar RM, Morris MD, Kohn DH. Ultrastructural Changes Accompanying the Mechanical Deformation of Bone Tissue: A Raman Imaging Study. Calcif Tissue Int 2003;72:166–75. https://doi.org/10.1007/s00223-002-1039-0.
[85] Unal M, Jung H, Akkus O. Novel Raman Spectroscopic Biomarkers Indicate That Postyield Damage Denatures Bone's Collagen. J Bone Miner Res 2016;31:1015–25. https://doi.org/10.1002/jbmr.2768.
[86] Solomon EI, Lever ABP. Inorganic Electronic Structure and Spectroscopy: Methodology. Wiley; 2006.
[87] Ichikawa M, Otaki M, Goto H. Polyaniline Hybrids with Biological Tissue, and Biological Polymers as Physiological—Electroactive Materials. Micro 2023;3:172–91. https://doi.org/10.3390/micro3010013.
[88] Morris MD, Finney WF. Recent developments in Raman and infrared spectroscopy and imaging of bone tissue. J Spectrosc 2004;18:765753. https://doi.org/10.1155/2004/765753.

4. Neutron powder diffraction

4.1. Introduction

Neutron powder diffraction is an analytical technique used to investigate the atomic structure of polycrystalline materials by analyzing the diffraction patterns produced when neutrons interact with the nuclei of a powdered material's atoms. The technique is based on the diffraction of neutrons by matter, which were discovered by J. Chadwick in 1932 [1], and was experimentally observed four years later by two independent groups: D. Mitchell and P. Powers [2], and H. von Halban and P. Preiswerk [3]. Significant advancements in methodology were achieved by E. O. Wollan and C. Shull in the 1940s, with Shull receiving the 1994 Nobel Prize in Physics for these contributions (Wollan had passed away a decade earlier) [4].

Neutron powder diffraction involves a beam of neutrons directed on a powdered sample, where the random orientation of crystallites produces diffraction patterns. These patterns provide detailed information about atomic arrangements, lattice parameters, thermal vibrations, and magnetic ordering. Neutron diffraction is often compared to X-ray diffraction (XRD), which is considered as a complementary technique that is also used to uncover structural information about materials. However, unlike XRD, which relies on interactions with the electronic cloud surrounding atoms, neutron diffraction involves direct interactions with the atomic nuclei. This distinction gives neutron diffraction specific advantages, such as sensitivity to light elements in the presence of heavy atoms and the ability to differentiate isotopes [5].

Advancements in neutron diffraction techniques have expanded their applicability to include time-of-flight methods [6], high-resolution powder diffraction [7], and in-situ diffraction for studying dynamic processes [8]. Neutron powder diffraction enables detailed analysis of crystalline

structures in a wide range of materials, including metals, ceramics, and complex compounds [9]. While the technique typically requires access to large-scale facilities such as nuclear reactors or spallation sources, its ability to yield comprehensive structural information makes it highly valuable for studying materials under varying conditions, such as extreme temperatures, pressures, or magnetic fields.

4.2. Theory of neutron diffraction

Diffraction is a wave phenomenon observed when waves encounter an obstacle, slit, or periodic structure, causing them to bend, spread out, or interfere. This behavior is exhibited by various types of waves, including light, sound, and particles, such as electrons and neutrons, and forms the basis for several analytical techniques used to probe the structure of matter. Diffraction occurs because waves interact with each other, producing patterns of constructive and destructive interference that can be analyzed to extract structural information about a system [10]. The study of the diffraction of neutrons from a material can provide detailed insight into atomic arrangements, lattice structures, and magnetic ordering within a material.

4.2.1. Neutrons

Neutrons are electrically neutral subatomic particles that were discovered by J. Chadwick in 1932 [1]. Together with the positively charged protons, they form the building blocks of atomic nuclei. A neutron's mass is slightly greater than that of a proton, weighing approximately $1.675\times10^{-27}kg$. Like protons and electrons, neutrons are spin-1/2 particles, designated as fermions [8].

The wave-like properties of neutrons, as described by de Broglie in 1924 [11], make them suitable for diffraction studies. De Broglie proposed that particles can exhibit wave-like behavior, with their wavelength related to their momentum. This relationship is expressed by de Broglie's equation, which connects the velocity (v) and wavelength (λ) of a particle as follows:

$$\lambda=\frac{h}{m\,v} \tag{4.1}$$

where $h=6.626068\times10^{-34}\,\mathrm{m^2\,kg/s}$ is Planck's constant and m is the particle's mass. For neutrons this equation can be simplified to:

$$\lambda=\frac{3.956}{v} \tag{4.2}$$

with λ measured in Å and v in km/s. The kinetic energy of the neutrons as a function of λ is given by:

$$E = \frac{h^2}{2 m \lambda^2} \tag{4.3}$$

There are three main processes through which neutrons are produced for diffraction experiments: fission, spallation, and low energy nuclear reactions (Fig. 4.1) [9,12].

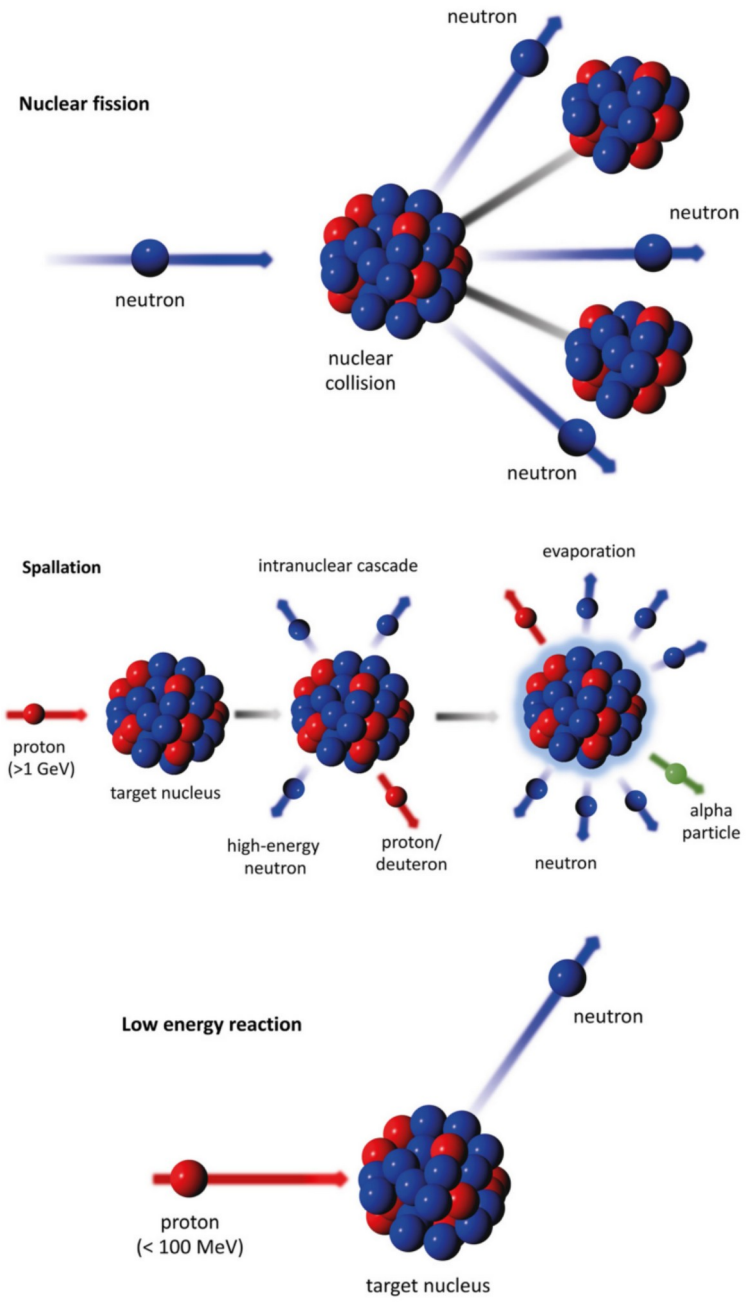

Figure 4.1: Neutron production processes for diffraction experiments: fission (top), spallation (middle), and low energy nuclear reactions (bottom). Figure from [9].

In fission (Fig. 4.1 (top)), neutrons are produced in nuclear reactors when heavy nuclei, such as uranium (^{235}U) or plutonium (^{239}Pu), undergo controlled chain reactions. In this process, a heavy nucleus absorbs a neutron and splits into two smaller nuclei, releasing approximately 2.5 neutrons per fission event along with a significant amount of energy [13]. Among the released neutrons, one must be slowed down (moderated) to an appropriate energy level to sustain the chain reaction. Moderation is achieved by passing the neutrons through materials like heavy water, graphite, or hydrogen-rich substances, which slow them down through elastic collisions [14].

In the process of spallation (Fig. 4.1 (middle)), protons are accelerated in a particle accelerator to high energies of approximately 1 GeV and directed at a heavy metal target, such as tungsten (W) or lead (Pb) [15]. The impact excites the nuclei in the target material which ejects neutrons, protons, and pions that further collide with the target's nuclei to produce more particles. This method is highly efficient, generating large quantities of so-called "evaporation neutrons", typically $10-30$ per incident proton, with energies around 2 MeV, and some high energy neutrons with energies up to the energy of the incident proton[16]. The process of spallation is highly efficient in producing high flux of neutrons.

Low-energy nuclear reactions (Fig. 4.1 (bottom)) at accelerator-driven neutron sources provide an alternative for neutron production, particularly at energies below 100 MeV. In this range, light metals like lithium (Li) and beryllium (Be) are effective targets, especially at lower energies around 30 MeV, while heavier elements become more efficient at higher energies [17]. Meanwhile, recent advancements in High-Current Accelerator-driven Neutron Sources (HiCANS) demonstrate the potential to achieve performance levels comparable to those of traditional fission and spallation neutron sources [18,19]. One key advantage of accelerator-driven sources is their ability to produce neutrons on demand, while their pulsed structure allows for the efficient use of a full neutron wavelength spectrum through time-of-flight methods [9].

In neutron diffraction experiments, the wavelength of neutrons is comparable to the distances between the atoms of the material under study, typically around 2 Å. Using Eq. 4.3, this range corresponds to neutron energies in the order of 50 meV. However, the processes of neutron production described earlier (fission, spallation, or low-energy nuclear reactions) generate high-energy neutrons in the MeV range. These neutrons must be moderated to lower their energy before they can be used in diffraction experiments.

Based on their energy after moderation, neutrons are categorized as hot (100–1000 meV), thermal (5–100 meV), or cold (0.05–5 meV). These categories correspond to the equivalent temperatures of the neutrons' kinetic energy after reaching thermal equilibrium with the moderator. Hot neutrons have a Maxwell-Boltzman energy distribution corresponding to approximately 2300 K, thermal neutrons to 300 K (room temperature), and cold neutrons to around 25 K, as shown in Fig. 4.2. The distribution of neutron flux (neutrons per second) for a Maxwellian source can be expressed in terms of λ by the relationship [20]:

$$\varphi(\lambda)=\varphi_0\frac{1}{\lambda^5}\exp\left(\frac{-h^2}{2mk_BT\lambda^2}\right) \tag{4.4}$$

where φ_0 is a normalization constant, m is the neutron's mass, $k_B=1.3807\times10^{-23}\,\mathrm{J/K}$ is Boltzman's constant, and T is the absolute temperature of the neutrons after reaching thermal equilibrium with the moderator. The peak of the Maxwellian, which corresponds to the most probable wavelength of the neutrons, is given by:

$$\lambda=\frac{h}{\sqrt{5mk_BT}} \tag{4.5}$$

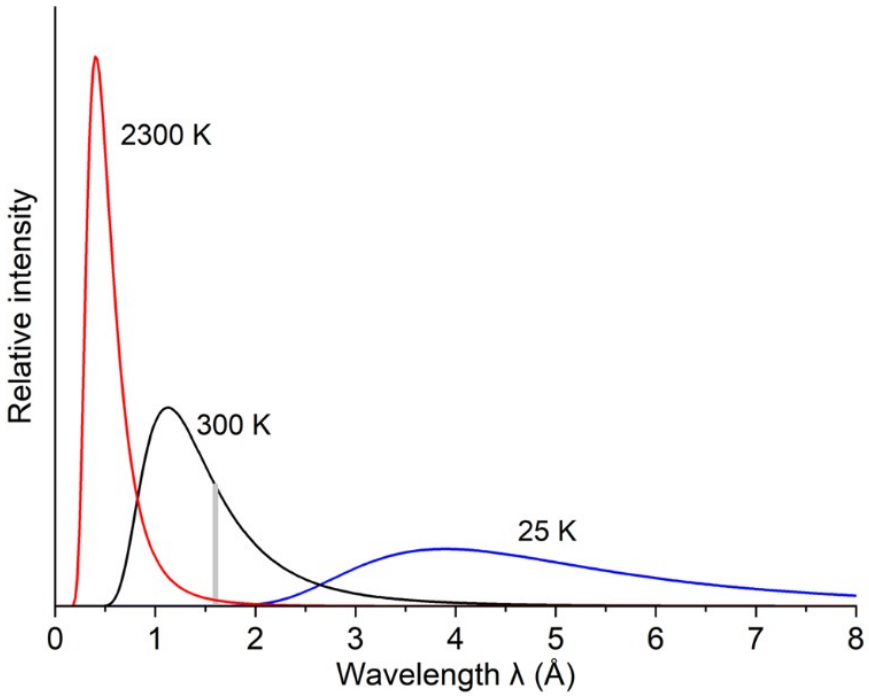

Figure 4.2: Maxwellian distributions of hot (T = 2300 K), thermal (T = 300 K), and cold (T = 25 K) neutrons. Figure from [9].

4.2.2. Bragg's law

The diffraction of waves from a crystal structure is governed by Bragg's law. In its simplest form, the crystal structure can be represented as a two-dimensional (2D) lattice, consisting of a periodic array of atoms. These atoms form parallel planes, each separated by a uniform distance d, which is referred to as the interplanar spacing. When a wave, such as a neutron wave, interacts with this 2D lattice, each plane acts as a scattering center, and the scattered waves from successive planes

interfere with each other. When the path difference between waves scattered from adjacent planes equals an integer multiple of the wavelength, constructive interference occurs, producing a diffraction peak. This condition, known as Bragg's law, is mathematically expressed as:

$$n\lambda = 2d\sin(\theta) \tag{4.6}$$

with n being an integer representing the order of diffraction, λ the wavelength of the incident beam of neutrons, d the interplanar spacing, and θ the angle between the incident wave and the crystal planes. Bragg diffraction of two parallel beams with the same wavelength and phase, scattered by the atoms of a square lattice with interplanar distance d, is shown in Fig. 4.3.

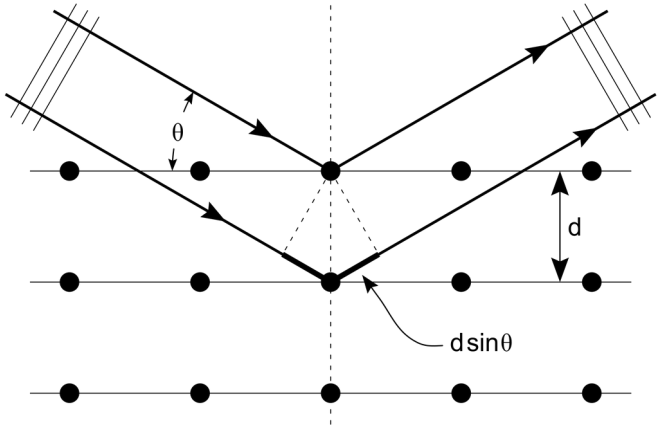

Figure 4.3: Diffraction of two parallel beams with the same wavelength and phase. The beams are scattered by the atoms of a square lattice with interplanar distance d and interfere constructively. Figure from [28].

Miller indices

The planes involved in diffraction are part of the crystal's periodic structure, which is defined by the unit cell. The unit cell is the smallest repeating unit that describes the entire crystal lattice when translated in three dimensions and is characterized by three lattice vectors ($\vec{a}$, $\vec{b}$, $\vec{c}$) that define its dimensions and orientation, as well as the angles between them (α, β, γ). Together the lattice vectors and angels comprise the parameters of the lattice [20]. The edges and angles of the unit cell are determined by the symmetry of the crystal, such as cubic, tetragonal, or hexagonal. The various combinations of the lattice parameters form seven crystal systems in total, presented in Table 2.

Planes within the crystal lattice are described in relation to the unit cell. These planes are sets of parallel, equally spaced atomic layers, which contribute to diffraction. The spacing between

adjacent planes depends on the orientation of the planes and the dimensions of the unit cell. To systematically label and describe these planes, a set of integers called Miller indices (hkl) is used. Miller indices represent the orientation of a plane by describing its intercepts with the crystal axes. They are calculated as the reciprocals of the fractional intercepts that the plane makes with the unit cell axes. For example, a plane with Miller indices (100) intersects the x-axis at one unit cell and is parallel to the y- and z-axes, while a plane with Miller indices (110) intersects both the x- and y-axes at one unit cell and is parallel to the z-axis. Fig. 4.4 presents sets of planes, as lines, with the same Miller indices in a two-dimensional square lattice.

Table 2: Lattice parameters for the seven crystal systems [20].

System	Lattice parameters
Triclinic	$a \neq b \neq c$, $\alpha \neq \beta \neq \gamma \neq 90\,°$
Monoclinic	$a \neq b \neq c$, $\alpha = \beta = 90\,°$, $\gamma \neq 90\,°$
Orthorombic	$a \neq b \neq c$, $\alpha = \beta = \gamma = 90\,°$
Trigonal (rhombohedral)	$a = b = c$, $\alpha = \beta = \gamma \neq 90\,°$
Hexagonal	$a = b \neq c$, $\alpha = \beta = 90\,°$, $\gamma = 120\,°$
Tetragonal	$a = b \neq c$, $\alpha = \beta = \gamma = 90\,°$
Cubic	$a = b = c$, $\alpha = \beta = \gamma = 90\,°$

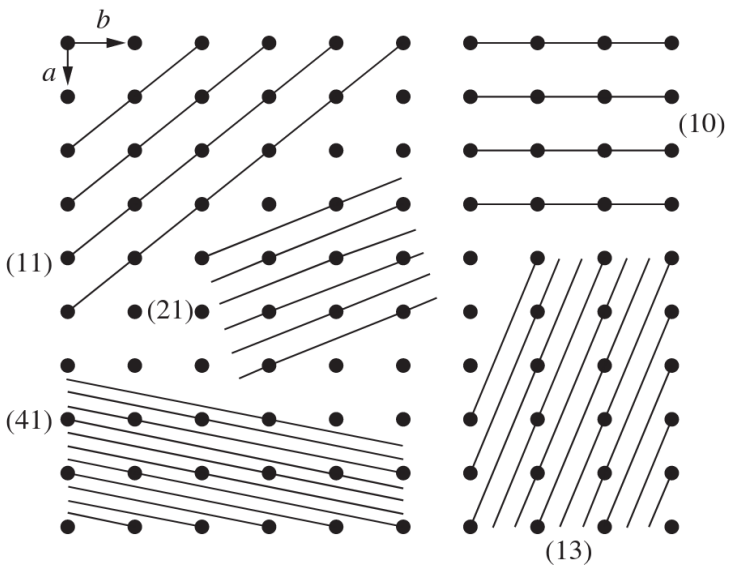

Figure 4.4: Sets of planes (lines) with the same Miller indices in a two-dimensional square lattice. Figure from [20].

The interplanar spacing d_{hkl} for a given set of planes can be calculated based on the lattice geometry. For cubic crystals, the spacing is given by:

$$d_{hkl} = \frac{a}{\sqrt{h^2 + k^2 + l^2}} \tag{4.7}$$

In non-cubic systems, the calculation of interplanar spacing becomes more complex as the lattice constants and angles vary. For example, in hexagonal systems, like the ones found in hydroxyapatite, the interplanar spacing d_{hkl} is calculated as:

$$d_{hkl} = \frac{a}{\sqrt{\frac{4}{3}\left(h^2 + hk + k^2\right) + \frac{a^2}{c^2} l^2}} \tag{4.8}$$

Bravais lattices

The periodic arrangement of atoms within a crystal lattice is described not only by the unit cell but also by the type of lattice symmetry it exhibits. These symmetries are systematically categorized using Bravais lattices, which define all possible three-dimensional lattice structures that can be formed by translating identical unit cells without overlap or gaps. There are 14 unique Bravais lattices, grouped into the seven crystal systems of Table 2 and based on their symmetry and geometric constraints.

Each Bravais lattice is characterized by the arrangement of points within the unit cell and their symmetry relations. They are categorized as: primitive (P), which contain lattice points only at the corners of the unit cell; body-centered (I), which contain an additional lattice point at the center of the unit cell; face-centered (F), which contain lattice points at the center of each face; base-centered (C), which contain lattice points at the centers of two opposing faces. The 14 Bravais lattices are shown in Fig 4.5.

Bravais lattices describe the symmetry and periodicity of atomic arrangements within crystals. This classification system also determines the orientation and spacing of atomic planes, as described by Miller indices. For instance, in cubic crystals, planes with the same Miller indices (e.g., (100), (110)) are equivalent due to their high symmetry, whereas in triclinic or monoclinic systems, such equivalence does not hold due to lower symmetry.

The symmetry of the Bravais lattice not only defines the geometric arrangement of atoms but also determines the selection rules for diffraction. These rules dictate which planes produce reflections in the diffraction pattern, as certain combinations of Miller indices (hkl) are allowed or forbidden

based on the lattice type. The selection rules for common Bravais lattices are shown in Table 3 [21]. These selection rules are fundamental for interpreting diffraction patterns and identifying the underlying lattice symmetry. For example, the absence of reflections for specific (hkl) indices can help distinguish between simple cubic and body-centered cubic lattices, or between face-centered cubic and hexagonal close-packed structures.

Table 3: Selection rules for common crystal structures [21].

Crystal type	Selection rule
Primitive	Reflection for any h, k, l
Body-centered	Reflection only if $h+k+l$ is even
Face-centered	Reflection only if h, k, l are all odd or all even
Base-centered	Reflection only if h, k, l are all odd or all even
Hexagonal close-packed	Reflection if: • $h+2k=3n$ with l odd, for integer n • $h+2k=3n$ with l even, for integer n • $h+2k=3n\pm1$ with l odd, for integer n • $h+2k=3n\pm1$ with l even, for integer n
Diamond	Reflection only if h, k, l are all odd or all even and $h+k+l\neq4n$, for integer n

By combining Bravais lattices with the concepts of unit cells, Miller indices, and interplanar spacing, a complete framework is established for analyzing diffraction patterns using Bragg's law. The symmetry of the Bravais lattice influences the positions and intensities of diffraction peaks, enabling the identification of crystal structures, lattice parameters, and phase compositions.

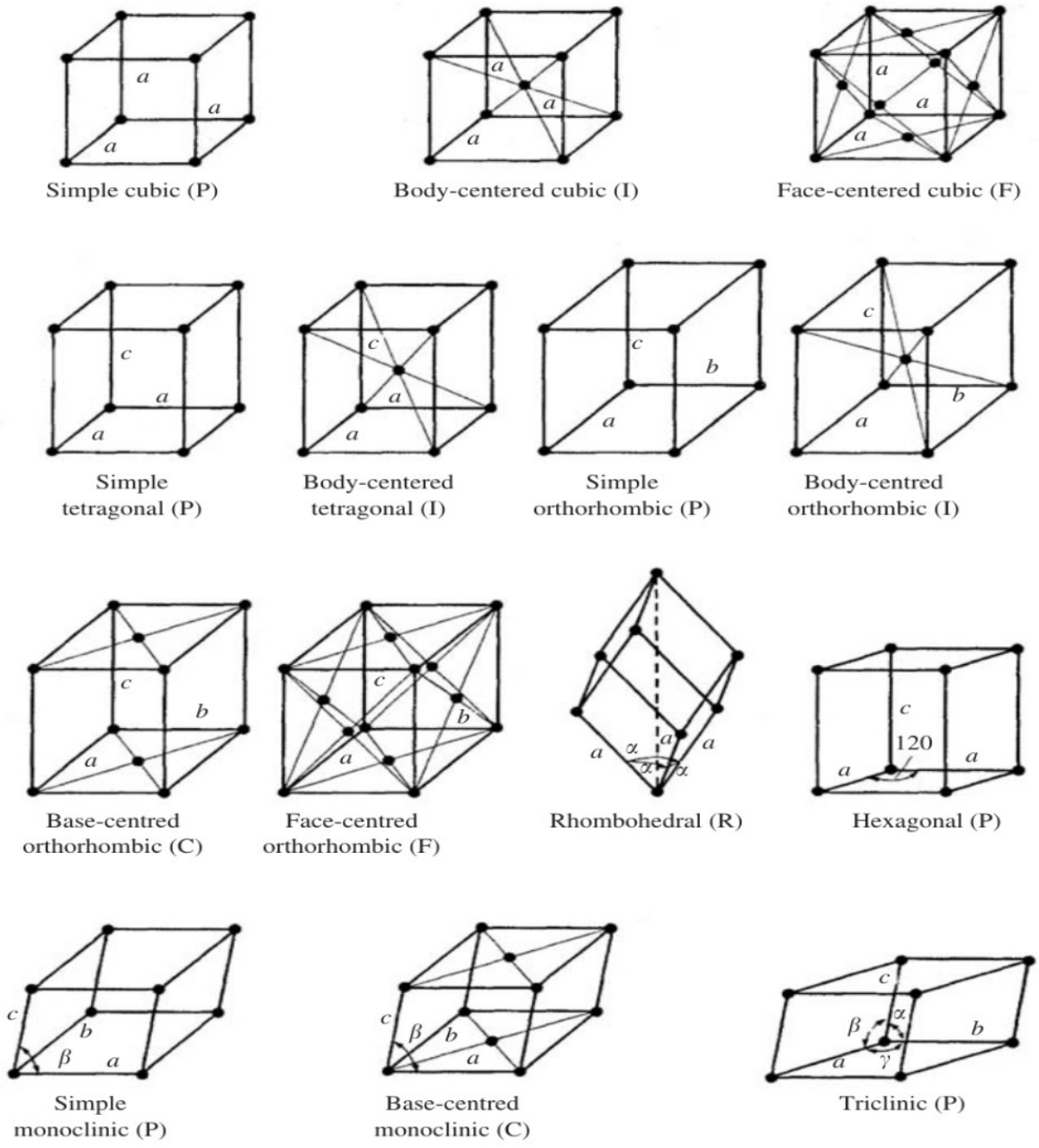

Figure 4.5: The 14 Bravais lattices. Figure from [20].

Lattice defects

While Bravais lattices describe the ideal periodic arrangement of atoms in a crystal, real materials often deviate from this perfect order. Inherent limitations of real crystals can affect their diffraction patterns, such as finite crystal size, where sizes smaller than 0.5 µm result in broadening of diffraction peaks, and vibrations of atoms around their mean position, which cause detectable phase shifts even at very low temperatures [20]. Additionally, structural irregularities, known as lattice imperfections or defects, play a critical role in determining the physical and mechanical properties of materials. Lattice imperfections are broadly classified into three main types: point defects, line defects, and planar defects. Some common lattice defects are shown in Fig. 4.6.

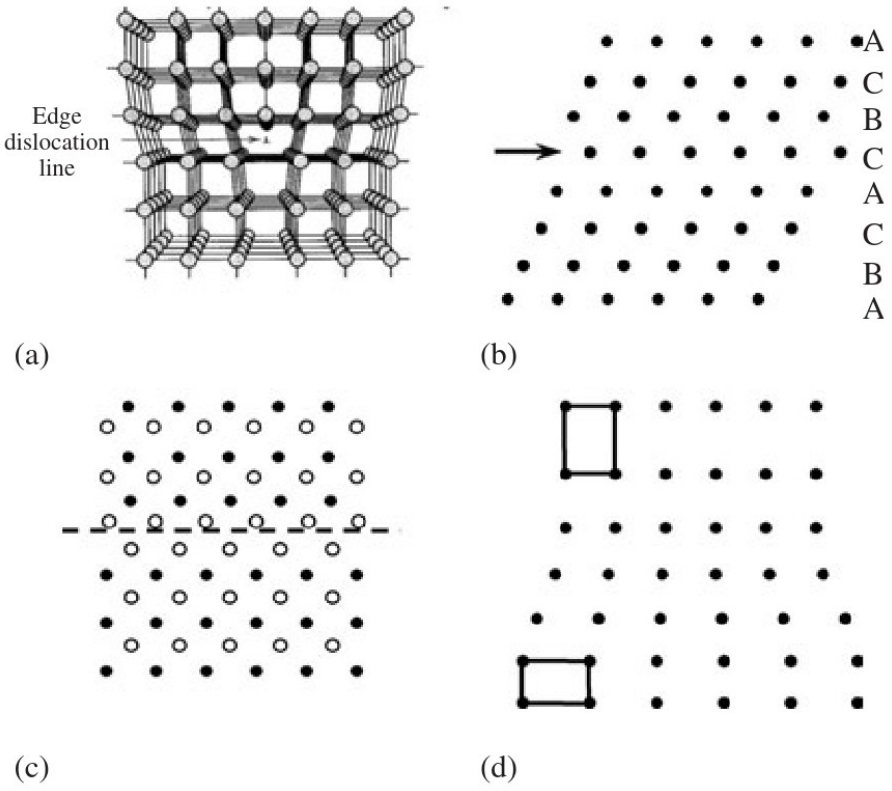

Figure 4.6: Common lattice defects. (a) Edge dislocation. (b) Stacking fault at the plane denoted by the arrow. (c) Anti-phase domain boundary. (d) 90° domain wall in a ferroic crystal. Figure from [20].

Point defects occur when the periodic arrangement of atoms is disrupted at a single point in the lattice [20,22]. Vacancies are common point defects, where atoms are missing from lattice sites. Interstitial defects, which are the opposite of vacancies, can also occur. In this type of defect, extra atoms are embedded in the crystal lattice in positions where atoms would not normally reside, introducing local strain. Substitutional defects are another common type of point defect. Even in highly pure materials, some impurities (foreign atoms) are present. These foreign atoms replace

the original atoms in the crystal lattice and, due to differences in size or oxidation state, may alter the structure and electronic properties of the material.

In addition to point defects, line defects, or dislocations, represent another category of lattice imperfections [20,22]. The two main types of dislocations are edge dislocations and screw dislocations. An edge dislocation (Fig. 4.6(a)) occurs when a plane of atoms terminates abruptly within the crystal lattice. This termination creates an extra half-plane of atoms, causing the surrounding atomic planes to bend and resulting in a localized distortion of the lattice structure. In screw dislocations, the atoms are displaced such that the lattice planes form a helical structure around the dislocation line.

Planar defects also occur when the periodicity of the lattice is disrupted across a two-dimensional plane [20,22]. Grain boundaries are among the most common planar defects and occur where the crystallographic orientation of the crystal lattice changes abruptly. These defects are typically found in regions where crystals of different orientations meet within a polycrystalline material. Another common planar defect is the stacking fault (Fig. 4.6(b)), where the regular stacking sequence of atomic layers in a crystal is disrupted. In the example of Fig. 4.6(b), the stacking sequence changes from ACB to CBC at the location indicated by the arrow, before returning to the original ABC sequence. In materials with ordered crystal structures, such as ordered alloys, anti-phase domain boundaries may also occur (Fig. 4.6(c)). These defects form when adjacent planes within the crystal have opposite phases, creating a boundary. In the example shown in Fig. 4.6(c), the normal sequence of black (B) and white (W) atoms, BWBWBWBWBWBW, is disrupted. The sequence changes to BWBWBWWBWBWB, forming a WW region at the boundary highlighted by the arrow.

Lattice imperfections influence the diffraction patterns observed in experiments in various ways. Dislocations and small (or nano) crystallite sizes introduce strain, resulting in broader diffraction peaks. Vacancies and substitutional defects alter lattice parameters, causing shifts in peak positions, while planar defects, such as grain boundaries, scatter waves incoherently, reducing peak intensities. By analyzing these changes in diffraction patterns, it is possible to quantify defect densities, estimate strain, and understand the microstructural features of materials. This ability to characterize imperfections complements the analysis of ideal crystal structures, making diffraction a powerful tool for both perfect and imperfect lattices.

4.3. Experimental configuration

There are various types of neutron diffractometers, including time-of-flight diffractometers [23], four-circle diffractometers [24], small-angle neutron scattering (SANS) instruments [25], and more. However, the two-axis diffractometer remains the most commonly used due to its simplicity and versatility in crystallographic studies [26].

The typical experimental configuration of the two-axis neutron diffractometer G41 at Laboratoire Léon Brillouin (LLB), Saclay, France, where we conducted neutron powder diffraction experiments, is typical for this kind and is shown in Fig. 4.7 [27]. The neutron beam was produced by a nuclear reactor and a single wavelength is selected by a vertical focusing pyrolitic graphite monochromator crystal based on Bragg's law. The monochromatic neutron beam was directed at the sample mounted at the center of the instrument and is further filtered using graphite filters. The powdered sample was placed on a holder to ensure uniform exposure to the neutron beam. The scattered neutrons are detected by a movable detector mounted on a goniometer arm, which measures the intensity of scattered neutrons at various diffraction angles, referred to as 2θ.

To enhance beam precision, collimators and slits are employed to define the beam profile and minimize background noise. The configuration can be adjusted based on experimental requirements, such as the use of cryostats for low-temperature studies or furnaces for high-temperature measurements, enabling the investigation of materials under a wide range of conditions.

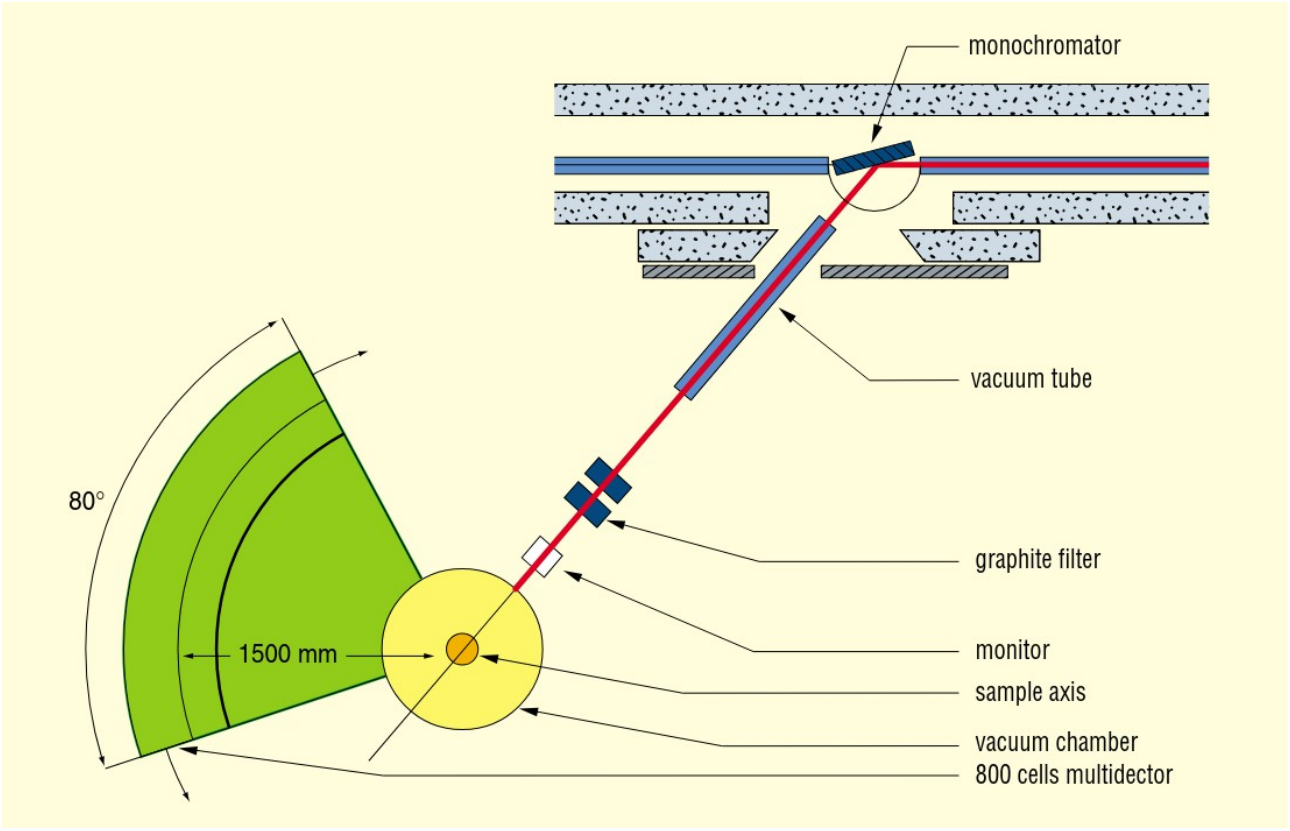

Figure 4.7: Schematic diagram of the two-axis diffractometer G41 at LLB. Figure from [27].

4.4. Advantages and limitations

Neutron powder diffraction presents several advantages which make it a preferable technique over other diffraction techniques such as XRD.

- It interacts with the atomic nuclei of the material under study, unlike XRD which interacts with the electronic clouds of the atoms, providing higher sensitivity in structural measurements, thus providing higher resolution diffraction diagrams.
- It is particularly sensitive to light elements such as hydrogen, lithium, carbon, and oxygen, making it useful for studying organic materials and materials containing light elements.
- In situ measurements enable the study of materials under high temperatures, pressures, or applied fields (magnetic or electric).
- It can distinguish between isotopes of the same element.

Despite its advantages, however, the technique has some important limitations.

- Neutron sources are limited to large-scale facilities such as reactors or spallation sources.
- Neutron beams typically have lower flux compared to X-ray sources, requiring longer data collection times.

4.5. Neutron diffraction of bone

Neutron diffraction of bone does not have specific "regions" analogous to the characteristic vibrational modes in Raman spectroscopy. Instead, it focuses on crystallographic information, providing insights into the atomic and molecular arrangement, particularly for crystalline phases like hydroxyapatite (HA). Neutron diffraction studies often analyze the crystalline phase of hydroxyapatite in bone, where diffraction peaks correspond to the lattice planes of HA. Changes in peak positions or intensities can reveal alterations in crystal structure, size, or strain. The technique can also quantify the degree of crystallinity, which, in bone, can reflect pathological states like osteoporosis. Furthermore, neutron diffraction is sensitive to elemental substitutions (such as carbonate replacing phosphate or hydroxyl groups in HA) and structural defects, both of which significantly impact diffraction patterns and are crucial for understanding bone quality and disease-related changes. Additionally, it provides information on the preferred orientation (texture) of hydroxyapatite crystallites, a parameter closely tied to bone's mechanical properties.

4.6. References

[1] Chadwick J. The existence of a neutron. Proc R Soc Lond Ser Contain Pap Math Phys Character 1932;136:692–708. https://doi.org/10.1098/rspa.1932.0112.

[2] Mitchell DP, Powers PN. Bragg Reflection of Slow Neutrons. Phys Rev 1936;50:486–7. https://doi.org/10.1103/PhysRev.50.486.2.

[3] Von Halban H. Preuve expérimentale de la diffraction des neutrons. Académie Sci 1936;203:73–5.

[4] Mason TE, Gawne TJ, Nagler SE, Nestor MB, Carpenter JM. The early development of neutron diffraction: science in the wings of the Manhattan Project. Acta Crystallogr A 2013;69:37–44. https://doi.org/10.1107/S0108767312036021.

[5] Copley JR. The Fundamentals of Neutron Powder Diffraction. NIST 2001.

[6] Clausen B, Brown DW, Noyan IC. Engineering Applications of Time-of-Flight Neutron Diffraction. JOM 2012;64:117–26. https://doi.org/10.1007/s11837-011-0119-x.

[7] Többens D, Stüßer N, Knorr K, Mayer HM, Lampert G. E9: The New High-Resolution Neutron Powder Diffractometer at the Berlin Neutron Scattering Center. Mater Sci Forum - MATER SCI FORUM 2001;378:288–93. https://doi.org/10.4028/www.scientific.net/MSF.378-381.288.

[8] Goonetilleke D, Sharma N. In situ neutron powder diffraction studies. Phys Sci Rev 2021;6. https://doi.org/10.1515/psr-2018-0155.

[9] Dronskowski R, Brückel T, Kohlmann H, Avdeev M, Houben A, Meven M, et al. Neutron diffraction: a primer. Z Für Krist - Cryst Mater 2024;239:139–66. https://doi.org/10.1515/zkri-2024-0001.

[10] Bouwkamp CJ. Diffraction Theory. In: Klem-Musatov K, Hoeber HC, Moser TJ, Pelissier MA, editors. Class. Mod. Diffr. Theory, vol. 29, Society of Exploration Geophysicists; 2016, p. 0.

[11] Broglie L de. Recherches sur la théorie des Quanta. phdthesis. Migration - université en cours d'affectation, 1924.

[12] Carpenter JM, Loong C-K. Elements of Slow-Neutron Scattering: Basics, Techniques, and Applications. 1st ed. Cambridge University Press; 2015. https://doi.org/10.1017/CBO9781139029315.

[13] Hopkins JC, Diven BC. Prompt neutrons from fission. Nucl Phys 1963;48:433–42. https://doi.org/10.1016/0029-5582(63)90182-2.

[14] Joyce M. Nuclear Engineering: A Conceptual Introduction to Nuclear Power. 1st edition. San Diego: Butterworth-Heinemann; 2017.

[15] Bauer GS. Physics and technology of spallation neutron sources. Nucl Instrum Methods Phys Res Sect Accel Spectrometers Detect Assoc Equip 2001;463:505–43. https://doi.org/10.1016/S0168-9002(01)00167-X.

[16] Le Couteur KJ, Lang DW. Neutron evaporation and level densities in excited nuclei. Nucl Phys 1959;13:32–52. https://doi.org/10.1016/0029-5582(59)90136-1.

[17] Jeon B, Kim J, Lee E, Moon M, Cho S, Cho G. Target-Moderator-Reflector system for 10–30 MeV proton accelerator-driven compact thermal neutron source: Conceptual design and neutronic characterization. Nucl Eng Technol 2020;52:633–46. https://doi.org/10.1016/j.net.2019.08.019.

[18] Ott F, Darpentigny J, Annighöfer B, Paulin MA, Meuriot J-L, Menelle A, et al. ICONE – Towards a French HiCANS Neutron Source for materials science and industry. EPJ Web Conf 2023;286:02001. https://doi.org/10.1051/epjconf/202328602001.

[19] Baggemann J, Gutberlet T, Zakalek P, Wolters J, Rücker U, Mauerhofer E, et al. High power target for the High Brilliance Neutron Source. Nucl Instrum Methods Phys Res Sect Accel Spectrometers Detect Assoc Equip 2024;1069:169912. https://doi.org/10.1016/j.nima.2024.169912.
[20] Kisi EH, Howard CJ. Applications of Neutron Powder Diffraction. Oxford University Press; 2008. https://doi.org/10.1093/acprof:oso/9780198515944.001.0001.
[21] Williams DB, Carter CB, editors. Transmission Electron Microscopy: A Textbook for Materials Science. 2nd ed. Boston, MA: Springer US; 2009. https://doi.org/10.1007/978-0-387-76501-3.
[22] Kittel C. Introduction to solid state physics. 8. ed., [repr.]. Hoboken, NJ: Wiley; 20.
[23] Ohhara T, Kiyanagi R, Oikawa K, Kaneko K, Kawasaki T, Tamura I, et al. SENJU: a new time-of-flight single-crystal neutron diffractometer at J-PARC. J Appl Crystallogr 2016;49:120–7. https://doi.org/10.1107/S1600576715022943.
[24] Chakoumakos BC, Cao H, Ye F, Stoica AD, Popovici M, Sundaram M, et al. Four-circle single-crystal neutron diffractometer at the High Flux Isotope Reactor. J Appl Crystallogr 2011;44:655–8. https://doi.org/10.1107/S0021889811012301.
[25] Mühlbauer S, Heinemann A, Wilhelm A, Karge L, Ostermann A, Defendi I, et al. The new small-angle neutron scattering instrument SANS-1 at MLZ—characterization and first results. Nucl Instrum Methods Phys Res Sect Accel Spectrometers Detect Assoc Equip 2016;832:297–305. https://doi.org/10.1016/j.nima.2016.06.105.
[26] Roisnel T, Rodríquez-Carvajal J, Pinot M, André G, Bourée F. Neutron Powder Diffraction Facilities at the Laboratoire Leon Brillouin. Mater Sci Forum 1994;166–169:245–50. https://doi.org/10.4028/www.scientific.net/MSF.166-169.245.
[27] Powder diffraction - IRAMIS 2024. https://iramis.cea.fr/en/llb/neutrons-3/powder-diffraction-2/ (accessed December 22, 2024).
[28] Hydrargyrum. English: Bragg diffraction from a cubic crystal lattice. Plane waves incident on a crystal lattice at angle. 2011.

5. Aim of this thesis

The aim of this thesis is to investigate the molecular-level changes in bone quality in an inflammation-mediated osteoporosis (IMO) model in New Zealand white rabbits. Raman spectroscopy is employed to detect chemical and structural alterations in the bone matrix, including variations in crystallinity, mineral-to-matrix ratios, carbonate substitution, and collagen quality. Complementing this, neutron powder diffraction examines the crystallographic properties of bone mineral, such as lattice parameters and crystallite size. By integrating these techniques, this study provides a comprehensive characterization of the subtle changes associated with osteoporosis, contributing to a deeper understanding of its effects on bone quality. Additionally, we conducted a pilot study to discriminate healthy and osteoporotic bone samples using Raman spectra collected from the periosteal surface. The study aims to assess the feasibility of a potential Spatially-offset Raman Spectroscopy (SORS) setup capable of discriminating pathological from healthy bone. With the ability of achieving sub-epidermal bone surface analysis by probing superficial scattering volumes, SORS is a promising technique for in vivo applications. Finally, an open-source Python package, PyFasma, is developed to provide a complete preprocessing and Raman analysis solution.

6. Materials and methods

6.1. Bone samples preparation

For the experimental procedure, excised biopsies were obtained from various skeletal sites of eight healthy and two osteoporotic female New Zealand white rabbits, aged 8 months. Inflammation-mediated osteoporosis (IMO) was induced to the diseased animals using a protocol that was successfully applied to New Zealand rabbits in previous studies and will be described in section 6.1.2 [1–3]. The animals were kept and bred in a natural environment and were euthanized using light ether anesthesia in a humane manner. All study protocols were approved by the Ioannina University Institutional Animal Care and Use Committee (2018)`.

6.1.1. Samples collection

Following euthanasia, the tibias, humeri, femurs, and ribs (Fig. 6.1) were surgically excised with sterilized materials to prevent tissue contamination and carefully cleaned to remove the majority of soft tissue. Then they were submerged in distilled water for 24 h. After 24 h, the bones were further cleaned from leftover tissue residues.

After external cleaning, the epiphyses of the long bones (tibias, humeri, and femurs) and the edges of the ribs were trimmed. The bones were subsequently centrifuged at 2500 rpm for 15 minutes to extract bone marrow, fat, and residual fluids. To further remove tissue residues and prevent water interference in subsequent experiments, the bones were successively submerged in ethanol/distilled water solutions with increasing ethanol concentrations:

- 20:80 ethanol/distilled water solution for 30 minutes

- 50:50 ethanol/distilled water solution for 30 minutes
- 80:20 ethanol/distilled water solution for 30 minutes

Following the final submersion, the bones were centrifuged at 2500 rpm for 2 minutes. Finally, the bones were dehydrated by freeze-drying them for approximately 2 h.

After cleaning and superficially dehydrating the excised bones, six transverse slices, each approximately 2 mm in width, were sectioned from the central, predominantly cortical regions of the left diaphyses of the tibias, humeri, and femurs of the healthy animals. For the osteoporotic animals, six transverse slices were similarly obtained from both the left and right diaphyses of the corresponding bones (tibias, humeri, and femurs). Additionally, six transverse slices of the same width were collected from the central region of a rib in both healthy and osteoporotic animals (highlighted in Fig. 6.1).

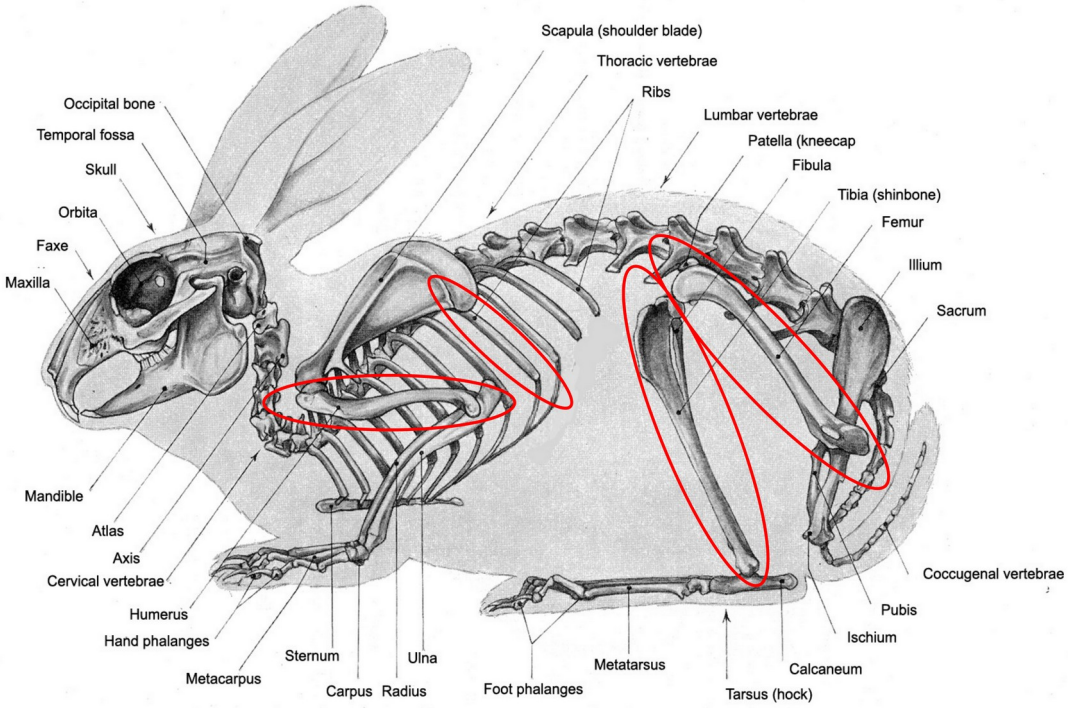

Figure 6.1: Skeletal system of a rabbit. The red ellipses highlight the sites used in our experiments. Figure from [13].

`In total we obtained 192 samples from the healthy animals and 84 samples form the osteoporotic animals. The number of samples for each skeletal site is presented analytically in Table 4.

Table 4: Number of samples obtained from each skeletal site.

Skeletal site	No. healthy	No. osteoporotic
Left tibia	48	12
Left humerus	48	12
Left femur	48	12
Right tibia	-	12
Right humerus	-	12
Right femur	-	12
Rib	48	12
Total	**192**	**84**

6.1.2. Inflammation-mediated osteoporosis protocol

Inflammation-mediated osteoporosis (IMO) was induced in two rabbits by applying the protocol described by Armour and Armour [4]. Despite the fact that this protocol was designed for rats, previous studies in our laboratory have demonstrated its effectiveness in rabbits [1–3]. The method involves the subcutaneous injection of magnesium silicate ($Mg_3Si_4O_{10}(OH)_2$), also known as talc, at various sites on the upper back and sides of the animals. The talc injections trigger an acute-phase response, leading to granulomatous reactions and chronic inflammation, and ultimately osteoporosis. The bone loss occurs due to a reduction in osteoblast numbers and decreased bone formation, while osteoclast numbers and resorptive activity remain largely unaffected. This mechanism closely mirrors the pathophysiology of human inflammation-mediated osteoporosis, which is associated with chronic inflammatory conditions such as inflammatory bowel disease and rheumatoid arthritis [5–7].

The IMO protocol that was followed has a total duration of 21 days and involves the following steps:

1. Weighting of the animals.
2. Preparation of the magnesium silicate solution. First, the magnesium silicate was sterilized by heating at 160°C for 1 hour. Then, an 80 mg/mL suspension was prepared in sterile saline (0.9% w/v NaCl).
3. Animals were anesthetized using an intraperitoneal injection of Vetalar (ketamine hydrochloride, 100 mg/mL) and Rompun (xylazine, 2% solution) at doses of 100 mg/kg and 20 mg/kg of body weight, respectively. The injection was administered into the lower left quadrant of the abdomen.

4. The prepared magnesium silicate suspension was injected using a 25 G needle at multiple sites on the upper back of the animals to deliver a total dose of 1.6 mg/g of body weight. Control animals receive the same volume of sterile saline at similar sites.
5. At 21 days after the magnesium silicate injection, the animals were euthanized and the bones were excised.

The choice of an animal model is critical for the accurate representation of human osteoporosis. While the ovariectomized rat is widely used as a model of human osteoporosis, it has significant limitations that can affect its applicability depending on the study's objectives. One major drawback is that the rat skeleton continues to grow throughout the animal's lifetime, with epiphyseal fusion not occurring during sexual maturation. Consequently, rats used in osteoporosis studies often have not achieved full skeletal maturity [3,8]. Moreover, rats lack Haversian systems and exhibit minimal to no intracortical remodeling, both of which are key features of human bone turnover [3].

In contrast, New Zealand rabbits reach skeletal maturity at 32–36 weeks, exhibit a high bone turnover rate, and possess Haversian systems similar to those of humans. Additionally, the long bones of aged rabbits demonstrate significant endosteal resorption and periosteal accrual, changes analogous to those observed in postmenopausal women [3]. These characteristics suggest that rabbits may be a more suitable model for studying human osteoporosis.

6.2. Experimental measurements

6.2.1. Raman spectroscopy measurements

Raman measurements were performed using a B&WTek i-Raman Plus portable Raman spectrometer equipped with a fiber-optic Raman probe (Fig. 6.2). The spectrometer utilizes an excitation wavelength of 785 nm (NIR) with a maximum power output of 340 mW at the probe. The probe has an 8 mm working distance and produces a spot with a radius of approximately 200 µm on the sample. This wavelength is well-suited for Raman measurements of biological samples, as it minimizes autofluorescence compared to visible or UV excitation, albeit at the expense of lower scattering intensity. The fiber-optic probe integrates excitation and collection fibers, allowing both the excitation and collection of Raman spectra from the same point. The collected Raman signal is transmitted via the collection fiber to the spectrometer's self-cooled charged-coupled device (CCD) detector, maintained at -2°C. The spectrometer covers a spectral range up to 3200 cm^{-1} with a nominal resolution of 4.5 cm^{-1} at 912 nm.

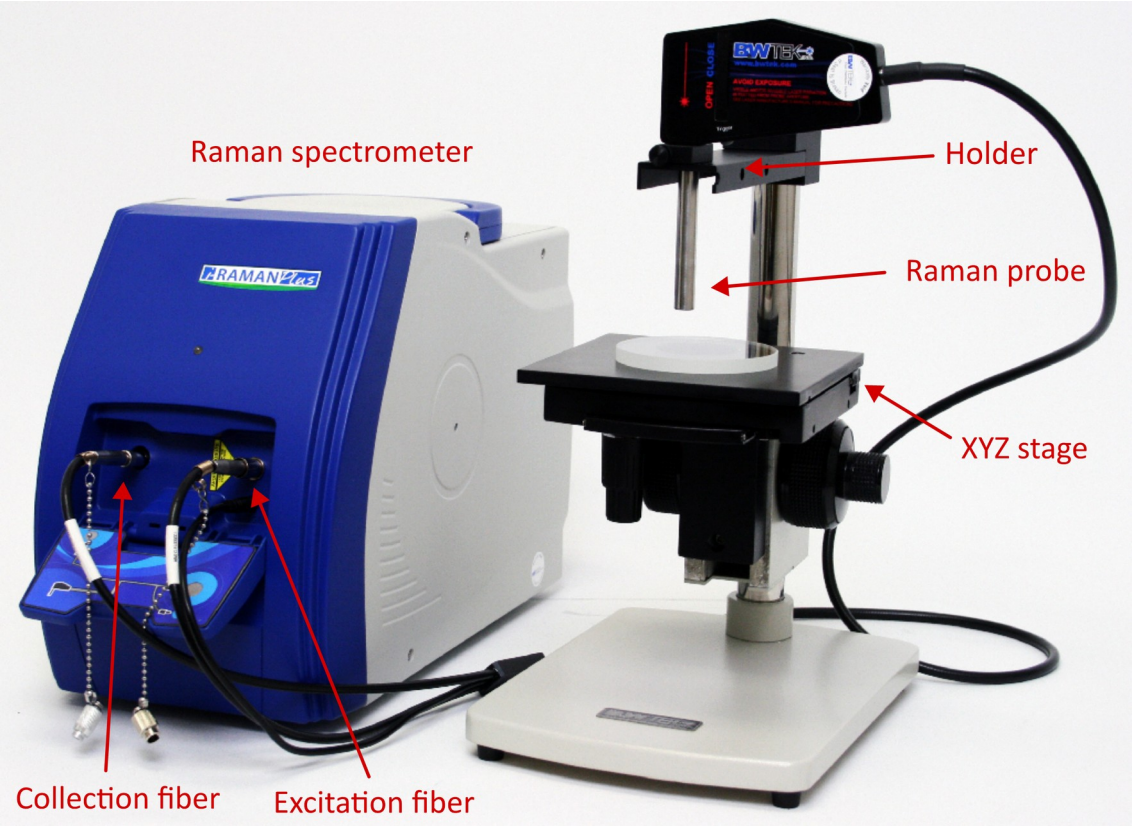

Figure 6.2: B&WTek i-Raman Plus portable Raman spectrometer. This spectrometer with the fiber probe on the holder and the sample on the XYZ stage was used for collecting Raman spectra from the healthy and osteoporotic bone samples.

For Raman measurements, the sample was placed on a tray mounted on the XYZ stage. The stage knobs were used to precisely position the sample, ensuring that the laser was focused on the desired region of interest. To achieve the correct working distance between the probe and the sample, a hollow cap was attached to the end of the probe. Spectra were acquired using the BWSpec software, which enabled control of the laser power output (0–100%), spectrum acquisition and averaging, automatic dark current subtraction, and basic analysis tools.

Two sets of Raman measurements were performed on slices obtained from the excised bones. In the first set, Raman spectra were collected from three distinct points on the transverse surface of each slice from the long bones (tibia, humerus, femur), spaced approximately 120° apart. In the second set, a single Raman spectrum was collected from the periosteal surface of slices from the left-side long bones and ribs. The total number of Raman spectra acquired from each skeletal site is summarized in Table 5.

Table 5: Number of Raman spectra obtained from the transverse and periosteal surfaces of each skeletal site.

	Healthy		Osteoporotic	
Skeletal site	**No. transverse**	**No. surface**	**No. transverse**	**No. surface**
Left tibia	144	48	36	12
Left humerus	144	48	36	12
Left femur	144	48	36	12
Right tibia	-	-	36	-
Right humerus	-	-	36	-
Right femur	-	-	36	-
Rib	-	48	-	12
Total	**432**	**192**	**216**	**48**

Raman spectra were collected using a laser power set to 60% of the maximum power and an acquisition time of 6 s. Before each measurement, a dark spectrum was acquired and automatically subtracted using the BWSpec software. Each Raman spectrum was saved as an SPC file with a unique filename, which included details about the source animal, its health status (healthy or osteoporotic), the skeletal site of the sample, as well as the specific slice and location where the spectrum was obtained.

The collected Raman spectra were then pre-processed and analyzed using PyFasma, an open-source Python 3 package that was developed as part of the thesis. The package's structure, functionality, and the procedures for analyzing Raman spectra will be described in Chapter 7.

6.2.2. Neutron powder diffraction measurements

For the neutron powder diffraction experiments, three slices from the left tibia of a healthy rabbit and three slices from the left tibia of an osteoporotic rabbit were used. The bone slices were grounded to powder using a mortar and pestle, ensuring uniform particle size and proper sample preparation for diffraction analysis. To minimize the large incoherent scattering cross-section of hydrogen, which exists in collagen, the samples were pre-heated to 350°C. Heat treatment at this temperature has no detectable effect on the size, crystallinity, or lattice spacing of the crystals of the hydroxyapatite, while it effectively removes most of the organic part in the samples [9]. The ground samples were stored in plastic tubes sealed with parafilm to prevent moisture absorption (Fig. 6.3(c)).

Neutron powder diffraction measurements were performed at the G41 two-axis diffractometer at the Laboratoire Léon Brillouin (LLB), Saclay, France (Fig. 6.3(a)). G41 is designed for high-resolution diffraction studies, enabling the detection of subtle structural changes, and in situ experiments can

be conducted under various temperature and pressure conditions, making it versatile for different research needs. The typical G41 configuration has been presented in section 4.3.

The incident neutron wavelength used in the experiments was 2.4266 Å. The powdered samples were placed inside a vanadium holder (Fig. 6.3(b)). Vanadium's very low neutron scattering cross-section ensures minimal interference with the neutron beam, making it an appropriate material for sample containment. The diffraction pattern was detected by a linear BF_3 multidetector with 800 cells covering an 10° to 90° - 2θ range. The configuration was equipped with an aluminum furnace that allowed heating the samples up to 1000°C.

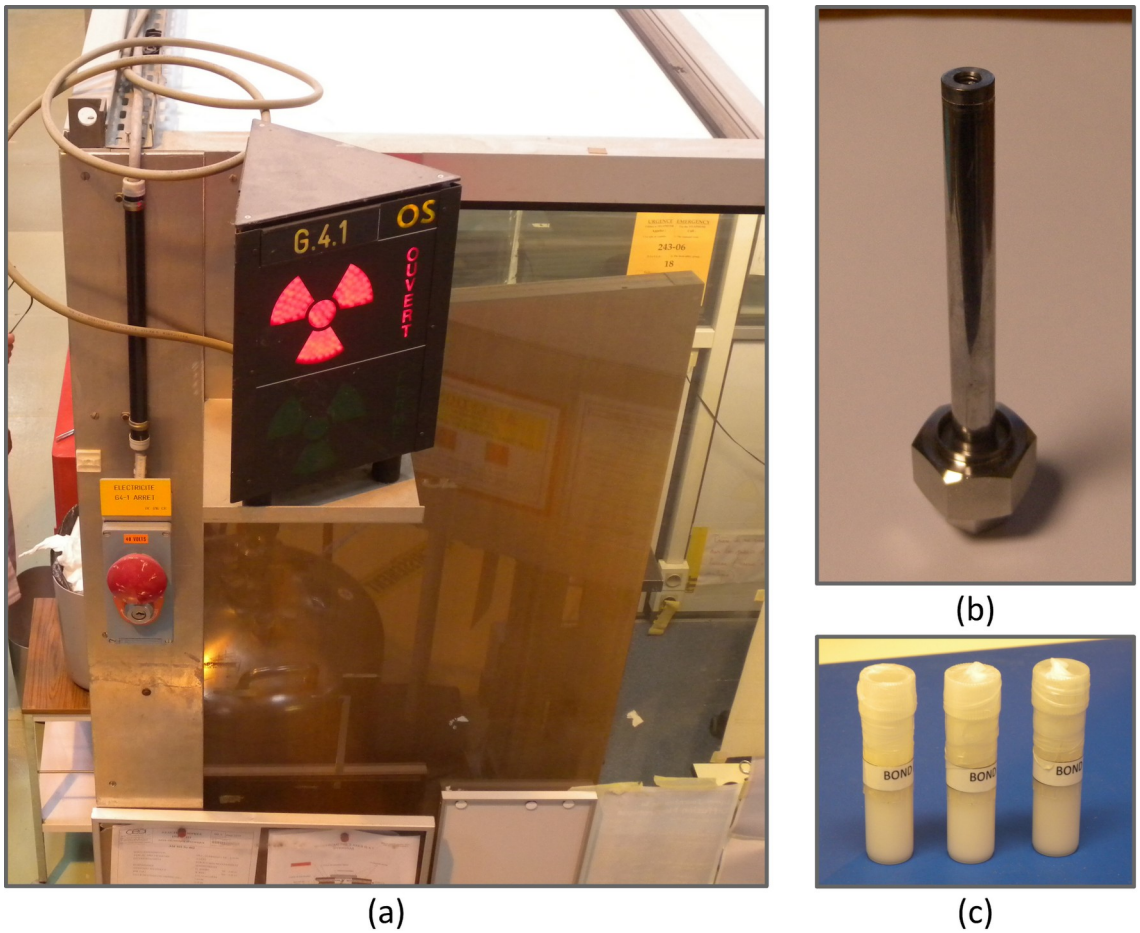

Figure 6.3: (a) Neutron powder diffraction chamber of the two-axis diffractometer G41 at LLB. (b) Vanadium sample holder. (c) Powdered bone samples.

The measurements performed at the G41 two-axis diffractometer showed the superior resolution of the neutron diffraction pattern compared with typical lab X-ray patterns (Fig. 6.4).

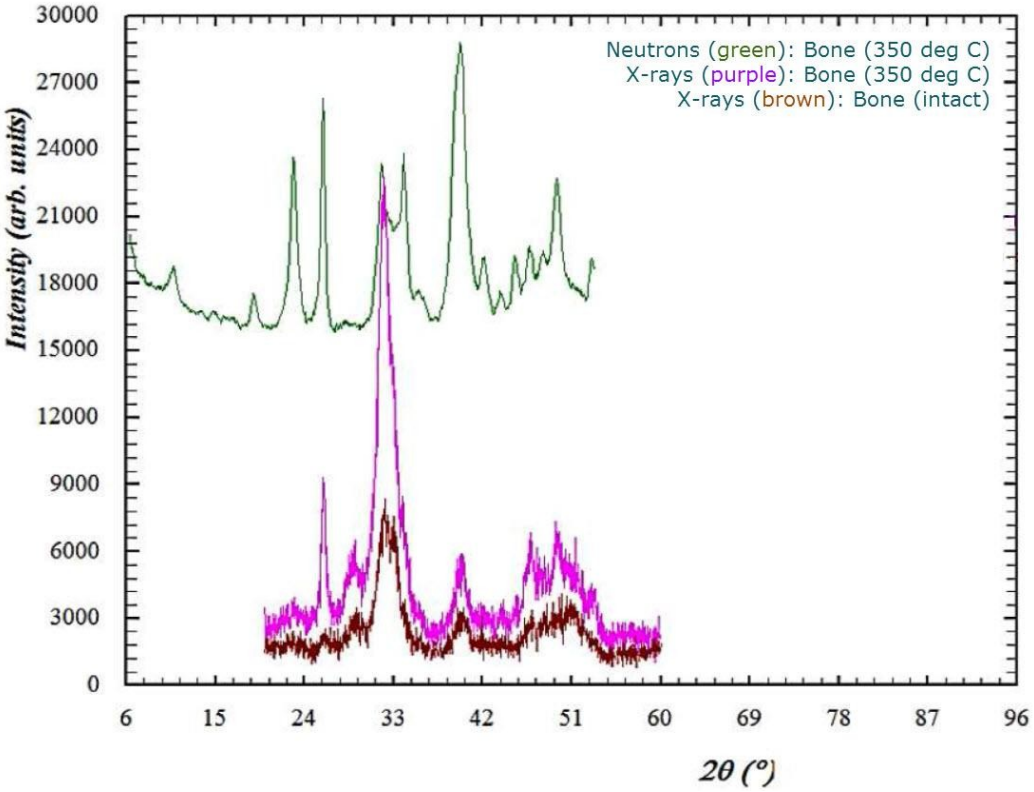

Figure 6.4: Comparison between neutron (green) and X-ray (purple and brown) powder diffraction data of bone samples.

In addition, we anticipated distinct differences between the patterns collected at increasing temperatures as it was evident in Fig. 6.5, due to the evolution of crystallinity.

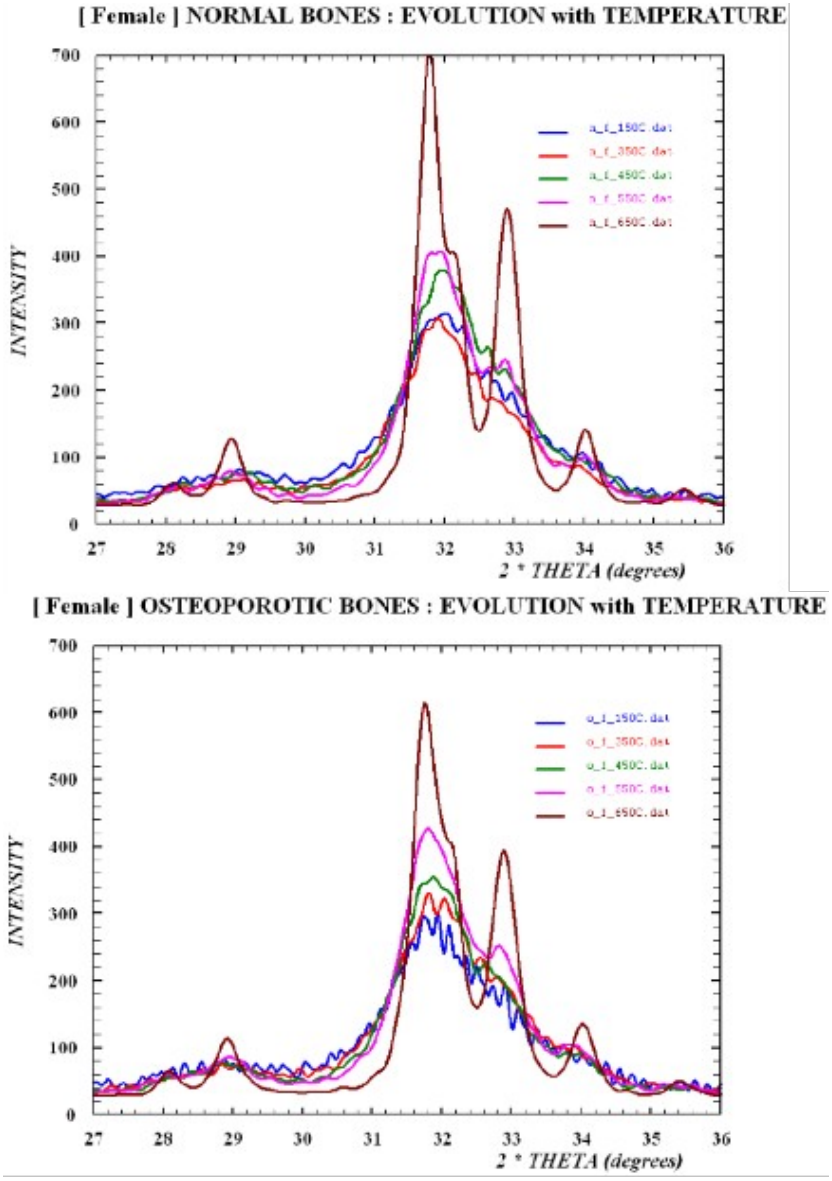

Figure 6.5: The influence of elevated temperatures on the resolution of biological Hap diffraction patterns as well as the different peak profiles between normal and osteoporotic patterns.

During the experiment, we managed to collect high quality data of three bone samples from normal and osteoporotic bones under an increasing temperature setup. After a group meeting, where the feasibility of our initial plan (increasing gradually the temperature, in situ, from 400°C in steps of 100°C) was discussed thoroughly, we decided to exclude the 500°C step from our experimental designb. This decision was based on the observation that no significant differences were found between the diffraction patterns at 400°C and 500°C. This adjustment allowed us to dedicate more time to collecting high-quality data up to 800°C and to focus on the 600°C to 700°C range, where significant transformations in HA crystallization occur.

Our goal was to carry out a full Rietveld refinement of the heat-treated crystal structure of biological HA, spotting any differences between healthy and osteoporotic samples, which could identify structural changes mostly related to crystallinity (crystal size and strain) and to diverse carbonate and phosphate substitutions. These parameters are also known to be interconnected, since literature data show an inversely related linear relationship between carbonation and crystallinity [10].

Neutron diffraction patterns were analyzed using LeBail analysis and Rietveld refinement using the GSAS-1 software [11,12]. LeBail analysis extracted diffraction intensities without adopting a structural model, allowing for the refinement of lattice parameters, and peak shapes as a preparatory step for the subsequent structural analysis. Rietveld refinement fitted the entire diffraction pattern to a structural model, enabling the determination of atomic positions, thermal parameters, and site occupancies.

All neutron experiments were performed within the 7th Framework Program of the European Union: Access Activities of the Integrated Infrastructure Initiative for Neutron Scattering and Muon Spectroscopy (NMI3); European Commission, French Atomic Energy Commission (Commissariat à l'énergie atomique), CEA-CNRS, Saclay, Paris, France.

6.3. Preprocessing and analysis of Raman spectra

The PyFasma Python package, developed as part of this thesis (details in Chapter 6), was used for preprocessing and analyzing Raman spectra. The spectra were collected as SPC files and organized in a hierarchical directory structure:

```
/type/skeletal_site/animal_ID/bone_slice/spectrum.SPC
```

- `type`: “transverse” or “surface”
- `skeletal_site`: “tibia,” “humerus,” “femur,” or “ribs”
- `animal_ID`: unique identifier for each animal
- `bone_slice`: bone slice from which spectra were obtained
- `spectrum.SPC`: unique spectrum file, incorporating identifiers from the directory path.

The spectra were first converted to CSV using PyFasma’s `fileio.spc2csv` function. CSV files from each type and skeletal site were then loaded as pandas DataFrames with the `fileio.load_csvs` function, interpolated to a common Raman shift axis, and merged into a single CSV file using `fileio.merge_CSV`.

The merged spectra were preprocessed through the following steps (details of PyFasma code in Chapter 6, Section 6.2.3):

1. Initial crop to the range 100—2400 cm^{-1}. This crop removed the Rayleigh line, the steeply increasing spectral region after that, and the high-wavenumber region of the spectra which was not used in our analysis. Cropping to this region also improves the application of the baseline correction algorithm, as steep changes of the background can cause deviations to the background estimation.
2. Removal of both positive and negative spikes which could arise as detector artifacts, cosmic rays, etc.
3. Smoothing using a Savitzky-Golay filter with a 17 points window and a 3rd degree polynomial to remove noise and improve the signal-to-noise ratio (SNR).
4. Baseline-correction using the SNIP algorithm in a decreasing manner with a `max_half_window` parameter of 20.
5. Normalization to the intensity of the main phosphate peak at 960 cm^{-1}.
6. Final crop to the fingerprint region (400—1800 cm^{-1}).

Fig. 6.6 illustrates an example of a raw Raman spectrum, alongside its denoised (smoothed and despiked) version and baseline estimation.

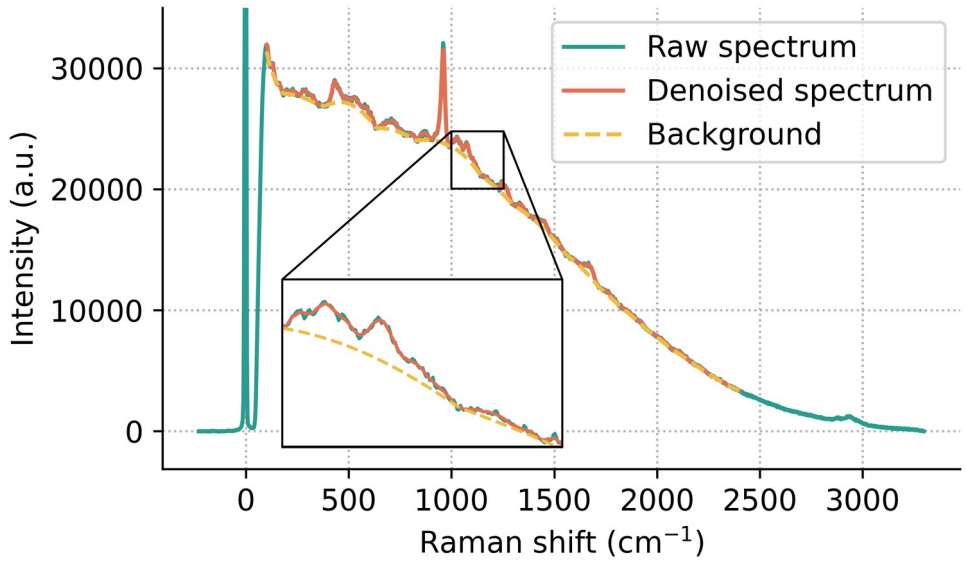

Figure 6.6: Typical raw Raman spectrum of bone overlayed by the denoised (despiked and smoothed) spectrum. The dashed line is the baseline estimation using the SNIP algorithm. The inset shows a more detailed view of the denoised spectrum and the baseline estimation in the 990—1230 cm^{-1} region.

The resulting preprocessed spectrum is shown in Fig. 6.7.

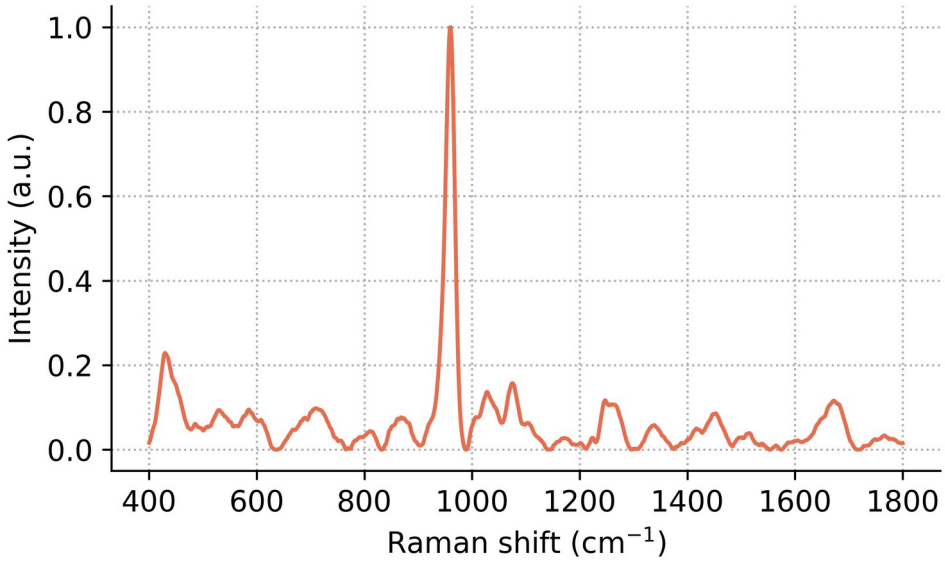

Figure 6.7: Typical preprocessed Raman spectrum of bone.

Following preprocessing, multivariate statistical analyses were performed. Principal Component Analysis (PCA) was applied using PyFasma's `modeling.PCA` class to explore data patterns. Partial Least Squares Discriminant Analysis (PLS-DA) was performed via `modeling.PLSDA` to develop predictive models distinguishing healthy and osteoporotic samples.

To further assess bone quality, Raman bands from the transverse surface spectra were deconvoluted into Gaussian components. The number and initial positions of Gaussian peaks were based on literature, second-derivative analysis of mean spectra, and spectral region characteristics. Bounds of ±2 cm^{-1} were applied to peak positions to allow small variations while ensuring meaningful results. Initial guesses for peak heights and full widths at half maxima (FWHM) were determined through trial-and-error and literature references, with bounds selected to maintain result validity. These deconvolutions enabled the calculation of bone-quality-related ratios, providing additional insights into the molecular composition of healthy and osteoporotic bone.

6.4. References

[1] Kourkoumelis N, Lani A, Tzaphlidou M. Infrared spectroscopic assessment of the inflammation-mediated osteoporosis (IMO) model applied to rabbit bone. J Biol Phys 2012;38:623–35. https://doi.org/10.1007/s10867-012-9276-6.

[2] Kourkoumelis N, Balatsoukas I, Tzaphlidou M. Ca/P concentration ratio at different sites of normal and osteoporotic rabbit bones evaluated by Auger and energy dispersive X-ray spectroscopy. J Biol Phys 2011;38:279. https://doi.org/10.1007/s10867-011-9247-3.
[3] Lani A, Kourkoumelis N, Baliouskas G, Tzaphlidou M. The effect of calcium and vitamin D supplementation on osteoporotic rabbit bones studied by vibrational spectroscopy. J Biol Phys 2014;40:401–12. https://doi.org/10.1007/s10867-014-9358-8.
[4] Armour KJ, Armour KE. Inflammation-Induced Osteoporosis: The IMO Model. Bone Res. Protoc., vol. 80, New Jersey: Humana Press; 2003, p. 353–60. https://doi.org/10.1385/1-59259-366-6:353.
[5] Andreassen H, Rungby J, Dahlerup JF, Mosekilde L. Inflammatory Bowel Disease and Osteoporosis. Scand J Gastroenterol 1997;32:1247–55. https://doi.org/10.3109/00365529709028155.
[6] Oelzner P, Müller A, Deschner F, Hüller M, Abendroth K, Hein G, et al. Relationship Between Disease Activity and Serum Levels of Vitamin D Metabolites and PTH in Rheumatoid Arthritis. Calcif Tissue Int 1998;62:193–8. https://doi.org/10.1007/s002239900416.
[7] Tanaka Y, Nakayamada S, Okada Y. Osteoblasts and osteoclasts in bone remodeling and inflammation. Curr Drug Targets Inflamm Allergy 2005;4:325–8. https://doi.org/10.2174/1568010054022015.
[8] Jee WS, Yao W. Overview: animal models of osteopenia and osteoporosis. J Musculoskelet Neuronal Interact 2001;1:193–207.
[9] Catanese III J, Featherstone JDB, Keaveny TM. Characterization of the mechanical and ultrastructural properties of heat-treated cortical bone for use as a bone substitute. J Biomed Mater Res 1999;45:327–36. https://doi.org/10.1002/(SICI)1097-4636(19990615)45:4<327::AID-JBM7>3.0.CO;2-L.
[10] Kourkoumelis N, Tzaphlidou M. Multivariate statistical evaluation of bone site and sex as parameters for the Fourier transform infrared spectroscopic study of normal bone. Spectroscopy 2010;24:99–104. https://doi.org/10.1155/2010/317263.
[11] Larson AC, Von Dreele RB. General Structure Analysis System (GSAS). Los Alamos National Laboratory; 2000.
[12] Toby BH. EXPGUI, a graphical user interface for GSAS. J Appl Crystallogr 2001;34:210–3. https://doi.org/10.1107/S0021889801002242.
[13] Barone R. Atlas d'anatomie du lapin.: Atlas of rabbit anatomy. Paris: Masson; 1973.

7. PyFasma – Software development

7.1. Introduction

Raman spectroscopy is an analytical technique used to investigate molecular vibrations and chemical compositions in a variety of materials, including biological tissues such as bone. However, the complexity of Raman spectra, combined with the challenges of preprocessing and analyzing large datasets, necessitates specialized tools tailored to specific research requirements.

Although numerous software tools for preprocessing and analysis exist, they are either closed-source and/or very expensive for many researchers, or require high-level knowledge of programming [1–6]. Closed-source software often lacks transparency in the methods applied, making it difficult to validate and reproduce results, which are critical aspects of scientific research. Moreover, many existing tools do not include preprocessing functionalities, necessitating the use of multiple software solutions for a complete analysis. This fragmented workflow increases the complexity of data analysis, introduces interoperability challenges, and risks inconsistencies that can complicate the interpretation of results.

In addition, while graphical user interface (GUI) software may seem more accessible to users, it often falls short when handling large datasets typical of Raman experiments. The reliance on repetitive actions, such as clicking through menus, can quickly become tedious and inefficient. These limitations make GUI-based tools impractical for high-throughput workflows, where automation and reproducibility are essential to avoid errors and ensure consistent results. In this context, there is a consistent need for a new, open-source, user-friendly but powerful preprocessing tool for Raman spectroscopy. A solution that integrates a command-line interface and a Jupyter Notebook framework could significantly enhance accessibility and usability by allowing users to customize and automate preprocessing steps within a standard, well-known,

interactive environment [7]. Additionally, the integration of a Jupyter Notebook interface would make it easier for users to document, share, and reproduce their workflows, enhancing both the transparency and reproducibility of Raman spectral analyses.

To address these limitations, a dedicated open-source Python package, named PyFasma, was developed as part of this thesis [8]. The name derives from the Latinized text of the Greek word “φάσμα” (fasma), meaning “spectrum.” PyFasma is designed to streamline the preprocessing and analysis of Raman spectra by providing robust and reproducible workflows for spectral data manipulation. With its modular architecture, the package integrates preprocessing tools, advanced analytical methods, and visualization capabilities, enabling users to efficiently derive meaningful insights from raw spectral data. Furthermore, all functions, classes, and methods in PyFasma are self-documented using Python docstrings, making the package transparent, user-friendly, and easier to adopt, even for those with limited programming experience.

While the functions, classes, and methods of PyFasma can be incorporated into Python scripts, the package’s true potential is realized when used interactively in a Jupyter Notebook environment. This interactivity is particularly advantageous for spectroscopy, as it facilitates iterative adjustments, such as selecting the optimal smoothing window for data through a trial-and-error process. This dynamic approach enables researchers to refine parameters and achieve optimal results with minimal effort.

The package has already been successfully applied in a variety of Raman spectroscopy studies. These include augmenting Raman data using Generative Adversarial Networks (GANs) [9], exploring the potential of spatially-offset Raman spectroscopy (SORS) for non-melanoma cancer diagnosis [10], and characterizing and differentiating *Candida auris* from other *Candida* species [11]. Although PyFasma was developed with Raman spectroscopy in mind, its versatility has extended to other spectroscopic techniques, as it was successfully utilized in a study to discriminate the salivary profiles of athletes using ATR-FTIR spectroscopy [12].

7.2. PyFasma package overview

PyFasma is a free and open-source Python package, licensed under the GNU General Public License (GPL), that offers a high level programming interface, providing users with all the necessary tools to preprocess Raman spectra and deconvolute complex Raman bands, apply Principal Components Analysis (PCA) and Partial Least Squares Discriminant Analysis (PLS-DA) to Raman data, and create publication-ready plots. The goal is to assist spectroscopists in exploring and analyzing Raman data in a streamlined and intuitive way, without requiring expert knowledge of Python (though such knowledge is always beneficial), allowing them to focus more on data interpretation rather than programming.

The package is developed for Python 3.12 and later versions and depends on several well-established scientific Python packages: LMFIT [13], Matplotlib [14], NumPy [15], pandas [16],

pybaselines [17], Seaborn [18], SciPy [19], scikit-learn [20], and Rohan Isaac's (rohanisaac) spc module [21]. PyFasma can be installed by following the instructions provided in the project's GitHub repository [22].

The central data structure that PyFasma works with is the pandas DataFrame, which has been extended to include additional spectroscopy-specific manipulation capabilities. DataFrames were chosen for their versatility and powerful functions for advanced data inspection and manipulation. Although pandas DataFrames may lack the speed and memory efficiency of performance-oriented structures like NumPy arrays, they excel in exploratory data analysis and interactivity, especially in Jupyter Notebooks, where iterative workflows are common.

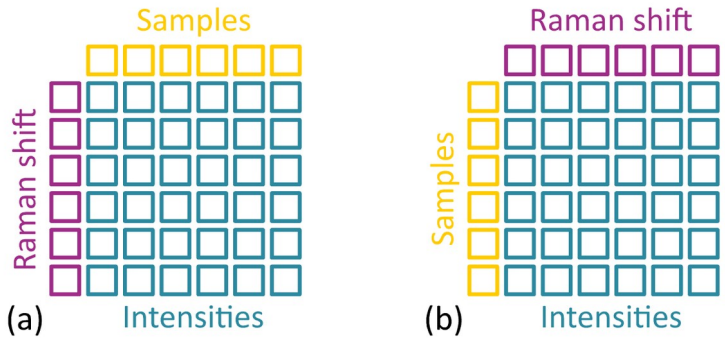

Figure 7.1: The pandas DataFrame is the central data structure in PyFasma. Two DataFrame formats are utilized: (a) A generic format with shape `(n_features, n_samples)` *used in most functions, and (b) a specific format with shape* `(n_samples, n_features)` *required by the modeling module to ensure compatibility and consistent workflows with scikit-learn. In the context of Raman spectroscopy,* `n_features` *represents the Raman shift and* `n_samples` *the samples.*

PyFasma consists of seven modules, namely: `helpers`, `fileio`, `numpyfuncs`, `dffuncs`, `plotting`, `modeling`, and `deconvolution`. Each of these modules addresses specific aspects of Raman spectroscopy workflows, creating a modular and cohesive system designed to meet the diverse needs of Raman spectroscopists. A graphical overview of the PyFasma package along with brief descriptions of its modules is presented in Fig. 7.2.

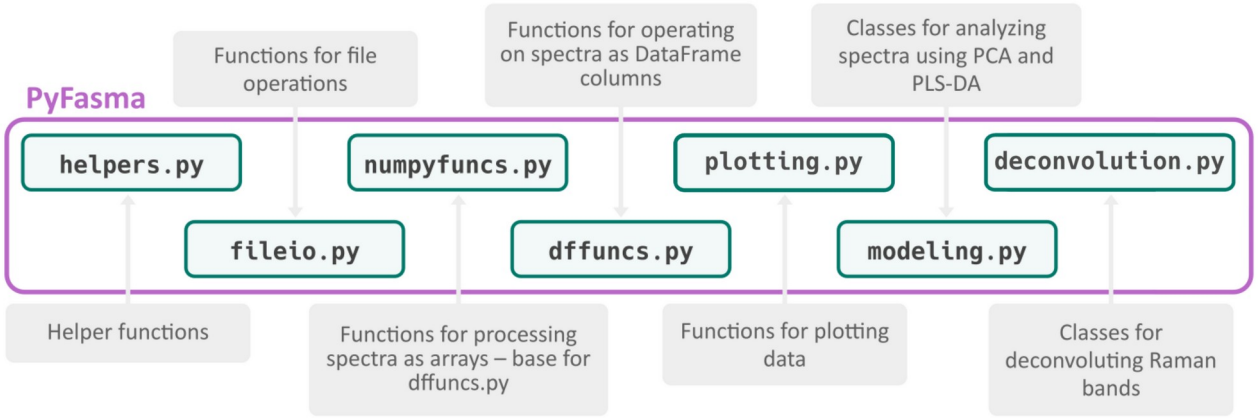

Figure 7.2: Graphical overview of the PyFasma package.

7.2.1. The `helpers` module

The `helpers` module, as its name suggests, contains utility functions designed to support the functionality of other modules in PyFasma. While these functions are accessible to end users, they are primarily intended for internal use and are not typically required in standard workflows. Since the module's role is auxiliary and its functions do not directly contribute to the main workflows or analytical processes of PyFasma, a detailed analysis of this module falls outside the scope of this thesis.

7.2.2. The `fileio` module

The `fileio` module in PyFasma provides functionality for efficiently handling spectroscopy data files, focusing on batch processing and format conversion. Its primary aim is to streamline the import, conversion, and merging of spectral data, ensuring compatibility with pandas DataFrames, the central data structure used in the package.

The module includes functions for loading (`load_csvs`) and merging (`merge_csvs`) multiple CSV (comma-separated values) files from a specified directory and its subdirectories. Users can filter files and directories to include or exclude based on their requirements. The loaded files are returned as pandas DataFrames, which can then be seamlessly integrated into PyFasma workflows. Additionally, the module supports merging multiple DataFrames into a single DataFrame, with options for data interpolation and customizable column labels.

The `fileio` module also enables batch conversion of SPC files, a proprietary file format supported by Thermo Scientific and widely used for storing spectroscopic data [23], into CSV format using the `spc2csv` function. This format is popular in Raman spectroscopy due to its efficiency in handling complex spectral data, making it a standard in many workflows. The conversion functionality

preserves directory structures if desired, offering flexibility in organizing and managing converted data. Users can preview conversion results before applying changes, minimizing the risk of errors. The process is highly customizable, allowing adjustments to delimiters and newline characters in the output CSV files.

7.2.3. The `numpyfuncs` and `dffuncs` modules

The `numpyfuncs` and `dffuncs` modules are designed to work in tandem within PyFasma, forming a comprehensive toolkit for preprocessing and analyzing Raman spectral data. Together, these modules enable efficient, reproducible, and flexible workflows by integrating low-level computational functions with high-level, DataFrame-based implementations tailored specifically for spectroscopy tasks.

The `numpyfuncs` module provides foundational methods for processing one-dimensional spectral data using NumPy arrays, ensuring computational efficiency. While these functions can operate independently on individual arrays, they primarily serve as the underlying framework for the `dffuncs` module, which extends their functionality to pandas DataFrames and Series. Advanced users can directly utilize these functions to customize or adapt them to specific needs.

The `dffuncs` module introduces the `.pyfasma` accessor, enabling users to seamlessly apply preprocessing and analytical operations directly to columns of a DataFrame. In this framework, the DataFrame should have the shape (`n_features`, `n_samples`), with the index representing Raman shifts and the columns containing intensity values for individual samples, as illustrated in Fig. 7.1(a). Using the `.pyfasma` accessor, PyFasma methods follow the general syntax `df.pyfasma.<method>`, where `df` is the DataFrame containing the spectral data, and `<method>` is the desired PyFasma method.

The functionalities provided by these modules include preprocessing and analysis methods, summarized as follows:

- Despiking (`despike` method): Removes positive, negative, or both types of spikes in spectra using a custom algorithm based on SciPy's `signal.find_peaks` function.
- Smoothing (`smooth` method): Applies filters such as Savitzky-Golay, moving average, and Gaussian to reduce noise and improve the signal-to-noise ratio.
- Baseline correction (`baseline_correct` method): Implements efficient algorithms like Improved Modified Polynomial (ImodPoly) [24], Statistics-sensitive Non-linear Iterative Peak-clipping (SNIP) [25], and Adaptive Iteratively Reweighted Penalized Least Squares (airPLS), provided by the pybaselines package.
- Normalization (`normalize` method): Offers several normalization techniques, including peak intensity normalization, integrated area normalization, L1 and L2 norms (also known

as Manhattan and Euclidean norms, respectively), min-max scaling, and mean absolute deviation (MAD).

- Cropping (`crop` method): Trims spectra to specified Raman shift ranges.
- Interpolation (`interpolate` method): Aligns spectra to uniform Raman shift grids using linear or cubic interpolation.
- Integration (`integrate` method): Computes the area under the spectral curve for defined regions using Simpson's rule [26].
- Differentiation (`differentiate` method): Calculates derivatives of arbitrary order, with optional smoothing.

These functionalities allow researchers to streamline data preparation and analysis, supporting both exploratory and automated workflows.

Both modules include built-in validation to ensure input data compatibility, such as checking that indices are numerical and monotonic, and that all values are numerical and non-null. This reduces the potential for errors and enhances reproducibility in Raman spectroscopy workflows.

By integrating `numpyfuncs` and `dffuncs`, PyFasma ensures modularity and flexibility. While `numpyfuncs` handles core computational operations efficiently, `dffuncs` offers an intuitive, high-level interface tailored for spectroscopy. Together, they provide a robust foundation for processing and analyzing Raman spectral data in PyFasma.

An example preprocessing pipeline, which is actually the one used to preprocess the Raman spectra is shown in Fig. 7.3.

```
import pyfasma.dffuncs as dff

data_df = pd.read_csv(...)

# initial crop
df_cropped = data_df.pyfasma.crop(xrange=[100, 2400])
# removal of positive and negative spikes larger than threshold
df_despiked = df_cropped.pyfasma.despike(threshold=1000)
# smoothing using Savitzky-Golay filter
df_smoothed = df_despiked.pyfasma.smooth([17, 3], kind='savgol')
# baseline correction using SNIP
df_baselined = df_smoothed.pyfasma.baseline_correct(kind='snip',
    decreasing=True, max_half_window=20)
# normalization to the maximum between 950 and 970 cm-1
df_normalized = df_baselined.pyfasma.normalize(kind='intensity',
    xrange=[950, 970])
# final crop to fingerprint region
df = df_normalized.pyfasma.crop(xrange=[400, 1800])
```

Figure 7.3: Pipeline used for preprocessing Raman spectra in a pandas DataFrame (data_df) using PyFasma.

7.2.4. The `modeling` module

The modeling module provides two classes for multivariate analysis: one for Principal Component Analysis (PCA) and another for Partial Least Squares Discriminant Analysis (PLS-DA). The PCA implementation is based on scikit-learn's `decomposition.PCA` class, while the PLS-DA implementation utilizes scikit-learn's `cross_decomposition.PLSRegression` class. To maintain consistency with scikit-learn, the input DataFrames for these classes must follow the format shown in Fig. 1(b), where rows correspond to sample intensity values and columns represent Raman shifts, resulting in a shape of `(n_samples, n_features)`.

Both classes offer flexible sample group assignments through the `hue` parameter, which accepts a list of strings representing sample group labels. This feature allows group definitions to be created either manually or dynamically using list comprehensions with conditional statements, as long as group identifiers can be derived from the sample names.

The module enhances usability by presenting all analysis results as pandas DataFrames and supporting commonly used visualizations, such as scores and loadings plots. These visualizations leverage the plotting module, with essential parameters exposed through keyword arguments for customization. Moreover, all plots return Matplotlib `Figure` and `Axes` objects, enabling users to further adjust them using Matplotlib's object-oriented API.

Principal Component Analysis (PCA)

Principal Component Analysis (PCA) is an unsupervised technique widely used in spectral data analysis for dimensionality reduction and other applications. As an unsupervised method, PCA operates without requiring labeled data, instead focusing on the relationships between variables in the dataset. Although often associated with dimensionality reduction, PCA is also frequently employed for trend identification, visualization of high-dimensional datasets, and filtering noise.

PCA works by calculating the covariance matrix of the data to quantify relationships between variables and projecting the dataset onto a new set of orthogonal axes, known as Principal Components (PCs). Each PC maximizes the variance it explains while remaining orthogonal to the previous ones. PCs are linear combinations of the original variables, with the coefficients of these combinations referred to as loadings. The projections of the original data points onto the PCs are called scores. The PCs are ranked by the variance they explain, with the first PC capturing the greatest variance, the second capturing the next highest variance, and so on.

In mathematical terms, the original dataset D of shape $n \times m$, where n is the number of samples and m is the number of features, is decomposed into matrices S and L such that [27]:

$$D = S L^T \tag{7.1}$$

where S is the $n \times p$ scores matrix that contains the projections of the samples onto the principal components, and L^T is the $p \times m$ loadings matrix that contains the weights (loadings) for each component.

(a)

```
import pyfasma.modeling as mdl

sample_class = ["Healthy" if "Rbhf" in col else "Osteoporotic" for col in df_final.columns]
pca = mdl.PCA(df_final.T, n_components=10, hue=sample_class)
```

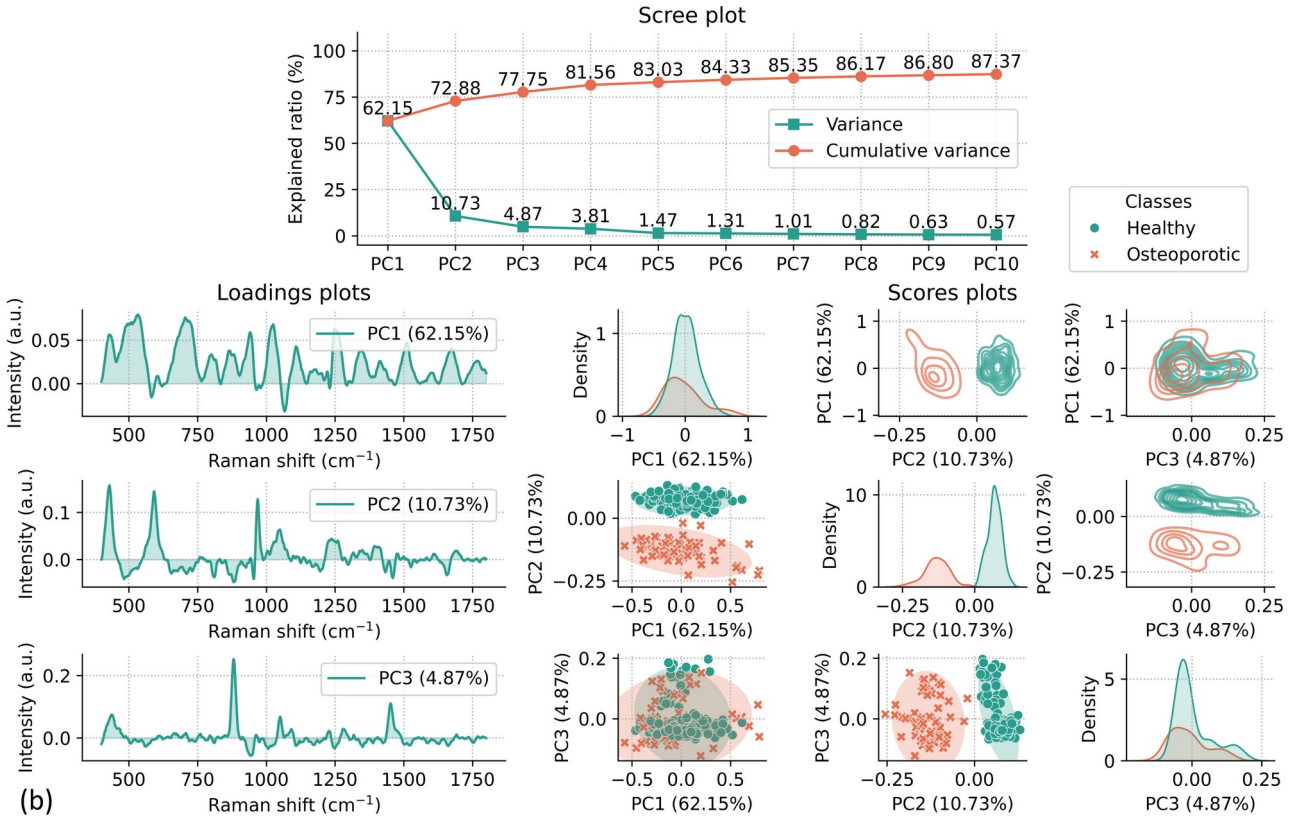

Figure 7.4: (a) PyFasma code required to create a PCA model with 10 components with PyFasma. (b) Summary plot containing a scree plot and loadings plots, scores plots (as scatter plots in the lower diagonal and as densities in the upper diagonal), and Kernel Density Estimate (KDE) plots (diagonal) for the first three PCs. The ellipses in the scores plots are the 95% covariance ellipses.

To perform PCA using PyFasma, users first import the `PCA` class from the `modeling` module. The class is initialized with a pandas DataFrame structured as shown in Fig. 7.2, and a `hue` list containing class labels for the samples, which are used to color-code the visualizations appropriately. By default, upon initialization, the class generates a summary plot. This plot includes a scree plot, displaying the explained variance and cumulative explained variance as functions of the PCs, which helps determine the optimal number of PCs to retain for dimensionality reduction. Additionally, it provides loadings plots, scores plots, and Kernel Density Estimate (KDE) plots for the

first three PCs. The initialized object provides access to class methods, including scores and loadings DataFrames, visualizations, and more.

The code required to create a PCA model for the Raman data obtained from the transverse surfaces of the healthy and osteoporotic tibias is shown in Fig. 7.4(a) and the resulting summary plot is shown in Fig. 7.4(b).

Partial Least Squares Discriminant Analysis (PLS-DA)

Partial Least Squares Discriminant Analysis (PLS-DA) is a supervised statistical technique adapted from Partial Least Squares Regression (PLSR) [28,29]. While PLSR is primarily used for predicting continuous outcomes, PLS-DA extends this methodology to the classification of categorical data represented numerically. In addition to classification, PLS-DA is also used for dimensionality reduction, trend identification, and feature selection in chemometrics and biomedical sciences [30–33].

PLS-DA constructs a linear model that maximizes the covariance between the X matrix of independent variables (e.g., Raman intensities) and the Y matrix of dependent variables (e.g., class labels). It identifies latent variables (LVs), which are linear combinations of the original variables, capturing significant variation and enabling class differentiation. The X and Y matrices are decomposed as follows:

$$X = T\,P^T + E \tag{7.2}$$

and

$$Y = U\,Q^T + F \tag{7.3}$$

where T and U are the scores matrices, P and Q are the loadings matrices, and E and F are the residual matrices. These scores and loadings provide insights into the contributions of variables and samples to the classification process.

Before applying PLS-DA, the dataset must be split into training and testing subsets. A 70/30 train/test split is commonly used in Raman spectroscopy datasets. The PLS-DA implementation of PyFasma requires the categorical class labels in the Y matrix to be transformed into a binary (one-hot encoded) representation to ensure compatibility with the algorithm. PyFasma automates this process using scikit-learn's `preprocessing.label_binarize` method. For instance, in a binary classification problem (e.g., "Healthy" and "Osteoporotic") where the Y matrix contains the classes corresponding to samples as strings in a list:

$$Y = [\text{Healthy}, \text{Healthy}, \text{Osteoporotic}, \text{Healthy}, \text{Osteoporotic}, \ldots] \tag{7.4}$$

the classes are encoded internally as:

$$Y = \begin{bmatrix} 1 & 0 \\ 1 & 0 \\ 0 & 1 \\ 1 & 0 \\ 0 & 1 \\ \vdots & \vdots \end{bmatrix} \tag{7.5}$$

Essential for evaluating the performance of a model and determining its generalizability is the technique of cross-validation [34]. A frequently used cross-validation method is k-fold cross-validation, in which the dataset is divided into k equal-sized subsets (folds) (Fig. 7.5). Each fold serves as a validation set once, while the remaining $k-1$ folds are used for training. This process is repeated k times, ensuring that each subset is used for validation exactly once. The performance metrics are calculated for each fold and then averaged to provide a robust estimate of the model's performance. Repeated k-fold cross-validation further enhances robustness by performing multiple rounds of cross-validation with different data splits. To address class imbalances in classification tasks, stratified k-fold cross-validation can be used, ensuring that each fold maintains the same class distribution as the original dataset. This stratification is crucial when working with imbalanced datasets to prevent biased evaluation metrics.

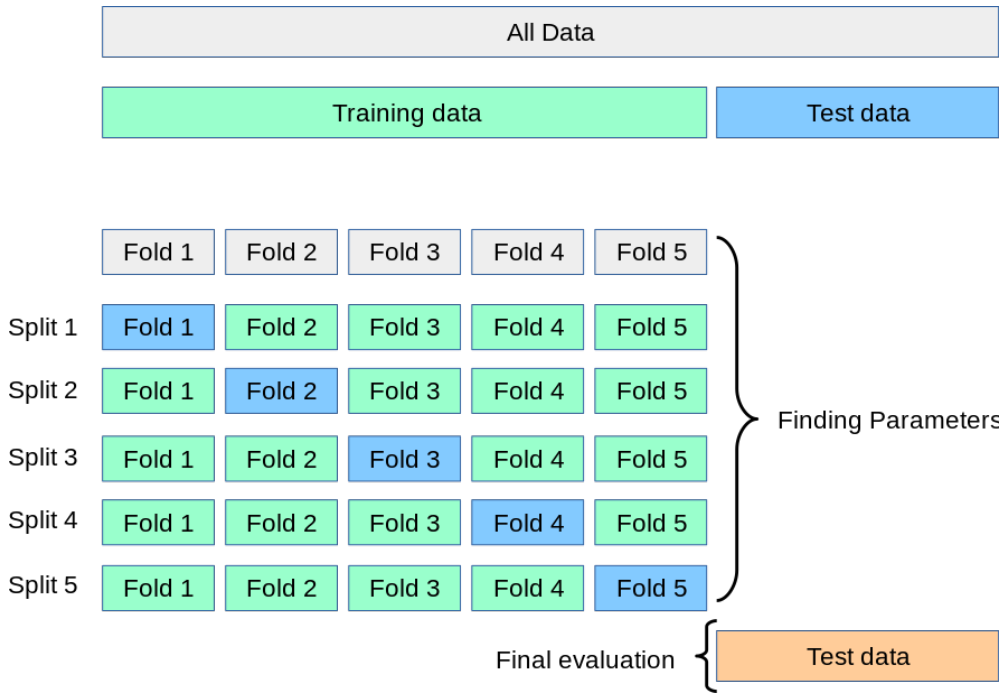

Figure 7.5: Illustration of k-fold cross-validation. The initial data are split to training and test, and the training data are split to k-folds (here 5). Each fold of the train data is used for validating/testing the model while the rest are used for training the model k times, each time using a different fold. Figure from [40].

Determining the optimal number of components is critical to avoid overfitting or underfitting the model. PyFasma simplifies this process by incorporating repeated stratified k-fold cross-validation. When the `PLSDA` class is initialized with the training (`x_train`, `y_train`) and testing (`x_test`, `y_test`) datasets, `cross_val=True`, and the number of components (n_components) for cross-validation, it performs cross-validation with the default parameters (repeated stratified 5-fold cross-validation). This process generates an evaluation metrics plot that assists in identifying the optimal number of components for the predictive model. The plot includes the following metrics accuracy, R^2, Q^2, and mean squared error (MSE). What these metrics represent and how they are calculated are detailed below [32,35]:

- Accuracy: The proportion of correctly classified samples, given by:

$$Accuracy = \frac{TP + TN}{TP + TN + FP + FN} \tag{7.6}$$

- R^2: The proportion of variance in the Y matrix explained by the model, given by:

$$R^2 = 1 - \frac{\sum (Y_{true} - Y_{pred})^2}{\sum (Y_{true} - \bar{Y})^2} \tag{7.7}$$

where Y_{true} are the actual class labels, Y_{pred} are the predicted labels, and $\bar{Y}$ is the mean of Y_{true}.

- Q^2: The predictive power of the model during cross-validation. It is computed similarly to R^2 but on the test data within each fold:

$$Q^2 = 1 - \frac{\sum (Y_{test} - Y_{test,pred})^2}{\sum (Y_{test} - \bar{Y}_{test})^2} \tag{7.8}$$

where Y_{test} are the test labels in each fold.

- MSE: The average squared difference between predicted and actual values, given by:

$$MSE = \frac{1}{n} \sum (Y_{true} - Y_{pred})^2 \tag{7.9}$$

The code for performing repeated stratified 5-fold cross-validation with 10 repeats, used to calculate evaluation metrics for selecting the optimal number of components for PLS-DA applied to Raman spectral data from healthy and osteoporotic tibias (after a 70/30 train/test split), is presented in Fig. 7.6(a). A bend (or “knee”) or peak at a specific number of components is often the indication of the optimal number. Fig. 7.6(b) suggests that the optimal number of components is 2.

(a)

```
pls = mdl.PLSDA(x_train, x_test, y_train, y_test,
    cross_val=True, n_components=10, stratify=True,
    n_splits=5, n_repeats=10)
```

(b)

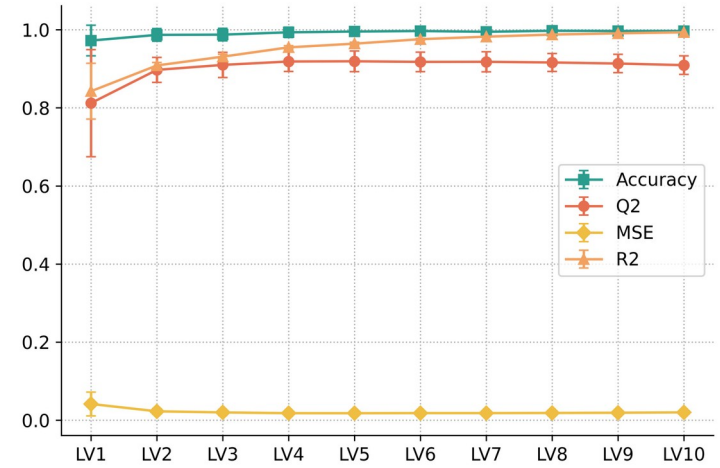

Figure 7.6: (a) PyFasma code required to perform a epeated stratified 5-fold cross-validation with 10 repeats to calculate the evaluation metrics for the PLS-DA model. (b) Evaluation metrics plot. The bend for LV2 suggests that the optimal number of components for this model should be 2.

Once the optimal number of components is determined through cross-validation, the PLSDA class is initialized with the training and testing datasets, setting `cross_val=False` and specifying the optimal number of components using the `n_components` parameter. During initialization, the class computes the PLS model with the specified number of components and provides access to tools for further analysis. Users can generate various visualizations, including X-scores and Y-scores plots, a confusion matrix, and performance metrics, to evaluate the model.

The X-scores plot visualizes the distribution of samples in the latent variable space derived from the predictor variables, helping to assess the separation between classes based on the independent variables. Similarly, the Y-scores plot shows the distribution of samples in the latent variable space derived from the response variables, providing insights into how the dependent variable drives class differentiation.

The confusion matrix provides a detailed breakdown of the model's classification performance, displaying the number of true positives (TP, correctly predicted samples belonging to the positive class), true negatives (TN, correctly predicted samples not belonging to the positive class), false positives (FP, incorrectly predicted samples as belonging to the positive class), and false negatives (FN, incorrectly predicted samples as not belonging to the positive class). For binary classification, the confusion matrix is a 2×2 matrix of the form shown in Fig. 7.7:

		Predicted condition	
	Total population = P + N	Positive (PP)	Negative (PN)
Actual condition	Positive (P)	True positive (TP)	False negative (FN)
	Negative (N)	False positive (FP)	True negative (TN)

Figure 7.7: Generic form of confusion matrix for binary classification. Figure from [41].

Besides accuracy (Eq. 7.6), the following metrics, calculated from these values and provided as a DataFrame, are used to assess the model's performance [36]:

- Precision: The proportion of true positive predictions out of all positive predictions, indicating the model's ability to avoid false positives:

$$Precision = \frac{TP}{TP + FP} \tag{7.10}$$

- Recall (Sensitivity): The proportion of true positives identified out of all actual positives, reflecting the model's ability to detect the target class:

$$Recall = \frac{TP}{TP + FN} \tag{7.11}$$

- Specificity: The proportion of true negatives out of all actual negatives, representing the model's ability to exclude non-target classes:

$$Specificity = \frac{TN}{TN + FP} \tag{7.12}$$

- F1 Score: The harmonic mean of precision and recall, balancing the trade-off between the two metrics:

$$F1\,score = \frac{2\,TP}{2\,TP + FP + FN} \tag{7.13}$$

The code for applying PLS-DA to Raman spectral data obtained from healthy and osteoporotic tibias after a 70/30 train/test split is shown in Fig. 7.8(a). The visual outputs, including X-scores and Y-scores plots, and a confusion matrix are shown in Fig. 7.8(b–d). These plots reveal the latent variable space, highlight class separation, and provide insights into the model's predictive capabilities.

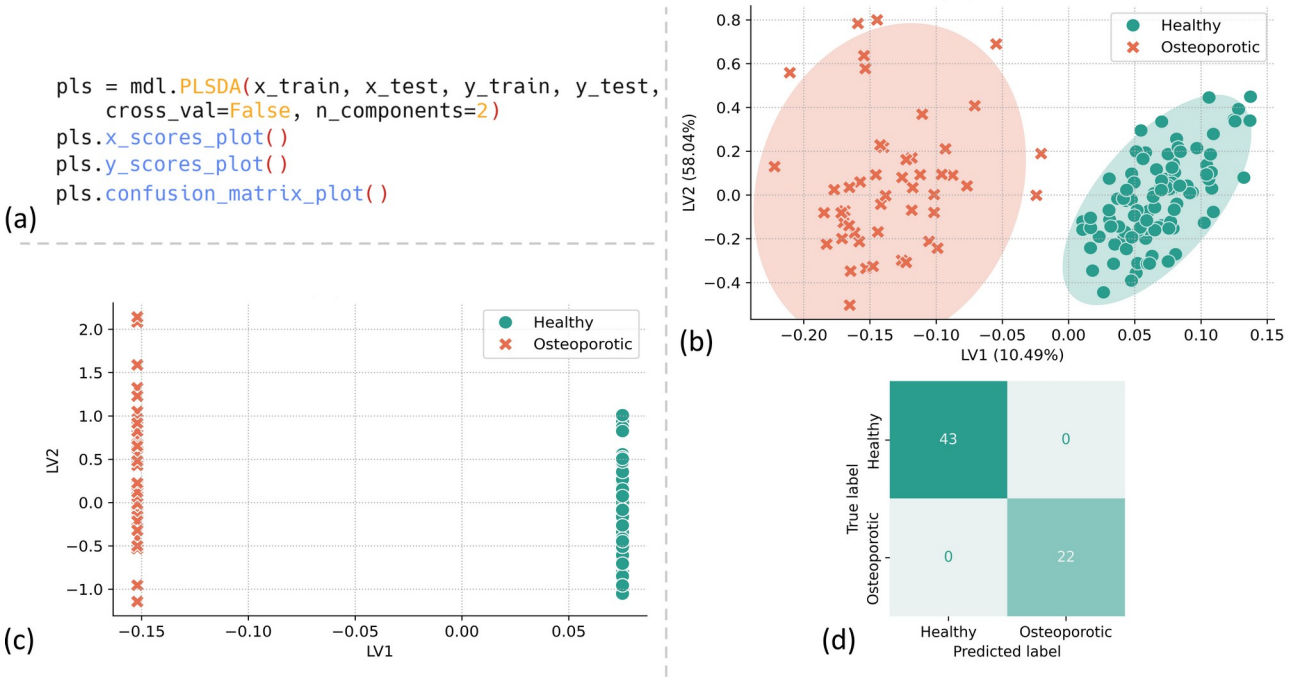

Figure 7.8: (a) PyFasma code pipeline required to create: a PLSDA model with two components, an X- and Y-scores plot for the training data, and a confusion matrix for the predictive model. (b) X-scores plot for the training data. (c) Y-scores plot for the training data. (d) Confusion matrix for the evaluation of the predictive model.

7.2.5. The `deconvolution` module

The `deconvolution` module in PyFasma is designed for fitting and deconvoluting complex Raman spectral bands and makes use of the LMFIT package. It offers three customizable multi-curve models: Gaussian, Lorentzian, and Voigt, implemented as independent classes. These models enable the resolution of overlapping spectral features, critical for detailed Raman spectroscopy analysis.

Unlike LMFIT's default implementation, PyFasma uses peak heights (intensities) and Full Widths at Half Maxima (FWHM) as fitting parameters instead of amplitudes (areas under curves) and sigmas/gammas (peak widths). This makes the module more intuitive and aligned with spectroscopic contexts, as peak heights and FWHMs are easier to estimate visually and conceptually. The input parameters for the model are provided as a list of dictionaries, each

representing a single curve. These dictionaries specify the initial guesses and optional bounds or constraints for the curve parameters. For example, initializing a multi-Gaussian model for fitting two overlapping peaks might involve parameter definitions as shown in Fig. 7.9.

```
data = pd.DataFrame(...)
params_list = [
    {"height": 10, "center": 5, "fwhm": 1},
    {"height": {"value": 8, "min": 5, "max": 15},
     "center": 10,
     "fwhm": 2},
]
fit = FitGaussian(data, params_list)
```

Figure 7.9: Example code for creating a model for fitting two Gaussian curves to the data.

PyFasma implements three fitting models, a Gaussian model, accessible through the `FitGaussian` class, a Lorentzian model, accessible through the `FitLorentzian` class, and a Voigt model, accessible through the `FitVoigt` class.

A Gaussian curve is suitable for symmetric peaks and is defined by the equation [37]:

$$G(x) = A \exp\left(-\frac{(x-\mu)^2}{2\sigma^2}\right) \tag{7.14}$$

with $A = H\,\sigma\sqrt{2\pi}$ being the amplitude, H the height of the curve, $\sigma = \frac{FWHM}{2\sqrt{(2\log(2))}}$ the standard deviation of the curve, and μ the center of the curve.

A Lorentzian curve is common for natural linewidths and is defined by the equation [38]:

$$L(x) = \frac{A}{\pi\gamma\left[1+\left(\frac{x-\mu}{\gamma}\right)^2\right]} \tag{7.15}$$

with $A = H\,\pi\,\gamma$ being the amplitude, H the height of the curve, $\gamma = \frac{FWHM}{2}$ the half width at half maximum (HWHM) of the curve, and μ the center of the curve.

A Voigt curve is given by the convolution of a Gaussian and a Lorentzian function and is suitable for asymmetric or mixed peaks. The Voigt curve is represented as [39]:

$$V(x)=\frac{A\,\mathrm{Re}[w(z)]}{\sigma\sqrt{2\pi}} \tag{7.16}$$

with $A=\frac{H\sigma\sqrt{2\pi}}{\mathrm{Re}\left(w\left(\frac{i\gamma}{\sigma\sqrt{2}}\right)\right)}$ being the amplitude, H the height of the curve, $\sigma=\frac{FWHM_{Gaussian}}{2\sqrt{(2\log(2))}}$ the standard deviation of the Gaussian curve, $\gamma=\frac{FWHM_{Lorentzian}}{2}$ the HWHM of the Lorentzian curve, $z=\frac{x-\mu+i\gamma}{\sigma\sqrt{2}}$, μ the center of the curve, and $w(z)=\exp(-z^2)\mathrm{ercf}(-iz)$ the Faddeeva function (ercf is the complementary error function).

Fig. 7.10 shows a Gaussian, a Lorentzian, and a Voigt curve of similar parameters:

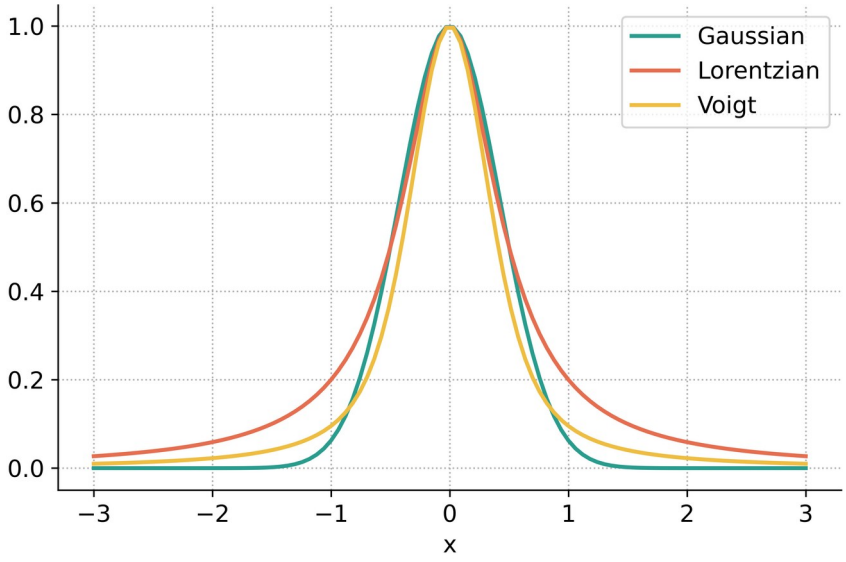

Figure 7.10: Gaussian, Lorentzian, and Voigt curves of similar parameters.

The deconvolution module generates composite models for multiple curves using its `MultiGaussianModel`, `MultiLorentzianModel`, and `MultiVoigtModel` functions, which dynamically assemble multiple components into a single fitting model. This ensures flexibility in fitting datasets with numerous overlapping peaks.

The results from the deconvolution are stored in an accessible and structured format. Parameter values and errors are saved as pandas DataFrames, facilitating seamless integration with Python's data analysis ecosystem. Fit statistics, including metrics like chi-square, reduced chi-square, R^2

values, etc., provide quantitative measures of fit quality. The best-fit curves and their residuals are also available for visualization and diagnostic purposes.

PyFasma includes built-in methods for visualizing fit results, such as overlay plots of the original data and the fitted curve, individual component curves, and residual plots for assessing model performance. The `plot_fit` and `plot_residuals` methods provide extensive customization options, allowing for the creation of publication-quality figures.

7.3. References

[1] Ezenarro J, Schorn-García D, Busto O, Boqué R. ProSpecTool: A MATLAB toolbox for spectral preprocessing selection. Chemom Intell Lab Syst 2024;247:105096. https://doi.org/10.1016/j.chemolab.2024.105096.

[2] Popp J, Biskup T. ASpecD: A Modular Framework for the Analysis of Spectroscopic Data Focussing on Reproducibility and Good Scientific Practice. Chemistry–Methods 2022;2:e202100097. https://doi.org/10.1002/cmtd.202100097.

[3] Sheehy G, Picot F, Dallaire F, Ember KJ, Nguyen T, Petrecca K, et al. Open-sourced Raman spectroscopy data processing package implementing a baseline removal algorithm validated from multiple datasets acquired in human tissue and biofluids. J Biomed Opt 2023;28:025002. https://doi.org/10.1117/1.JBO.28.2.025002.

[4] Flores E, Mozhzhukhina N, Li X, Norby P, Matic A, Vegge T. PRISMA: A Robust and Intuitive Tool for High-Throughput Processing of Chemical Spectra. Chemistry–Methods 2022;2:e202100094. https://doi.org/10.1002/cmtd.202100094.

[5] Georgiev D, Pedersen SV, Xie R, Fernández-Galiana Á, Stevens MM, Barahona M. RamanSPy: An Open-Source Python Package for Integrative Raman Spectroscopy Data Analysis. Anal Chem 2024;96:8492–500. https://doi.org/10.1021/acs.analchem.4c00383.

[6] Demšar J, Curk T, Erjavec A, Gorup C, Hocevar T, Milutinovic M, et al. Orange: Data Mining Toolbox in Python. J Mach Learn Res 2013;14:2349–53.

[7] Jupyter Development Team. Project Jupyter 2015. https://jupyter.org (accessed December 27, 2024).

[8] Pavlou E, Kourkoumelis N. Preprocessing and Analyzing Raman Spectra Using Python. Eng Proc 2023;56:28.

[9] Pavlou E, Kourkoumelis N. Deep adversarial data augmentation for biomedical spectroscopy: Application to modelling Raman spectra of bone. Chemom Intell Lab Syst 2022;228:104634. https://doi.org/10.1016/j.chemolab.2022.104634.

[10] Vardaki MZ, Pavlou E, Simantiris N, Lampri E, Seretis K, Kourkoumelis N. Towards non-invasive monitoring of non-melanoma skin cancer using spatially offset Raman spectroscopy. The Analyst 2023;148:4386–95. https://doi.org/10.1039/D3AN00684K.

[11] Petrokilidou C, Pavlou E, Velegraki A, Simou A, Marsellou I, Filis G, et al. Characterization and Differentiation of Candida auris on Dixon's Agar Using Raman Spectroscopy. Pathogens 2024;13:978. https://doi.org/10.3390/pathogens13110978.

[12] Chrimatopoulos C, Pavlou E, Kourkoumelis N, Sakkas V. Discriminating the salivary profile of athletes using ATR-FTIR spectroscopy and chemometrics. Chemom Intell Lab Syst 2022;230:104660. https://doi.org/10.1016/j.chemolab.2022.104660.

[13] Newville M, Stensitzki T, Allen DB, Ingargiola A. LMFIT: Non-Linear Least-Square Minimization and Curve-Fitting for Python 2014. https://doi.org/10.5281/zenodo.598352.
[14] Hunter JD. Matplotlib: A 2D Graphics Environment. Comput Sci Eng 2007;9:90–5. https://doi.org/10.1109/MCSE.2007.55.
[15] Harris CR, Millman KJ, van der Walt SJ, Gommers R, Virtanen P, Cournapeau D, et al. Array programming with NumPy. Nature 2020;585:357–62. https://doi.org/10.1038/s41586-020-2649-2.
[16] McKinney W. Data Structures for Statistical Computing in Python, Austin, Texas: 2010, p. 56–61. https://doi.org/10.25080/Majora-92bf1922-00a.
[17] Erb D. pybaselines: A Python library of algorithms for the baseline correction of experimental data 2024. https://doi.org/10.5281/ZENODO.5608581.
[18] Waskom ML. seaborn: statistical data visualization. J Open Source Softw 2021;6:3021. https://doi.org/10.21105/joss.03021.
[19] Virtanen P, Gommers R, Oliphant TE, Haberland M, Reddy T, Cournapeau D, et al. SciPy 1.0: fundamental algorithms for scientific computing in Python. Nat Methods 2020;17:261–72. https://doi.org/10.1038/s41592-019-0686-2.
[20] Pedregosa F, Varoquaux G, Gramfort A, Michel V, Thirion B, Grisel O, et al. Scikit-learn: Machine Learning in Python. J Mach Learn Res 2011;12:2825–30.
[21] Rohan I. spc. GitHub 2014. https://github.com/rohanisaac/spc/ (accessed November 16, 2020).
[22] Pavlou E, Kourkoumelis N. PyFasma 2024. https://gitlab.com/lepa22/pyfasma (accessed December 20, 2024).
[23] Thermo Scientific. Thermo Scientific SPC File Format. Thermo Fish Sci 2024. http://ftirsearch.com/Features/converters/SPCFileFormat.asp (accessed December 23, 2024).
[24] Zhao J, Lui H, McLean DI, Zeng H. Automated autofluorescence background subtraction algorithm for biomedical Raman spectroscopy. Appl Spectrosc 2007;61:1225–32. https://doi.org/10.1366/000370207782597003.
[25] Morháč M, Kliman J, Matoušek V, Veselský M, Turzo I. Background elimination methods for multidimensional coincidence γ-ray spectra. Nucl Instrum Methods Phys Res Sect Accel Spectrometers Detect Assoc Equip 1997;401:113–32. https://doi.org/10.1016/S0168-9002(97)01023-1.
[26] Misra S, Wahab MF, Patel DC, Armstrong DW. The utility of statistical moments in chromatography using trapezoidal and Simpson's rules of peak integration. J Sep Sci 2019;42:1644–57. https://doi.org/10.1002/jssc.201801131.
[27] Beattie JR, Esmonde-White FWL. Exploration of Principal Component Analysis: Deriving Principal Component Analysis Visually Using Spectra. Appl Spectrosc 2021;75:361–75. https://doi.org/10.1177/0003702820987847.
[28] Wold S, Sjöström M, Eriksson L. PLS-regression: a basic tool of chemometrics. Chemom Intell Lab Syst 2001;58:109–30. https://doi.org/10.1016/S0169-7439(01)00155-1.
[29] Brereton RG, Lloyd GR. Partial least squares discriminant analysis: taking the magic away. J Chemom 2014;28:213–25. https://doi.org/10.1002/cem.2609.
[30] Gromski PS, Muhamadali H, Ellis DI, Xu Y, Correa E, Turner ML, et al. A tutorial review: Metabolomics and partial least squares-discriminant analysis – a marriage of convenience or a shotgun wedding. Anal Chim Acta 2015;879:10–23. https://doi.org/10.1016/j.aca.2015.02.012.

[31] Boulesteix A-L, Strimmer K. Partial least squares: a versatile tool for the analysis of high-dimensional genomic data. Brief Bioinform 2006;8:32–44. https://doi.org/10.1093/bib/bbl016.
[32] Szymańska E, Saccenti E, Smilde AK, Westerhuis JA. Double-check: validation of diagnostic statistics for PLS-DA models in metabolomics studies. Metabolomics 2012;8:3–16. https://doi.org/10.1007/s11306-011-0330-3.
[33] Bai P, Wang J, Yin H, Tian Y, Yao W, Gao J. Discrimination of Human and Nonhuman Blood by Raman Spectroscopy and Partial Least Squares Discriminant Analysis. Anal Lett 2017;50:379–88. https://doi.org/10.1080/00032719.2016.1176033.
[34] Bates S, Hastie T, Tibshirani R. Cross-Validation: What Does It Estimate and How Well Does It Do It? J Am Stat Assoc 2024;119:1434–45. https://doi.org/10.1080/01621459.2023.2197686.
[35] Lee LC, Liong C-Y, Jemain AA. Partial least squares-discriminant analysis (PLS-DA) for classification of high-dimensional (HD) data: a review of contemporary practice strategies and knowledge gaps. Analyst 2018;143:3526–39. https://doi.org/10.1039/C8AN00599K.
[36] Fawcett T. An introduction to ROC analysis. Pattern Recognit Lett 2006;27:861–74. https://doi.org/10.1016/j.patrec.2005.10.010.
[37] Nadarajah S. A generalized normal distribution. J Appl Stat 2005;32:685–94. https://doi.org/10.1080/02664760500079464.
[38] Johnson NL, Kotz S, Balakrishnan N. Continuous univariate distributions. 2. ed., 3. [print.]-1994. New York: Wiley; 1994.
[39] Zaghloul MR, Ali AN. Algorithm 916: Computing the Faddeyeva and Voigt Functions. ACM Trans Math Softw 2011;38:1–22. https://doi.org/10.1145/2049673.2049679.
[40] 3.1. Cross-validation: evaluating estimator performance. Scikit-Learn n.d. https://scikit-learn/stable/modules/cross_validation.html (accessed January 2, 2025).
[41] Confusion matrix. Wikipedia 2024. https://en.wikipedia.org/w/index.php?title=Confusion_matrix (accessed October 25, 2024).

8. Results and discussion

8.1. Raman measurements (transverse)

8.1.1. Tibia

The mean healthy and osteoporotic preprocessed Raman spectra from the transverse surface of the tibias are shown in Fig. 8.1. All Raman bands relevant to bone are observed with the exception of phenylalanine (1003 cm^{-1}) which appears as a shoulder in the lower end of the carbonate band at the 1000-1130 cm^{-1} region. The overall appearance of both spectra is similar, with the main differences observed at the v_2 and v_4 vibrations of phosphate at 430 cm^{-1} and 580 cm^{-1}, respectively. These variations may suggest alterations in the mineral component of the bone. Small differences are also observed in the 1034 cm^{-1} peak of carbonate and in the amide III region at 1200-1350 cm^{-1}.

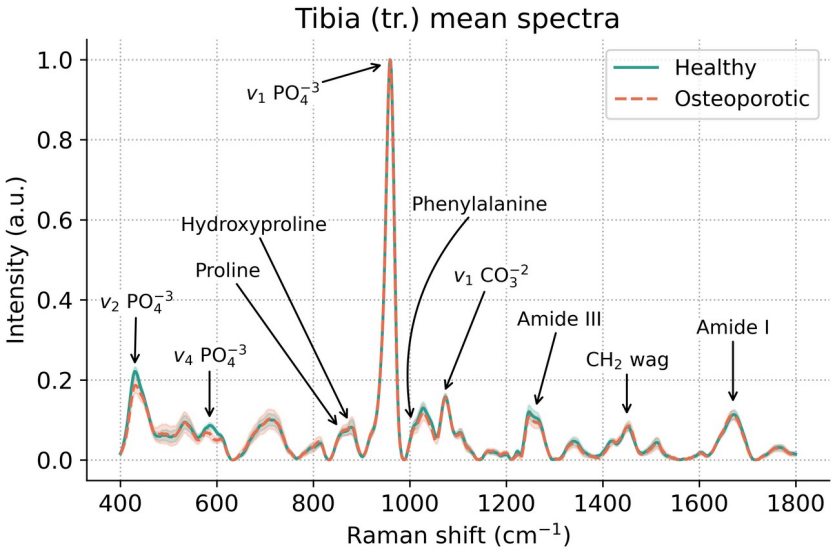

Figure 8.1: Mean preprocessed healthy and osteoporotic spectra from the transverse surface of the tibias. The main Raman bands are annotated. The shaded regions represent the standard deviations.

Multivariate analysis

Principal Components Analysis (PCA)

PCA was performed to explore the inherent variance in the Raman spectra of tibia samples and identify clustering patterns between healthy and osteoporotic groups. A summary plot of PCA is presented in Fig. 8.2.

The PC1-PC2 scores plots revealed clear separation between healthy and osteoporotic samples along PC2, which accounts for 10.35% of the total variance. This separation can be also observed in the PC2 KDE plot (diagonal of the scores plots). Combined with PC1, which explains 62.77% of the variance, these two components capture 73.11% of the total observed variance. No separation between the two classes was observed along PC1, with the corresponding loading indicating nearly equal contributions from all bone Raman bands. This aligns with expectations, as osteoporosis primarily induces microscopic and molecular alterations to bone quality, while the overall composition remains largely similar. Furthermore, the PC1-PC2 scores plot shows that the osteoporotic samples are more loosely clustered compared to the healthy samples. This observation suggests greater variability among osteoporotic samples, likely reflecting the heterogeneity in bone quality alterations associated with osteoporosis.

In the PC2 loading, three prominent peaks were identified: a peak at 430 cm^{-1}, a peak at 592 cm^{-1}, and a peak at 965 cm^{-1}, just beyond the primary phosphate peak. The first two peaks correspond to the ν_2 and ν_4 bending vibrations of phosphate and are consistent with the spectral differences observed in the mean spectra (Fig. 8.1). The third peak highlights the need for a closer examination of the main phosphate band at 960 cm^{-1}. As shown in Fig. 8.3, the osteoporotic samples exhibit a

narrower width of the main phosphate band compared to the healthy samples. This narrower width suggests an increase in mineral crystallinity in osteoporotic samples, consistent with the inverse relationship between crystallinity and the FWHM of the main phosphate band [1,2]. The remaining bands also contribute to the variance in PC2, albeit to a lesser extent. This indicates that the primary factor distinguishing healthy from osteoporotic tibia samples is the alteration in the mineral component of the bone.

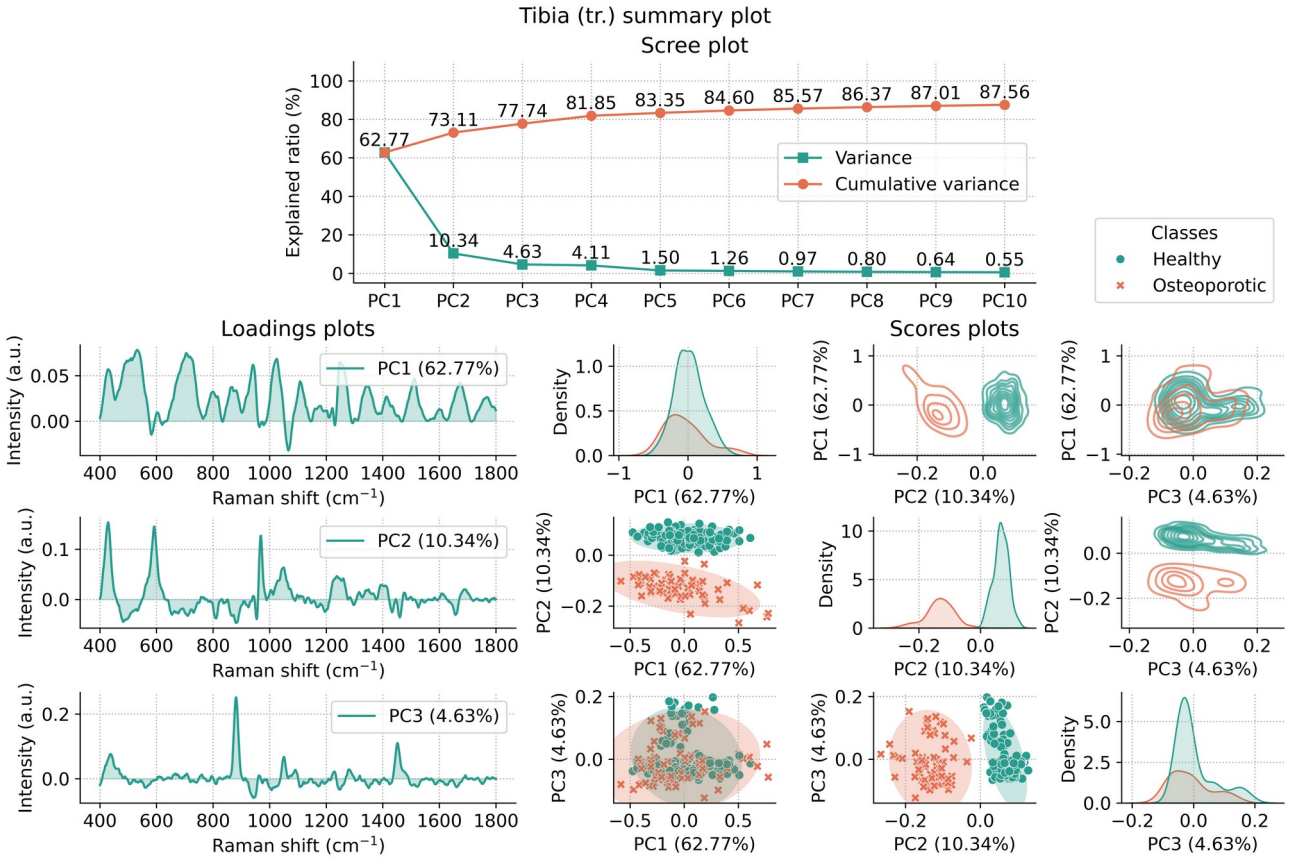

Figure 8.2: Summary plot of PCA results for the spectra collected from the transverse surfaces of the tibias.

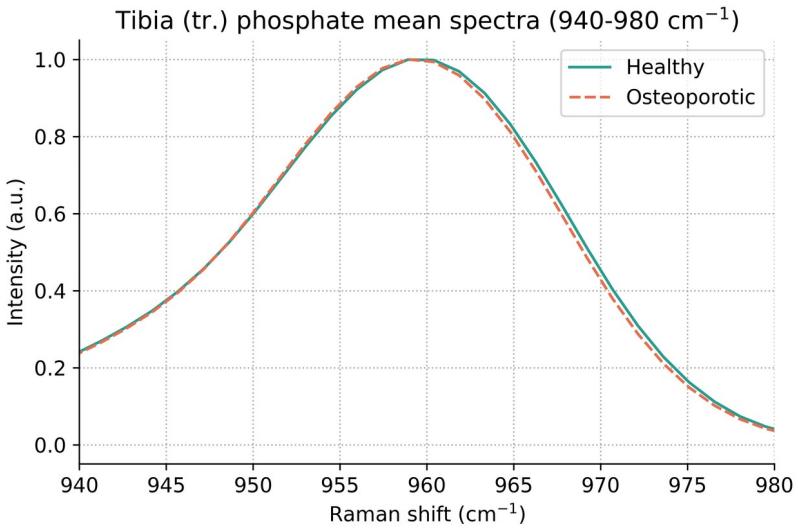

Figure 8.3: Mean spectra of tibia samples at the 940-980 cm^{-1} spectral region. A decreased width of the main phosphate band is observed for osteoporotic samples.

Of particular interest is the behavior of the amide I region (1580-1720 cm^{-1}) in the PC2 loading, where the lower half of the band exhibits negative variance, while the higher half shows positive variance. A closer examination of this spectral region in the mean spectra (Fig. 8.4), shows a shift of the amide I peak from 1672 cm^{-1} to 1669 cm^{-1} in osteoporotic samples. Additionally, the lower end of the amide I band in osteoporotic samples has higher intensity compared to the healthy samples, while the higher end has lower intensity. This peak shift in the amide I band may suggest alterations in collagen cross-linking, indicating increased collagen maturity in osteoporotic tibias [1].

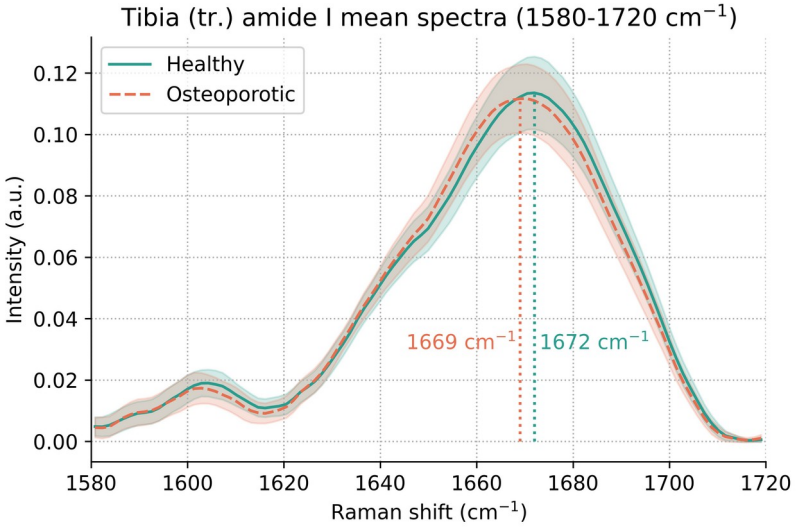

Figure 8.4: Mean spectra of tibia samples at the 1580-1720 cm^{-1} spectral region. A shift of the amide I peak from 1672 cm^{-1} to 1669 cm^{-1} is observed for the osteoporotic samples.

Partial Least Squares Discriminant Analysis (PLS-DA)

In addition to PCA, we performed PLS-DA to create a a predictive model. For this model, the spectra were split in 70/30 train/test ratio in a stratified manner using scikit-learn's `model_selection.train_test_split` function. This resulted to 151 spectra (101 healthy and 50 osteoporotic) for training the model and 65 spectra (43 healthy and 22 osteoporotic) for assessing the model's predictive capabilities.

To determine the number of components that should be used in the predictive model, we performed 5-fold stratified cross-validation with 10 repeats. The resulting evaluation metrics plot is shown in Fig. 8.5. The metrics indicate that the optimal number of components is 2. For this configuration, the model achieves an accuracy of nearly 100% with small MSE. Additionally, the values of R^2 and Q^2, which assess the goodness of fit and predictive power of the model, respectively, are closely aligned, indicating that the model is neither overfit nor underfit. Furthermore, the small standard deviations observed for 2 components suggest that the model is stable and consistent.

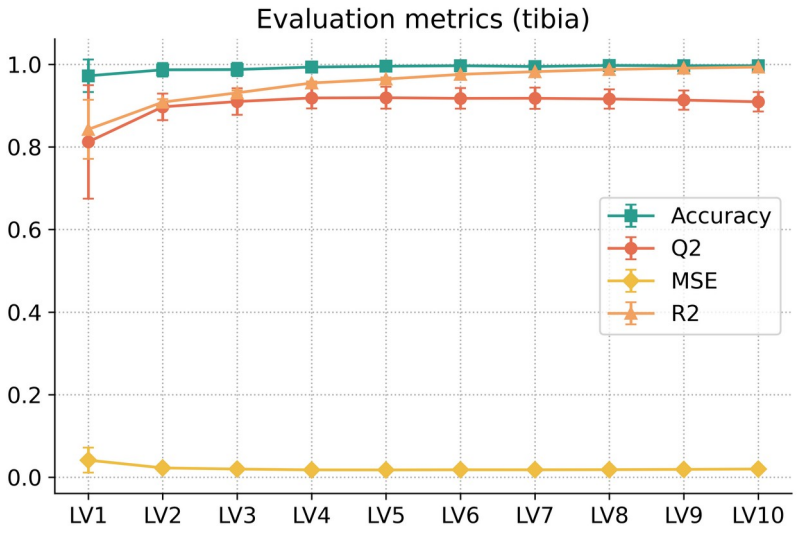

Figure 8.5: Cross-validation evaluation metrics of the PLS-DA model of tibias.

Following cross-validation, we created a PLS-DA model with 2 components. The X- and Y-scores of the training data for this model are shown in Fig. 8.6 and Fig. 8.7, respectively. Excellent separation between the two classes (healthy and osteoporotic) is observed. As in PCA, the osteoporotic samples show higher variation than the healthy samples which clustered together more tightly. Additionally, the Y-scores demonstrate clear class separation, further validating the model's ability to distinguish between healthy and osteoporotic samples.

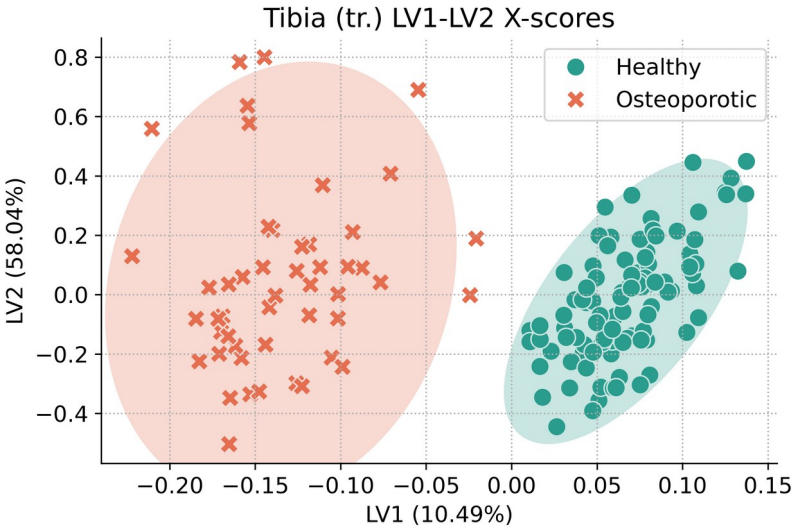

Figure 8.6: X-scores plot for the training data of the PLS-DA model of tibias with 2 components. The ellipses represent the 95% confidence ellipses.

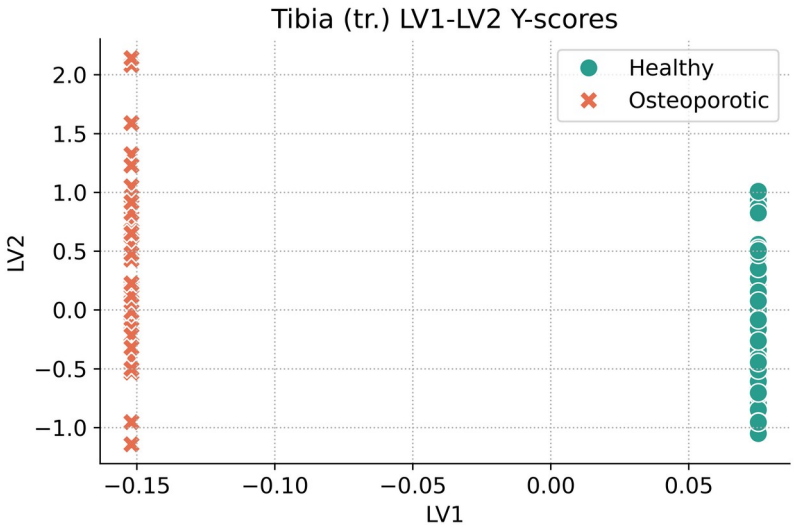

Figure 8.7: Y-scores plot for the training data of the PLS-DA model of tibias with 2 components.

Similar to PCA, the coefficients plot (Fig. 8.8) indicates that the primary factor contributing to the separation between the classes is the mineral content. This is reflected in the prominence of the ν_2 and ν_4 phosphate bands, as well as the narrower width of the main phosphate peak in osteoporotic samples.

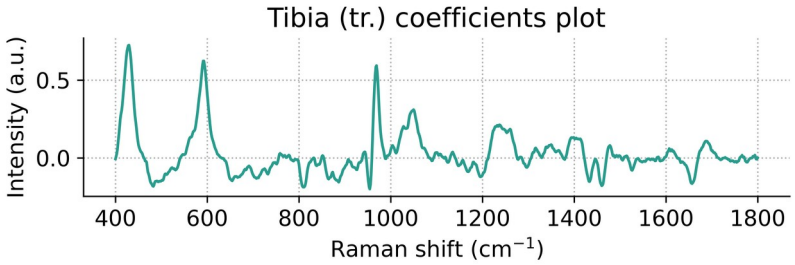

Figure 8.8: PLS-DA coefficients plot for the model of tibias.

Finally, the model's performance on the test data was evaluated using a confusion matrix and a Receiver Operating Characteristic (ROC) curve (Fig. 8.9). The confusion matrix indicates no misclassified samples, leading to 100% accuracy, sensitivity, specificity, and F1 score, while the ROC curve yields an Area Under Curve (AUC) of 1.This performance suggests that the model can reliably discriminate and classify samples from the tibias of healthy and osteoporotic rabbits.

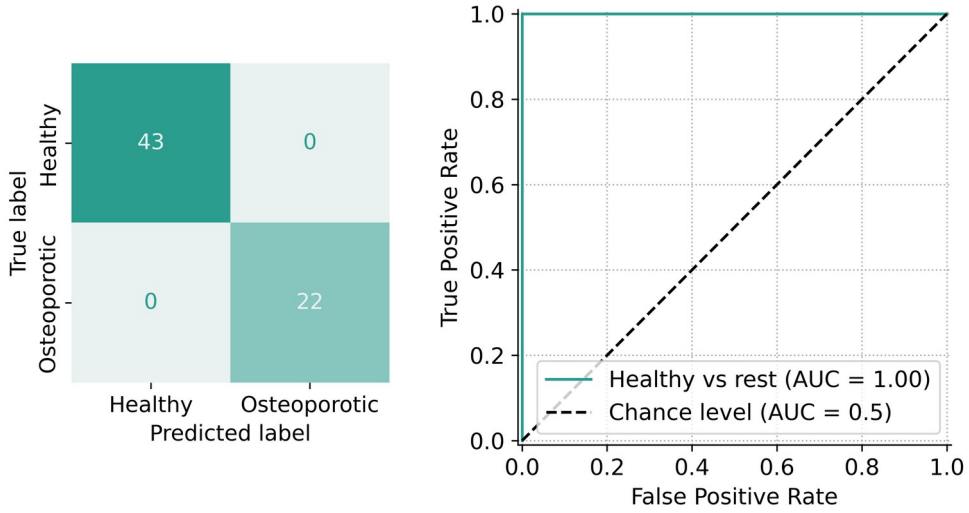

Figure 8.9: Confusion matrix (left) and ROC-AUC curve (right) used for the evaluation of the predictive PLS-DA model of tibias.

Bone quality assessment

To evaluate how osteoporosis affects bone quality at the molecular level compared to healthy bone, the following parameters were calculated from the spectra: crystallinity (a measure of mineral crystal size and perfection), mineral-to-matrix ratio (MMR; indicating the relative amount of mineral to organic matrix), carbonate-to-phosphate ratio (CPR; reflecting carbonate substitution

in the mineral lattice), collagen maturity (assessing cross-linking and age of collagen), and the hydroxyproline-to-proline ratio (Hyp/Pro ratio; related to collagen stability and turnover).

These parameters were derived by performing peak deconvolution on specific bands in the Raman spectra. Crystallinity was calculated from the FWHM of the main phosphate band at 960 cm^{-1}. The MMR was determined as the integrated area ratio of the main phosphate band at 960 cm^{-1} to the amide I band at 1660 cm^{-1}. The CPR was calculated as the ratio of the intensity of the carbonate band at 1070 cm^{-1} to the intensity of the main phosphate band. Collagen maturity was assessed using the relative intensities of amide I bands at 1660 cm^{-1} and 1690 cm^{-1}. The Hyp/Pro ratio was obtained by the relative intensity ratio of the peaks associated with hydroxyproline and proline in the 830–900 cm^{-1}.

The deconvoluted spectral features provided the data necessary for calculating the parameters described above. Below, we present the results for each key spectral region.

Phosphate band (900-990 cm^{-1}) deconvolution

The spectral region from 900 to 990 cm^{-1} is dominated by the symmetric stretching vibration (ν_1) of the phosphate group (PO_4^{3-}), which is a key feature of the mineral component in bone. This band provides insights into the crystallinity and composition of the bone mineral. To analyze this region, we applied two fitting approaches: a single Gaussian fit and a four-Gaussian decomposition. The single Gaussian fit, commonly used for determining crystallinity, provided the Full Width at Half Maximum (FWHM) as a measure of mineral crystallinity [1,2]. In osteoporotic samples, the FWHM was narrower compared to healthy samples, indicating increased crystallinity. A representative fit is shown in Fig. 8.10.

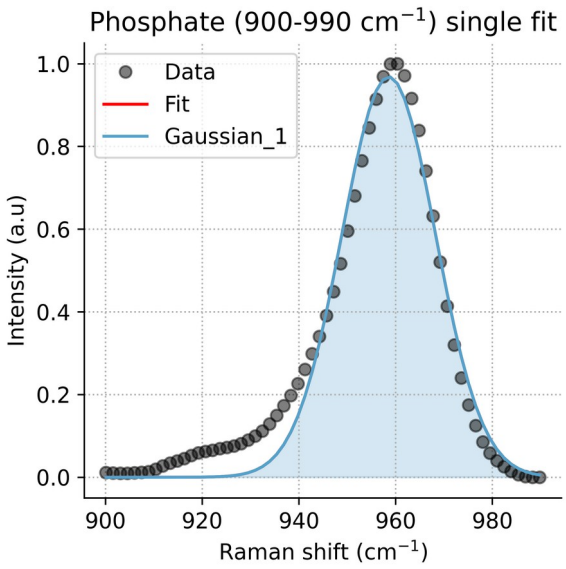

Figure 8.10: Fit of the main phosphate band (900–990 cm^{-1}) of tibias using a single Gaussian curve. The FWHM of the Gaussian is used to calculate the crystallinity of the samples.

The four-Gaussian decomposition provided a more detailed analysis of the band's structure, revealing underlying components that contribute to the overall shape of the main phosphate band. To estimate the number of peaks in the band and determine initial guesses for deconvolution, we calculated the second derivative of the mean spectra in this region (Fig. 8.11). The second derivative indicated the presence of two prominent features at 917 cm^{-1} and 960 cm^{-1}. However, based on literature references and the observation that using four peaks significantly improved the overall fit quality, we employed four Gaussian curves for the deconvolution [3,4].

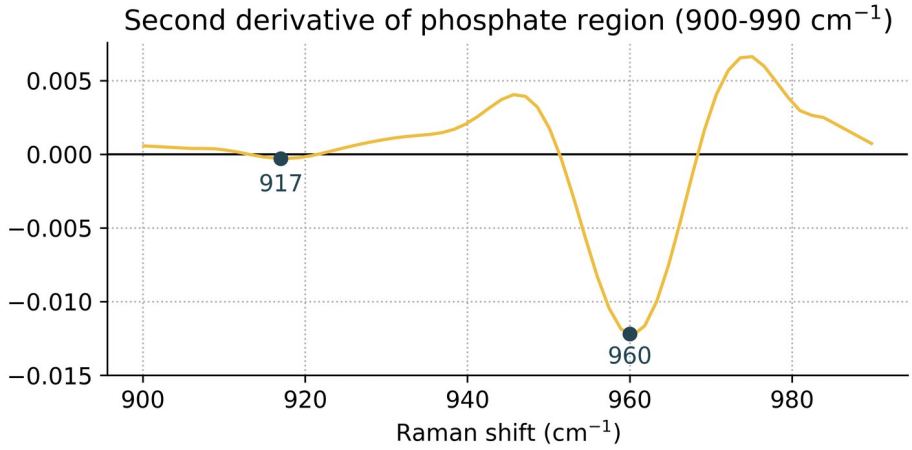

Figure 8.11: Second derivative of the main phosphate band (900–990 cm^{-1}) of tibias. Two prominent peaks are observed and annotated.

Fig. 8.12 shows a representative deconvoluted phosphate band, highlighting the individual Gaussian components. The fitted curves were centered approximately at 920 cm^{-1} (attributed to the *v*(C-C) vibration of proline), 940 cm^{-1} (also associated with the *v*(C-C) vibration of proline on collagen's backbone), 948 cm^{-1} (associated to the v_1 vibration of phosphate with Type B substitutions of carbonate), and 960 cm^{-1} (belonging to the v_1 vibration of phosphate), consistent with previously reported bands in the literature for this spectral region [3,5].

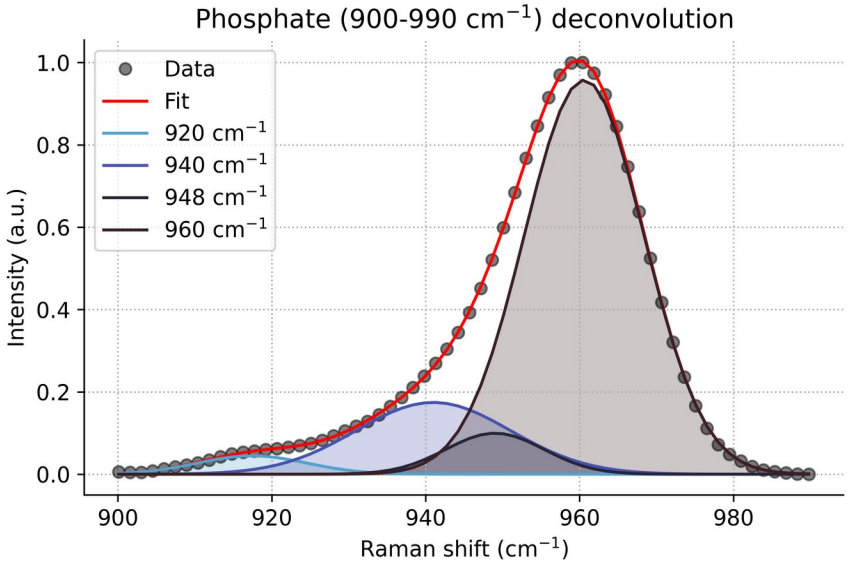

Figure 8.12: Deconvolution of the main phosphate band (900–990 cm^{-1}) of tibias with four Gaussian curves.

Amide I band (1580-1720 cm^{-1}) deconvolution

The amide I region (1580–1720 cm^{-1}) is a key spectral feature of bone, primarily associated with C=O stretching vibrations of the peptide backbone [4]. This region is sensitive to changes in the organic matrix, providing insights into collagen properties and molecular organization. Deconvolution of the amide I band was performed using multiple Gaussian curves to resolve overlapping features and quantify contributions within the region. To determine the number of peaks and their initial positions, the second derivative of the mean spectra was calculated (Fig. 8.13). The analysis revealed four prominent features at approximately 1604 cm^{-1}, 1641 cm^{-1}, 1671 cm^{-1} and 1694 cm^{-1}. Based on these observations and literature references, we used four Gaussian curves for deconvolution.

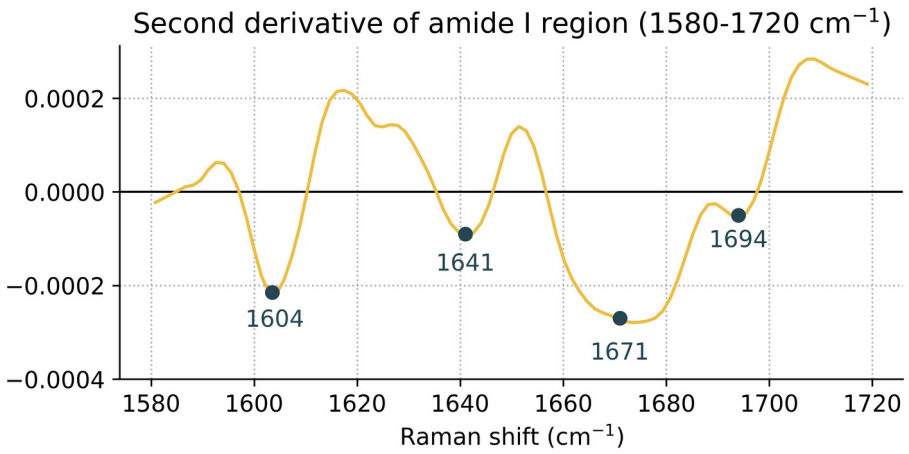

Figure 8.13: Second derivative of the amide I band (1580–1720 cm^{-1}) of tibias. Four prominent peaks are observed and annotated.

Fig. 8.14 shows a representative deconvoluted amide I region, highlighting the individual Gaussian components. The fitted peaks were centered at approximately 1605 cm^{-1} (representing the *δ*(C=C) vibrations of amino acids phenylalanine and tyrosine), 1640 cm^{-1} (associated with the *ν*(C-C) vibration of the α-helical structure of collagen), 1667 cm^{-1} (associated with the *ν*(C=O) vibration of amide I), and 1688 cm^{-1} (associated with denatured collagen). These peak positions align well with those reported in the literature [1,3,4]. Notably, the peak at 1667 cm^{-1} corresponds to the commonly reported 1660 cm^{-1} peak. The slight deviations from the reported positions are consistent with observations in other bone studies and are justified by variations in experimental conditions, sample preparation, and/or tissue heterogeneity [1].

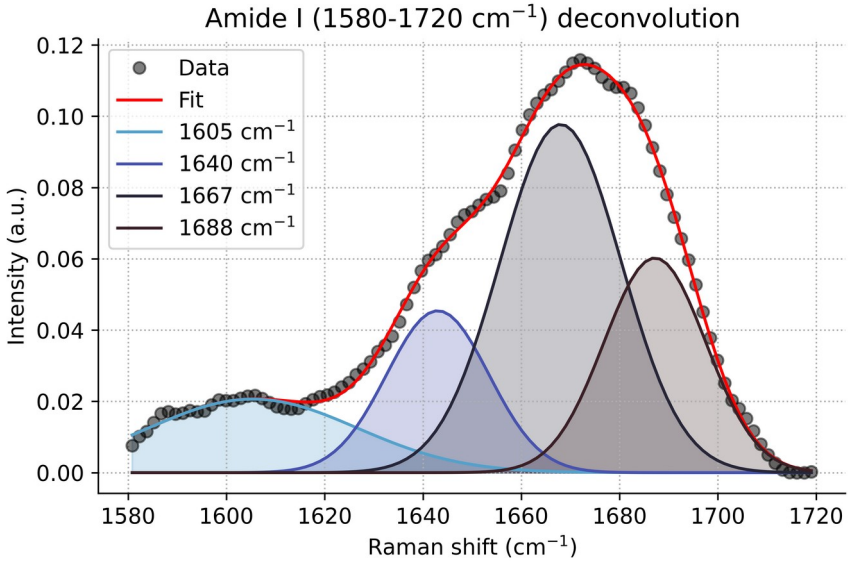

Figure 8.14: Deconvolution of the amide I band (1580–1720 cm^{-1}) of tibias with four Gaussian curves.

Carbonate band (990-1140 cm^{-1}) deconvolution

The spectral region from 1000 to 1130 cm^{-1} is dominated by the carbonate band, primarily attributed to the symmetric stretching vibration (v_1) of the carbonate ion (CO_3^{2-}) [2]. This band is an important indicator of carbonate Type B substitution within the hydroxyapatite lattice, which affects bone mineral composition. Deconvolution of the carbonate band was performed to resolve the band to its components. Initial guesses for the peak positions were determined using the second derivative of the mean spectra (Fig. 8.15). Six prominent peaks are found at 1006 cm^{-1}, 1027 cm^{-1}, 1045 cm^{-1}, 1073 cm^{-1}, 1106 cm^{-1}, and 1127cm^{-1}. Using these values as starting points, we fitted the carbonate band with six Gaussian curves. It must be noted that the 1070 cm^{-1} (1073 cm^{-1} in our case) peak of carbonate is reported to overlap with the 1076 cm^{-1} peak of phosphate [1,6]. That overlapping may affect the intensity and area of the carbonate peak. However, in our spectra we were not able to identify any contribution from a band at 1076 cm^{-1}, so we proceeded with the six bands identified by the second derivative.

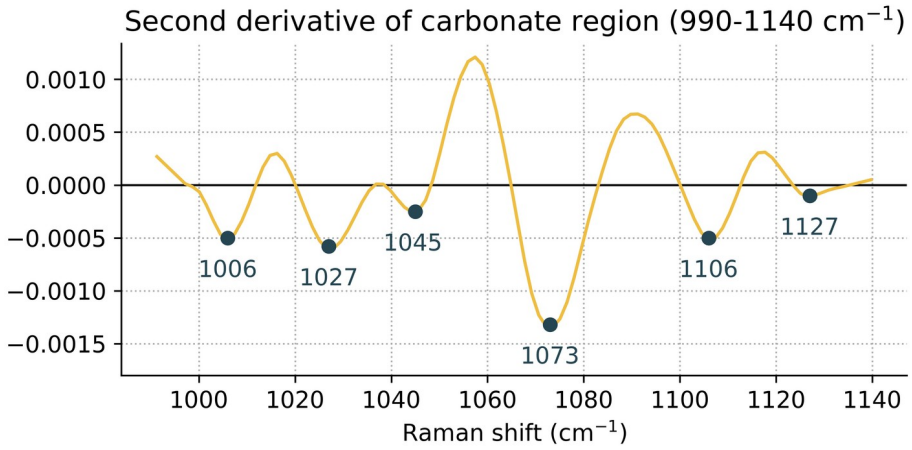

Figure 8.15: Second derivative of the carbonate band (1580–1720 cm^{-1}) of tibias. Six prominent peaks are observed and annotated.

Fig. 8.16 shows a representative deconvoluted carbonate band, highlighting the individual Gaussian components. The fitted peaks were centered at approximately 1005 cm^{-1} (belonging to the *v*(C-C) vibration of phenylalanine), 1025 cm^{-1} (associated with the v_3 vibration of phosphate), 1044 cm^{-1} (also associated with the v_3 vibration of phosphate), 1074 cm^{-1} (belonging to the v_1 vibration of carbonate), 1104 cm^{-1} and 1127 cm^{-1} (the last two don't have a clear association with a specific vibration). These peaks are in good agreement with the ones found in literature [1,3,4]. The peak at 1074 cm^{-1} is the main peak of the carbonate region corresponds to the v_1 carbonate band (usually reported at 1070 cm^{-1}). This band is associated with Type B substitution, where carbonate ions replace phosphate in the hydroxyapatite lattice.

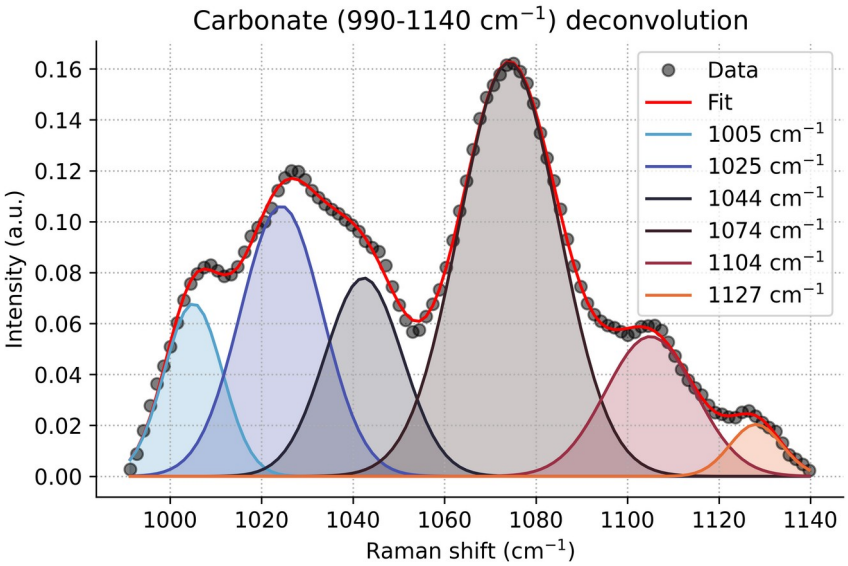

Figure 8.16: Deconvolution of the carbonate band (990–1140 cm^{-1}) of tibias with six Gaussian curves.

Proline-Hydroxyproline band (830-900 cm^{-1}) deconvolution

The region 830-900 cm^{-1} is associated with the vibrations of proline and hydroxyproline, which are amino acids of collagen. They can provide information about the composition and turnover of collagen. The band was deconvoluted to resolve its components. The second derivative of the mean spectra indicated two prominent peaks at 853 cm^{-1} and 882 cm^{-1} (Fig. 8.17). Based on the literature, however, and the wellness of fit on the spectra, we also included peaks at 840 cm^{-1} and 890 cm^{-1} [3].

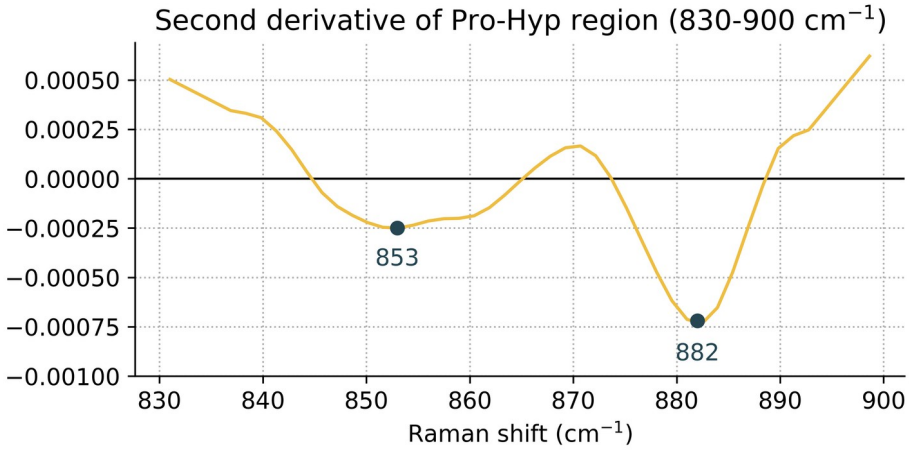

Figure 8.17: Second derivative of the proline-hydroxyproline band (830–900 cm^{-1}) of tibias. Two prominent peaks are observed and annotated.

A representative deconvoluted proline-hydroxyproline band is shown in Fig. 8.18. The fitted peaks were centered at approximately 842 cm^{-1}, 856 cm^{-1} (associated with proline), 876 cm^{-1} (associated with hydroxyproline), and 888 cm^{-1}. The fitted peaks are in agreement with literature [3,4].

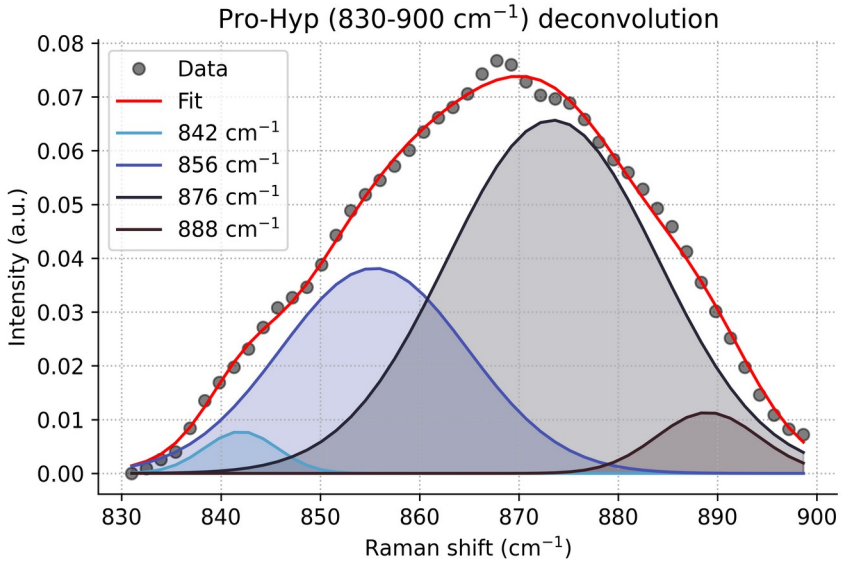

Figure 8.18: Deconvolution of the proline-hydroxyproline band (830–900 cm^{-1}) of tibias with four Gaussian curves.

Bone quality parameters

The deconvoluted Raman bands were used to calculate parameters for assessing bone quality differences between healthy and osteoporotic spectra. The distribution of each parameter was tested for normality using the Shapiro-Wilk test, implemented through SciPy's `stats.shapiro` function [7]. The Shapiro-Wilk test evaluates the null hypothesis that the data follow a normal distribution. A *p*-value of less than 0.05 indicates that the null hypothesis is rejected, suggesting that the data do not follow a normal distribution. Depending on the normality test results, statistical comparisons of the bone quality parameters were performed using either a two-sided t-test, implemented with SciPy's `stats.ttest_ind` function for normally distributed data, or a two-sided Mann-Whitney U test, implemented with SciPy's `stats.mannwhitneyu` function for non-normally distributed data. The two-sided t-test evaluates whether the means of two independent groups are significantly different, assuming the data are normally distributed. The Mann-Whitney U test, on the other hand, assesses whether there is a significant difference in the distributions of two independent groups, making no assumption about normality. A difference is considered significant when the *p*-value is less than 0.05. It should also be noted that during the calculation of the bone quality parameters, extreme outliers were identified and excluded from further analysis to ensure data reliability and accuracy.

It should be noted that during the calculation of the bone quality parameters, extreme outliers were identified and excluded from further analysis to ensure data reliability and accuracy.

The parameters that were evaluated are:

- Crystallinity, calculated as the inverse of the FWHM of the main phosphate band at 960 cm^{-1} fitted with a single Gaussian.
- Mineral-to-matrix ratio (MMR), calculated as the ratio of the integrated area (IA) of the phosphate band at 960 cm^{-1}, as obtained by the deconvolution using four Gaussian curves, to the integrated area of the of the main amide I band at 1667 cm^{-1}.
- Carbonate-to-phosphate ratio (CPR), calculated as the intensity ratio of the deconvoluted carbonate peak at 1074 cm^{-1} to the main phosphate peak at 960 cm^{-1} as it was determined by four-band deconvolution.
- Collagen maturity, calculated as the ratio of the IA area of the main amide I band at 1667 cm^{-1} to the IA of the band at 1688 cm^{-1}.
- Hydroxyproline-to-proline (Hyp/Pro) ratio, calculated as the intensity ratio of the hydroxyproline peak at 876 cm^{-1} to the proline peak at 856 cm^{-1}.

Boxplots of the bone quality parameters are shown in Fig. 8.19.

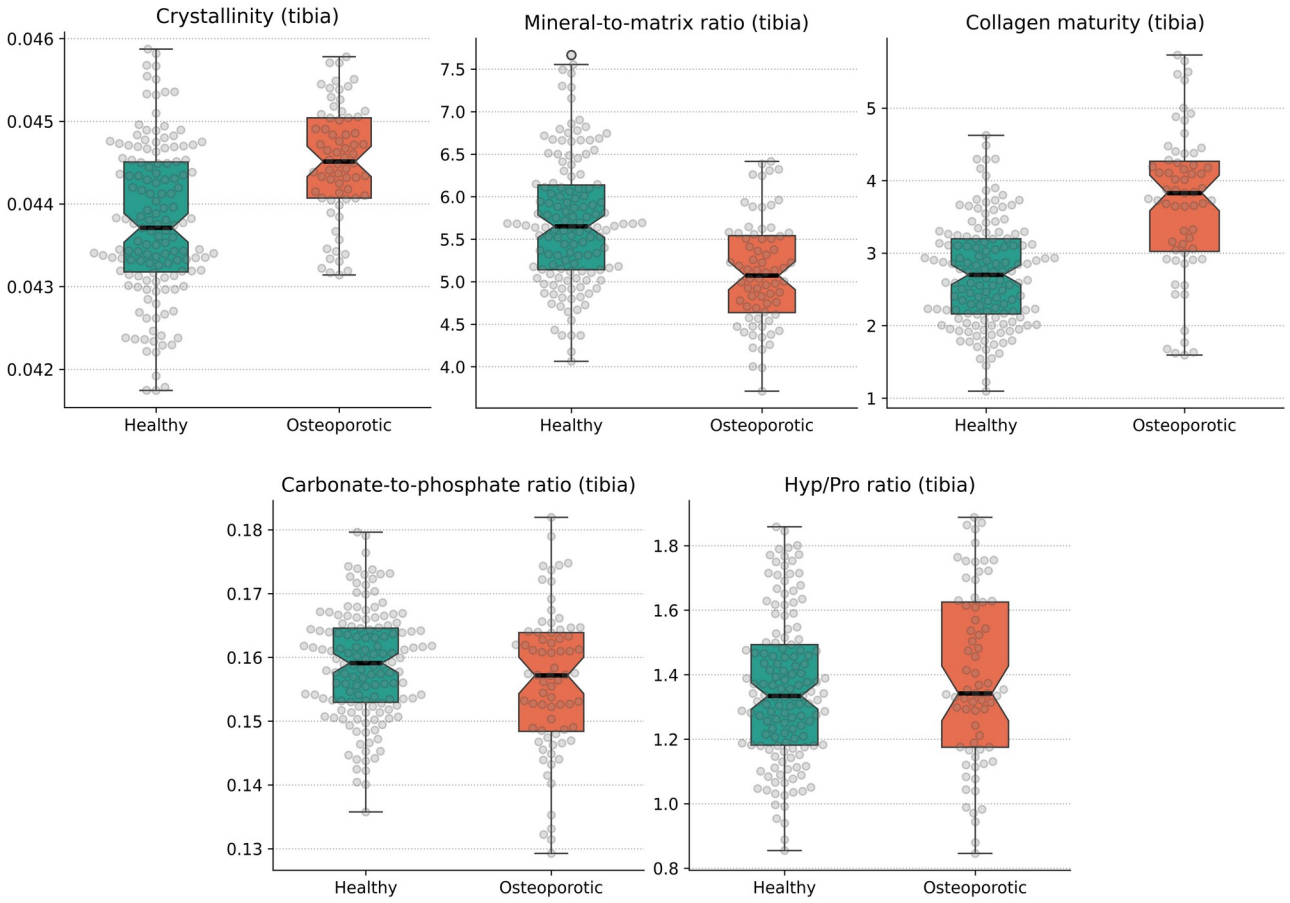

Figure 8.19: Bone quality parameters boxplots for the healthy and osteooporotic tibias.

The values of the bone quality parameters are presented in Table 6.

Table 6: Bone quality parameters for the healthy and osteoporotic tibias.

Parameter	Healthy (mean ± std)	Osteoporotic (mean ± std)	Test	*p*-value
Crystallinity (1/FWHM[960 cm^{-1}])	0.0438 ± 0.0009	0.0445 ± 0.0007	T	< 0.001
MMR (IA_{1667}/IA_{960})	5.7 ± 0.8	5.1 ± 0.6	T	< 0.001
Collagen maturity (IA_{1667}/IA_{1988})	2.7 ± 0.7	3.7 ± 1	T	< 0.001
CPR (I_{1070}/I_{960})	0.159 ± 0.009	0.156 ± 0.011	T	NS
Hyp/Pro (I_{876}/I_{856})	1.3 ± 0.2	1.4 ± 0.3	U	NS

T: t-test; U: Mann-Whitney U test; NS: not significant

8.1.2. Humerus

The mean healthy and osteoporotic preprocessed Raman spectra from the transverse surface of the humeri are shown in Fig. 8.20. All Raman bands relevant to bone are observed. As in the case of the tibia, the only exception is the phenylalanine (1003 cm^{-1}) which appears as a shoulder in the lower end of the carbonate band at the 1000-1130 cm^{-1} region. The overall appearance of both spectra is similar, with the main differences observed at the v_2 and v_4 vibrations of phosphate at 430 cm^{-1} and 580 cm^{-1}, respectively. These variations may suggest alterations in the mineral component of the bone.

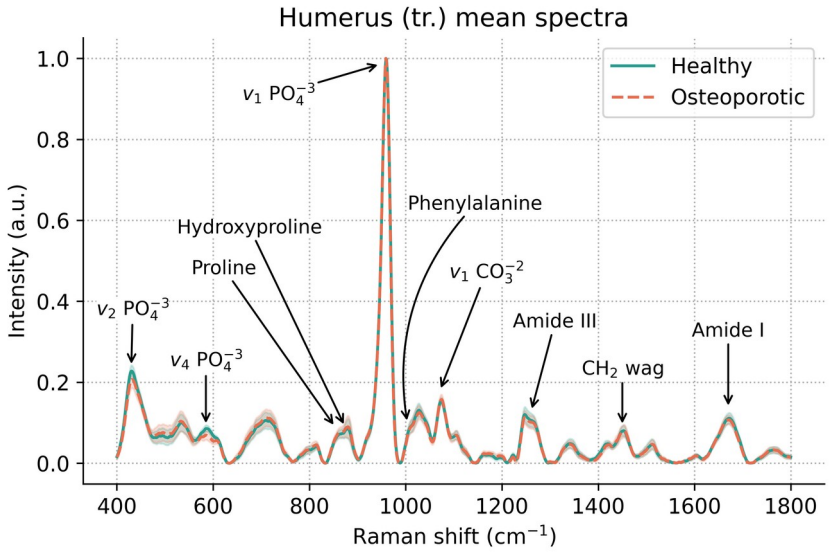

Figure 8.20: Mean preprocessed healthy and osteoporotic spectra from the transverse surface of the humeri. The main Raman bands are annotated. The shaded regions represent the standard deviations.

Multivariate analysis

Principal Components Analysis (PCA)

We employed PCA with the purpose of uncovering insights and clustering patterns in the Raman spectra of the healthy and osteoporotic samples obtained from the humeri of the rabbits. The summary plot of PCA is shown in Fig. 8.21.

As shown, the two classes are separated along PC3, which accounts for 6.97% of the total variance. However, this separation is partial, with some overlap observed between the two classes. This contrasts with the case of tibias, where the classes are completely separated along PC2. The separation along PC2 in the tibias suggests that the spectral differences driving class separation are more pronounced in the tibial spectra compared to those of the humeri. In the PCA of humeri PC1 accounts for 63.81% and PC2 for 7.94%, with the total variance explained by the first three PCs being 78.73%.

In the PC3 loading, the peaks with the highest intensity are observed at 430 cm^{-1}, 592 cm^{-1}, corresponding to the ν_2 and ν_4 bending vibrations of phosphate, the same as in the case of the tibias. Similarly to the case of the tibias, a third, positive prominent peak at 965 cm^{-1} also occurs, which corresponds to narrower main phosphate band at 960 cm^{-1} for the osteoporotic samples, indicating increased crystallinity (Fig. 8.22). All other bands in the PC3 loading show smaller contributions to the variance. Equal contributions from all bands are observed in the PC1 loading.

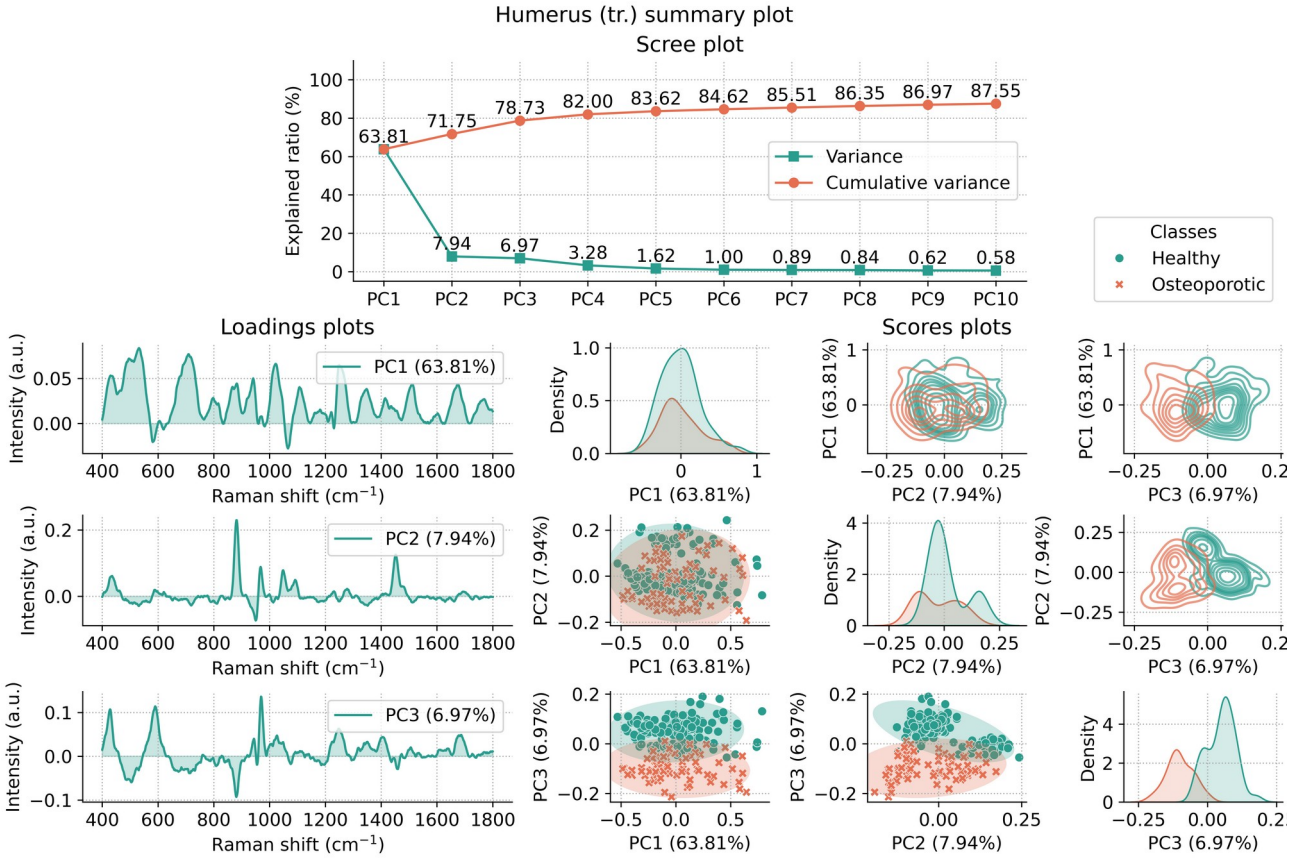

Figure 8.21: Summary plot of PCA results for the spectra collected from the transverse surfaces of the humeri.

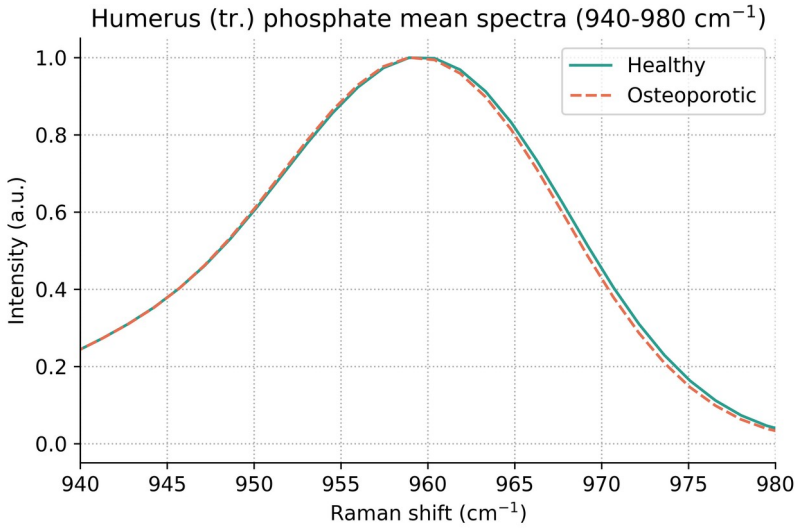

Figure 8.22: Mean spectra of humerus samples at the 940-980 cm-1 spectral region. A decreased width of the main phosphate band is observed for osteoporotic samples.

The amide I region (1580-1720 cm^{-1}) in the PC3 loading does not display the same behavior as in the tibia, where the first half was negative and the second half was positive. However, the first half

of the amide I region does display decreased intensity. Furthermore, as shown in Fig. 8.23, a smaller shift in the amide I peak is observed for the humeri (from 1672 cm^{-1} to 1671 cm^{-1}) compared to the tibias (from 1672 cm^{-1} to 1669 cm^{-1}). This suggests that alterations in the cross-linking of collagen are less pronounced in the osteoporotic humeri.

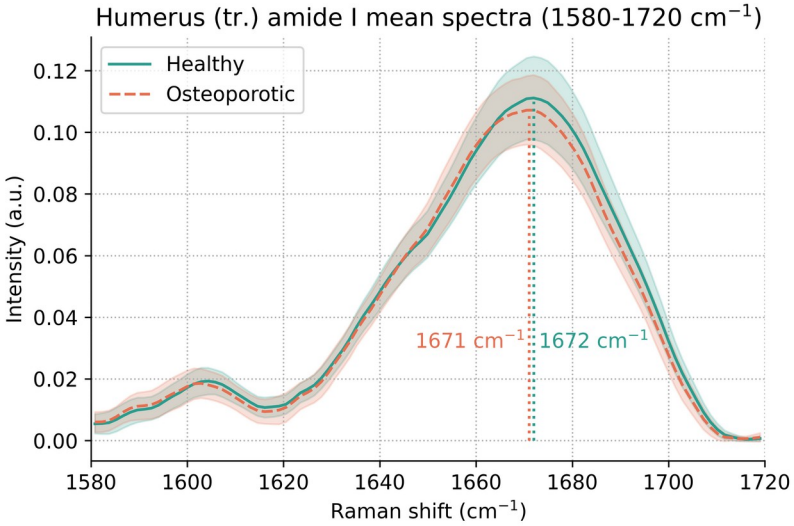

Figure 8.23: Mean spectra of humerus samples at the 1580-1720 cm^{-1} spectral region. A small shift of the amide I peak from 1672 cm^{-1} to 1671 cm^{-1} is observed for the osteoporotic samples.

Partial Least Squares Discriminant Analysis (PLS-DA)

In addition to PCA, PLS-DA was employed to create a predictive model. The spectra were split in 70/30 train/test ratio in a stratified manner using scikit-learn's `model_selection.train_test_split` function. This resulted to 151 spectra (101 healthy and 50 osteoporotic) for training the model and 65 spectra (43 healthy and 22 osteoporotic) for assessing the model's predictive capabilities.

The optimal number of components was determined using 5-fold stratified cross-validation with 10 repeats. The relevant evaluation metrics plot is shown in Fig. 8.24. From this plot we determined that the optimal number of components is 2, since this number yields maximum accuracy, minimum MSE, and similar values of R^2 and Q^2, with small standard deviation for all metrics. These metrics suggest that the 2 components model is well-fit and stable.

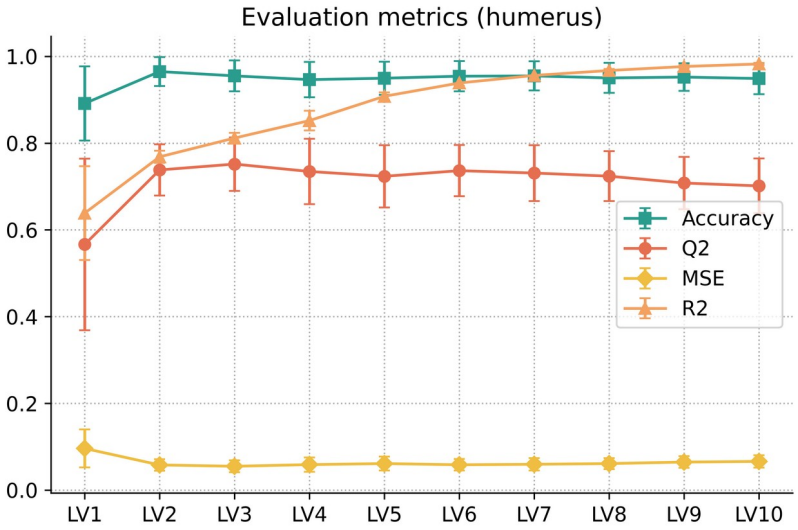

Figure 8.24: Cross-validation evaluation metrics of the PLS-DA model of humeri.

Subsequently, we created the PLS-DA model with 2 components, with the X- and Y-scores of the training data shown in Fig. 8.25 and Fig. 8.26, respectively. As in the PCA, separation between healthy and osteoporotic samples exists in the X-scores plot, however some overlap is present. The Y-scores are well-separated.

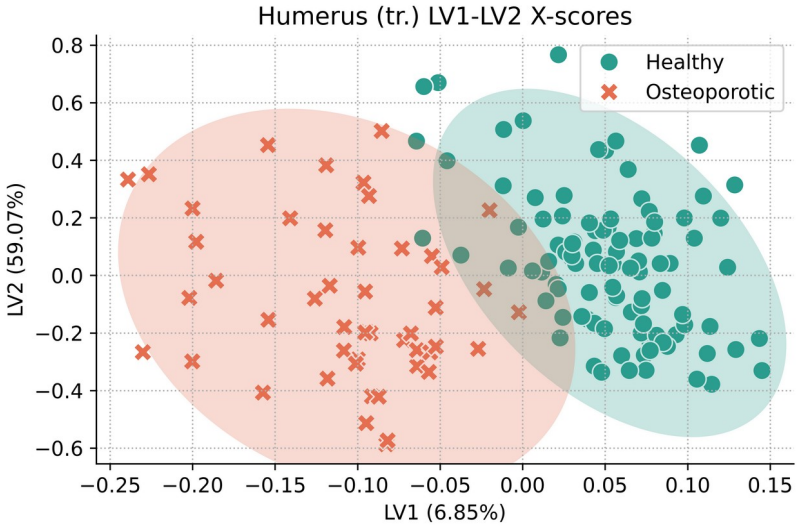

Figure 8.25: X-scores plot for the training data of the PLS-DA model of humeri with 2 components. The ellipses represent the 95% confidence ellipses.

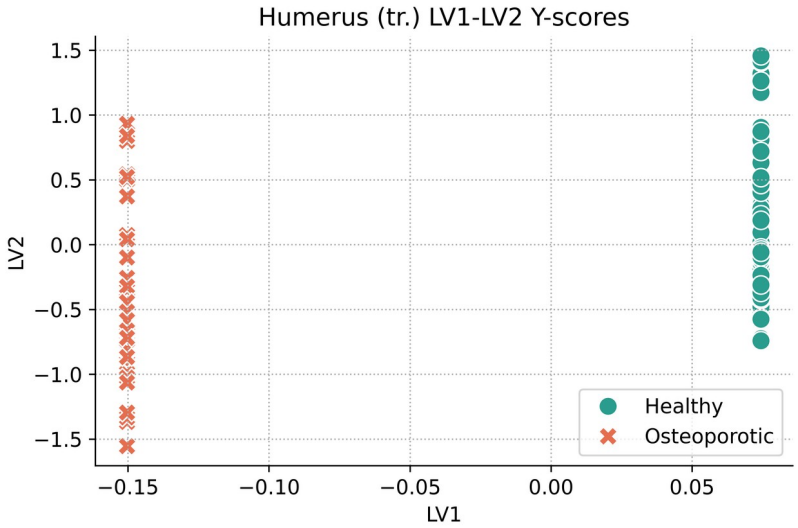

Figure 8.26: Y-scores plot for the training data of the PLS-DA model of humeri with 2 components.

The coefficients plot (Fig. 8.27) is similar to the case of PCA and to the case of the tibias, indicating that the phosphate-related bands (v_2 and v_4 phosphate bands and the narrower main phosphate band in osteoporotic samples) are the primary contributors to the discrimination of the classes.

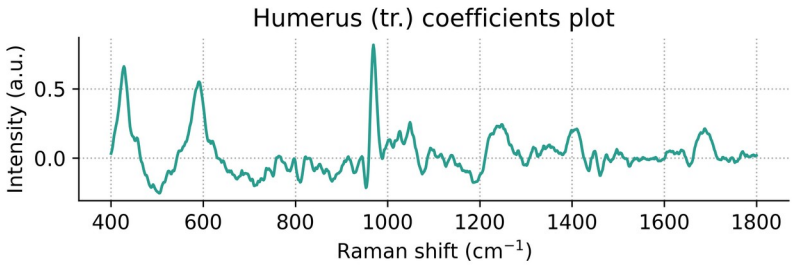

Figure 8.27: PLS-DA coefficients plot for the model of humeri.

The model's prediction capability was assessed using the confusion matrix and ROC curve (Fig. 8.28). The confusion matrix indicates that two osteoporotic samples were misclassified as healthy. This corresponds to an accuracy of 96.9%, a sensitivity of 95.5%, a specificity of 100%, and an F1 score of 97.7%. The AUC for this model is 0.99. While these results demonstrate that the PLS-DA model for the humeri performs very well in distinguishing healthy from osteoporotic samples, its performance is slightly lower than that of the tibial model.

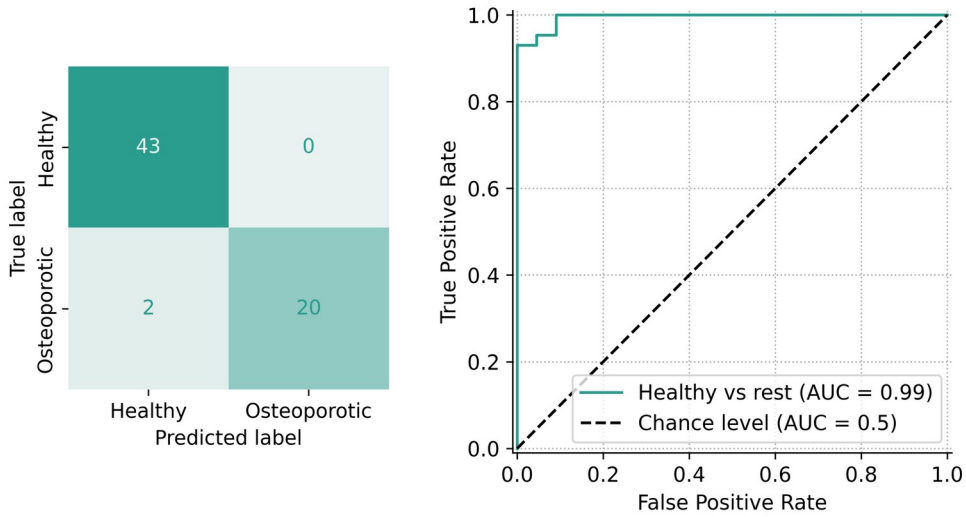

Figure 8.28: Confusion matrix (left) and ROC-AUC curve (right) used for the evaluation of the predictive PLS-DA model of humeri.

Bone quality assessment

The same parameters used to assess bone quality differences between healthy and osteoporotic tibias were also calculated for the humeri. Before calculating the bone quality parameters, band deconvolution was performed to extract the relevant spectral information required for the analysis.

Phosphate band (900-990 cm^{-1}) deconvolution

The phosphate band at 900-990 cm^{-1} was fitted with a single Gaussian and multiple Gaussians. The single-Gaussian fit is shown in Fig. 8.29. The FWHM was found decreased for the osteoporotic samples compared to the healthy.

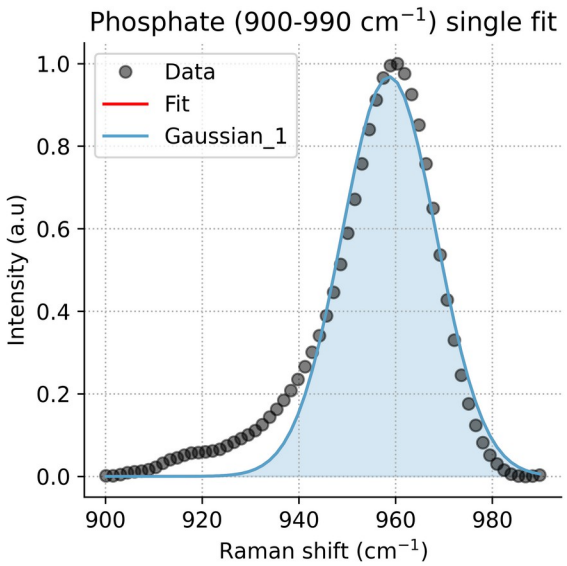

Figure 8.29: Fit of the main phosphate band (900–990 cm^{-1}) of humeri using a single Gaussian curve. The FWHM of the Gaussian is used to calculate the crystallinity of the samples.

The same band was also fitted with multiple Gaussians. The second derivative of the mean spectra was used to estimate the number of peaks contained in the band and to get estimates for the initial guesses of the deconvolution parameters (Fig. 8.30). The situation remained unchanged compared to the tibias, with two prominent features at 917 cm^{-1} and 960 cm^{-1}. Again, based on literature references and the observation that the use of four peaks presented significantly improvement to the overall fit quality, we employed four Gaussian curves for the deconvolution.

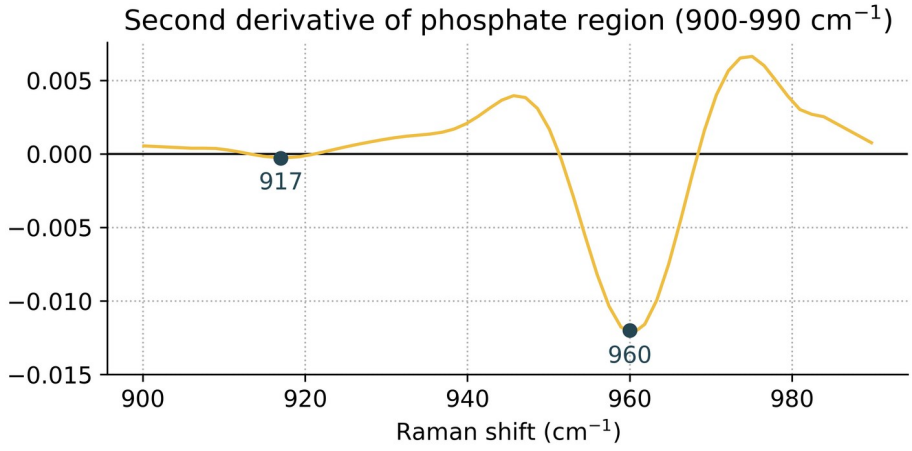

Figure 8.30: Second derivative of the main phosphate band (900–990 cm^{-1}) of humeri. Two prominent peaks are observed and annotated.

A representative deconvoluted phosphate band is shown in Fig. 8.31. The bands are the same as in the case of the tibias, at 920 cm^{-1}, 941 cm^{-1}, at 948 cm^{-1}, and 960 cm^{-1}, and are consistent with bands reported in the literature for this spectral region [3,4].

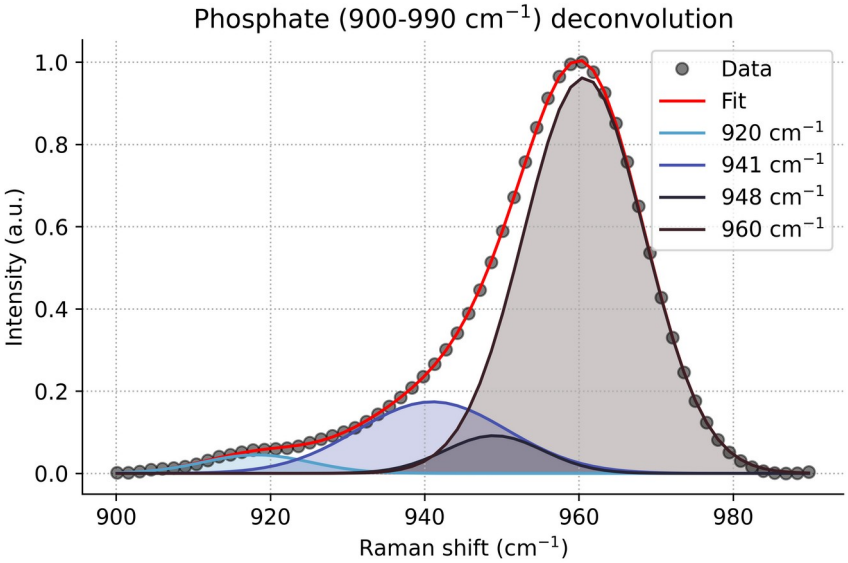

Figure 8.31: Deconvolution of the main phosphate band (900–990 cm^{-1}) of humeri with four Gaussian curves.

Amide I band (1580-1720 cm^{-1}) deconvolution

Similarly to the tibias, for deconvoluting the amide I band in the 1580-1720 cm^{-1} region we resorted to second derivative analysis. The second derivative of the mean spectra (Fig. 8.32) showed four prominent peaks at 1604 cm^{-1}, 1641 cm^{-1}, 1672 cm^{-1}, and 1694 cm^{-1}. These peaks were used as guidance for the initial guesses for the deconvolution of the region using four Gaussians.

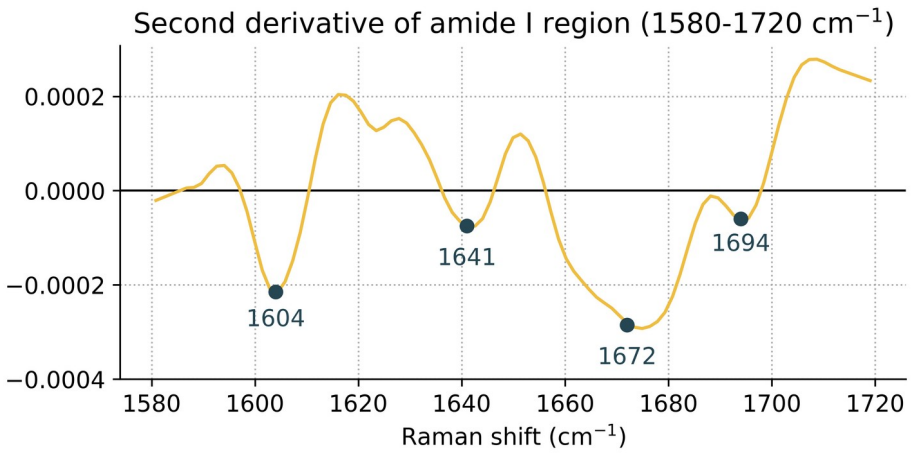

Figure 8.32: Second derivative of the amide I band (1580–1720 cm^{-1}) of humeri. Four prominent peaks are observed and annotated.

A representative deconvoluted amide I region is shown in Fig. 8.33. The deconvoluted peak positions are essentially the same as in the case of the tibias, at 1605 cm^{-1}, 1641 cm^{-1}, 1667 cm^{-1}, and 1688 cm^{-1}, consistent with peaks in this region reported by other studies [1,3,4].

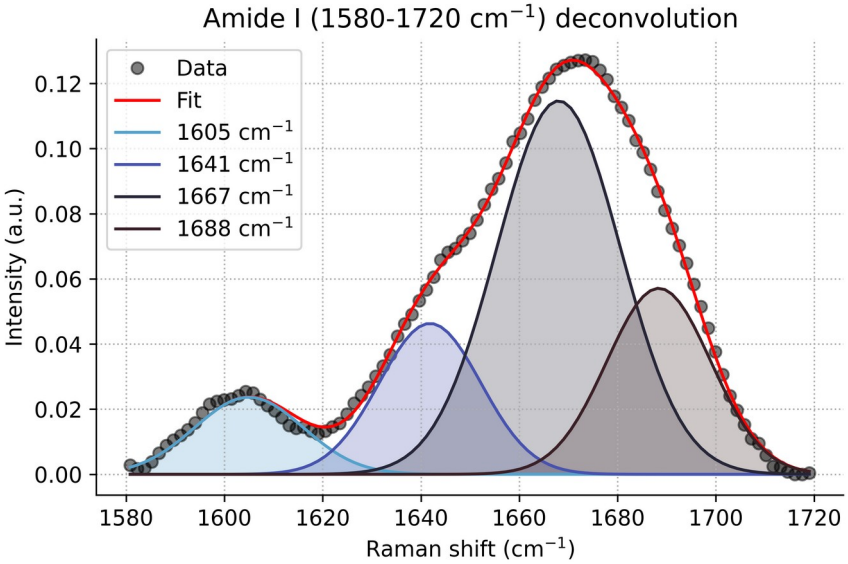

Figure 8.33: Deconvolution of the amide I band (1580-1720 cm^{-1}) of humeri with four Gaussian curves.

Carbonate band (990-1140 cm^{-1}) deconvolution

As with the tibias, the second derivative of the mean spectra of humeri was used for the deconvolution of the carbonate band in the 990-1140 cm^{-1} region. The second derivative of the

mean spectra (Fig. 8.34) showed six prominent peaks at 1006 cm^{-1}, 1027 cm^{-1}, 1045 cm^{-1}, 1073 cm^{-1}, 1106 cm^{-1}, and 1127cm^{-1}. Using these peaks as guidance for the initial guesses, we performed deconvolution of this region with six Gaussians.

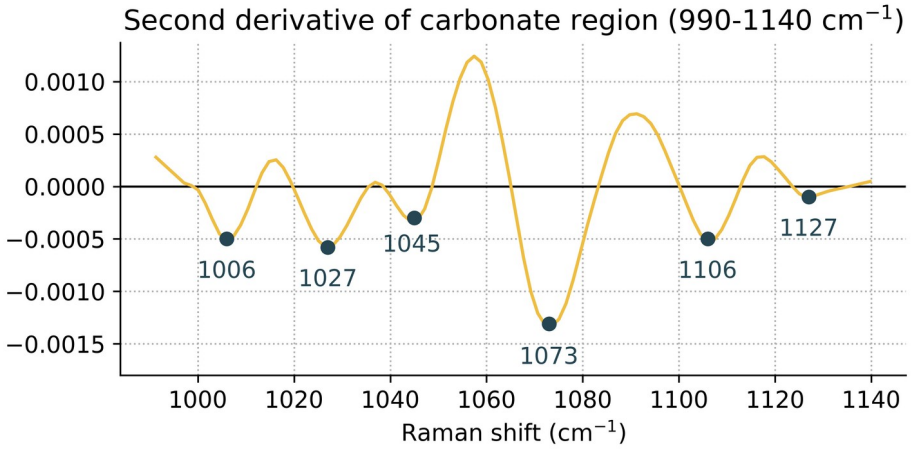

Figure 8.34: Second derivative of the carbonate band (990-1140 cm^{-1}) of humeri. Six prominent peaks are observed and annotated.

A representative deconvoluted amide I region is shown in Fig. 8.35. The deconvoluted peak positions are the same as in the case of the tibias, at 1005 cm^{-1}, 1025 cm^{-1}, 1044 cm^{-1}, 1074 cm^{-1}, 1104 cm^{-1}, and 1127cm^{-1}, consistent with the literature [1,3,4].

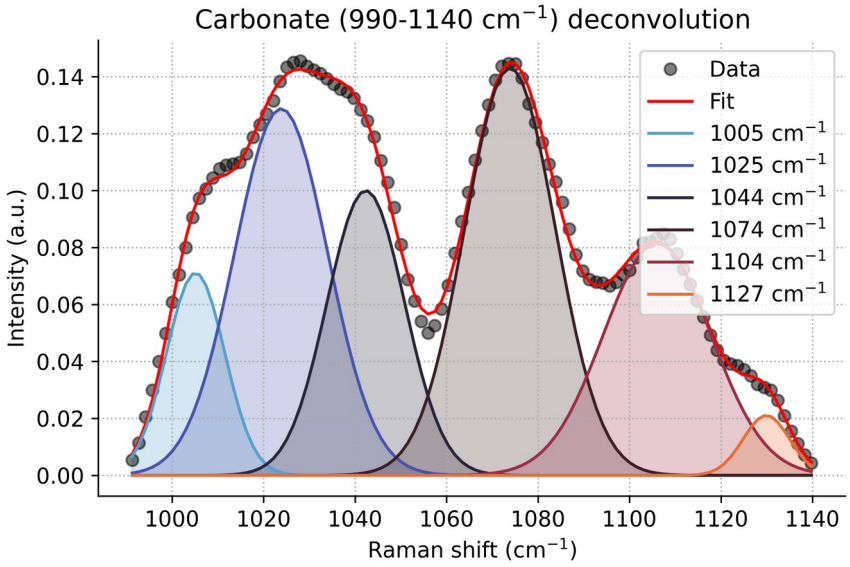

Figure 8.35: Deconvolution of the carbonate band (990-1140 cm^{-1}) of humeri with six Gaussian curves.

Proline-Hydroxyproline band (830-900 cm^{-1}) deconvolution

The second derivative of the mean spectra of the proline and hydroxyproline region (830-900 cm^{-1}) indicated two prominent peaks at 853 cm^{-1} and 882 cm^{-1} (Fig. 8.36). As we did for the tibias, based on the literature and the wellness of fit on the spectra, we also included peaks at 840 cm^{-1} and 890 cm^{-1} [3].

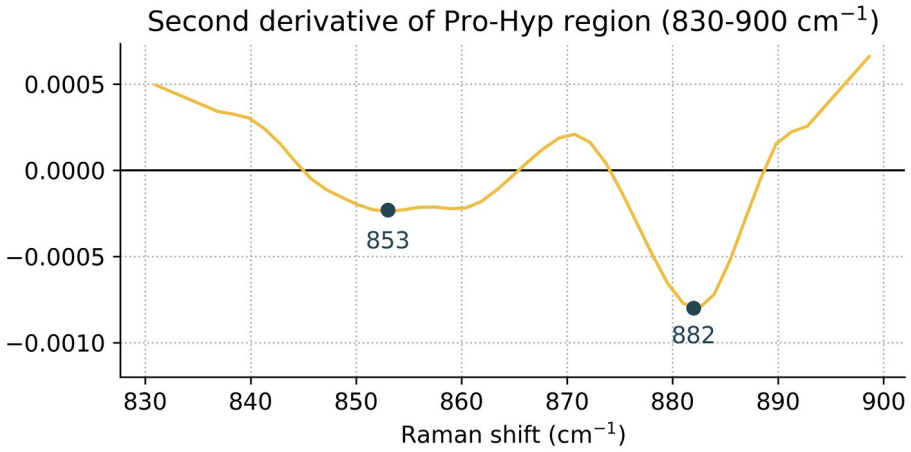

Figure 8.36: Second derivative of the proline-hydroxyproline band (830–900 cm^{-1}) of humeri. Two prominent peaks are observed and annotated.

A representative deconvoluted proline-hydroxyproline band is shown in Fig. 8.37. The fitted peaks were centered at approximately 842 cm^{-1}, 857 cm^{-1}, 878 cm^{-1}, and 890 cm^{-1}, all in agreement with literature [3,4].

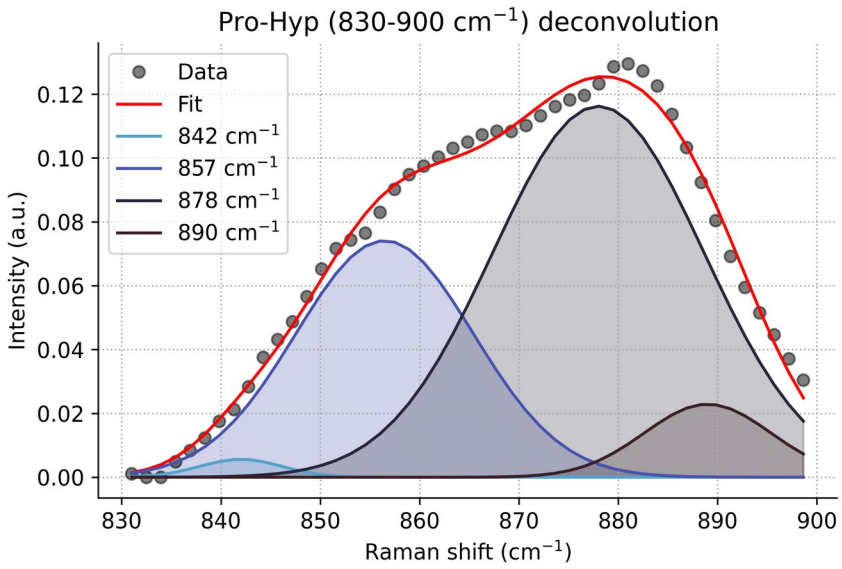

Figure 8.37: Deconvolution of the proline-hydroxyproline band (830–900 cm^{-1}) of humeri with four Gaussian curves.

Bone quality parameters

The bands obtained through deconvolution were used, as with the tibias, to calculate the following bone quality parameters: crystallinity, MMR, CPR, collagen maturity, and the Hyp/Pro ratio. The Shapiro-Wilk test was employed to assess the normality of the data. Depending on the results, either a two-sided t-test (for data satisfying the normality condition) or a Mann-Whitney U test (for data not satisfying the normality condition) was used to statistically evaluate differences in the means of these parameters between healthy and osteoporotic humeri. Extreme outliers, when identified, were excluded from further analysis to maintain data reliability and accuracy.

Boxplots of the bone quality parameters are shown in Fig. 8.38.

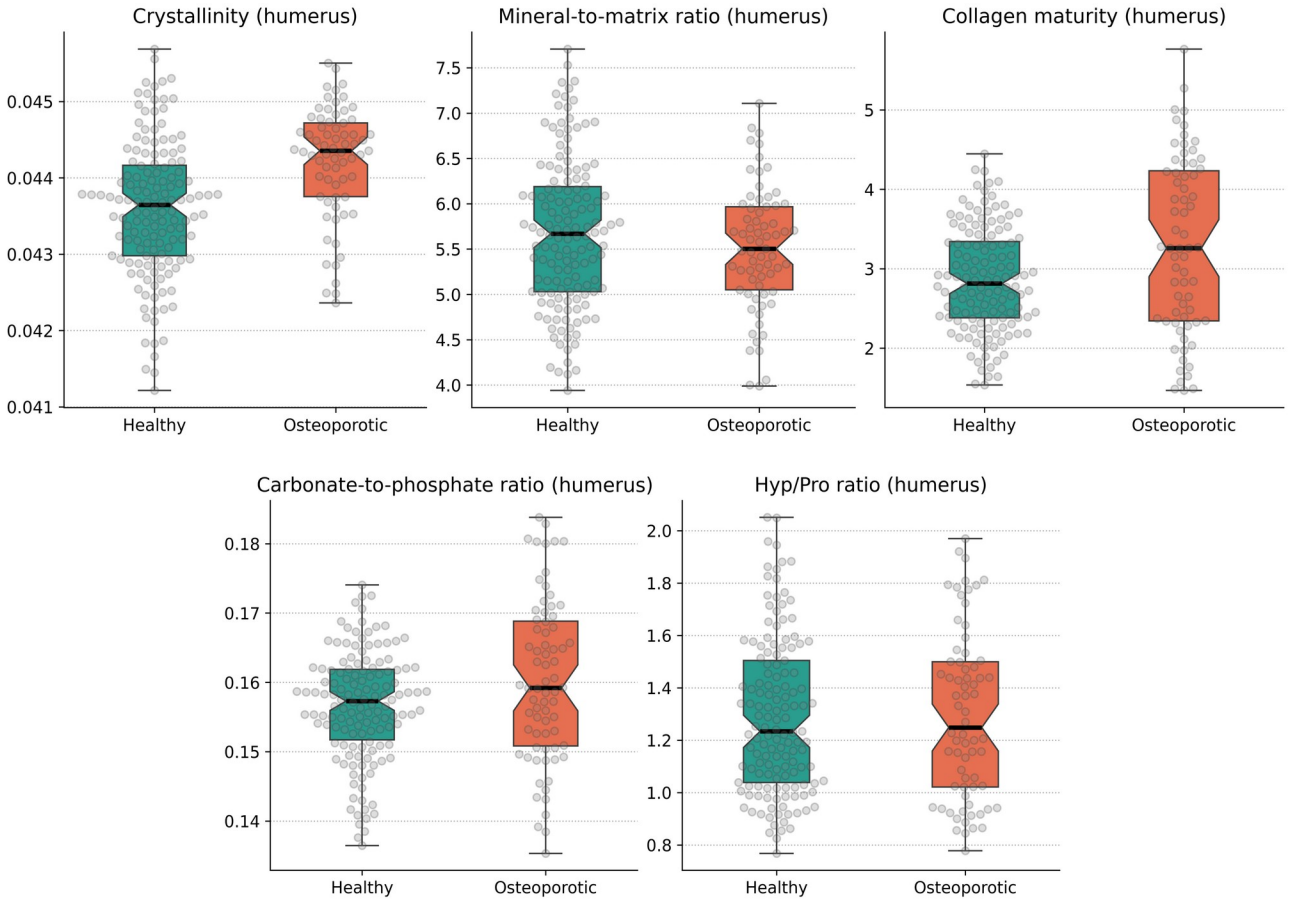

Figure 8.38: Bone quality parameters boxplots for the healthy and osteooporotic humeri.

The values of the bone quality parameters are presented in Table 7.

Table 7: Bone quality parameters for the healthy and osteoporotic humeri.

Parameter	Healthy (mean ± std)	Osteoporotic (mean ± std)	Test	*p*-value
Crystallinity (1/FWHM[960 cm^{-1}])	0.0436 ± 0.0009	0.0442 ± 0.0007	T	< 0.001
MMR (IA_{1667}/IA_{960})	5.7 ± 0.8	5.5 ± 0.7	T	NS
Collagen maturity (IA_{1667}/IA_{1988})	2.9 ± 0.7	3.3 ± 1.1	U	< 0.01
CPR (I_{1070}/I_{960})	0.157 ± 0.008	0.160 ± 0.012	T	< 0.01
Hyp/Pro (I_{876}/I_{856})	1.3 ± 0.2	1.4 ± 0.3	U	NS

T: t-test; U: Mann-Whitney U test; NS: not significant

8.1.3. Femur

The mean healthy and osteoporotic preprocessed Raman spectra from the transverse surface of the femurs are shown in Fig. 8.39. All Raman bands relevant to bone are observed. As in the case of the tibia and humerus, the only exception is the phenylalanine (1003 cm^{-1}) which appears as a shoulder in the lower end of the carbonate band at the 1000-1130 cm^{-1} region. The overall appearance of both spectra is similar, with the main differences observed at the v_2 and v_4 vibrations of phosphate at 430 cm^{-1} and 580 cm^{-1}, respectively, although these differences are less prominent than the ones observed in the mean spectra of tibia and humerus. Additionally, the top of the healthy spectra in the proline-hydroxyproline region (830-900 cm^{-1}) appears flatter compared of the mean healthy spectra of tibia and humerus at the same region (Fig. 8.40).

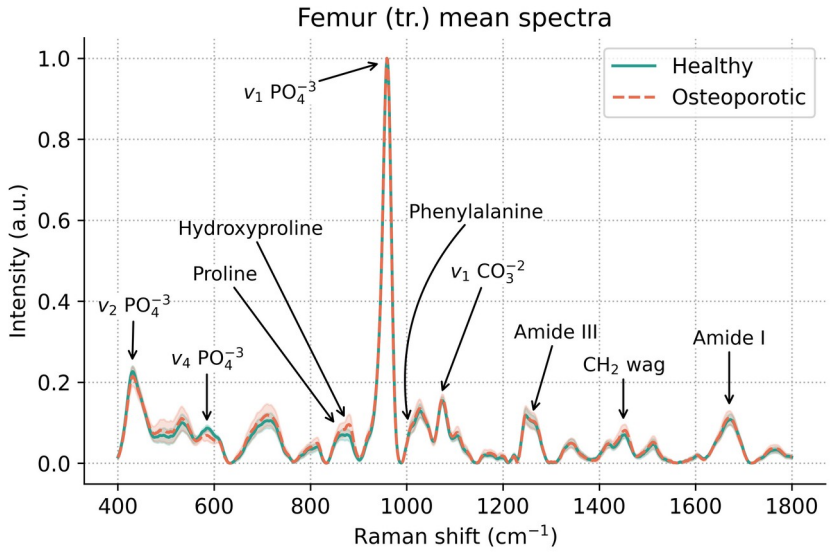

Figure 8.39: Mean preprocessed healthy and osteoporotic spectra from the transverse surface of the femurs. The main Raman bands are annotated. The shaded regions represent the standard deviations.

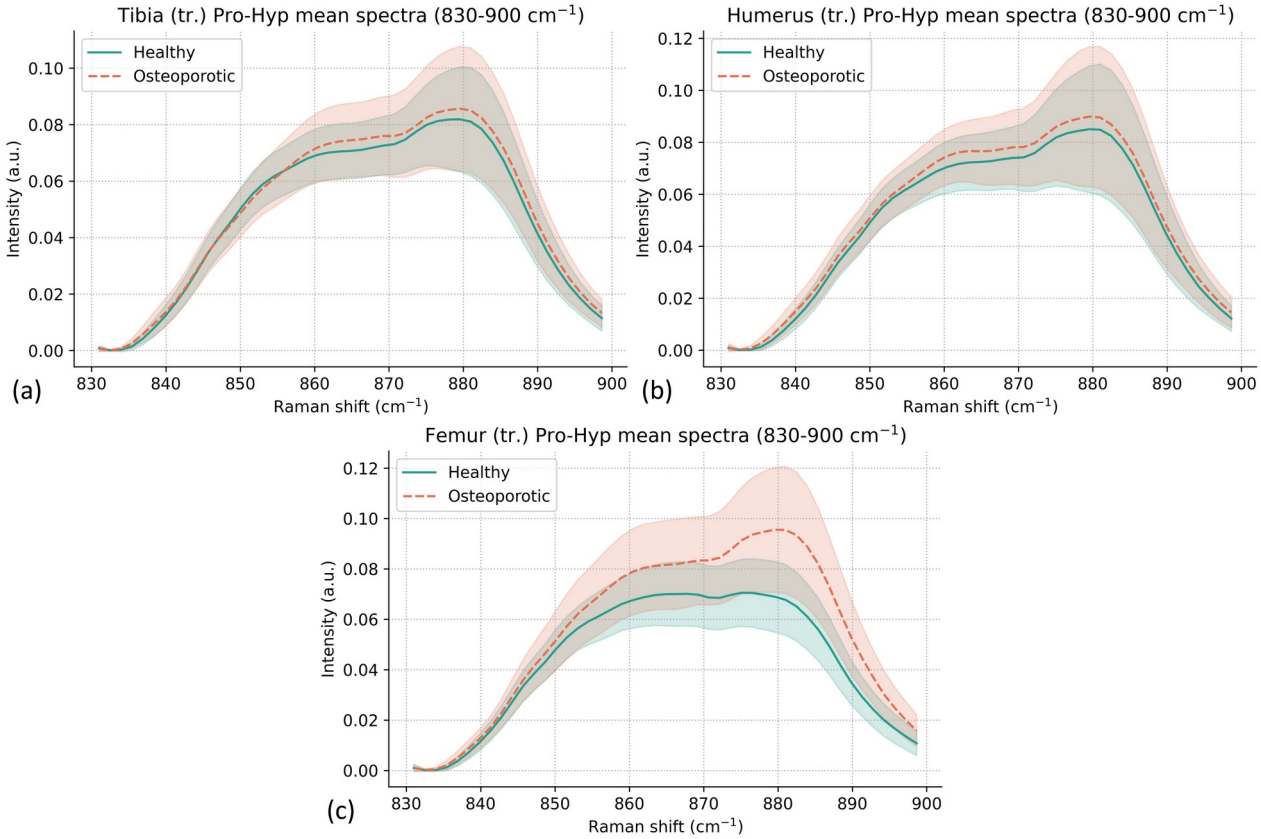

Figure 8.40: Mean spectra of roline-hydroxyproline regions of (a) tibias, (b) humeri, and (c) femurs. The healthy mean spectra for the femurs are flatter compared to the others.

Multivariate analysis

Principal Components Analysis (PCA)

We employed PCA with the purpose of uncovering insights and clustering patterns in the Raman spectra of the healthy and osteoporotic samples obtained from the femurs of the rabbits. The summary plot of PCA is shown in Fig. 8.41.

Partial separation of the two classes is observed in the PC1-PC3 and PC2-PC3 scores plots, with the separation occurring primarily along PC3 and secondarily along PC2, as also evident in the KDE plots (diagonal of scores plots) of PC2 and PC3. PC2 accounts for 5.68% of the total variance and PC3 for 5.30%, and together with PC1 explain 81.02% of the observed variance. Since the separation occurs at higher principal components compared to the PCA of tibias and humeri, this suggests that the effects of osteoporosis in the femurs are less pronounced.

In the PC3 loading, where most of the separation occurs, the peaks with the highest intensity are observed at 430 cm^{-1}, 592 cm^{-1}, corresponding to the ν_2 and ν_4 bending vibrations of phosphate, the same as in the cases of the tibias and humeri. Unlike these cases, however, the peak at 965 cm^{-1}, that appears due to the narrowing (increased crystallinity) of the main phosphate peak in osteoporosis, is less intense, suggesting a narrower phosphate peak compared to the healthy samples, but overall wider compared to the phosphate peaks observed in osteoporotic tibias and femurs (Fig. 8.42). All other bands in the PC3 loading show smaller contributions to the variance. Equal contributions from all bands are observed in the PC1 loading, while the most intense peak in the PC2 loading corresponds to hydroxyproline.

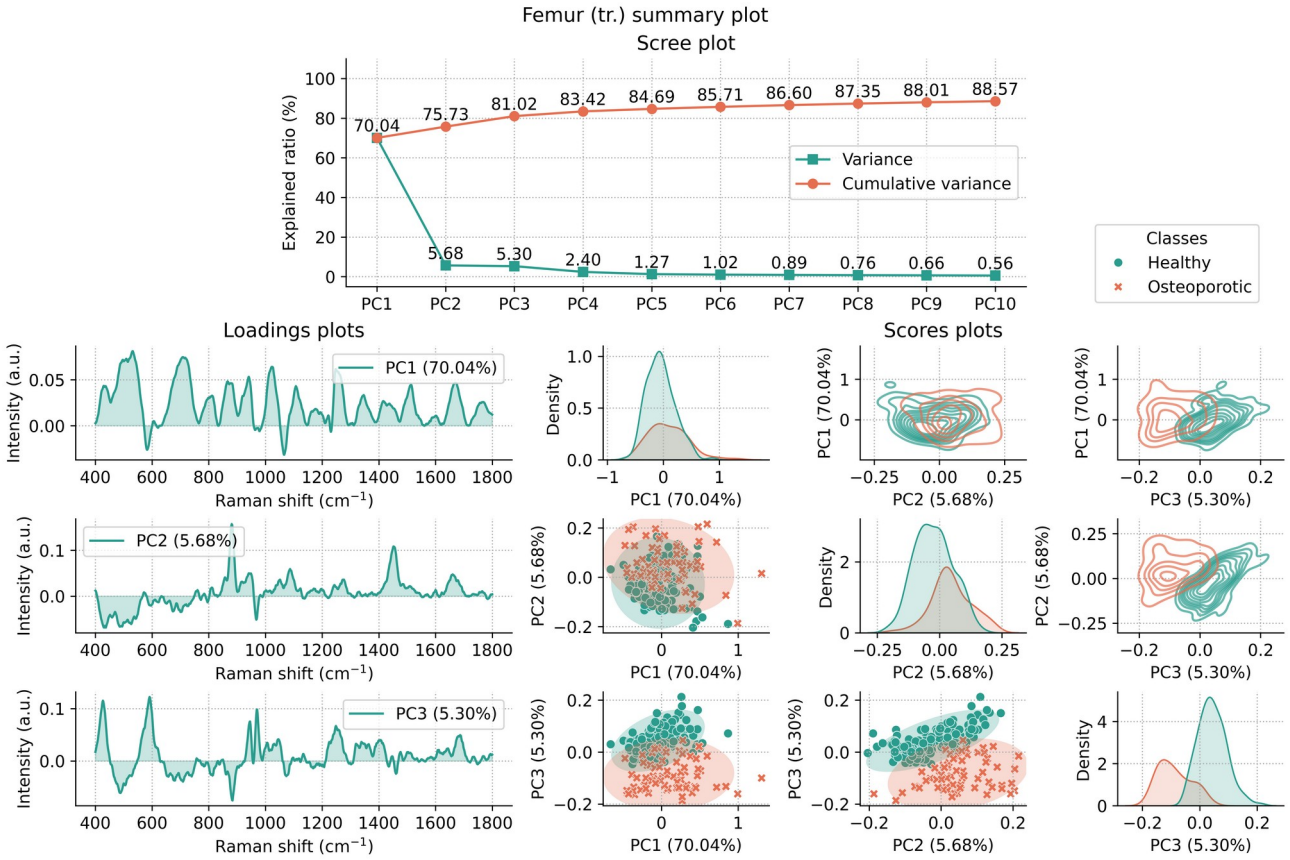

Figure 8.41: Summary plot of PCA results for the spectra collected from the transverse surfaces of the femurs.

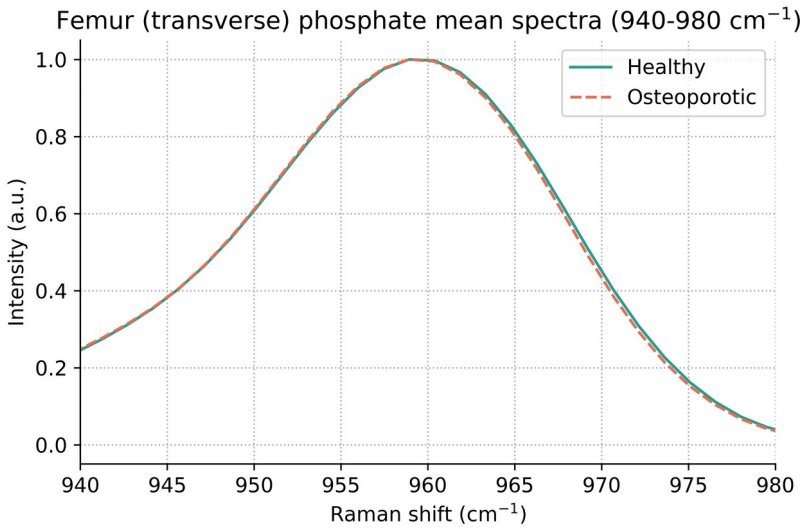

Figure 8.42: Mean spectra of femur samples at the 940-980 cm^{-1} spectral region. A decreased width of the main phosphate band is observed for osteoporotic samples, although the healthy and osteoporotic bands appear closer together compared to the cases for the tibia and the humerus.

The amide I region (1580-1720 cm^{-1}) in the PC3 loading does not display the same behavior as in the tibia, where the first half was negative and the second half was positive. However, the first half of the amide I region does display decreased intensity, similar to the humerus. Furthermore, as shown in Fig. 8.43, a shift in the amide I peak is observed for the femurs (from 1672 cm^{-1} to 1670 cm^{-1}) which is larger than in the case of the humerus (from 1672 cm^{-1} to 1671 cm^{-1}). This suggests alterations in the cross-linking of collagen during osteoporosis. These alterationss are more pronounced in the osteoporotic femurs compared to the humeri.

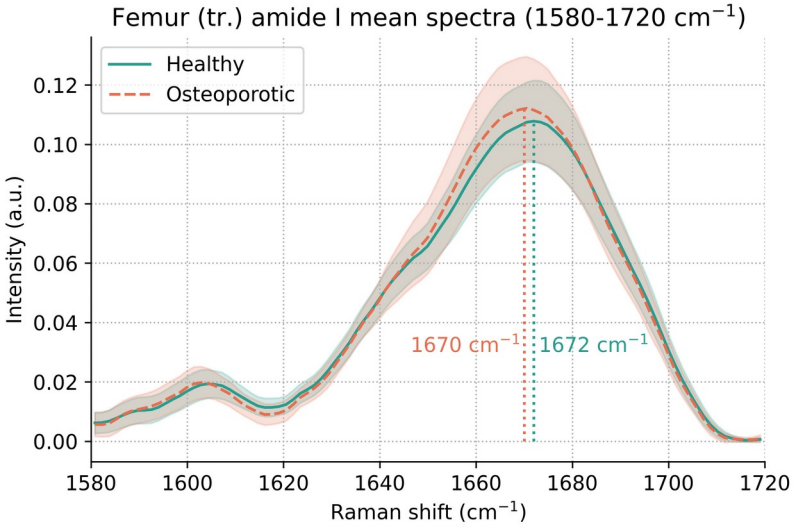

Figure 8.43: Mean spectra of femur samples at the 1580-1720 cm^{-1} spectral region. A shift of the amide I peak from 1672 cm^{-1} to 1670 cm^{-1} is observed for the osteoporotic samples.

Partial Least Squares Discriminant Analysis (PLS-DA)

In addition to PCA, PLS-DA was employed to create a predictive model. The spectra were split in 70/30 train/test ratio in a stratified manner using scikit-learn's `model_selection.train_test_split` function. This resulted to 151 spectra (101 healthy and 50 osteoporotic) for training the model and 65 spectra (43 healthy and 22 osteoporotic) for assessing the model's predictive capabilities.

The optimal number of components was determined using 5-fold stratified cross-validation with 10 repeats. The relevant evaluation metrics plot is shown in Fig. 8.44. From this plot we determined that the optimal number of components is 2, since this number yields high accuracy, minimum MSE, and similarly high values of R^2 and Q^2, with small standard deviation for all metrics. These metrics suggest that the 2 components model is well-fit and stable.

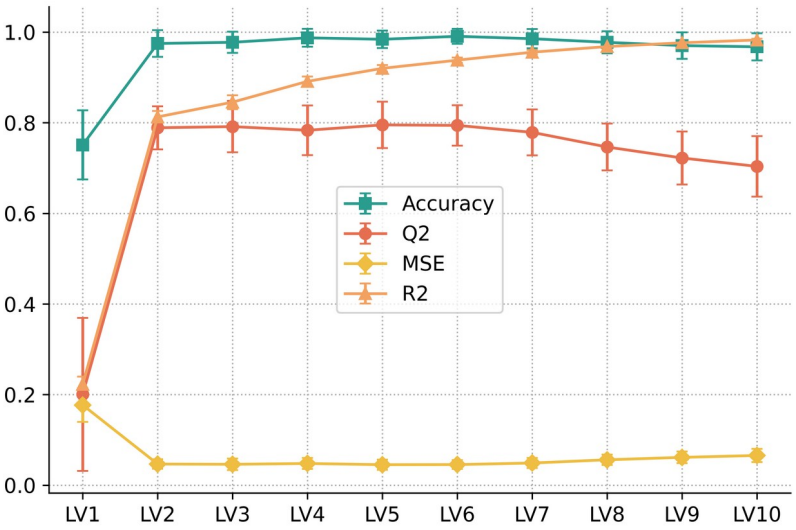

Figure 8.44: Cross-validation evaluation metrics of the PLS-DA model of femurs.

Subsequently, we created the PLS-DA model with 2 components, with the X- and Y-scores of the training data shown in Fig. 8.45 and Fig. 8.46, respectively. Good separation is observed between healthy and osteoporotic samples in the X-scores plot, with some overlap of the confidence ellipses. The Y-scores are well-separated.

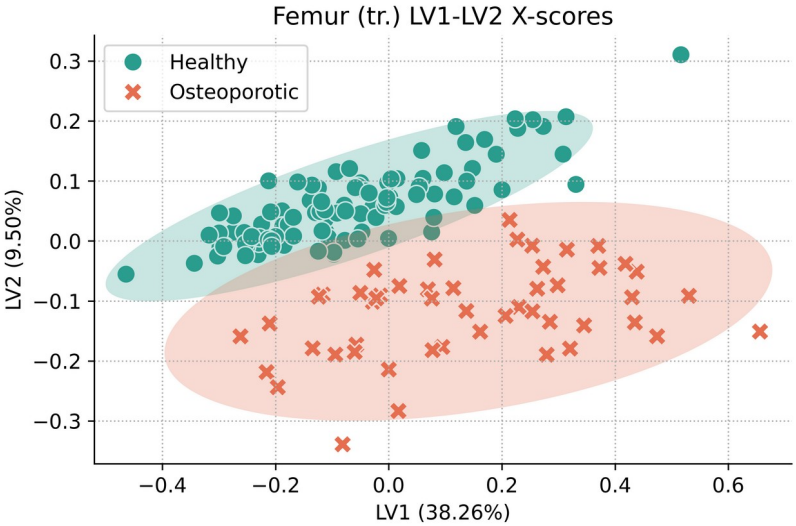

Figure 8.45: X-scores plot for the training data of the PLS-DA model of femurs with 2 components. The ellipses represent the 95% confidence ellipses.

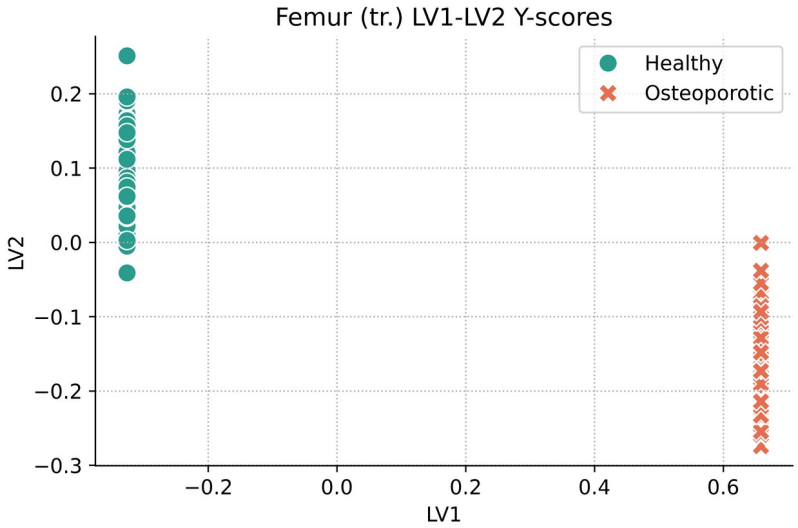

Figure 8.46: Y-scores plot for the training data of the PLS-DA model of femurs with 2 components.

The coefficients plot (Fig. 8.47) is similar to the case of PCA and to the case of the tibias and jumeri, indicating that the phosphate-related bands (v_2 and v_4 phosphate bands and the narrower main phosphate band in osteoporotic samples) are the primary contributors to the discrimination of the classes. An additional negative peak corresponding to hydroxyproline is also evident.

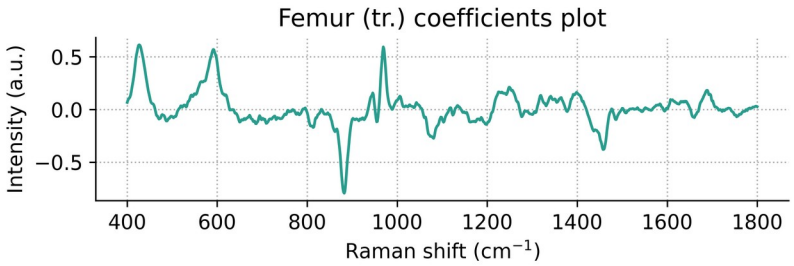

Figure 8.47: PLS-DA coefficients plot for the model of femurs.

The model's prediction capability was assessed using the confusion matrix and ROC curve (Fig. 8.48). The confusion matrix indicates that one osteoporotic sample was misclassified as healthy. This corresponds to an accuracy of 98.4%, a sensitivity of 97.7%, a specificity of 100%, and an F1 score of 98.8%. The AUC for this model is 1. While these results demonstrate that the PLS-DA model for the femurs performs very well in distinguishing healthy from osteoporotic samples, its performance is slightly lower than that of the tibial model.

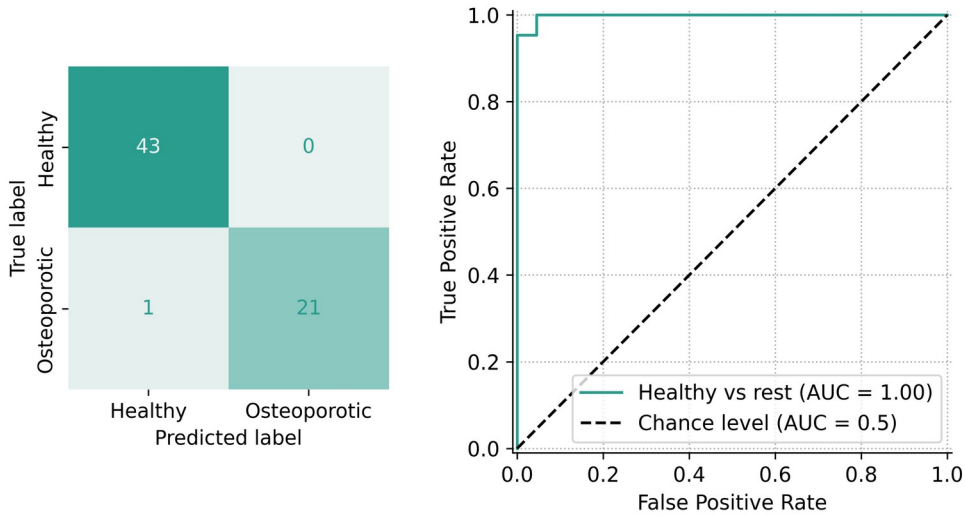

Figure 8.48: Confusion matrix (left) and ROC-AUC curve (right) used for the evaluation of the predictive PLS-DA model of femurs.

Bone quality assessment

The same parameters used to assess bone quality differences between healthy and osteoporotic tibias and humeri were also calculated for the femurs. Before calculating the bone quality parameters, band deconvolution was performed to extract the relevant spectral information required for the analysis.

Phosphate band (900-990 cm^{-1}) deconvolution

The phosphate band at 900-990 cm^{-1} was fitted with a single Gaussian and multiple Gaussians. The single-Gaussian fit is shown in Fig. 8.49. The FWHM was found decreased for the osteoporotic samples compared to the healthy.

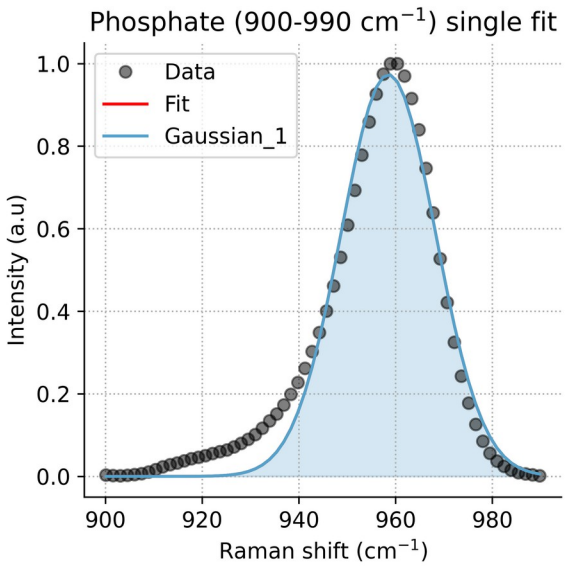

Figure 8.49: Fit of the main phosphate band (900–990 cm^{-1}) of femurs using a single Gaussian curve. The FWHM of the Gaussian is used to calculate the crystallinity of the samples.

The same band was also fitted with multiple Gaussians. The second derivative of the mean spectra was used to estimate the number of peaks contained in the band and to get estimates for the initial guesses of the deconvolution parameters (Fig. 8.50). The situation remained unchanged compared to the tibias and humeri, with two prominent features at 917 cm^{-1} and 960 cm^{-1}. Again, based on literature references and the observation that the use of four peaks presented significantly improvement to the overall fit quality, we employed four Gaussian curves for the deconvolution.

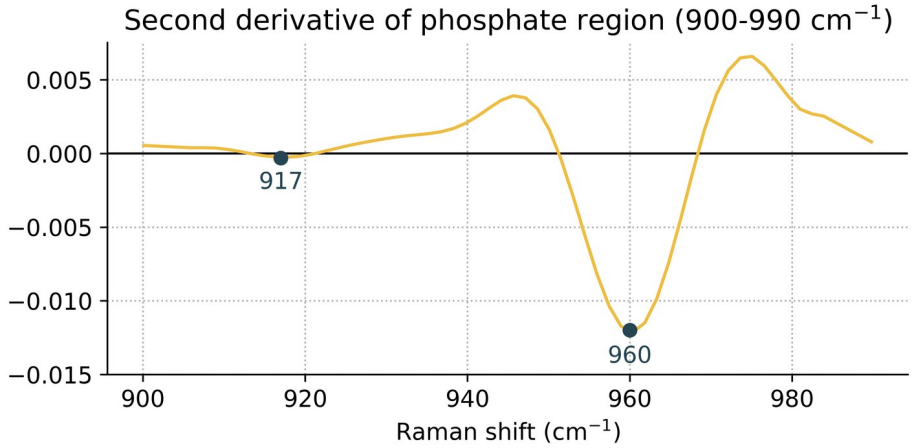

Figure 8.50: Second derivative of the main phosphate band (900–990 cm^{-1}) of femurs. Two prominent peaks are observed and annotated.

A representative deconvoluted phosphate band is shown in Fig. 8.51. The bands are the same as in the case of the tibias and humeri, at 920 cm^{-1}, 941 cm^{-1}, at 948 cm^{-1}, and 960 cm^{-1}, and are consistent with bands reported in the literature for this spectral region [3,4].

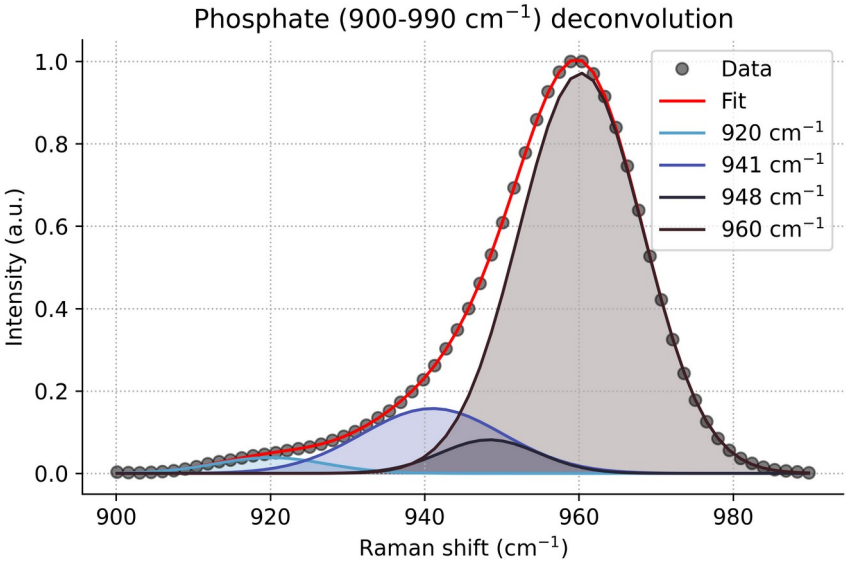

Figure 8.51: Deconvolution of the main phosphate band (900–990 cm^{-1}) of femurs with four Gaussian curves.

Amide I band (1580-1720 cm^{-1}) deconvolution

Similarly to the tibias and humeri, for deconvoluting the amide I band in the 1580-1720 cm^{-1} region we employed second derivative analysis. The second derivative of the mean spectra (Fig. 8.52) showed four prominent peaks at 1604 cm^{-1}, 1641 cm^{-1}, 1672 cm^{-1}, and 1694 cm^{-1}. These peaks were used as guidance for the initial guesses for the deconvolution of the region using four Gaussians.

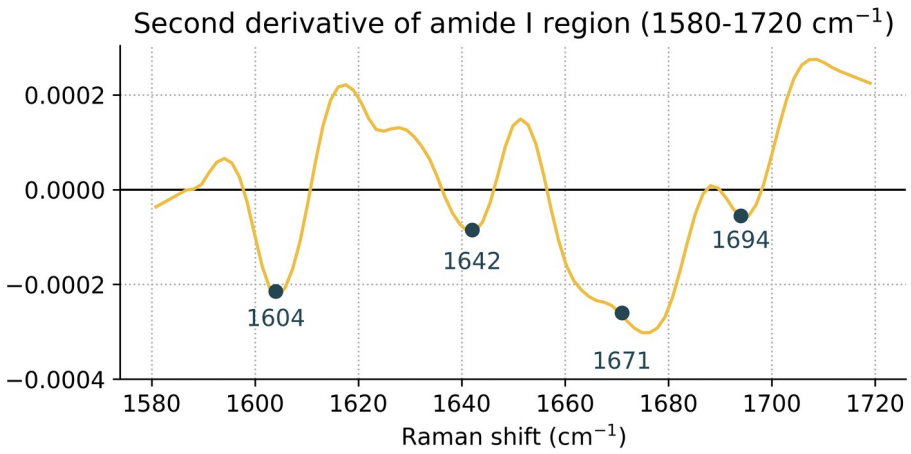

Figure 8.52: Second derivative of the amide I band (1580–1720 cm^{-1}) of femurs. Four prominent peaks are observed and annotated.

A representative deconvoluted amide I region is shown in Fig. 8.53. The deconvoluted peak positions are essentially the same as in the case of the tibias and humeri, at 1605 cm^{-1}, 1641 cm^{-1}, 1667 cm^{-1}, and 1688 cm^{-1}, consistent with peaks in this region reported by other studies [1,3,4].

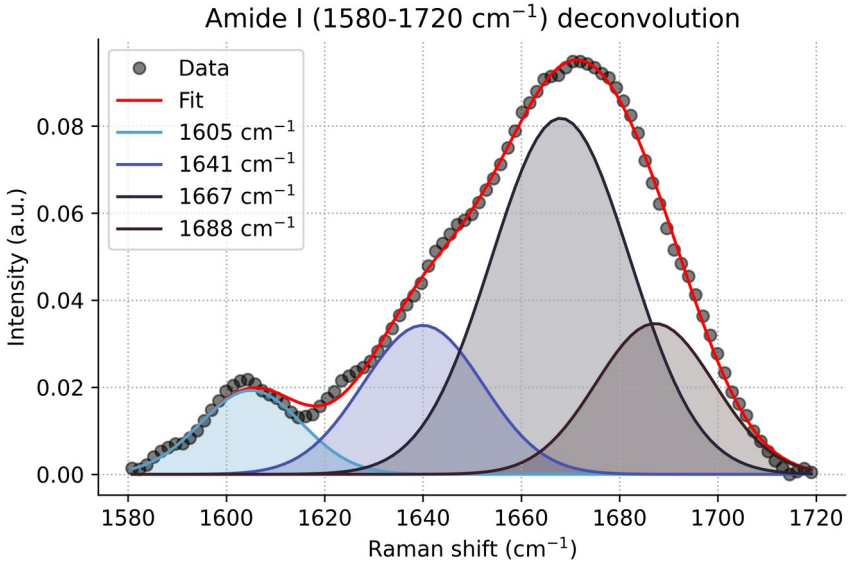

Figure 8.53: Deconvolution of the amide I band (1580-1720 cm^{-1}) of femurs with four Gaussian curves.

Carbonate band (990-1140 cm^{-1}) deconvolution

As with the tibias and humeri, the second derivative of the mean spectra of femurs was used for the deconvolution of the carbonate band in the 990-1140 cm^{-1} region. The second derivative of the

mean spectra (Fig. 8.54) showed six prominent peaks at 1006 cm^{-1}, 1027 cm^{-1}, 1045 cm^{-1}, 1073 cm^{-1}, 1106 cm^{-1}, and 1127cm^{-1}. Using these peaks as guidance for the initial guesses, we performed deconvolution of this region with six Gaussians.

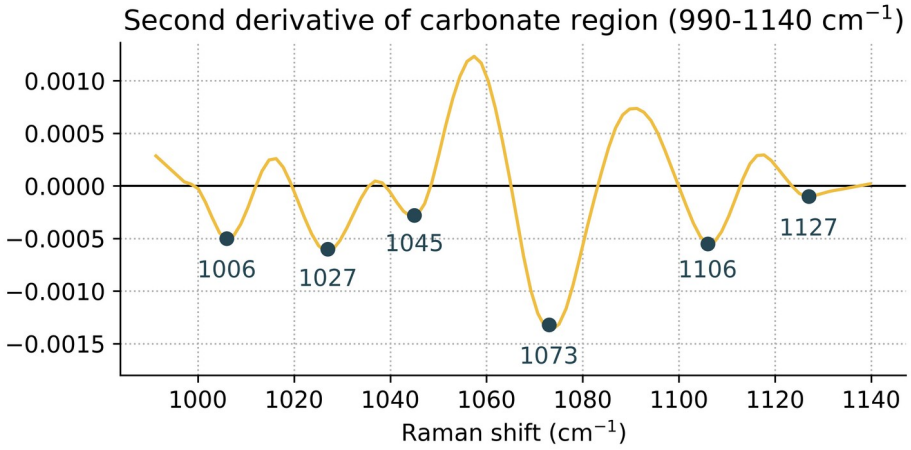

Figure 8.54: Second derivative of the carbonate band (990-1140 cm^{-1}) of femurs. Six prominent peaks are observed and annotated.

A representative deconvoluted amide I region is shown in Fig. 8.55. The deconvoluted peak positions are the same as in the case of the tibias and humeri, at 1005 cm^{-1}, 1025 cm^{-1}, 1044 cm^{-1}, 1074 cm^{-1}, 1104 cm^{-1}, and 1127cm^{-1}, consistent with the literature [1,3,4].

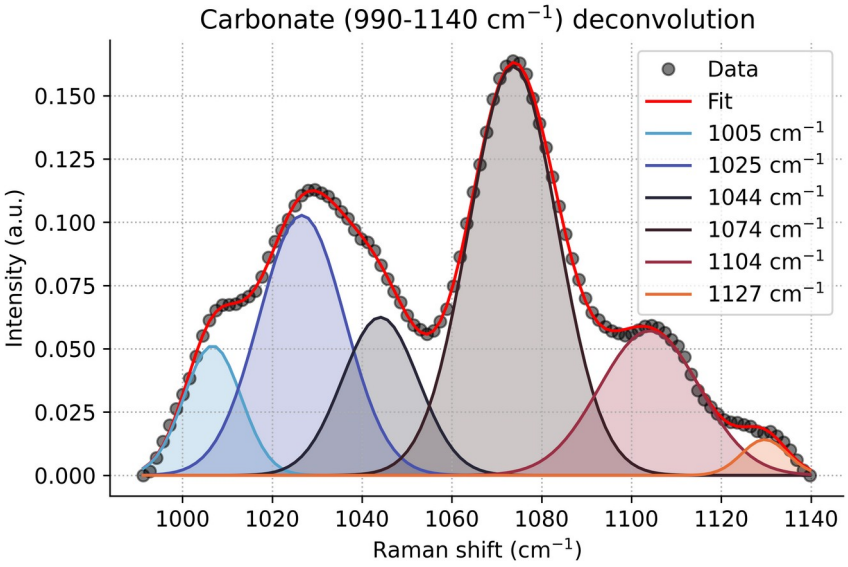

Figure 8.55: Deconvolution of the carbonate band (990-1140 cm^{-1}) of femurs with six Gaussian curves.

Proline-Hydroxyproline band (830-900 cm^{-1}) deconvolution

The second derivative of the mean spectra of the proline and hydroxyproline region (830-900 cm^{-1}) indicated two prominent peaks at 853 cm^{-1} and 882 cm^{-1} (Fig. 8.56). As we did for the tibias and humeri, based on the literature and the wellness of fit on the spectra, we also included peaks at 840 cm^{-1} and 890 cm^{-1} [3].

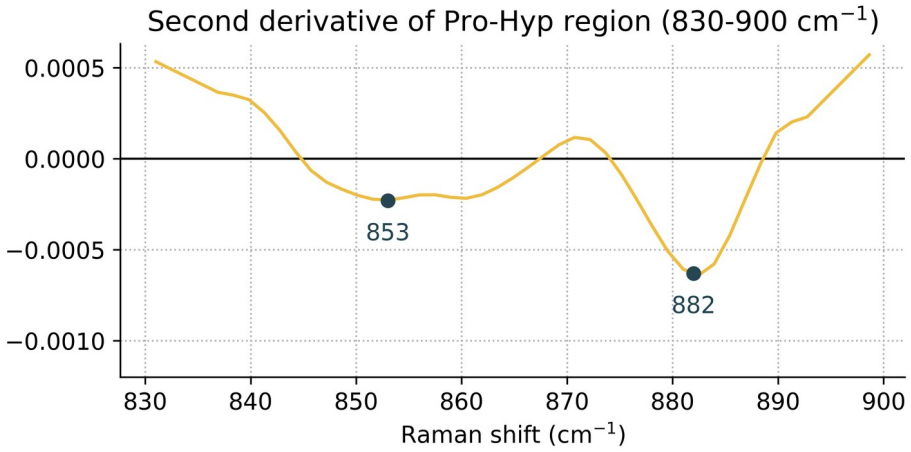

Figure 8.56: Second derivative of the proline-hydroxyproline band (830–900 cm^{-1}) of femurs. Two prominent peaks are observed and annotated.

A representative deconvoluted proline-hydroxyproline band is shown in Fig. 8.57. The fitted peaks were centered at approximately 842 cm^{-1}, 857 cm^{-1}, 877 cm^{-1}, and 890 cm^{-1}, all in agreement with literature [3,4].

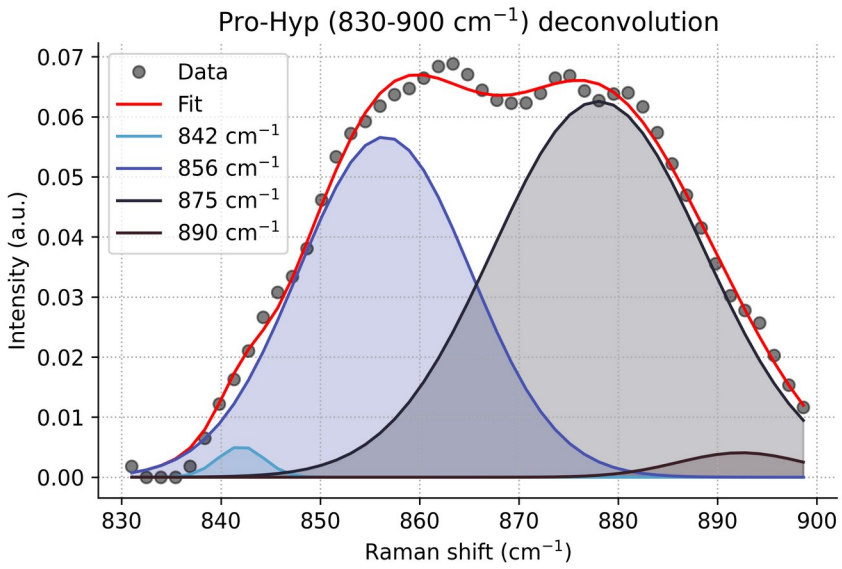

Figure 8.57: Deconvolution of the proline-hydroxyproline band (830–900 cm^{-1}) of femurs with four Gaussian curves.

Bone quality parameters

The bands obtained through deconvolution were used, similarly to the tibias and humeri, to calculate the following bone quality parameters: crystallinity, MMR, CPR, collagen maturity, and the Hyp/Pro ratio. The Shapiro-Wilk test was employed to assess the normality of the data. Depending on the results, either a two-sided t-test (for data satisfying the normality condition) or a Mann-Whitney U test (for data not satisfying the normality condition) was used to statistically evaluate differences in the means of these parameters between healthy and osteoporotic humeri. Extreme outliers, when identified, were excluded from further analysis to maintain data reliability and accuracy.

Boxplots of the bone quality parameters are shown in Fig. 8.58.

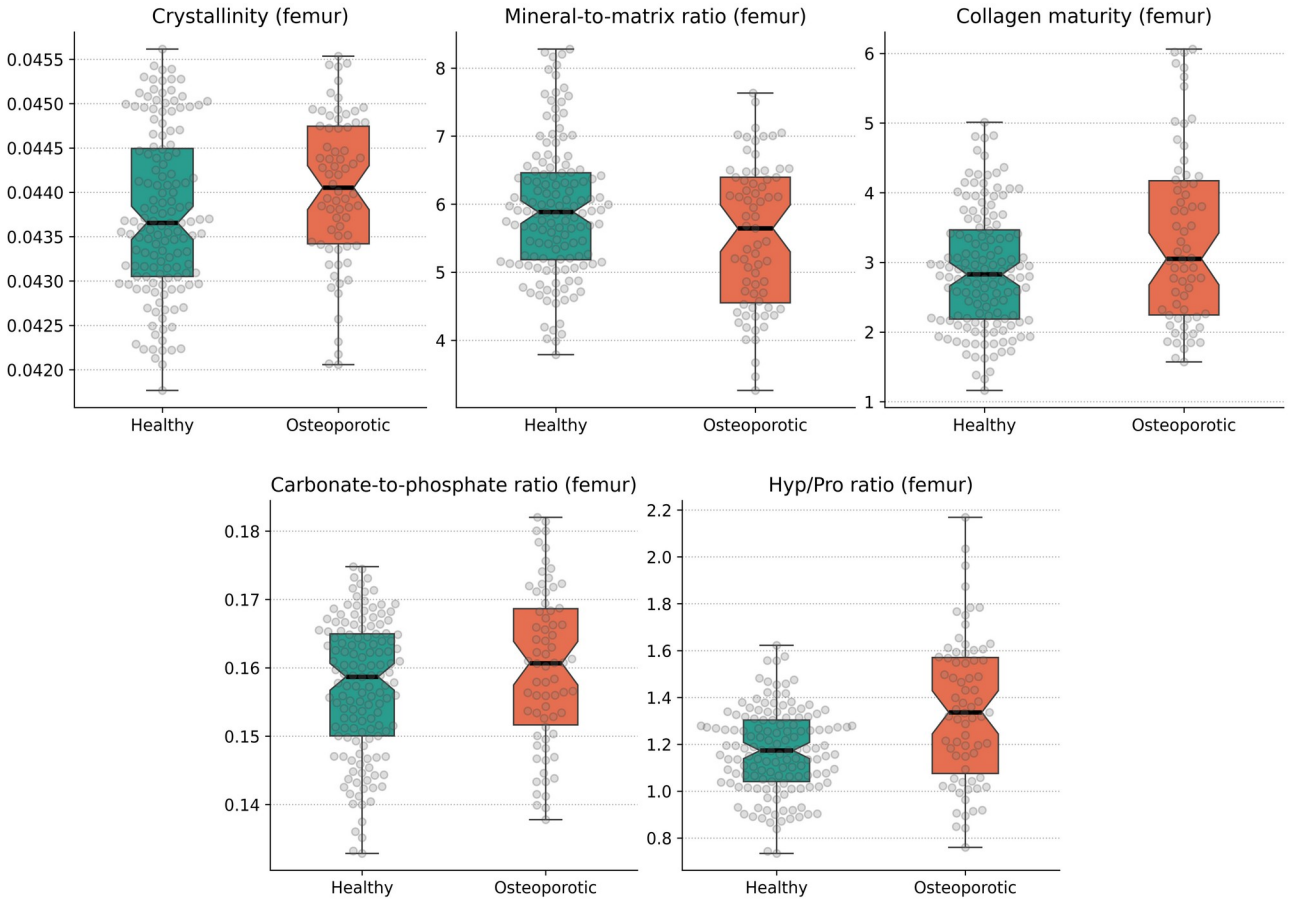

Figure 8.58: Bone quality parameters boxplots for the healthy and osteooporotic femurs.

The values of the bone quality parameters are presented in Table 8.

Table 8: Bone quality parameters for the healthy and osteoporotic femurs.

Parameter	Healthy (mean ± std)	Osteoporotic (mean ± std)	Test	*p*-value
Crystallinity (1/FWHM[960 cm^{-1}])	0.0438 ± 0.0009	0.0440 ± 0.0009	M	< 0.05
MMR (IA_{1667}/IA_{960})	5.9 ± 1.0	5.5 ± 1.1	M	< 0.05
Collagen maturity (IA_{1667}/IA_{1988})	2.3 ± 0.5	2.7 ± 1.3	M	< 0.05
CPR (I_{1070}/I_{960})	0.157 ± 0.010	0.160 ± 0.012	U	NS
Hyp/Pro (I_{876}/I_{856})	1.2 ± 0.2	1.3 ± 0.3	T	< 0.001

T: t-test; U: Mann-Whitney U test; NS: not significant

8.1.4. Discussion

The molecular changes in bone quality parameters across the tibias, humerus, and femurs provide a comprehensive view of the effects of osteoporosis on bone composition and structure, as revealed through Raman spectroscopy. The analysis of crystallinity, mineral-to-matrix ratio (MMR), collagen maturity, carbonate-to-phosphate ratio (CPR), and the hydroxyproline-to-proline ratio (Hyp/Pro) reveals site-specific trends and significant alterations in both the mineral and collagen matrix.

Crystallinity, an important indicator of mineral organization and size, exhibited significant increases in all three skeletal sites. In the tibias, the difference in crystallinity was highly significant (t-test, $p < 0.001$), reflecting the growth of larger, more ordered hydroxyapatite crystals due to reduced remodeling turnover. Similar trends were observed in the humerus and femurs, with significant increases ($p < 0.001$ and $p < 0.05$, respectively), suggesting consistent remodeling dysregulation across skeletal sites. These findings align with those of Paschalis et al. [8], who used FTIR spectroscopy to demonstrate increased mineral crystal size and perfection in osteoporotic bone, attributed to prolonged crystal maturation caused by reduced remodeling turnover. Similarly, Ruppel et al. confirmed that osteoporotic bone exhibits larger and more ordered hydroxyapatite crystals, which, while structurally stable, compromise mechanical properties by increasing brittleness and reducing energy dissipation [9].

The MMR, reflecting the balance between the inorganic and organic components of bone, showed significant reductions in the tibias (t-test, $p < 0.001$) and femurs (Mann-Whitney U test, $p < 0.05$) but no significant difference in the humerus (p = NS). These findings suggest impaired mineral deposition and increased resorption in osteoporotic bone at weight-bearing sites, consistent with other studies of animal models [3,10,11]. In contrast, the lack of significant change in the humerus may reflect regional variability in mineralization, potentially influenced by differences in biomechanical loading or remodeling dynamics.

Collagen maturity, indicative of cross-linking profiles, exhibited significant increases across all skeletal sites, with the tibias showing the most pronounced change (t-test, $p < 0.001$), followed by the humeri (Mann-Whitney U test, $p < 0.01$) and femurs (Mann-Whitney U test, $p < 0.05$). These findings are consistent with reports by Orkoula et. al, who observed altered Raman spectral signatures associated with increased non-enzymatic cross-links in osteoporotic bone [3]. The accumulation of advanced glycation end-products (AGEs) in collagen reduces its toughness, contributing to fragility across skeletal sites. This regional consistency underscores the systemic nature of collagen alterations in osteoporosis.

The CPR, which indicates the extent of carbonate substitution in hydroxyapatite, showed no significant differences in the tibias and femurs (p = NS) but was significantly increased in the osteoporotic humerus (Mann-Whitney U test, $p < 0.01$). The increased CPR in the humerus suggests a greater degree of carbonate incorporation into the hydroxyapatite lattice, which can weaken the mineral's structural stability and stiffness. This regional variability may be attributed to differences in local remodeling dynamics and metabolic activity.

The Hyp/Pro ratio, reflecting collagen hydroxylation levels, showed mixed results. No significant differences were observed in the tibias and humeri, suggesting stable hydroxylation levels in these regions. However, a significant increase was detected in the femurs (t-test, $p < 0.001$), indicating localized changes in collagen post-translational modifications.

Overall, the findings highlight both systemic and site-specific alterations in bone quality due to osteoporosis. Increased crystallinity and altered collagen crosslinking are consistent features across all skeletal sites, underscoring their pivotal role in reducing bone's mechanical competence. Site-specific differences in MMR, CPR, and Hyp/Pro further emphasize the complexity of osteoporotic changes and their dependence on local remodeling dynamics and mechanical loading. Raman spectroscopy has proven capable of capturing these changes in the IMO model of New Zealand rabbits, offering a detailed and non-destructive means of studying the molecular basis of bone fragility.

8.2. Prospects for Spatially-offset Raman Spectroscopy (SORS)

The Raman spectra that were collected from the periosteal surface of the tibia, humerus, femur, and ribs were used for a pilot study to assess the feasibility of using the inflammation-mediated

osteoporosis (IMO) model in rabbits to investigate osteoporosis-induced changes with SORS. SORS is a Raman technique that allows the extraction of Raman signal from deeper layers within a tissue by varying the offset between the point of excitation and the point of signal collection [12]. The study aimed to determine whether osteoporotic samples could be distinguished from healthy samples based on Raman measurements from the periosteal surface. Given our lab's development of a custom SORS configuration [13], this work represents a step toward applying SORS to differentiate healthy and osteoporotic ex-vivo bone samples. The ultimate goal is to translate this technique into clinical practice for in-vivo assessment of osteoporosis in humans by capturing sub-epidermal Raman spectra of bone.

The mean preprocessed healthy and osteoporotic spectra collected from the periosteal surfaces of tibias, humeri, femurs, and ribs are shown in Fig. 8.59. All characteristic spectral features of bone are present, with the exception, as in the case of the transverse measurements, of the phenylalanine peak at ∼1003 cm^{-1}, which appears as a shoulder on the lower end of the carbonate band. The healthy and osteoporotic spectra from tibias, humeri, and femurs appear largely similar, with only small differences in corresponding band intensities. However, the spectra from the ribs show larger differences in corresponding bands, with osteoporotic bands being much lower in intensity compared tho the healthy. Additionally, larger standard deviations are observed for the ribs, highlighting greater variability for this skeletal site.

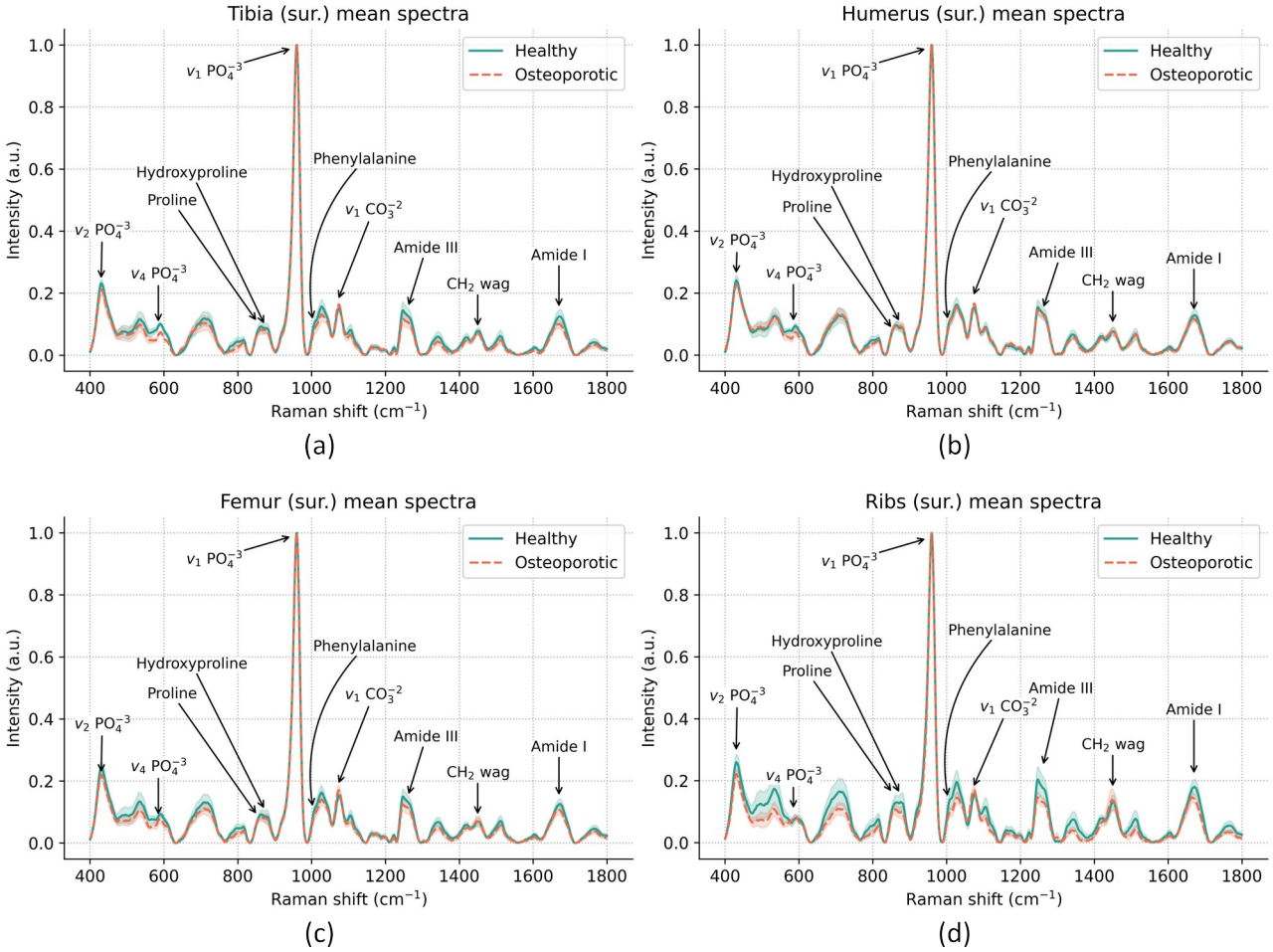

Figure 8.59: Mean preprocessed healthy and osteoporotic spectra from the surfaces of (a) tibias, (b) humeri, (c) femurs, (d) ribs. The shaded regions represent the standard deviations of the means.

PCA was used for all skeletal sites to uncover any clustering patterns that could indicate separation between the two classes, thus supporting the feasibility of future SORS experiments. Summary plots of the PCAs of all skeletal sites are shown in the following series of figures (Fig. 8.60-8.63).

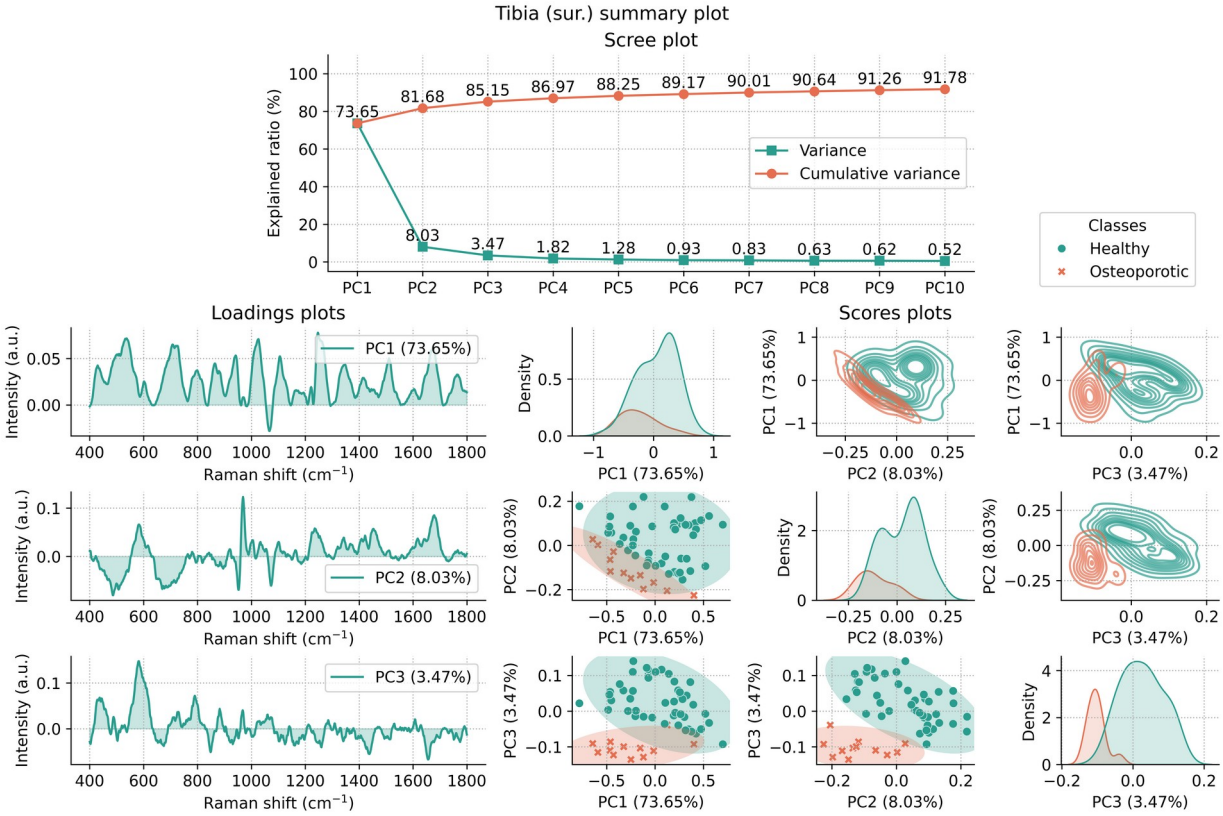

Figure 8.60: Summary plot of PCA results for the spectra collected from the periosteal surface of the tibias.

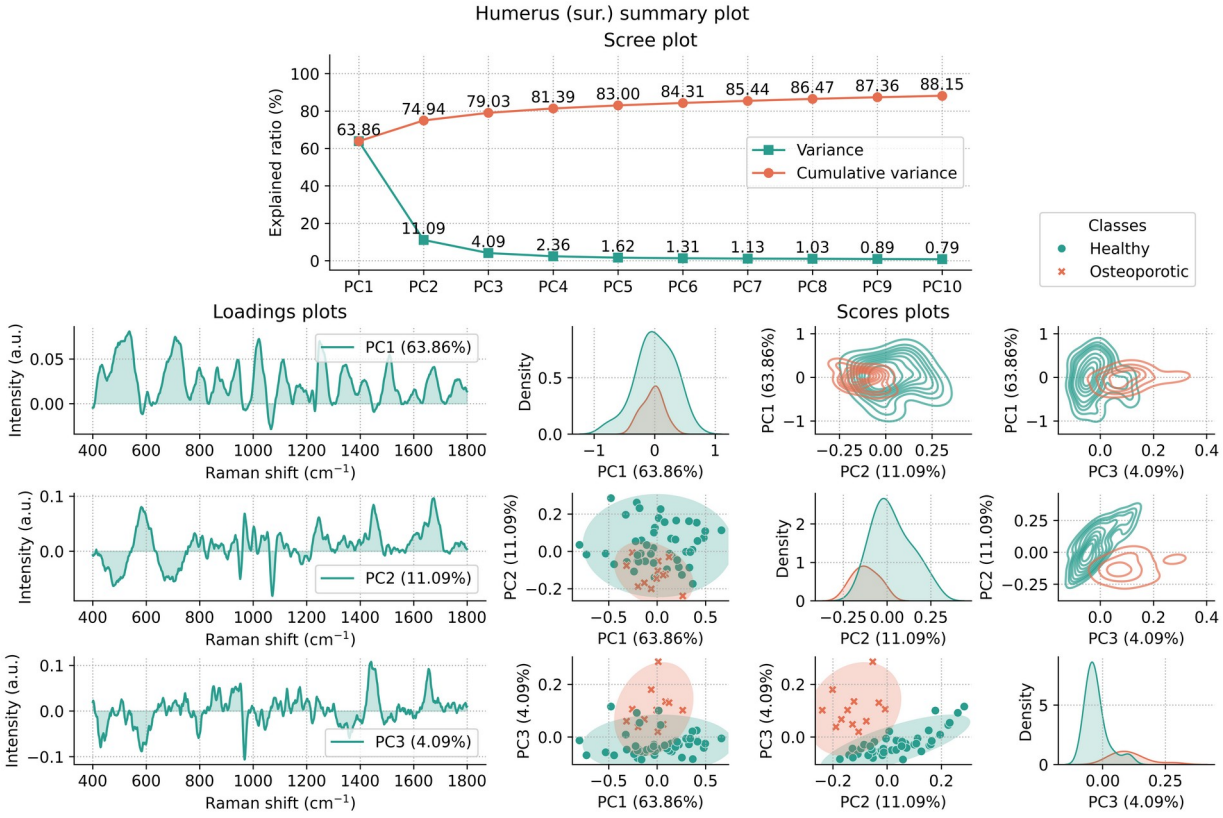

Figure 8.61: Summary plot of PCA results for the spectra collected from the periosteal surface of the humeri.

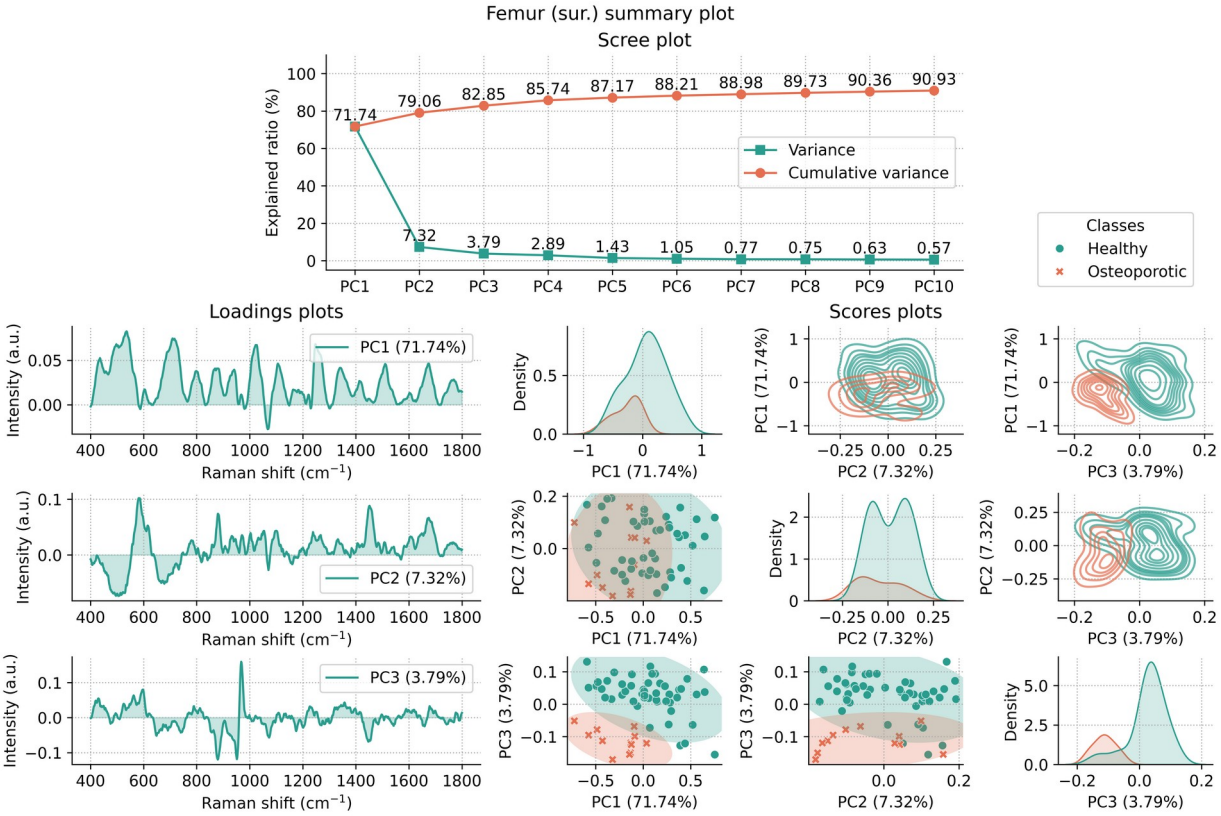

Figure 8.62: Summary plot of PCA results for the spectra collected from the periosteal surface of the femurs.

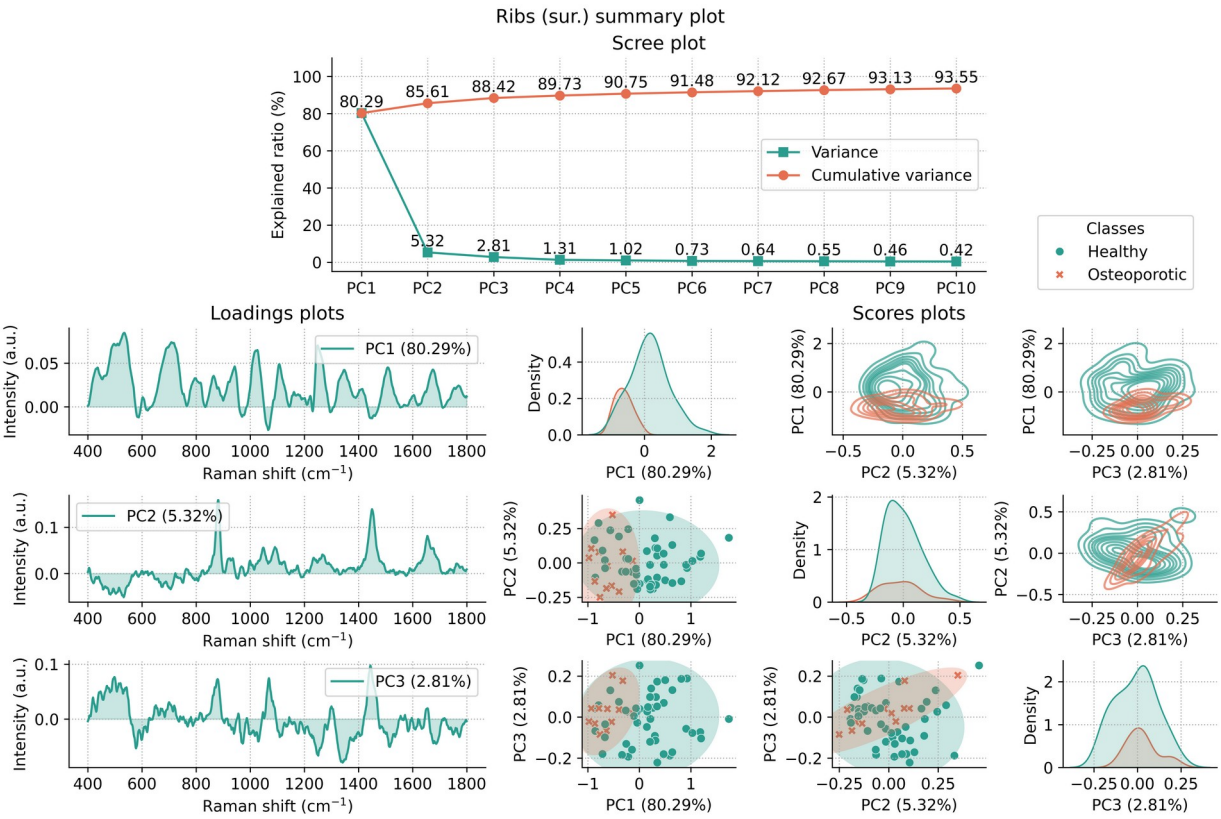

Figure 8.63: Summary plot of PCA results for the spectra collected from the periosteal surface of the ribs.

In the PCA of the tibias, separation can be observed in the PC2-PC3 scores plot, primarily along the PC3 axis, with PC2 explaining 8.03% of the variance and PC3 explaining 3.47% of the variance. Along with PC1, these three PCs explain 85.15% of the total variance. Similarly, in the humerus case, there is separation between the two classes in PC2-PC3, with the separation mainly occurring along PC3. PC1, PC2, and PC3 account for 63.86%, 11.09%, and 4.09% of the variance, and together explain 79.03% of the observed variance. The PCA of the femurs also shows class separation in the PC1-PC3 plot, primarily along PC3. PC1 accounts for 71.74% of the variance of the data, PC3 accounts for 3.79% of the variance, and, adding PC2 (7.32%), the first three PCs explain 82.85% of the variance. No separation is observed for the case of ribs. Excluding the ribs, the loadings of all other skeletal sites present similarities with the spectra obtained from the transverse surfaces of the corresponding sites, with prominent features related to the mineral content.

These findings demonstrate that the IMO model in New Zealand rabbits induces alterations in both cortical bone and the periosteal surface of long bones (tibia, humerus, femur), which are detectable using Raman spectroscopy. This pilot study highlights the potential of the IMO model as a controlled osteoporosis model suitable for investigation with SORS.

8.3. Neutron diffraction

Lab X-ray diffraction patterns of biological apatite suffer from decreased resolution due to the largely amorphous part of HA. Furthermore, the scattering power is dependent of 2-theta, making Bragg peaks indistinguishable at higher degrees. It is evident that no successful Rietveld analysis can be performed with data similar to that from the representative patterns shown in Fig. 8.64, where a pattern from a healthy bone sample (blue) is compared to a pattern from an osteoporotic one (red). Small differences, mainly localized at the FWHM peak values, were associated with the crystal size under the same instrumental configuration.

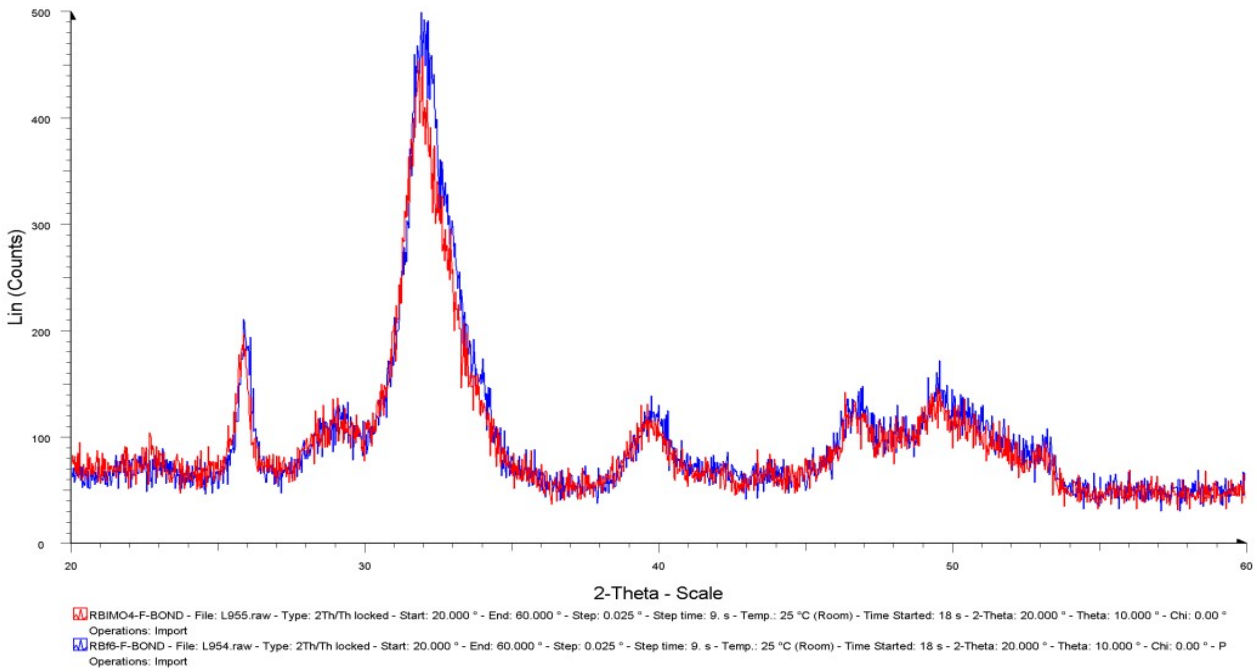

Figure 8.64: Typical X-ray diffraction spectra of mildly heat-treated (150°C) healthy (blue) and osteoporotic (red) bones (bones were heated for water removal).

On the other hand, the large incoherent scattering cross-section of hydrogen, which exists in collagen, is an obstacle for neutron diffraction studies. This problem, however, can be minimized by heating the samples up to 350°C. Heat treatment at this temperature has no detectable effect on the size, crystallinity, or lattice spacing of the crystals of the Ha, while at the same time it effectively removes most of the organic part [14].

Scanning Electron Microscopy (SEM) coupled with Energy Dispersive X-ray (EDX) analysis was conducted to evaluate the elemental composition ratios of the heated samples, confirming notable variations in these ratios. (Fig. 8.65). Specifically, the SEM/EDX results revealed a Ca/P ratio of 1.53 in normal bone samples, compared to 1.32 in osteoporotic bone samples (Table 9).

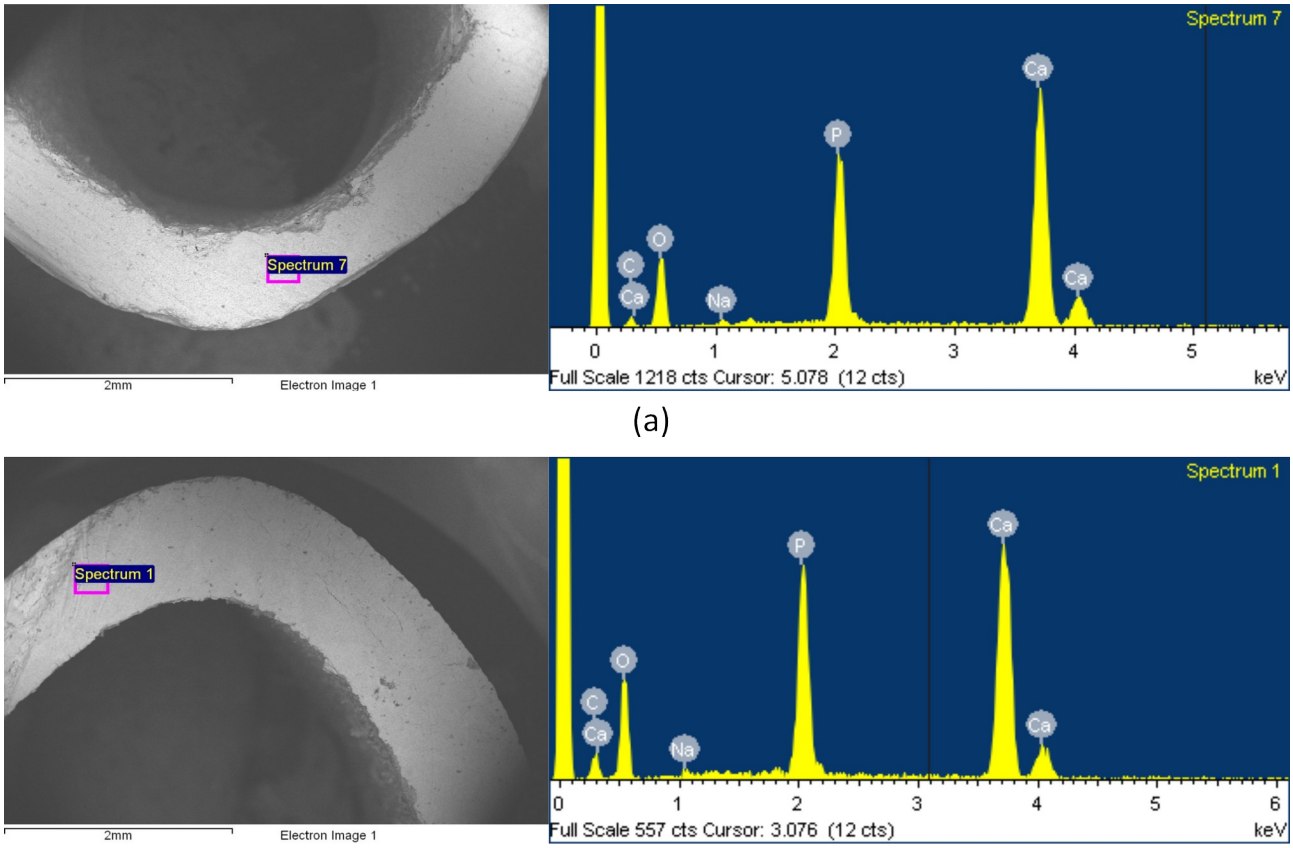

Figure 8.65: (a) Left: SEM image of the transverse surface of healthy bone. Right: EDX spectrum corresponding to the highlighted region of the SEM image. (b) Left: SEM image of the transverse surface of osteoporotic bone. Right: EDX spectrum corresponding to the highlighted region of the SEM image.

Table 9: Elemental analysis of healthy and osteoporotic bone samples.

	Healthy				Osteoporotic			
Element	Weight%	Atomic%	Compd%	Formula	Weight%	Atomic%	Compd%	Formula
C K	6.57	11.34	24.07	CO_2	9.94	15.97	36.41	CO_2
Na K	0.72	0.65	0.97	Na_2O	0.76	0.64	1.02	Na_2O
P K	14.79	9.90	33.90	P_2O_5	13.38	8.34	30.65	P_2O_5
Ca K	29.35	15.18	41.06	CaO	22.82	10.99	31.92	CaO
O	48.57	62.93			53.11	64.08		
Totals	100.00				100.00			

After heating the samples to 700°C, the resolution of the X-ray diffraction pattern increased significantly (Fig. 8.66), permitting us to continue with the analysis using high-temperature data.

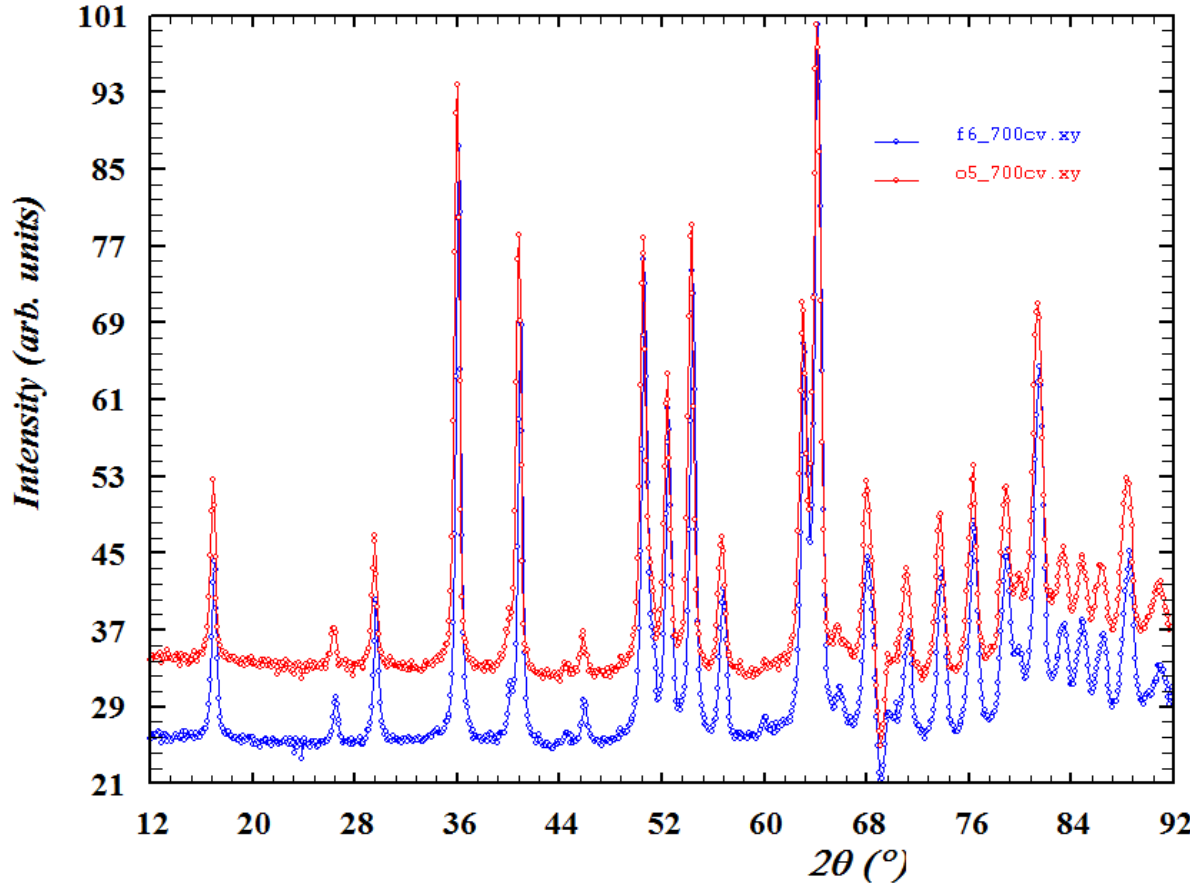

Figure 8.66: X-ray diffraction patterns of healthy (blue) and osteoporotic (red) samples at 700°C.

We performed LeBail and Rietveld refinements on the neutron diffraction patterns to investigate potential differences in the structural organization of HA between normal and osteoporotic bones. Additionally, we evaluated variations in the role of the CO_3^{2-} anion based on its structural position. We note the importance of studying biological apatites in contrast to synthetic ones, due to the ongoing controversy surrounding the exact configuration of carbonate substitution in the lattice of B-type carbonate HA [15]. This issue remains unresolved, as current models for carbonate substitution are derived indirectly from fitting powder diffraction patterns obtained from a limited number of synthetic specimens, which do not offer a fully convincing crystallographic model.

We tested two models, by Ivanova et al. [16] and Wilson et al. [17], which explore the structural models of carbonated HA with a focus on carbonate substitution at different phosphate sites using neutron diffraction. Both studies used the Rietveld method, to investigate the structural impacts of carbonate inclusion and the resulting charge compensation mechanisms. Despite their shared focus on Type B carbonated HA, there are notable similarities and differences in their approaches and findings. Both papers emphasize the replacement of PO_4^{3-} ions by CO_3^{2-} ions in the lattice and investigate the resulting structural adjustments. They discuss the mechanisms compensating for

the charge imbalance caused by this substitution, with both studies highlighting the role of vacancies, particularly in calcium and hydroxyl sites. Additionally, they report lattice parameter modifications due to carbonate substitution, including a reduction in the α parameter.

However, the proposed structural models differ significantly. Ivanova et al. propose a model that emphasizes disorder in the O3 site, splitting its occupancy into O3p and O3c positions. They identify carbonate ions as occupying sloping faces of the PO4 tetrahedra.

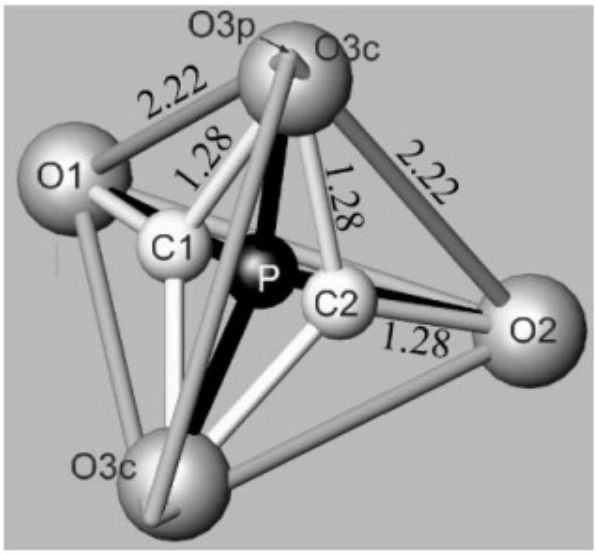

Figure 8.67: A PO_4^{3-}tetrahedron with CO_3^{2-} triangles on its faces. The C-O and O-O distances are indicated (in Å). Figure from [16].

In contrast, Wilson et al. test multiple structural models, including the "Face," "Mirror Plane," and "Side" models, ultimately refining a model in which CO_3^{2-} ions are disordered between mirror symmetry-related faces of vacant PO_4^{3-} sites. Their model positions the CO_3^{2-} ions at an angle of approximately 30° to the c-axis.

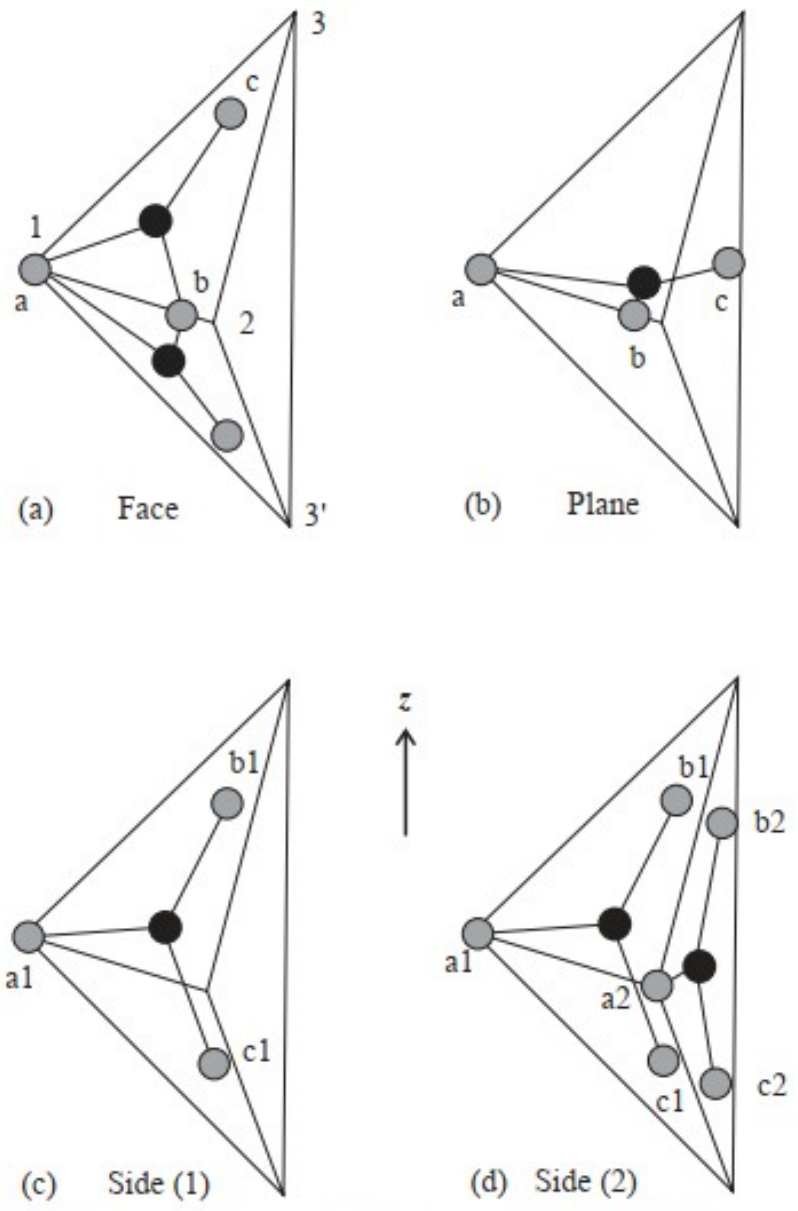

Figure 8.68: Schematic diagrams of the models tested by Wilson et al. The "Face" model (a) was proposed as the one that agrees more with chemical analyses. In this model, the CO_3^{2-} ions are disordered between the two-mirror symmetry-related faces of a vacant PO_4^{3-} site. The normal to the plane of the CO_3^{2-} ion was oriented at approximately 30° to the c-axis, a result consistent with previous polarized IR measurements on francolite and human dental enamel. Figure from [17].

Representative neutron diffraction data for healthy and osteoporotic samples heated at four different temperatures (400, 600, 700, and 800°C) are shown below (Fig. 8.69-8.72 and Fig. 8.73-8.76 for the healthy and osteoporotic samples, respectively). The LeBail fit is presented and demonstrates a strong correlation with the data.

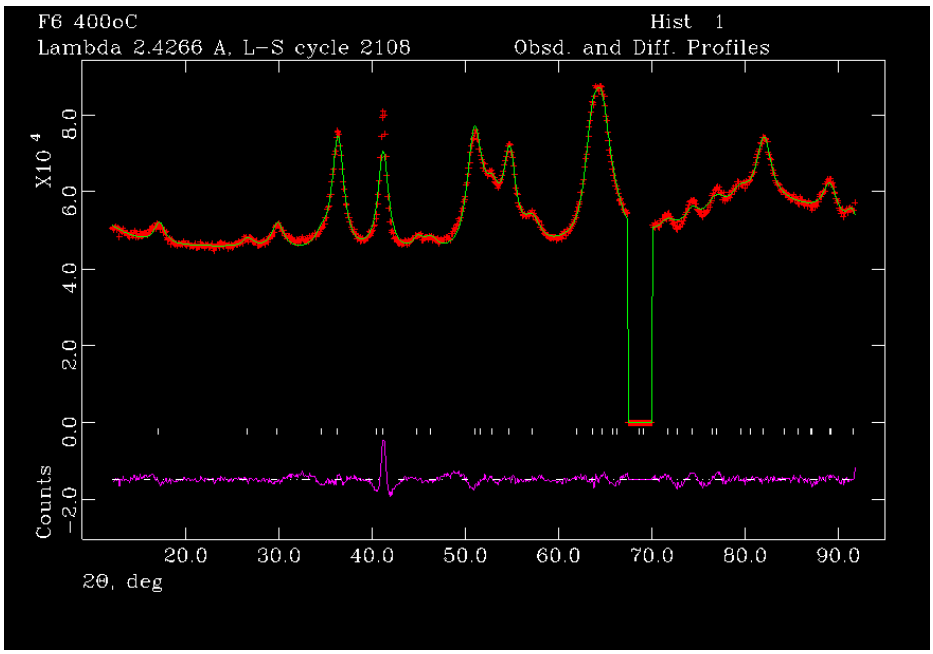

Figure 8.69: Representative Rietveld fit of the neutron diffraction data (red crosshairs) obtained from healthy samples at 400°C.

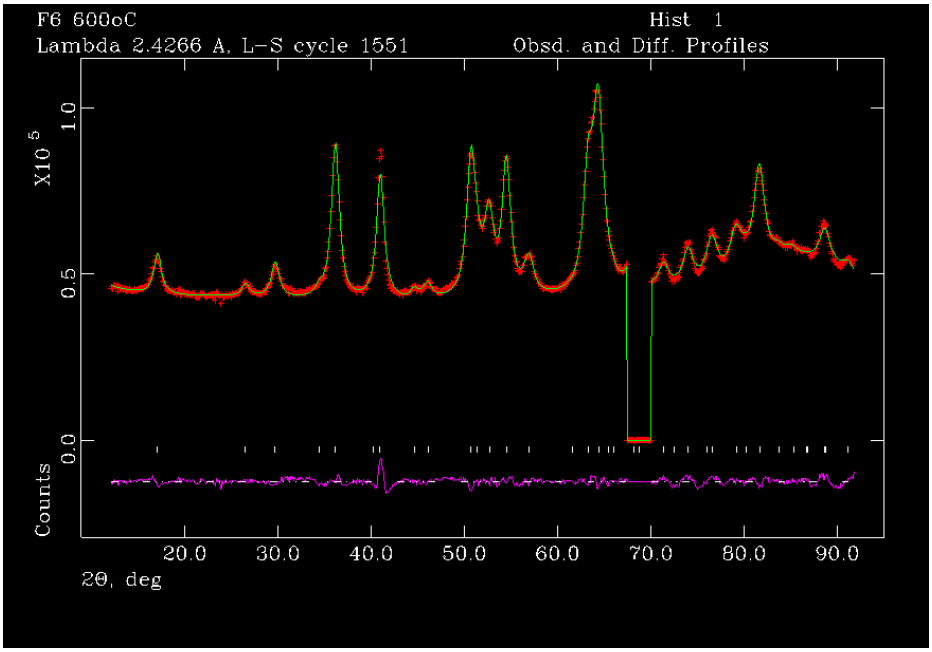

Figure 8.70: Representative Rietveld fit of the neutron diffraction data (red crosshairs) obtained from healthy samples at 600°C.

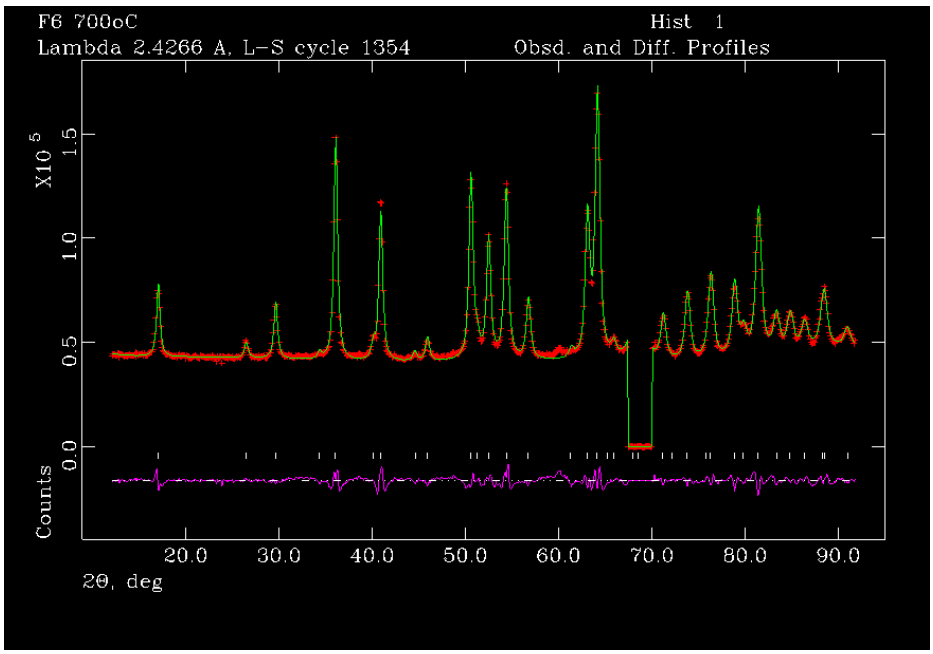

Figure 8.71: Representative Rietveld fit of the neutron diffraction data (red crosshairs) obtained from healthy samples at 700°C.

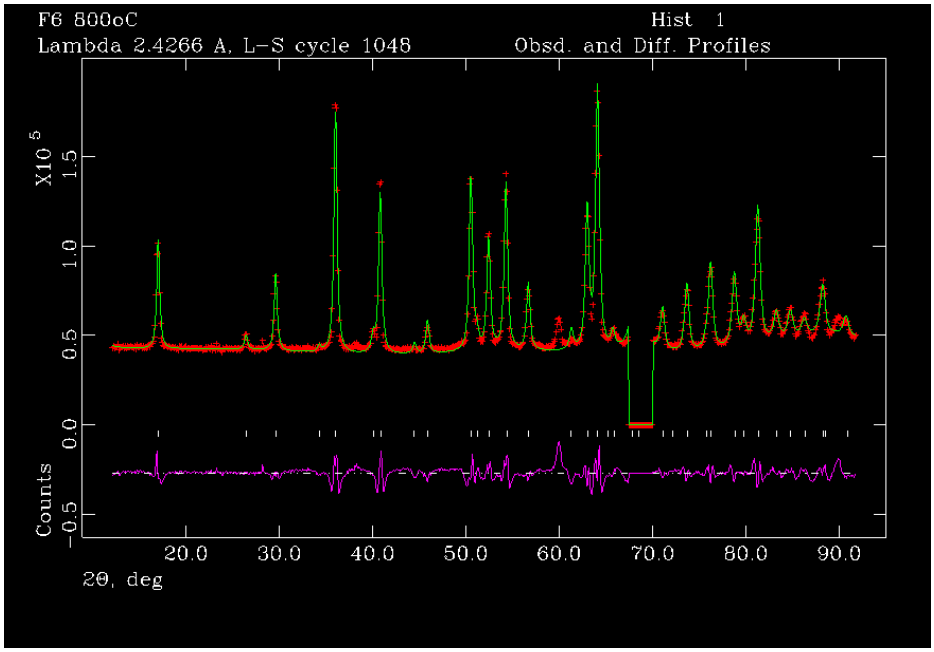

Figure 8.72: Representative Rietveld fit of the neutron diffraction data (red crosshairs) obtained from healthy samples at 800°C.

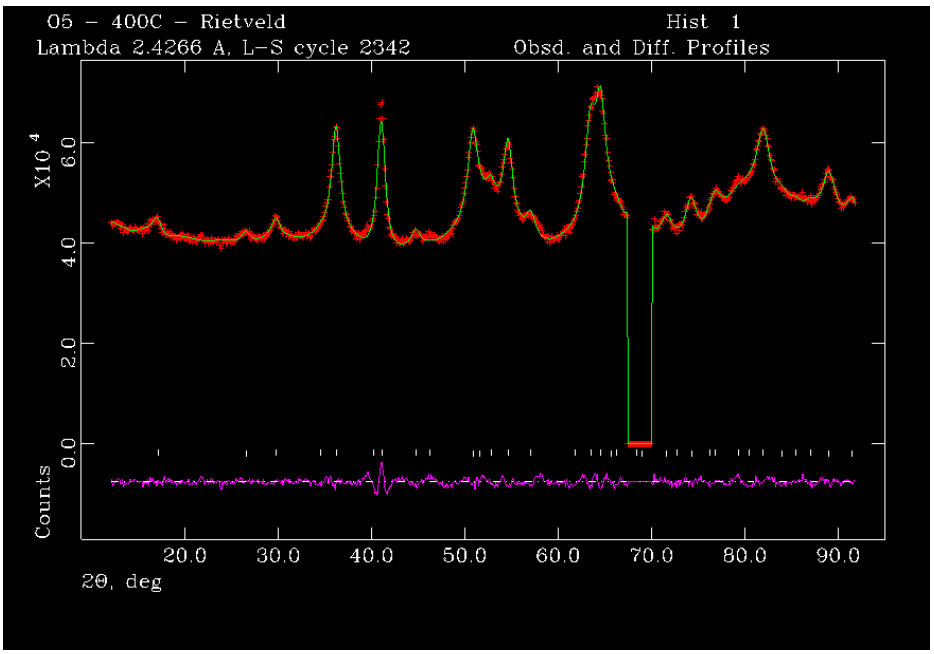

Figure 8.73: Representative Rietveld fit of the neutron diffraction data (red crosshairs) obtained from osteoporotic samples at 400°C.

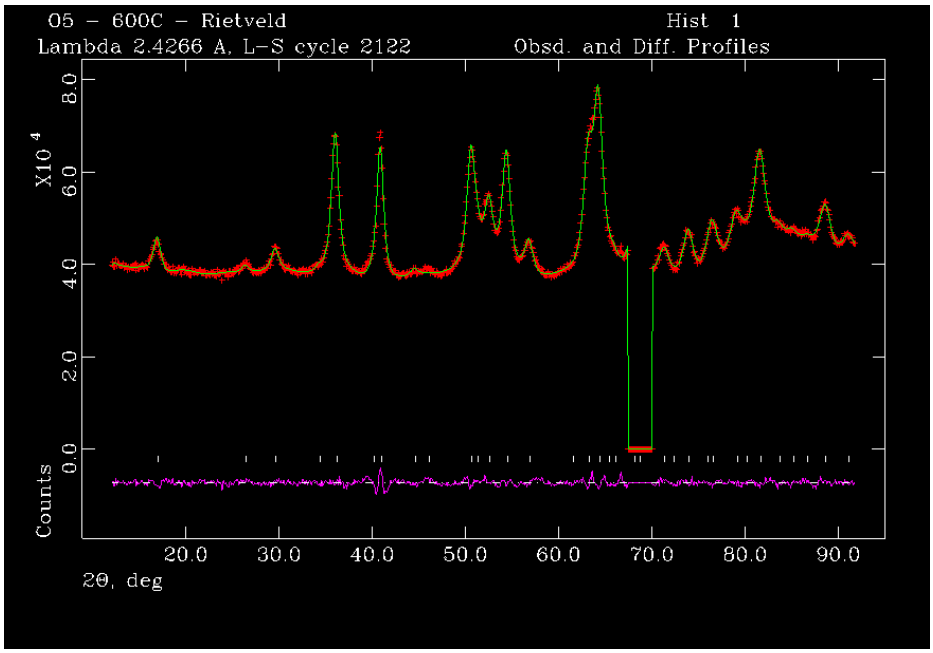

Figure 8.74: Representative Rietveld fit of the neutron diffraction data (red crosshairs) obtained from osteoporotic samples at 600°C.

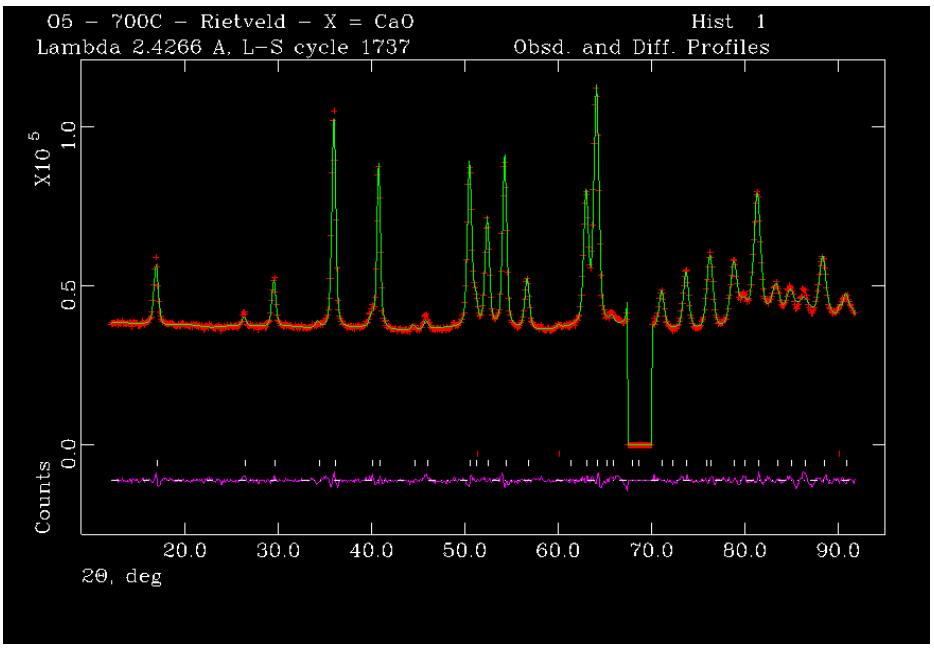

Figure 8.75: Representative Rietveld fit of the neutron diffraction data (red crosshairs) obtained from osteoporotic samples at 700°C.

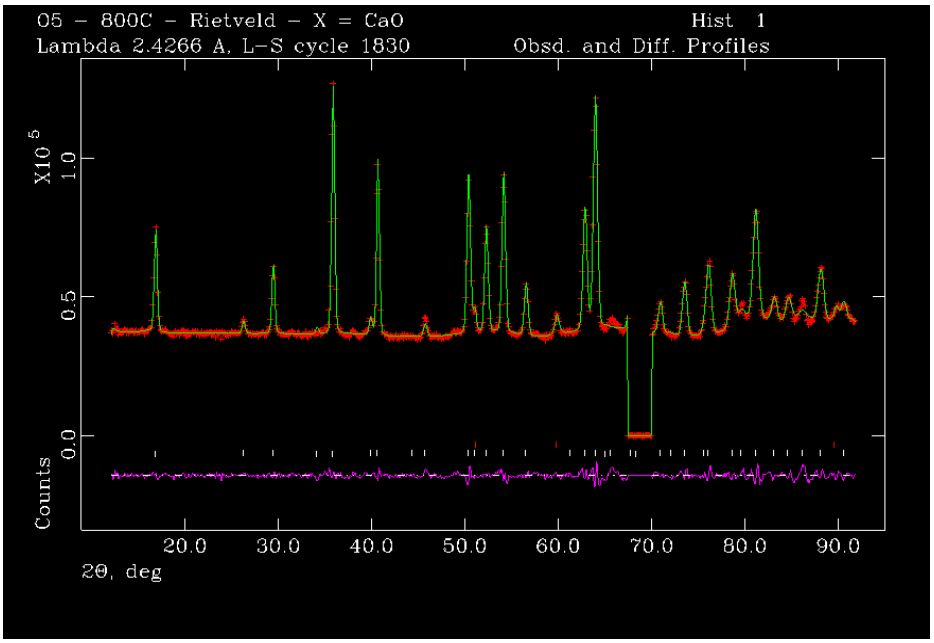

Figure 8.76: Representative Rietveld fit of the neutron diffraction data (red crosshairs) obtained from osteoporotic samples at 800°C.

During the Rietveld refinement, a spurious Bragg peak was evident in both types of samples at 60° 2θ, attributed to the evolution of CaO at high temperatures and fitted as an additional structural phase.

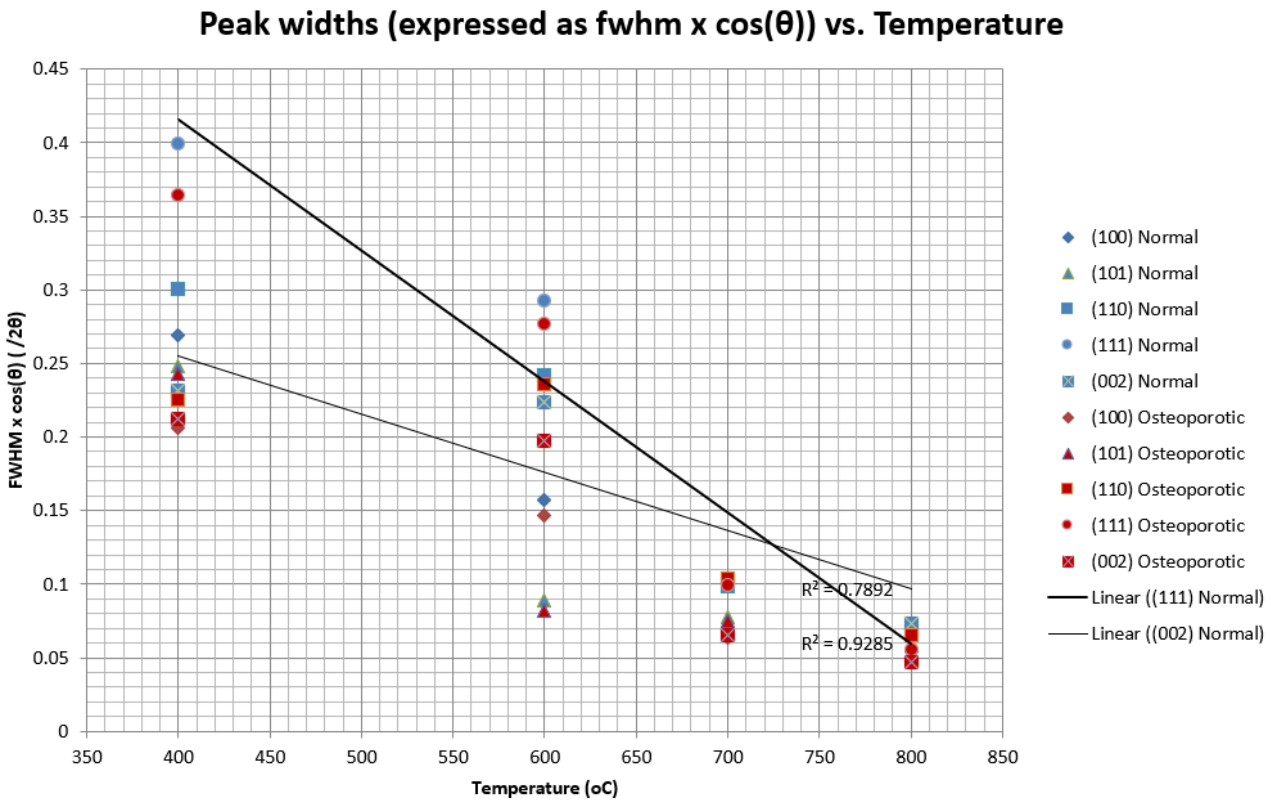

Figure 8.77: Normalized crystallinity as measured by 2ϑ vs FWHM for all samples across all temperatures.

To assess the crystallinity, we evaluated the expression $FWHM \times \cos(\theta)/\lambda$, which is often used as a measure of the broadening of diffraction peaks. Here, FWHM quantifies the width of a diffraction peak, with broader peaks indicating smaller crystallite sizes and/or higher lattice strain, both of which correspond to lower crystallinity. The inclusion of $\cos(\theta)$ accounts for the angular dependence of the diffraction peaks, ensuring consistency across peaks at different angles. The λ (wavelength) term normalizes the calculation, making it independent of the radiation source used, whether X-rays or neutrons. Hence, the above expression provides a normalized measure of peak broadening, which is inversely proportional to crystallite size and directly related to lattice strain. As a result, lower values of $FWHM \times \cos(\theta)/\lambda$ generally indicate sharper peaks and higher crystallinity, while higher values suggest greater disorder, smaller crystallites, or strain within the material.

Fig. 8.77 shows the relationship between $FWHM \times \cos(\theta)/\lambda$ (a measure related to diffraction peak broadening) and temperature for different Bragg peaks of HA in both normal and osteoporotic

samples. As temperature increases, the FWHM decreases for both the (111) and (002) reflections, indicating an improvement in crystallinity with thermal treatment. The linear trends fitted to the data, particularly for the (002) peak, show a strong correlation, with R^2 = 0.92 for the (002) peak and R^2 = 0.79 for the (111) peak. Thus, crystallinity improves consistently with heating, especially along the c-axis (002 reflection). At lower temperatures (400–600°C), the osteoporotic samples exhibit narrower peaks (lower FWHM values) compared to the healthy samples suggesting higher initial crystallinity in the osteoporotic samples. The difference is mostly noticeable in the low-angle (002) peak, which is more responsive to thermal treatment. As the temperature increases, both sample types undergo significant structural improvements, and by 800°C, the differences between healthy and osteoporotic samples diminish, reflecting similar levels of crystallinity. The (002) peak shows a more pronounced reduction in FWHM with temperature compared to the (111) peak, indicating that the structural order along the c-axis is more sensitive to thermal treatment than other lattice directions [18]. This trend highlights the strong influence of temperature in reducing defects, relieving lattice strain, and promoting grain growth, particularly along the c-axis. Our results suggest that osteoporotic HA initially possesses higher crystallinity, but thermal treatment effectively enhances the structural quality of both healthy and osteoporotic samples, eventually resulting in comparable crystallinity at higher temperatures.

Through Rietveld refinement, we confirmed that the Wilson model is more plausible compared to the one proposed by Ivanova. Table 10 presents the unit cell parameters for all samples across various temperatures and Table 11 presents the differences of the Ca/P ratio, and a and c unit cell parameters between healthy and osteoporotic samples.

Table 10: Stoichiometric and unit cell parameters for healthy and osteoporotic samples across measured temperatures.

Type	Temperature (°C)	Ca	P	Ca/P	C (CO_3^{2-})	*a* (Å)	*c* (Å)
Healthy	400	9.21	5.25	1.75	0.43	9.494	6.937
	600	9.86	5.72	1.72	0.14	9.514	6.955
	700	8.99	4.64	1.93		9.529	6.965
	800	8.78	4.55	1.92		9.539	6.980
Osteoporotic	400	8.72	5.48	1.59	0.24	9.484	6.929
	600	9.34	5.65	1.65	0.11	9.510	6.951
	700	9.43	4.95	1.90		9.517	6.965
	800	8.89	4.63	1.91		9.530	6.976

Table 11: Differences of the Ca/P ratio, and a and c unit cell parameters between healthy and osteoporotic samples across measured temperatures.

Temperature (°C)	Diff. Ca/P	Diff. *a* (Å)	Diff. *c* (Å)
400	0.16	0.010	0.008
600	0.07	0.004	0.004
700	0.03	0.012	0.000
800	0.01	0.009	0.004

The tables provide a comparative analysis of elemental composition, carbonate content, and unit cell parameters between healthy and osteoporotic HA samples across temperatures from 400°C to 800°C. The Ca/P ratio increases with temperature in both sample types, reflecting structural adjustments likely caused by carbonate decomposition. At lower temperatures, healthy samples exhibit a higher Ca/P ratio (e.g., 1.75 at 400°C compared to 1.59 in osteoporotic samples), larger unit cell dimensions (a and c), and higher carbonate content, indicative of greater structural integrity. These differences diminish at higher temperatures, as thermal treatment improves crystallinity and reduces structural defects in both samples, equalizing their properties by 800°C. Literature highlights that osteoporotic bone generally has a lower degree of mineralization, smaller crystallites, and higher carbonate substitution than healthy bone, contributing to its reduced mechanical strength [19,20]. This aligns with the table's observation of lower initial Ca/P ratios and smaller unit cell dimensions in osteoporotic HA. Additionally, the reduction in carbonate content with increasing temperature in both sample types is consistent with the thermal instability of carbonate ions in HA. As the temperature increases, the carbonate content in HA is expected to diminish due to the thermal instability of carbonate ions within the structure. This occurs through thermal decomposition where carbonate ions break down and release carbon dioxide (CO_2). In Type B carbonated HA, where CO_3^{2-} replaces PO_4^{3-}, the carbonate ions are more stable compared to Type A (where CO_3^{2-} replaces OH^-), but decomposition still occurs around 600–800°C depending on the sample's composition and crystallinity. Additionally, the removal of CO_3^{2-} impacts the lattice parameters, often resulting in a contraction as the carbonate ions are replaced by the smaller PO_4^{3-} groups or vacancies.

Healthy and osteoporotic HA samples are expected to exhibit distinct differences in carbonate content and thermal behavior due to variations in crystallinity and structural properties. Osteoporotic samples, with higher crystallinity, generally have lower initial carbonate content as highly crystalline HA incorporates less carbonate, whereas healthy samples may contain higher carbonate levels due to their lower crystallinity. The carbonate ions in osteoporotic samples are likely more tightly integrated into the lattice, making them slightly more thermally stable and resistant to decomposition at lower temperatures, while healthy samples may lose carbonate ions more rapidly upon heating, due to their less ordered structure. Phase transformations (like the presence of CaO) in osteoporotic samples are expected to occur more uniformly and at higher

temperatures, reflecting their greater structural order, whereas healthy samples may show more irregular transformations at lower temperatures due to higher lattice disorder. This is evident in Fig. 8.69-8.76 where the purple line denotes the goodness of fit. Consistently, healthy samples have lower quality fitting metrics than osteoporotic ones. Additionally, as CO_3^{2-} diminishes, osteoporotic samples are likely to exhibit predictable lattice parameter changes, consistent with stoichiometric trends, while healthy samples may show more significant and irregular fluctuations due to structural heterogeneity.

8.4. References

[1] Unal M, Ahmed R, Mahadevan-Jansen A, Nyman JS. Compositional assessment of bone by Raman spectroscopy. The Analyst 2021;146:7464. https://doi.org/10.1039/d1an01560e.

[2] Morris MD, Mandair GS. Raman Assessment of Bone Quality. Clin Orthop Relat Res 2011;469:2160–9. https://doi.org/10.1007/s11999-010-1692-y.

[3] Orkoula MG, Vardaki MZ, Kontoyannis CG. Study of bone matrix changes induced by osteoporosis in rat tibia using Raman spectroscopy. Vib Spectrosc 2012;63:404–8. https://doi.org/10.1016/j.vibspec.2012.09.016.

[4] Mandair GS, Morris MD. Contributions of Raman spectroscopy to the understanding of bone strength. BoneKEy Rep 2015;4:620. https://doi.org/10.1038/bonekey.2014.115.

[5] Mandair GS, Bateman TA, Morris MD. Raman spectroscopy of murine bone in response to simulated spaceflight conditions. Opt. Bone Biol. Diagn., vol. 7166, SPIE; 2009, p. 52–61. https://doi.org/10.1117/12.810048.

[6] Awonusi A, Morris MD, Tecklenburg MMJ. Carbonate Assignment and Calibration in the Raman Spectrum of Apatite. Calcif Tissue Int 2007;81:46–52. https://doi.org/10.1007/s00223-007-9034-0.

[7] Shapiro SS, Wilk MB. An analysis of variance test for normality (complete samples). Biometrika 1965;52:591–611. https://doi.org/10.1093/biomet/52.3-4.591.

[8] Paschalis EP, DiCarlo E, Betts F, Sherman P, Mendelsohn R, Boskey AL. FTIR microspectroscopic analysis of human osteonal bone. Calcif Tissue Int 1996;59:480–7. https://doi.org/10.1007/BF00369214.

[9] Ruppel ME, Miller LM, Burr DB. The effect of the microscopic and nanoscale structure on bone fragility. Osteoporos Int 2008;19:1251–65. https://doi.org/10.1007/s00198-008-0579-1.

[10] Kourkoumelis N, Zhang X, Lin Z, Wang J. Fourier Transform Infrared Spectroscopy of Bone Tissue: Bone Quality Assessment in Preclinical and Clinical Applications of Osteoporosis and Fragility Fracture. Clin Rev Bone Miner Metab 2019;17:24–39. https://doi.org/10.1007/s12018-018-9255-y.

[11] Gadeleta SJ, Boskey AL, Paschalis E, Carlson C, Menschik F, Baldini T, et al. A physical, chemical, and mechanical study of lumbar vertebrae from normal, ovariectomized, and nandrolone decanoate-treated cynomolgus monkeys (*macaca fascicularis*). Bone 2000;27:541–50. https://doi.org/10.1016/S8756-3282(00)00362-8.

[12] Matousek P, Clark IP, Draper ERC, Morris MD, Goodship AE, Everall N, et al. Subsurface Probing in Diffusely Scattering Media Using Spatially Offset Raman Spectroscopy. Appl Spectrosc 2005;59:393–400. https://doi.org/10.1366/0003702053641450.

[13] Vardaki MZ, Pavlou E, Simantiris N, Lampri E, Seretis K, Kourkoumelis N. Towards non-invasive monitoring of non-melanoma skin cancer using spatially offset Raman spectroscopy. The Analyst 2023;148:4386–95. https://doi.org/10.1039/D3AN00684K.
[14] Catanese III J, Featherstone JDB, Keaveny TM. Characterization of the mechanical and ultrastructural properties of heat-treated cortical bone for use as a bone substitute. J Biomed Mater Res 1999;45:327–36. https://doi.org/10.1002/(SICI)1097-4636(19990615)45:4<327::AID-JBM7>3.0.CO;2-L.
[15] Leventouri Th. Synthetic and biological hydroxyapatites: Crystal structure questions. Biomaterials 2006;27:3339–42. https://doi.org/10.1016/j.biomaterials.2006.02.021.
[16] Ivanova TI, Frank-Kamenetskaya OV, Kol'tsov AB, Ugolkov VL. Crystal Structure of Calcium-Deficient Carbonated Hydroxyapatite. Thermal Decomposition. J Solid State Chem 2001;160:340–9. https://doi.org/10.1006/jssc.2000.9238.
[17] Wilson RM, Elliott JC, Dowker SEP, Smith RI. Rietveld structure refinement of precipitated carbonate apatite using neutron diffraction data. Biomaterials 2004;25:2205–13. https://doi.org/10.1016/j.biomaterials.2003.08.057.
[18] Trzaskowska M, Vivcharenko V, Przekora A. The Impact of Hydroxyapatite Sintering Temperature on Its Microstructural, Mechanical, and Biological Properties. Int J Mol Sci 2023;24:5083. https://doi.org/10.3390/ijms24065083.
[19] Bala Y, Farlay D, Boivin G. Bone mineralization: from tissue to crystal in normal and pathological contexts. Osteoporos Int 2013;24:2153–66. https://doi.org/10.1007/s00198-012-2228-y.
[20] Taylor EA, Mileti CJ, Ganesan S, Kim JH, Donnelly E. Measures of Bone Mineral Carbonate Content and Mineral Maturity/Crystallinity for FT-IR and Raman Spectroscopic Imaging Differentially Relate to Physical–Chemical Properties of Carbonate-Substituted Hydroxyapatite. Calcif Tissue Int 2021;109:77–91. https://doi.org/10.1007/s00223-021-00825-4.

9. Conclusions

This thesis has explored the molecular and structural changes in bone under healthy and osteoporotic conditions using advanced spectroscopic and diffraction techniques. Raman spectroscopy and neutron powder diffraction provided complementary insights into bone composition and crystallographic structure, enabling a deeper understanding of bone quality and its response to pathological conditions. By combining these approaches, the study contributes to a more comprehensive characterization of bone's molecular and structural properties.

Raman spectroscopy revealed significant variations in bone quality parameters across skeletal sites, including the tibia, humerus, and femur. Parameters such as mineral-to-matrix ratios, collagen maturity, and crystallinity were quantified through spectral deconvolutions and band fitting methods. Multivariate analyses, including Principal Components Analysis (PCA) and Partial Least Squares Discriminant Analysis (PLS-DA), demonstrated the ability of Raman spectroscopy to effectively differentiate between healthy and osteoporotic bone. These findings highlight the diagnostic potential of Raman spectroscopy for assessing bone quality and detecting pathological changes.

Neutron powder diffraction provided insights into the crystallographic properties of bone mineral, particularly hydroxyapatite. The analysis confirmed that inflammation-induced osteoporosis results in measurable changes to mineral crystallinity and lattice parameters, reflecting alterations in bone's structural integrity. This technique offered a detailed perspective on how the crystallographic structure of bone is impacted under pathological conditions, complementing the molecular-level insights obtained through Raman spectroscopy.

Finally, this thesis contributed to methodological advancements by developing a Python package for preprocessing and analyzing Raman spectra. The software provides tools for standardized and customizable analyses, improving reproducibility and efficiency in spectroscopic research. These

developments not only supported the analyses in this study but also offer a framework for future investigations of bone and other complex biomaterials.

Περίληψη

Η οστεοπόρωση, μια μεταβολική διαταραχή των οστών που χαρακτηρίζεται από ελαττωμένη οστική μάζα και εξασθενημένη μικροαρχιτεκονική, αποτελεί σημαντική πρόκληση λόγω της συσχέτισής της με αυξημένο κίνδυνο καταγμάτων. Η παρούσα διατριβή ερευνά τις μοριακές και δομικές αλλαγές που σχετίζονται με την οστεοπόρωση χρησιμοποιώντας μια διεπιστημονική προσέγγιση, συνδυάζοντας τη φασματοσκοπία Raman, την περίθλαση νετρονίων σε σκόνη, και ένα μοντέλο οστεοπόρωσης που προκαλείται από φλεγμονή. Συνολικά οι μέθοδοι αυτές παρέχουν πληροφορίες σχετικά με τη σύνθεση και τις κρυσταλλογραφικές ιδιότητες του οστού, επιτρέποντας μια ολοκληρωμένη αξιολόγηση της οστικής ποιότητας.

Αναλύθηκαν δείγματα οστών που ελήφθησαν από διαφορετικές περιοχές (κνήμη, βραχίονα, μηρό, και πλευρό) υγιών ζώων και ζώων στα οποία προκλήθηκε οστεοπόρωση μέσω φλεγμονής. Η φασματοσκοπία Raman χρησιμοποιήθηκε για τη διερεύνηση φασματικών περιοχών που σχετίζονται με την οστική ποιότητα, όπως οι περιοχές των φωσφορικών και ανθρακικών ιόντων, του αμιδίου Ι, και περιοχές που σχετίζονται με το κολλαγόνο, χρησιμοποιώντας προηγμένες τεχνικές προεπεξεργασίας και υπολογιστικά εργαλεία. Εξειδικευμένο λογισμικό που αναπτύχθηκε για την παρούσα διατριβή διευκόλυνε την εφαρμογή μεθόδων πολυπαραμετρικής ανάλυσης, συμπεριλαμβανομένων της ανάλυσης κυρίων συνιστωσών (Principal Component Analysis; PCA), της ανάλυσης διάκρισης μερικών ελαχίστων τετραγώνων (Partial Least Squares Discriminant Analysis; PLS-DA), καθώς και την αποσυνέλιξη κορυφών. Πραγματοποιήθηκε ποσοτικός προσδιορισμός των παραμέτρων της οστικής ποιότητας, συμπεριλαμβανομένων της κρυσταλλικότητας του υδροξυαπατίτη, του λόγου του ανόργανου μέρους του οστού προς το οργανικό, η ωριμότητα του κολλαγόνου, και η ανθρακική υποκατάσταση, με σκοπό τον προσδιορισμό συστημικών αλλαγών και αλλαγών που οφείλονται στη θέση του οστού.

Η περίθλαση νετρονίων σε σκόνη παρείχε λεπτομερείς πληροφορίες για την κρυσταλλογραφική δομή του ανόργανου τμήματος του οστού. Η τεχνική αυτή προσέφερε πολύτιμες πληροφορίες για την ατομική διάταξη και τη σύνθεση των φάσεων του υδροξυαπατίτη, ενισχύοντας την κατανόηση των δομικών μεταβολών που σχετίζονται με την οστεοπόρωση.

Τα αποτελέσματα κατέδειξαν σημαντικές διαφοροποιήσεις στη μοριακή σύνθεση και τις κρυσταλλογραφικές ιδιότητες σε όλες τις σκελετικές περιοχές, υπογραμμίζοντας τον αντίκτυπο της οστεοπόρωσης που προκαλείται από φλεγμονή. Με τον συνδυασμό της φασματοσκοπίας Raman, της περίθλασης νετρονίων και του μοντέλου προκλητής οστεοπόρωσης μέσω φλεγμονής, η εργασία αυτή δημιουργεί ένα αναλυτικό πλαίσιο για τη μελέτη της υγείας του σκελετού. Επιπλέον, το εξειδικευμένο λογισμικό που αναπτύχθηκε στο πλαίσιο αυτής της έρευνας συμβάλλει στην ακρίβεια και την αναπαραγωγιμότητα αναλύσεων φασματοσκοπίας Raman και παρέχει ένα ακόμη εργαλείο για φασματοσκοπικές αναλύσεις στην επιστημονική κοινότητα.

Abstract

Osteoporosis, a metabolic bone disorder characterized by reduced bone mass and compromised microarchitecture, presents a significant challenge due to its association with increased fracture risk. This thesis investigates the molecular and structural changes in bone associated with osteoporosis using a multidisciplinary approach, combining Raman spectroscopy, neutron powder diffraction, and an inflammation-mediated osteoporosis (IMO) model. These methods collectively provide insights into the compositional, and crystallographic properties of bone, enabling a comprehensive evaluation of bone quality.

Bone samples, including healthy and osteoporotic specimens generated using the IMO model, were analyzed across multiple skeletal sites—tibia, humerus, femur, and rib. Raman spectroscopy was employed to explore bone quality-specific spectral regions, such as phosphate, carbonate, amide I, and collagen-related bands, using advanced preprocessing techniques and computational tools. Custom software developed for this thesis facilitated multivariate analyses, including Principal Component Analysis (PCA), Partial Least Squares Discriminant Analysis (PLS-DA), as well as band deconvolution. Quantitative bone quality parameters, including mineral crystallinity, mineral-to-matrix ratio, collagen maturity, and carbonate substitution, were calculated to reveal site-specific and systemic changes.

Neutron powder diffraction complemented these findings by providing detailed information on the crystallographic structure of bone mineral. This technique offered valuable insights into the atomic arrangement and phase composition of hydroxyapatite, enhancing the understanding of structural alterations associated with osteoporosis.

The results reveal significant trends and variations in molecular composition and crystallographic properties across skeletal sites, underscoring the impact of inflammation-induced osteoporosis. By combining Raman spectroscopy, neutron diffraction, and the IMO model, this work establishes a robust analytical framework for studying skeletal health. Furthermore, the custom software developed as part of this research advances the precision and reproducibility of Raman spectral analysis and provides another tool for spectroscopic analyses to the scientific community.

Published work

The publications directly related to the work presented in this thesis are as follows:

1. Pavlou E, Zhang X, Wang J, Kourkoumelis N. *Raman spectroscopy for the assessment of osteoarthritis*. Ann Joint. 2018 Oct;3:83–83.
2. Pavlou E, Kourkoumelis N. *Deep adversarial data augmentation for biomedical spectroscopy: Application to modelling Raman spectra of bone.* Chemometrics and Intelligent Laboratory Systems. 2022 Sep;228:104634.
3. Pavlou E, Kourkoumelis N. *Preprocessing and Analyzing Raman Spectra Using Python.* Engineering Proceedings. 2023; 56(1):28.

In addition to these thesis-related publications, I have also contributed to several other works during my PhD, which are not directly included in this thesis but reflect broader research efforts and collaborations:

4. Petrokilidou C, Pavlou E, Gaitanis G, Bassukas ID, Saridomichelakis MN, Velegraki A, et al. *The lipid profile of three Malassezia species assessed by Raman spectroscopy and discriminant analysis*. Molecular and Cellular Probes. 2019 Jun 25;101416.
5. Chrimatopoulos C, Pavlou E, Kourkoumelis N, Sakkas V. *Discriminating the salivary profile of athletes using ATR-FTIR spectroscopy and chemometrics.* Chemometrics and Intelligent Laboratory Systems. 2022 Nov;230:104660.
6. Vardaki MZ, Pavlou E, Simantiris N, Lampri E, Seretis K, Kourkoumelis N. *Towards non-invasive monitoring of non-melanoma skin cancer using spatially offset Raman spectroscopy.* Analyst. 2023;148(18):4386–95.
7. Pavlou E, Gaitanis G, Bassukas ID, Kourkoumelis N. *BCC and Immunocryosurgery scar differentiation through computational resolution-enhanced OCT images and skin optical attenuation: A proof-of-concept study.* Experimental Dermatology. 2024 Jan;33(1):e15019.
8. Petrokilidou C, Pavlou E, Velegraki A, Simou A, Marsellou I, Filis G, et al. *Characterization and Differentiation of Candida auris on Dixon's Agar Using Raman Spectroscopy.* Pathogens. 2024 Nov;13(11):978.

Conference proceedings:

1. Petrokilidou C, Pavlou E, Toli A, Economou E, Kalef-Ezra J, Kourkoumelis N. T*he effect of ambient evaporative loss on the reproducibility of deuterium oxide dilution measurements assessed by FTIR spectroscopy.* IAEA International Symposium; 2018 13/12; Vienna, Austria.
2. Vardaki M, Seretis K, Pavlou E, Lampri E, Gaitanis G, Bassukas I, et al. *Towards non-invasives monitoring of non-melanoma skin cancer using spatially offset Raman spectroscopy.* Spec 2022 - 12th International Conference on Clinical Spectroscopy; 2022 23/06; Dublin, Ireland.
3. Pavlou E, Kourkoumelis N. *PyFasma: an open-source Python package for the pre-processing and multivariate analysis of Raman spectra*. Spec 2024 - 13th International Conference on Clinical Spectroscopy; 2024 06/06; Ioannina, Greece.
4. Petrokilidou C, Pavlou E, Velegraki A, Simou A, Marcellou I, Gaitanis G, et al. *Raman spectroscopy for the evaluation of Candida auris metabolomics.* Spec 2024 - 13th International Conference on Clinical Spectroscopy; 2024 06/06; Ioannina, Greece.
5. Pavlou E, Kourkoumelis N. *A versatile and intuitive workflow for the analysis of Raman spectra using Python*. 2nd Panhellenic Congress of Medical Physics; 2024 06/10; Athens, Greece.
6. Petrokilidou C, Pavlou E, Velegraki A, Simou A, Marcellou I, Gaitanis G, et al. *Raman Spectroscopy towards the evaluation of Candida auris metabolomics*. 2nd Panhellenic Congress of Medical Physics; 2024 06/10; Athens, Greece.